

Gazetas, Orestis (2025) *Tracing the origin of methane using clumped isotope geochemistry*. PhD thesis

https://theses.gla.ac.uk/85591/

Copyright and moral rights for this work are retained by the author

A copy can be downloaded for personal non-commercial research or study, without prior permission or charge

This work cannot be reproduced or quoted extensively from without first obtaining permission from the author

The content must not be changed in any way or sold commercially in any format or medium without the formal permission of the author

When referring to this work, full bibliographic details including the author, title, awarding institution and date of the thesis must be given

Enlighten: Theses
<a href="https://theses.gla.ac.uk/">https://theses.gla.ac.uk/</a>
research-enlighten@glasgow.ac.uk

# Tracing the Origin of Methane Using Clumped Isotope Geochemistry

# **Orestis Gazetas**

Submitted in fulfilment of the requirements for the degree of Doctor of Philosophy

Scottish Universities Environmental Research Centre
College of Science and Engineering
University of Glasgow

#### **Abstract**

Methane (CH<sub>4</sub>) is the main component of natural gas and the second most abundant greenhouse gas produced by natural and anthropogenic sources. Stable isotopic compositions of carbon and hydrogen ( $\delta^{13}$ C and  $\delta$ D) have improved our understanding on the production and sink pathways of methane in the atmosphere, subsurface, freshwater and marine environments. However, the overlapping of  $\delta^{13}$ C and  $\delta D$  values between diverse sources, produce ambiguous results difficult to interpret. Due to technological advancements, the clumped isotopic compositions  $\Delta^{13}CH_3D$  and  $\Delta^{12}CH_2D_2$  can be measured using HR-IRMS, providing additional insights into the formation temperature and origin of methane. This PhD thesis includes a description of the work carried out for testing, establishing, and validating methods for the purification of methane, the preparation of the equilibrated aliquots, and the measurement of bulk and clumped isotopologues at the Clumped Isotope Laboratory in SUERC. In this thesis, those methods were applied to understand the methane formation in a world-class helium deposit in Virginia gas field (Witwatersrand basin). The results suggest a dominant microbial source of the gas with smaller but ultimately significant contribution from abiotic sources. The data suggest negligible at best contributions from thermogenic sources. The large  $\Delta^{13}$ CH<sub>3</sub>D values (>7‰) and the trend identified were consistent with a scenario for anaerobic oxidation of methane by methanotrophs, with no more than ~1.6% CH<sub>4</sub> consumption. Additionally, this PhD thesis includes work on calcite veins associated with a fracture network, in order to identify any potential relationship between calcites and methane in the Virginia gas field. The origin of carbon was assessed in the calcites through measuring the  $\delta^{13}$ C, and has been suggested to be a mixture of marine sources and carbon deriving from the oxidation of organic matter. The  $\delta^{18}$ O of the calcites and the precipitation temperatures of the calcites T<sub>47</sub>, indicate a mixture of two precipitating fluids; one related to hydrothermal sources and one consistent with a palaeometeoric origin. The T<sub>47</sub> of the calcites veins indicate that the calcite precipitation has preceded the formation of the dominant microbial CH<sub>4</sub>, as the precipitation temperatures are in average greater than the limit of life at 122°C. Overall, no clear relationship between the calcites and methane is identified, however I discuss the different scenarios.

# Table of Contents

Table of Contents	3
List of Tables	7
List of Figures	8
Glossary of Abbreviations and Definitions	16
1. Introduction	17
1.1. Natural Gas	18
1.2. Atmospheric Methane (CH <sub>4</sub> )	21
1.3. Tracers of Methane	26
1.4. Thesis Overview	28
2. Geochemistry of Methane	30
2.1. Chapter Overview	30
2.2. Conventional Stable Isotopic Compositions	30
2.2.1. Introduction	30
2.2.2. Theory and Definitions	30
2.2.3. Stable Isotope Signatures of Methane	32
2.2.4. Measurement Techniques	33
2.2.5. Methane Sources	38
2.2.6. Molecular and Isotopic Compositions	57
2.2.7. Methane (CH <sub>4</sub> ) Sinks	62
2.3. Clumped Isotopes of Methane	69
2.3.1. Fundamentals	70
2.3.2. Methane Sources & Clumped Isotopic Signatures	72
2.3.3. Isotopic Effects of Non-equilibrium Processes	76
3. Analytical methods	88
3.1 Overview	88
3.2 Purification and Preparation of Methane	88
3.2.1 Purification	88
3.2.2 Preparation	90
3.3 Equilibrated Gases	91
3.3.1 Introduction	91
3.3.2 High-temperature Experiments	92
3.3.3 Low-temperature Experiments	93
3.4 Mass Spectrometer-Ultra 253	94
3.5 Methane Measurements	99
2.5.1 Proliminary Charles	00

3.5.2	Measurement of $\delta^{13}$ C & $\delta^{13}$ CH <sub>3</sub> D	101
3.5.3	Measurement of $\delta^{12}CH_2D_2$	103
3.5.4	Measurement of δD	104
3.6 D	Data Processing	106
3.6.1.	Validation of Methods	106
3.6.2.	Calculation of Isotopic Compositions	109
3.6.3.	Error Propagation	114
4. Origin	of Methane in Virginia gas field	117
4.1 Ir	ntroduction	117
4.2	Geological Context	119
4.2.1	Geology	119
4.2.2	Methane in Witwatersrand	119
4.3 N	1ethods	120
4.3.1	Gas Sampling	120
4.3.2	Laboratory Methods	121
4.4 R	Results	122
4.4.1	Gas Compositions	122
4.4.2	Molecular and Isotopic Compositions	123
4.4.3	Clumped Isotopic compositions	125
4.5 C	Discussion	127
4.5.1	Temporal Evolution of δ <sup>13</sup> C	127
4.5.2	Diffusion	129
4.5.3	Isotope Exchange with H <sub>2</sub> O	130
4.5.4	Mixing	132
4.5.5	Anaerobic Oxidation of Methane (AOM)	135
4.5.6	Model	138
4.6. C	Conclusions	140
5. Origin	of Carbonate in the Virginia Gas Field Reservoir Rocks	141
5.1. Ir	ntroduction	141
5.2. N	Nomenclature & Stable Isotopes	143
5.2.1.	Introduction	143
5.2.2.	Carbon Isotopes.	144
5.2.3.	Oxygen Isotopes	146
5.3. C	Clumped Isotope Thermometry	149
5.4. V	Vitwatersrand Basin	150
5.5. N	1ethods	150
5.5.1.	Sampling	150

5.5.2. Stable and Clumped Isotope Measurements	152
5.5.3. Data Processing	153
5.6. Results	155
5.6.1. $\delta^{13}$ C and $\delta^{18}$ O	155
5.6.2. $\Delta_{47}$ and Apparent Temperatures	156
5.7. Discussion	158
5.7.1. Thermal History of the Witwatersrand Basin	158
5.7.2. Origin of Carbon	161
5.7.3. Isotopic Constraints on the Precipitating Fluid	164
5.7.4. Calcite-CH <sub>4</sub> Relationship	167
5.8. Conclusions	170
6. Conclusions	171
6.1. Overview	171
6.1.1. Analytical Developments	171
6.1.2. Methane in Virginia Gas Field	172
6.1.3. Calcites in Virginia Gas Field	173
Appendices	175
Appendix I: Calculations of isotopic signatures for non-equilibrium processes.	175
Appendix II: Monte Carlo Simulations	177
Appendix III: Gas Chromatography and Mass Spectrometry Methodology	180
Gas Chromatography in SUERC	180
Preparation	180
Injection	181
Working gas measurement	181
Data processing	184
Appendix IV: Sampling map	187
Appendix V: Molecular and Isotopic Composition of Virginia samples	188
Appendix VI: AOM model outputs	189
Appendix VII: Calcites Results and Data Processing	190
Correction Scheme	190
Appendix VIII: Example of Monte Carlo simulation for error propagation	191
References	192

# **List of Tables**

Table 1.1: CO <sub>2</sub> emissions per energy unit for various fossil fuels19
Table 1.2: List of GHGs with their corresponding atmospheric lifetime and GWP (IPCC,
2007)
Table 2.1: List of different IRMS and laser spectroscopy instruments able to measure stable
and/or clumped isotopologues of CH <sub>4</sub> , including the internal precision of each system38
Table 2.2: Physiological characteristics corresponding to each methanogenic order. Obtained
from Angelidaki et al. (2011).
Table 2.3: Summary of fractionation factors at room temperature for methane oxidation
through OH and Cl reactions. Fractionation factors are defined as in equation 2.367
Table 2.4: Summary of fractionation factors at room temperature for AOM and AeOM68
Table 2.5: Summary of fractionation factors at room temperature for methane oxidation
through OH and Cl reactions81
Table 3.1: List of equilibrated samples prepared in SUERC and reported in Eldridge et al.
(2019), including temperature and duration of heating93
Table 3.2: Overview of CH <sub>4</sub> isotopologues measurements using the SUERC 253 Ultra. The
rarest isotopologues for each measurement are <sup>13</sup> CH <sub>3</sub> D <sup>+</sup> for the first measurement, <sup>12</sup> CH <sub>2</sub> D <sub>2</sub> <sup>+</sup>
for the second measurement and ${}^{12}\text{CH}_3\text{D}^+$ for the third measurement101
Table 4.1: Gas compositions measured for Virginia gas samples. Values normalised to 100%.
Table 4.2: Intercomparison of the molecular and stable isotopic compositions measured for
the wells in Virginia from this study, Karolyte et al. (2022) and using conventional IRMS in
SUERC

# **List of Figures**

Figure 1.1: Energy mixture distribution and trends from 1971 to 2015. The y-axis is expressed in millions of tons of oil equivalent (MTOE). Figure derived from Bothun (2021).
Figure 1.2: Energy mixture in 2011 and projected for year 2040. Figure from Bothun (2021) Under this scenario it is assumed that the crude oil use will diminish significantly by 2040.
Figure 1.3: Latest global methane budget from 2010 to 2019 including emissions estimations
from emission inventories (bottom-up) and inverse modelling (top-down) approaches
(Saunois et al., 2024)24
Figure 1.4: Atmospheric concentration of CH <sub>4</sub> since 1983 (Lan et al., 2024)25
Figure 1.5: Pie chart displaying the distribution of different environments for the methane
samples reported in the global database (Milkov and Etiope, 2018)
Figure 2.1: Distribution of isotopic compositions of C and H in CH <sub>4</sub> . Panel A) shows the
distribution of $\delta^{13}$ C in a compilation of data for 17,683 natural gases measured worldwide.
B) shows the distribution of $\delta D$ in compilation of data for 7,027 natural gases measured
worldwide. Figures adjusted from Milkov and Etiope (2018)
Figure 2.2: Plain schematic of hydrogen isotopologue measurement using IRMS (Kelly et
al., 2018)
Figure 2.3: TILDAS spectra for methane isotopologue measurements. Left panel shows the
laser targeting the stable isotopologues <sup>13</sup> CH <sub>4</sub> , <sup>12</sup> CH <sub>3</sub> D and clumped isotopologue <sup>12</sup> CH <sub>2</sub> D <sub>2</sub>
Right panel shows the laser spectra targeting the stable isotopologues <sup>13</sup> CH <sub>4</sub> , <sup>12</sup> CH <sub>3</sub> D and
clumped isotopologue <sup>13</sup> CH <sub>3</sub> D. Figure taken from Gonzalez et al. (2019)37
Figure 2.4: Schematic diagram describing the processes resulting to petroleum products and
hydrocarbon generation through maturation of organic matter (Shuai et al., 2018)39
Figure 2.5: Historical and projected natural gas production from conventional and
unconventional (Shale gas, Tight gas, Coalbed methane) resources in the United States of
America (IEA, 2016)
Figure 2.6: Global map of unconventional natural gas resources (Rajput and Thakur, 2016).
Figure 2.7: Summary of the three main pathways of methanogenesis (DasSarma et al., 2009).
Figure 2.8: Sources of microbial methane and their associated contributions in global
microbial emissions (Lyu et al., 2018)
Figure 2.9: Relative proportion of generated gases during maturation of organic matter.
Microbial methane can be produced initially by microbial processes at temperatures between
20-60°C in the source rock, while thermogenic methane is produced at temperatures >65 °C
Derived from Hunt (1979)
Figure 2.10: $\delta^{13}$ C vs $\delta^{2}$ H isotopic signatures (Schoell plot) for biotic (thermogenic and
microbial) and abiotic methane found in different geological settings (Etiope and Schoell
2014)
<u> </u>

Figure 2.11: $\delta^{13}$ C vs $\delta$ D plot, indicating the areas for microbial fermentation (green).
microbial carbonate reduction (light blue), thermogenic (red) and abiotic (purple) sources.
Figure 2.12: Types of AOM according to electron acceptor and microorganism involved (Cui et al., 2015)
Figure 2.13: The stable isotopologues of methane and their relative abundances by assuming
stochastic distribution of the isotopes and $\delta^{13}C = \delta D = 0$ %. Information derived from Stolper
et al. (2014b)
produced by thermogenic, abiotic and microbial sources fall on the thermodynamic equilibrium line. This refers to either the expected formation temperatures for each source
or the experimental/natural samples already reported in literature. Plot inspired by Liu et al. (2023)
Figure 2.15: Mixing scenarios for thermogenic- microbial mixtures with in $\Delta^{13}$ CH <sub>3</sub> D -
$\Delta^{12}\text{CH}_2\text{D}_2$ space a) typical mixing curve for gas mixtures with different bulk isotopic
compositions (Thermogenic: $\delta^{13}C = -35\%$ , $\delta D = -220\%$ , Microbial: $\delta^{13}C = -60\%$ , $\delta D = -60\%$
120%) and b) mixing path for gases with identical $\delta D$ at -220%, the mixing line nearly
coincides with the thermodynamic equilibrium line
Figure 2.16: a) Modelled diffusion pathway when assuming a gas with initial bulk isotopic
compositions $\delta^{13}C = -60\%$ and $\delta D = -220$ (shift by approximately +10% at 50% gas loss)
b) Modelled diffusion pathway in $\Delta^{13}CH_3D$ - $\Delta^{12}CH_2D_2$ space when assuming a gas with
initial compositions $\Delta^{13}\text{CH}_3\text{D} = 6\%$ and $\Delta^{12}\text{CH}_2\text{D}_2 = 20\%$ (shift by approximately -0.75% at 50% gas loss). Arrowhead indicates 50% gas loss79
Figure 2.17: Oxidation paths for Anaerobic oxidation of methane – green line (AOM) (Liu
et al., 2023), Aerobic oxidation of methane – grey line (AeOM- in closed system) (Krause
et al., 2022), oxidation by Cl and OH radicals (Haghnehagdar et al., 2017), when assuming a gas with initial compositions $\Delta^{13}$ CH <sub>3</sub> D = 6‰ $\Delta^{12}$ CH <sub>2</sub> D <sub>2</sub> = 20‰83
Figure 2.18: Geometric representation of statistical clumped isotope compositions. Derived
from Röckmann et al., 2016.
Figure 2.19: The impact of combinatorial effects due to the isotopic contrast between two
molecules (examples are given for the clumping of carbon, nitrogen and chlorine heavy
isotopes). Figure taken from Yeung (2016)87
Figure 3.1: Photograph of the vacuum apparatus and procedures used for handling and
purifying CH <sub>4</sub> -contained samples. Red colour indicates the removal of gases using vacuum
pumps. GC refers to the injection point for a gas syringe in order to sample gas for major
gas composition analysis using gas chromatography89
Figure 3.2: Diagram of the vacuum apparatus and inlet used for handling and purifying CH <sub>4</sub> -
contained samples. Red circle depicts the injection point for a gas syringe to measure major
gas compositions. A Pirani gauge and a pressure gauge are used to monitor the pressure at different points in the vacuum line90
Figure 3.3: Schematic depiction of the main components of the Ultra including the ion source
the electrostatic analyser (ESA), the transfer optics before and after the magnetic section,
and finally the detector array consisting of 9 collectors
Figure 3.4: Photograph of the Ultra 253 hosted in the Clumped Isotope laboratory at SUERC.
98

Figure 3.5: Illustration of the definition for the calculation of mass resolving power m/ $\Delta$ m
(Eiler et al., 2013). Qtegra software provides the calculation for either mass side (relatively
to the peak) automatically after a magnet scan
Figure 3.6: Peak scan for the measurement of <sup>12</sup> CH <sub>4</sub> <sup>+</sup> , <sup>13</sup> CH <sub>4</sub> <sup>+</sup> , <sup>13</sup> CH <sub>3</sub> D <sup>+</sup> using collectors L4,
L2, H2CDD (all in log-scale), respectively. Blue vertical line indicates approximately the position of measurement
Figure 3.7: Peak scan for the measurement of <sup>12</sup> CH <sub>4</sub> <sup>+</sup> and <sup>12</sup> CH <sub>2</sub> D <sub>2</sub> <sup>+</sup> using collectors L4 and
H4CDD (in log-scale), respectively. We require the "valleys" between <sup>13</sup> CH <sub>3</sub> D <sup>+</sup> and <sup>13</sup> CH <sub>5</sub> <sup>+</sup> ,
<sup>12</sup> CH <sub>2</sub> D <sub>2</sub> <sup>+</sup> and <sup>12</sup> CH <sub>4</sub> D <sup>+</sup> to be as close to zero as possible to ensure sufficient peak separation,
and a flat peak for <sup>12</sup> CH <sub>2</sub> D <sub>2</sub> <sup>+</sup> to minimise the measurement error. Blue vertical line indicates
approximately the position of measurement
Figure 3.8: Peak scan for the measurement of <sup>12</sup> CH <sub>4</sub> <sup>+</sup> and <sup>12</sup> CH <sub>3</sub> D <sup>+</sup> using collectors L2 and
H4CDD (in log-scale), respectively. Blue vertical line indicates approximately the position of measurement
Figure 3.9: Results for the equilibrated gases produced and measured in SUERC. The results
are reported against the absolute thermodynamic reference frame. Error bars refer to 1 S.E.
These equilibration experiments covered the temperature range from 250°C to 500°C. Every
point is a separately prepared and equilibrated aliquot of gas
Figure 4.1: Cross-section of wells sampled in Virginia gas field. Figure modified from Turner
et al. (2016).
Figure 4.2: $\delta^{13}$ C (reported against VPDB), against the ratio of abundances (C <sub>1</sub> /C <sub>2+</sub> ) of
methane (C <sub>1</sub> ) and higher hydrocarbons such as ethane, propane, butane (C <sub>2+</sub> ). This is a
compilation of data from this study (blue dots), data from Karolyte et al., (2022) (navy dots)
for Virginia wells, data from local gold mines (Virginia mines) such as Beatrix, Masimong,
Merriespruit from Ward et al., (2004) and Simkus et al. (2016) (grey diamonds), and data
- · · · · · · · · · · · · · · · · · · ·
from Witwatersrand coal and gold mines such as Evander, Middelbult, Driefontein, Kloof,
Mponeng, Tau Tona, Moab Khotsong from Ward et al. (2004), Sherwood Lollar et al. (2006),
Simkus et al. (2016), Nisson et al. (2023) (grey squares) Samples with $C_1/C_{2+}$ above 100,000,
have been capped at this value. The microbial (dark green), thermogenic (red) and abiotic
(yellow) areas are designed based on review by Milkov and Etiope (2018)
Figure 4.3: $\delta^{13}$ C (reported against VPDB) versus the isotopic composition of hydrogen in
methane, δD (reported against VSMOW). Symbols and fields derived from same sources as
in Figure 4.2. 125
Figure 4.4: Clumped isotopic compositions ( $\Delta^{13}CH_3D$ vs $\Delta^{12}CH_2D_2$ ) for gases from this
study (Virginia wells- blue dots), samples from Virginia mines (Beatrix and Masimong-
orange squares) and Witwatersrand mines (Kloof, Tau Tona- grey squares) reported in Young
et al. (2017). Microbial (green), low temperature abiotic (yellow), thermogenic (red) areas
are plotted based on previous studies (Young et al., 2017). Microbial area plotted based on
mesophiles and thermophiles temperature range (15°C- 65°C). Abiotic methane area refers
to low temperature methanation by Fischer- Tropsch reactions typically below 120 °C
(Etiope, 2013)
Figure 4.5: Diffusion scenarios considering the isotopic fractionation in bulk and clumped
isotopic compositions. Green arrow displays the diffusion trend for the residual gas, while
black arrow displays the trend for the diffused gas. All diffusive scenarios are calculated

using Graham's law and $\beta = 0.25$ (diffusion through water column). Arrow head's pointing at expected isotopic fractionation trend and indicates 50% loss
Figure 4.6: $\Delta^{13}\text{CH}_3\text{D}$ and $\Delta^{12}\text{CH}_2\text{D}_2$ plotted vs the fractionation between methane and
associated formation waters. This fractionation is reported as $\varepsilon_{\text{methane-water}}$ ( $\varepsilon_{\text{methane-water}}$
(D/H) <sub>methane</sub> /(D/H) <sub>water</sub> – 1). The equilibrium curve is calculated using Horibe and Craig
(1995) calibration. No water samples were collected in this study, calculations based on ar
average value for data reported in Warr et al. (2021) and $\delta D_{water}$ = -42%. Symbols as in Figure
4.1
Figure 4.7: $\delta^{13}$ C (reported against VPDB) versus the isotopic composition of hydrogen in
methane, $\delta D$ (reported against VSMOW). Dashed line indicates the mixing trend proposed
Figure 4.8: $\Delta^{13}CH_3D$ vs $\Delta^{12}CH_2D_2$ plot including the mixing lines amongst thermogenic
$(\delta^{13}C = -36.1\%, \delta D = -323.6\%)$ , microbial at equilibrium $(\delta^{13}C = -58.8\%, \delta D = -220\%)$
microbial out of equilibrium ( $\delta^{13}$ C = -58.8%, $\delta$ D = -220%), and abiotic ( $\delta^{13}$ C = -35%, $\delta$ D
= -225‰) endmembers. Clumped isotopic compositions based on the findings by Young e
al. (2017) for Kloof mine (thermogenic), Birchtree mine (microbial at equilibrium)
Methanococcus thermolithotrophicus (microbial out of equilibrium), Kidd Creek mine
(abiotic). Bulk isotopic compositions from microbial and abiotic endmembers derived from
this study
Figure 4.9: Clumped isotopic compositions in Witwatersrand with AOM model. ~1%
methane consumption
Figure 4.10: Clumped isotopic compositions in Witwatersrand with AOM model. Paths
indicate the two scenarios of 1 and 1.6% methane loss due to AOM
Figure 4.11: Schematic of the conceptual model including the geology and the processes
taking place within the basin. Blue circled areas symbolise the fracture fluid. Black polygons
depict the radiolytic elements (U, Th, K)
Figure 5.1: Diagram of carbon cycle and carbonate formation through the AOM in the
sediments of a shallow marine environment (Akam et al., 2020)
Figure 5.2: Variations in $\delta^{13}$ C (against VPDB) for carbon-bearing compounds in natura
environments (Wagner et al., 2018)
Figure 5.3: Typical variations of $\delta^{18}$ O (against SMOW) for materials from natura
environments within the atmosphere, hydrosphere and lithosphere (Grossman, 1998)147
Figure 5.4: Variations of $\delta^{18}$ O (against SMOW & VPDB) for materials from natural systems
Arrows and numbers indicate sources and processes (Delaygue, 2009)
Figure 5.5: Quartz-calcite vein sampled of approximately 16cm thickness The
Klipriviersberg lavas are noted.
Figure 5.6: The $\delta_{47}$ (difference between a sample and a heated gas at 1000°C) against $\Delta_4$
values expressed in permil (‰) of the carbonate standards (ETH1 to ETH4) in comparison
to natural and synthetic carbonate samples (Bernasconi et al., 2021)
Figure 5.7: $\delta^{13}$ C vs $\delta^{18}$ O values of calcite veins from the Witwatersrand basin. Blue squares
from this study, orange circles from Jaguin et al. (2010) for Masimong mine, grey squares
for other Witwatersrand mines from Jaguin et al. (2010) and Nisson et al. (2023) for other
Witwatersrand mines (Moab Khotsong, Orkney, Evander)
Figure 5.8: $\delta^{13}$ C vs T <sub>47</sub> values for the calcites sampled in Virginia gas field
Figure 5.9: $\delta^{18}$ O vs T <sub>47</sub> values for the calcites sampled in Virginia gas field

Figure 5.10: T <sub>47</sub> vs $\delta^{18}$ C	(VSMOW) of	the fluids	proposed	to occur	r within	the	fracture
system							166

#### Acknowledgements

Firstly, I would like to express my deepest gratitude to my three supervisors for giving me the opportunity to pursue this PhD and for their patience throughout. Matthieu, you have been an amazing mentor, and always there to guide and support me throughout this journey. I have learned so much from you and I will always be grateful.

A huge thank you to Fin, who has been a constant source of guidance, especially during the more challenging moments of this project. I will always cherish our conversations in Joburg.

To Issaku, thank you for our insightful discussions and for offering me a fresh perspective when I needed it the most.

I am also incredibly grateful to my friends and colleagues at SUERC (Melissa, Ugur, Alex, Andrew, Hamdan, and Papali) for bringing light to my days. To my amazing friends from Glasgow (Kostas, Aggelos, Nikos, Klimis, Giorgos, Spyros), who made Friday evenings something to look forward to, and to my dear friends from Greece (Vasilis, Theodosis, Ilias, Mpakis, Panos, Thodoris), who have supported me through every step of my life.

To my siblings, Giorgos, Thanasis, and Fei, your emotional support has meant everything to me. To my nephews, Philippos and Orfeas, who kept me busy during the summer, I miss you both dearly. And to my mother, Maria, for standing by my side through thick and thin, offering emotional and financial support especially at the last run. To my teacher Bedros, who I will always be grateful.

Finally, to the friends and family who left too soon but will never be forgotten. To my father, Vangelis, whose memory I carry with me every day. And to my dear friends, Giannakis and Harrys, who will forever remain in my heart.

#### Ithaka

As you set out for Ithaka
hope your road is a long one,
full of adventure, full of discovery.

Laistrygonians, Cyclops,
angry Poseidon—don't be afraid of them:
you'll never find things like that on your way
as long as you keep your thoughts raised high,
as long as a rare excitement
stirs your spirit and your body.

Laistrygonians, Cyclops,
wild Poseidon—you won't encounter them
unless you bring them along inside your soul,
unless your soul sets them up in front of you.

Keep Ithaka always in your mind.

Arriving there is what you're destined for.

But don't hurry the journey at all.

Better if it lasts for years,

so you're old by the time you reach the island,
wealthy with all you've gained on the way,
not expecting Ithaka to make you rich.

Ithaka gave you the marvellous journey.

Without her you wouldn't have set out.

She has nothing left to give you now.

And if you find her poor, Ithaka won't have fooled you.

Wise as you will have become, so full of experience,
you'll have understood by then what these Ithakas mean.

#### C.P. Cavafy: Collected Poems (Princeton University Press, 1975)

**Author's Declaration** 

I declare, except where explicit reference is made to the contribution of others, that this thesis

is the result of my own work and has not been submitted for any other degree at the

University of Glasgow or any other institution.

Printed Name: Orestis Gazetas

Signature:

O.Gazetas

15

## Glossary of Abbreviations and Definitions

**AOM** – Anaerobic oxidation of methane

**AeOM** – Aerobic oxidation of methane

**Combinatorial (statistical) effects** – A statistical artifact when two or more identical atoms occur within a molecule and may cause anticlumping signatures.

**Internal equilibrium** – The thermodynamic state where the distribution of isotopologues within a molecule, reflects equilibrium conditions at a specific temperature.

**Stochastic (random) distribution** – The distribution of isotopes at theoretically infinite temperatures.

**Working gas** – A reference gas of known bulk and clumped isotopic compositions used as in-laboratory standard.

δ (small delta) – Expresses the isotopic contrast between a sample and a reference gas (e.g. working gas or standard).

 $\Delta$  (capital delta) – Expresses the deviation of clumped isotopologue abundances from the stochastic distribution.

 $\Delta_{47}$  – The excess abundance of clumped isotopologues in mass 47 in CO<sub>2</sub> molecules relative to a random distribution, used as a proxy to reconstruct formation temperatures.

#### 1. Introduction

Methane is the simplest and most abundant alkane in nature, consisting of one carbon atom and four hydrogen atoms. Methane is a colourless and odourless gas initially identified by van Helmont and Brownrigg in the early 17<sup>th</sup> century (Tomory et al., 2010), followed by observations from Benjamin Franklin in 1764 and Alessandro Volta in 1776 who both observed CH<sub>4</sub> being emitted from freshwater environments (Etiope, 2015). However, these have not been the first records of methane occurrence in the history of humankind. Methane has been linked with myths and religious ceremonies in ancient times. For instance, the gas seepage and the burning flame of Chimaera (Antalya province, Turkey) has been linked with the mythological creature of Chimaera, which was believed to breath fire in Greek mythology, while the seepage is located next to the ruins of the temple devoted to the god of fire Hephaestus (Etiope, 2015). Other ancient fires located in Iran, Indonesia, Azerbaijan and Italy have been worshipped by ancient civilisations acting in many cases as sanctuaries devoted to religious figures (Bersani et al., 2013; Etiope, 2015). Nowadays, we know that those fires were preserved by gas seepage in those sites, associated predominantly with hyperalkaline waters (Etiope, 2015).

Methane occurs in a variety of terrestrial and extraterrestrial environments. In terrestrial environments, methane can be found in oxic and anoxic environments including marine and freshwater settings, permafrost, wetlands, the digestive tract of ruminants, geothermal and volcanic systems, and unconventional and conventional petroleum systems, often associated with oil (Milkov and Etiope, 2018). Methane has been detected in extraterrestrial bodies within and beyond our solar system (Blamey et al., 2015; Taubner et al., 2018; Madhusudhan et al., 2023), and has been considered as a potential biosignature (sign of life) for exoplanets (Harrison et al., 2021; Knutsen et al., 2021; Thompson et al., 2022). In our solar system, methane has been detected in Mars and Martian meteorites (Blamey et al., 2015, Yung et al., 2018), the upper atmosphere of Jupiter (Sánchez-López et al., 2022), in the atmosphere of Titan (Toon et al., 1988), and the oceans of Saturn's satellite Enceladus (Bouquet et al., 2015). The source of CH<sub>4</sub> in extraterrestrial environments has been a point of debate across the scientific community, with abiotic and microbial sources often proposed (Knutsen et al., 2021). If CH<sub>4</sub> were found to be microbial, it would provide clear evidence of life beyond Earth.

In this chapter, I highlight the importance of CH<sub>4</sub> as natural gas and as one of the greenhouse gases responsible for climate change. Briefly, I describe the ability of isotopes to provide

information about the sources of methane in the subsurface and atmosphere, and finally I present the structure of this thesis.

#### 1.1. Natural Gas

Methane is the primary constituent of natural gas and constitutes approximately 70–90% of the gas mixture. The remaining 10-30% typically includes C<sub>2</sub>-C<sub>5</sub> hydrocarbons, carbon dioxide, nitrogen, oxygen, and noble gases (predominantly He and Ar). The predominance of methane in natural gas underpins its significant economic role, as natural gas is a widely utilized energy resource globally.

Methane in nature can be generated by three main ways: biological, abiotic, and thermogenic processes. In a typical natural gas reservoir methane is produced primarily by the thermal breakdown of large organic molecules (Tissot and Welte, 1978), although mixtures of thermogenic and microbial methane have been detected worldwide (Stolper et al., 2015; Moore et al., 2018). Abiotic gas can be formed by different processes in the mantle or the subsurface but typically is not as abundant as microbial or thermogenic methane (Etiope and Sherwood Lollar, 2013; Etiope, 2015). The formation temperature range vary depending on the source of methane. For example, microbial gas typically forms at temperatures up to 60°C, which is the temperature range where methanogens thrive (Nozhevnikova et al., 2001). However, this depends on the strain of microorganism (Takai et al., 2008). Thermogenic gas usually forms at a temperature range between 80 °C to 220 °C, where the organic matter starts to break down into smaller organic molecules (Clayton, 1991; Thiagarajan et al., 2020). The temperature range of the abiotic methane formation is the least constrained due to the different settings where these processes occur. Some processes occur at approximately 100°C such as gas-water-rock interactions, while magmatic processes occur at temperatures above 500 °C (Etiope and Sherwood Lollar, 2013). In Chapter 2, the generation mechanisms for all sources of CH<sub>4</sub> are described in detail.

The global natural gas reserves are estimated at approximately 188 trillion cubic meters or equivalently at 6641 trillion cubic feet (BP, 2021). The majority of those reserves is located in Middle East (~40%), Central Asia and Russia (~30%), the North and South America (~12%) and China (~4.5%) (Fa et al., 2022). It is important to mention that these figures refer to the proven reserves, hence, those which can be recovered with the current economic and technological conditions (Fa et al., 2022). Further details about the natural gas reserves can be found in Chapter 2.

Since the early 20<sup>th</sup> century, natural gas has been utilised widely as an energy source compared to other fossil fuels due to the large global resources inventory of natural gas in a variety of environments. However, the consumption of natural gas coincided with environmental targets aiming to mitigate climate change. The combustion of natural gas produces lower CO<sub>2</sub> emissions per energy unit (Dones et al., 2004). In the table below, I present the relative values for different fossil fuels used globally as an energy source.

Table 1.1: CO<sub>2</sub> emissions per energy unit for various fossil fuels.

Fossil fuel	CO <sub>2</sub> emissions/energy unit (kg/GJ)
Oil	72
Coal	101
LPG	72
Natural gas	56

Another significant advantage of natural gas usage is the fact that is a cleaner energy source than oil or coal in terms of air pollution (Hannun and Razzaq, 2022). Ideally, when natural gas is combusted produces only carbon dioxide and water. Consequently, the preference of natural gas against coal and oil (or oil derivatives) can improve the air quality as the emissions of the main air pollutants such as particulate matter (PM<sub>10</sub>, PM<sub>2.5</sub>), nitrogen oxides and sulphur oxides are eliminated or at least reduced when natural gas is used (Kuang and Lin, 2023). Therefore, this results to an improvement in air quality with positive impacts on human health and ecosystems (Schneidemesser et al., 2020). However, natural gas produces CO<sub>2</sub> when combusted and CH<sub>4</sub> (the main constituent) is a greenhouse gas itself. Therefore, the consumption for energy generation or the leakage of natural gas contributes to global warming (Gursan and Gooyert, 2021).

The global natural gas consumption for electricity production and heating has increased by approximately 45% from 1971 to 2019 (Warsame et al., 2024). This coincides with the trends for other fossil fuels and energy sources as the energy demand has grown by approximately 2.5 times compared to 1971 levels (Bothun, 2021). Specifically for electricity generation, natural gas has increased its share in the energy mixture by approximately two times, accounting for 12.1% in 1973 and 22.9% in 2015 (Bothun, 2021).

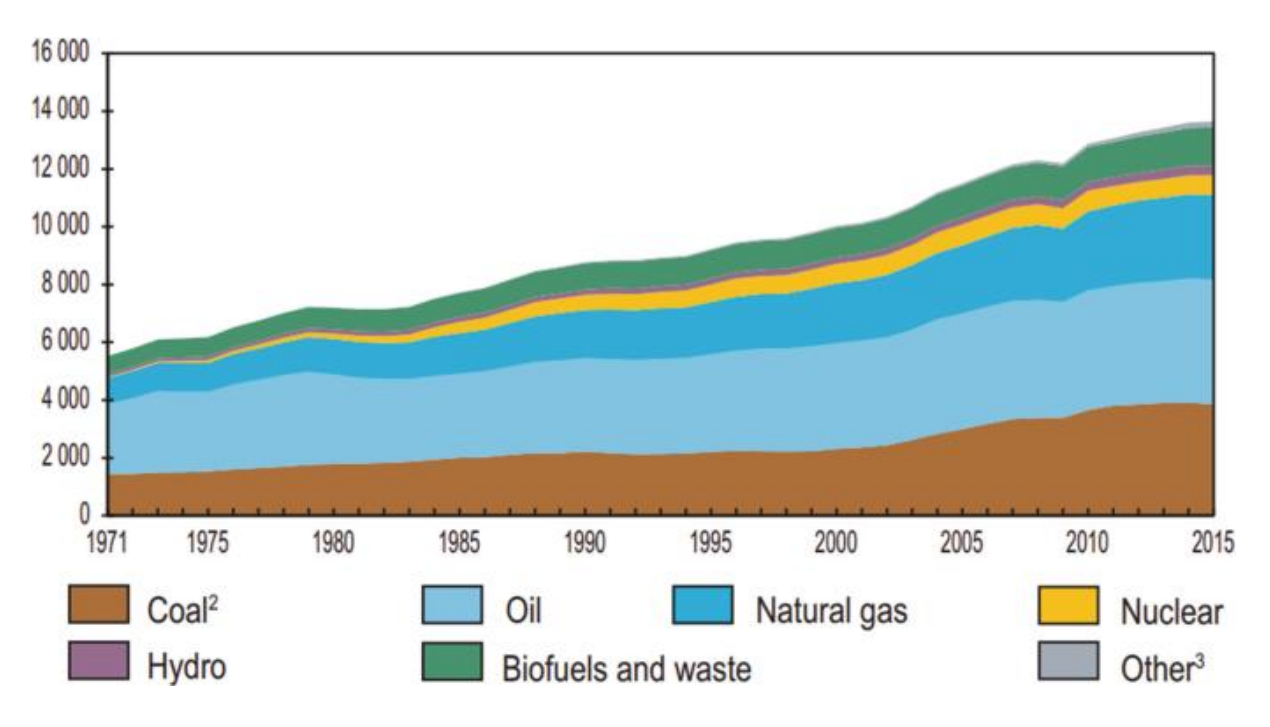


Figure 1.1: Energy mixture distribution and trends from 1971 to 2015. The y-axis is expressed in millions of tons of oil equivalent (MTOE). Figure derived from Bothun (2021).

Despite natural gas being a fossil fuel and a source of CO<sub>2</sub> when burned, under the Net Zero scenarios it is not expected to be removed from the energy mixture before 2100 (Dubey et al., 2023). This is due to the abundant resources of natural gas in various locations (Bothun, 2021), the convenience to store it and transfer it through pipelines, and as liquefied natural gas (LNG) (IEA, 2021). Under the majority of 1.5°C increase scenarios, the global gas usage will be reduced by 35% in 2050 and 70% in 2100, compared to the global gas usage in 2019 (Dubey et al., 2023). According to IEA (2021), global gas usage is expected to decline by approximately 3% per year from 2020 to 2050, driven by significant reductions in OECD and EU countries and simultaneous increases of natural gas usage in Asia, South America and Africa until 2050. Overall, the future of natural gas usage is tightly connected with the efficacy, capacity and deployment of carbon capture and storage (CCS) systems (Dubey et al., 2023).

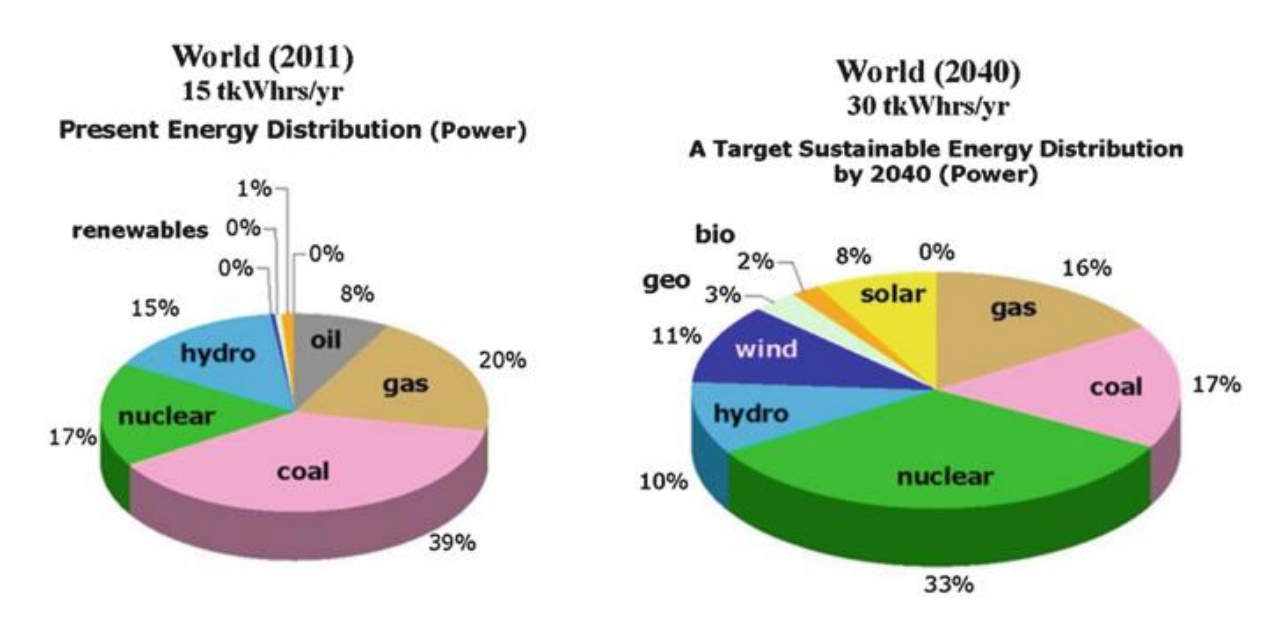


Figure 1.2: Energy mixture in 2011 and projected for year 2040. Figure from Bothun (2021). Under this scenario it is assumed that the crude oil use will diminish significantly by 2040.

To achieve the Net Zero targets by year 2050, low carbon footprint fuel alternatives are required for energy generation. For example, hydrogen has a key role in energy transition (Nnabuife et al., 2023). However, the most established and technologically mature process of hydrogen production requires CH<sub>4</sub> under the following reaction (Taipabu et al., 2022):

$$CH_4 + H_2O \leftrightarrow CO + 3H_2$$
,  $\Delta H = 206 \, kJ/mol \, (1.1)$ 

In this case methane reacts with water vapour at 700-1000°C in the presence of a catalyst. This process (steam methane reforming; SMR) generates approximately 50% of the global hydrogen production. The future of SMR is dependent of the efficacy of carbon and capture systems connected with the process (Farooqi et al., 2025).

## 1.2. Atmospheric Methane (CH<sub>4</sub>)

Methane is a potent greenhouse gas (GHG) with atmospheric lifetime of ~8-12 years; short compared to other GHGs (Nisbet et al., 2023). Additionally, CH<sub>4</sub> plays a significant role in the atmospheric chemistry and its occurrence in the atmosphere produces other air pollutants such as ozone (Isaksen et al., 2014) and reduces the oxidative capacity of the atmosphere by reacting with OH· radicals (Liu et al., 2024).

Methane has a large global warming potential (GWP) which is approximately 20 times higher per molecule than CO<sub>2</sub> in a 100-year time horizon (IPCC, 2007), which means that

one molecule of methane traps more effectively the infrared radiation than a molecule of carbon dioxide.

Table 1.2: List of GHGs with their corresponding atmospheric lifetime and GWP (IPCC, 2007).

GHG	<b>Atmospheric</b> lifetime	GWP
	(years)	(100-year horizon)
CO <sub>2</sub>	50-200	1
CH <sub>4</sub>	8-12	21
N <sub>2</sub> O	109	290
CFC-12	100	7390-12,200
HFC-23	270	124-14,800
SF <sub>6</sub>	3200	22,800

For those reasons, methane emissions might be a key target to combat climate change in the short term. However, methane has a range of natural and anthropogenic sources in a variety of environments. Therefore, the reduction of methane emissions requires diverse mitigation strategies and not a single solution. For example, methane is emitted in majority by anthropogenic activities including the usage, production and distribution of fossil fuels (coal, natural gas and oil), agricultural activities and waste management processes (such as ruminant livestock, manure handling, rice paddies, waste treatment and etc.) (Figure 1.3). Hence, even within the anthropogenic sources there is a range of solutions required to mitigate effectively the emissions of CH<sub>4</sub>, including the improvement of fossil fuel distribution infrastructure (Alvarez et al., 2012; Mac Kinnon et al., 2018), feed additives for regulating the ruminants digestion (EFSA, 2021), and applying different cultivation methods for rice production (Gathorne-Hardy et al., 2013).

GHG emissions is typically calculated using two different methods. The most common one is using a bottom-up approach such as global emission inventories (e.g. EDGARv6) assuming an emission factor for each activity producing GHGs (Crippa et al., 2021). Top-down approaches such as inverse modelling, on the other hand, employ atmospheric measurements and atmospheric transport models in order to calculate the fluxes of GHGs and their spatial distribution within an area (Bergamaschi et al., 2018). Until recently, there has been a significant discrepancy in the emission estimations by atmospheric inversions and inventories (Saunois et al., 2016; Saunois et al., 2020). These differences have been attributed to the large number of methane sources, differences in methodology of the

atmospheric inversion models (Allen, 2014), uncertainties in the magnitude and of the temporal variations of methane sources (Vaughn et al., 2018; Johnson et al., 2019; Liu et al., 2020; Rosentreter et al., 2024), uncertainties in OH· concentrations in the atmosphere (Murray et al., 2021) and difficulty in quantifying the contribution from episodic release events (Poursanidis et al., 2024). In the last methane budget reported by Saunois et al. (2024), global inventories estimated higher methane emissions (669 Tg/yr) than those calculated by atmospheric inversions (575 Tg/yr) by 94 Tg/yr, although for the first time those two approaches produce results which overlap within their relative uncertainties. More efforts are needed to reduce the uncertainty in the inventory estimations for natural CH<sub>4</sub> emissions, especially for wetlands and freshwater systems (Saunois et al., 2020). The same discrepancy between bottom-up and top-down methods is evident also in the estimations of CH<sub>4</sub> removed from the atmosphere (Saunois et al., 2024) by processes such asthe reactions of CH<sub>4</sub> with OH and Cl radicals and the methane loss by methanotrophic communities in the soils (Kirsche et al., 2013). Global inventories estimate the natural removal of CH<sub>4</sub> at 633 Tg/yr which is 79 Tg/yr higher than 554 Tg/yr estimated from atmospheric inversions (Saunois et al., 2024).

Anthropogenic sources account for 54% of the total emissions based on inventories estimations. Inversion models predict 64% of the total emissions to be attributed to anthropogenic sources (Saunois et al., 2024). Based on global inventories reported in Saunois et al., (2024), anthropogenic emissions in the period 2010-2019 were dominated by the agriculture and waste sectors (~59%), the fossil fuel sector (~34%) with coal mining contributing 33% of those emissions, and the biomass and biofuel burning (~7%). For the same time period, natural CH<sub>4</sub> emissions were dominated by wetlands (bogs, fens, marshes, swamps) with 159 Tg/yr, inland freshwater systems (lakes, ponds, rivers, streams and etc.) with 89 Tg/yr, and other sources including geological sources, wild animals, termites and permafrost thawing with 63 Tg/yr (Lauerwald et al., 2023b; Saunois et al., 2024). Wetlands, freshwater systems and other geological sources account for approximately 51%, 29% and 20%, respectively, of the total natural emissions.

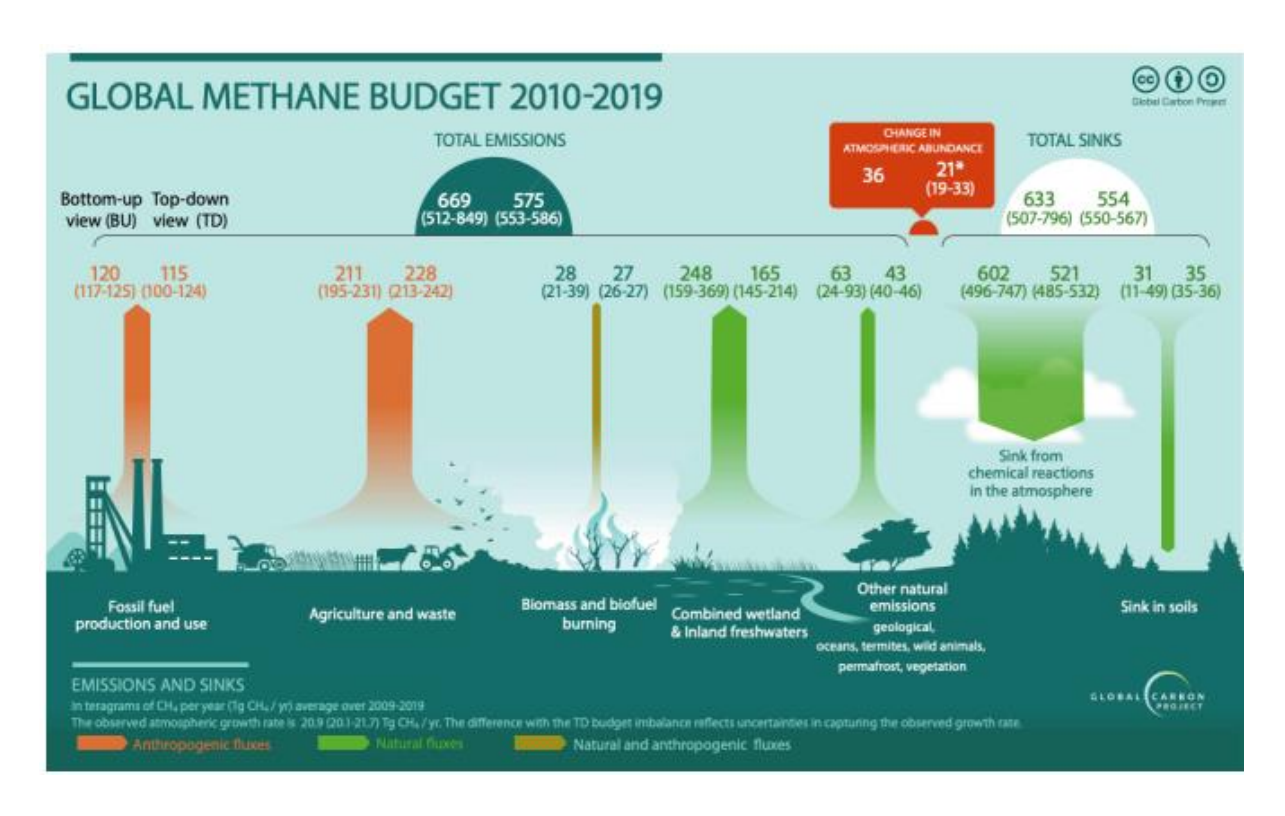


Figure 1.3: Latest global methane budget from 2010 to 2019 including emissions estimations from emission inventories (bottom-up) and inverse modelling (top-down) approaches (Saunois et al., 2024).

Using top-down approaches, we can infer the spatial distribution of the methane emissions worldwide. According to Saunois et al. (2024), the tropical areas emit 64% of the total CH<sub>4</sub> emissions, followed by mid-latitudes emissions of 32%, and 4% of high latitudes (>60°N). For 2010-2019, South Asia, China and Southeast Asia account for approximately 1/3 of the total CH<sub>4</sub> emissions, while China, USA and Russia are amongst the countries with the largest anthropogenic CH<sub>4</sub> emissions (Saunois et al. 2024).

Atmospheric concentrations of CH<sub>4</sub> are increasing and are significantly higher than the preindustrial levels. In September 2024, methane concentrations reached 1,936 ppb which are approximately 2.8 times greater than the levels in 1750 (Etheridge et al., 1998; Lan et al., 2024). This increase is largely due to increased anthropogenic emissions (Skeie et al., 2023). The annual growth has ranged from -4.7 ppb in 2004 to +17.6 ppb in 2021 (Lan et al., 2024). Methane concentrations have followed three distinct trends since the 1980s (Skeie et al., 2023):

I. An increase of methane concentrations from approximately 1635 ppb to 1770 ppb between 1983 and 1999, with high annual growth rates (>10 ppb) in the 1980s and a slower growth rate (<5 ppb) throughout the 1990s.

- II. A period of stabilisation from 2000 to 2006 at approximately 1775 ppb.
- III. Increase during the period from 2006 to 2024, with relatively slow annual growth rates (~5 ppb) between 2006 and 2014, and larger growth rates (~10 ppb) from 2014 onwards.

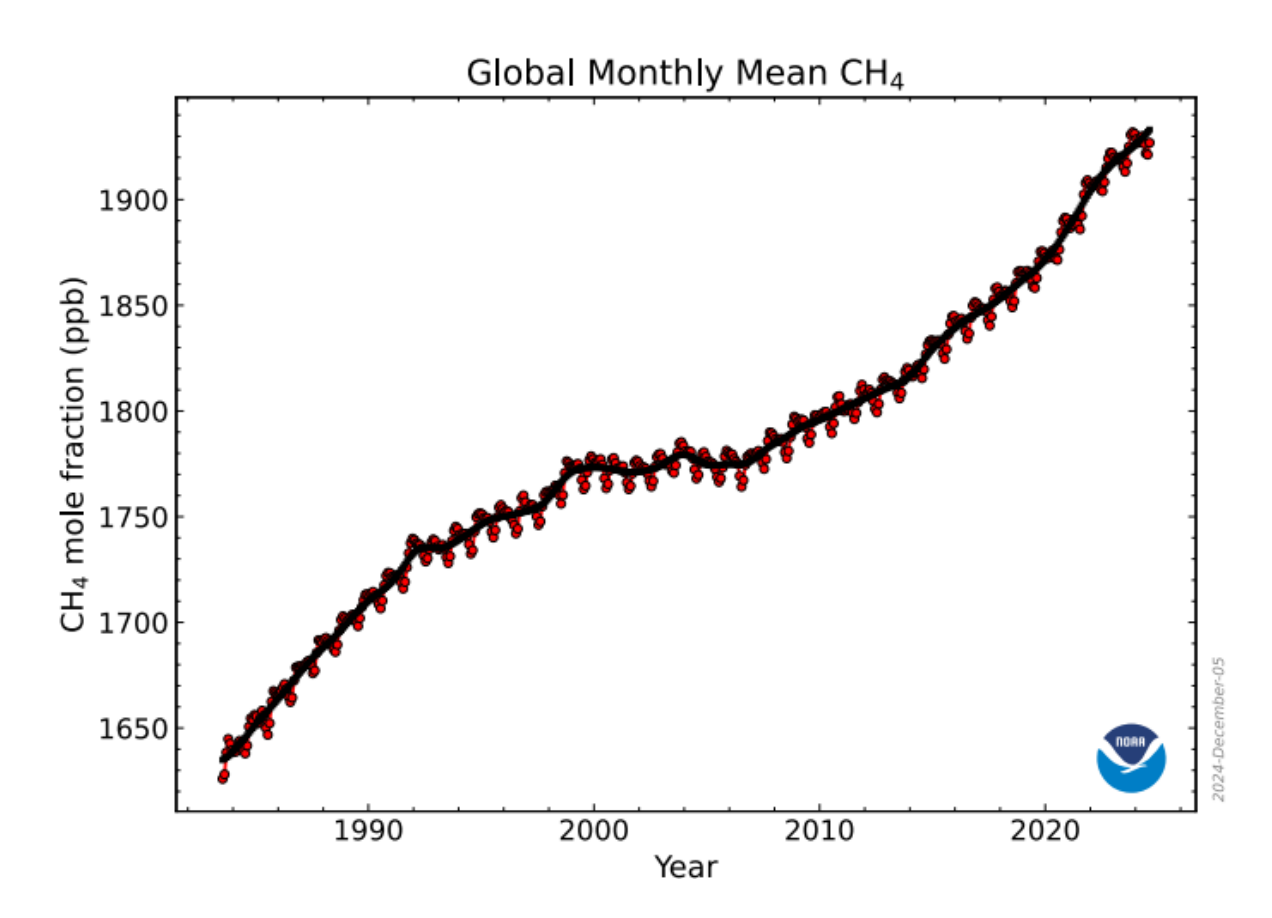


Figure 1.4: Atmospheric concentration of CH<sub>4</sub> since 1983 (Lan et al., 2024).

While definitive explanations are challenging to validate due to uncertainties in emission estimates and the complex chemistry of the atmospheric boundary layer, several potential explanations have been proposed. According to Kirsche et al. (2013), the trend between 1983 to 2000 was likely driven by increased microbial emissions (wetlands, freshwater, agriculture, waste sector) accompanied by stable fossil fuel emissions (Aydin et al., 2011). The stability of atmospheric methane in 2000-2006 is still a matter of debate and possibly a sum of different processes. For example, Kirsche et al. (2013) argued in favour of decreasing fossil fuel emissions and increasing microbial emissions, while Skeie et al. (2023) linked the stabilisation period to changes in the ambient concentrations of the OH radical. The rising atmospheric methane concetration from 2006 is likely related to several factors that include an increase of wetland and freshwater emissions particularly in the tropical regions (Kirsche et al., 2013; Saunois et al., 2016; Saunois et al. 2020; Saunois et al., 2024), the rise of shale

gas (North America) and coal (South Asia) extraction in (Kirsche et al, 2013), and a reduction in the OH radical concentrations in the atmosphere (Skeie et al., 2023).

#### 1.3. Tracers of Methane

Traditional and novel tracers such as isotopic and molecular compositions enable us to distinguish the sources of methane in the atmosphere, marine environments and geological systems. Since the 1970s, the stable isotopic composition of C ( $\delta^{13}$ C) and H ( $\delta$ D) (defined and discussed in detail in Chapter 2) have been widely employed to determine the origin of hydrocarbons in natural gas systems along with the generation mechanisms of natural gas (Stahl, 1974; Stahl, 1977; Schoell, 1980). When combined with the molecular compositions of natural gases, especially the C<sub>1</sub>/C<sub>2+</sub> (the ratio of the abundances of methane to higher hydrocarbons), numerous studies have successfully determined the origin of natural gases from different settings (). Milkov and Etiope (2018) compiled data from more than 20,000 gas samples in order to determine the origin of gases from conventional petroleum systems, coalbeds, unconventional petroleum systems, volcanic and geothermal settings, marine sediments and others.

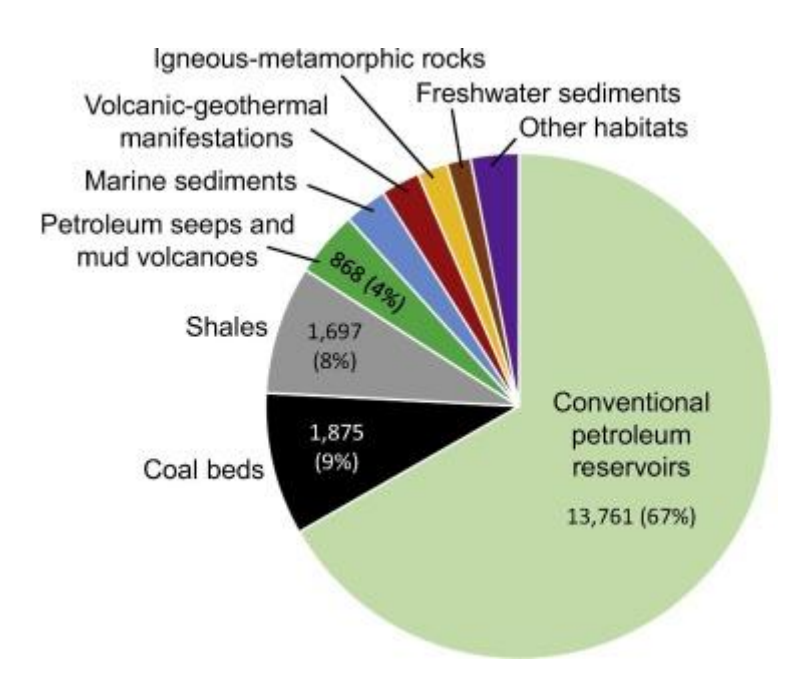


Figure 1.5: Pie chart displaying the distribution of different environments for the methane samples reported in the global database (Milkov and Etiope, 2018).

In the atmosphere, the stable isotopic compositions  $\delta^{13}$ C and  $\delta$ D have been widely used in order to fingerprint the sources of CH<sub>4</sub> and hence, mitigate the emissions from those sources when possible (Quay et al., 1999; Townsend- Small et al., 2016; Nisbet et al., 2019). While the  $\delta^{13}$ C signature has been widely measured and used, the  $\delta D$  data remain relatively sparse temporally and spatially (Nisbet et al., 2019), mainly due to practical challenges of the hydrogen isotopes measurements. Potential further developments in infrared spectroscopy, such as those reported by Ono et al. (2014), could enable the routine measurement of  $\delta D$  in atmosphere and point sources in the next few years. However, the  $\delta^{13}$ C signature have been routinely measured in the atmosphere due to developments in infrared spectroscopy techniques (Zazzeri et al., 2017; Takriti et al., 2021). By monitoring the variations of  $\delta^{13}$ C and δD in the atmosphere, information can be inferred about the sources and sinks of CH<sub>4</sub> (Schwietzke et al., 2016). For example, the increasing methane concentrations, after the stabilisation period of 2000-2006, have been accompanied by a negative trend in  $\delta^{13}$ C. This has been interpreted as an increase on microbial emissions from wetlands, agriculture and freshwater systems, and/or an increase of fossil fuel emissions (Nisbet et al., 2019). Therefore, the isotopic signatures can be employed for understanding the trends of methane concentrations and constructing the global methane budget.

Additional information can be offered using radioactive isotopes. For example, the usage of radiocarbon (<sup>14</sup>C) can provide information about the partitioning of fossil fuel against biogenic emissions of methane, based on the lack of radiocarbon in the fossil fuels (Kirsche et al., 2013; Graven et al., 2019; Zazzeri et al., 2023). However, this method requires an accurate determination of nuclear plant emissions which emit methane enriched in <sup>14</sup>C (Kirsche et al., 2013; Graven et al., 2018).

Novel tracers such as clumped isotopes of methane <sup>13</sup>CH<sub>3</sub>D and <sup>12</sup>CH<sub>2</sub>D<sub>2</sub> have been used in the past decade in order to understand the origin of methane in different settings, the conditions (e.g temperature) during the natural gas generation, and to identify any post-generation processes in a range of environments, including natural gas systems (Thiagarajan et al., 2020), volcanic and geothermal settings (Young et al., 2017; Nothaft et al., 2021), marine sediments (Giunta et al., 2021; Giunta et al., 2022) and others. The clumped isotopic compositions may indicate the origin of gas when the bulk isotope compositions are ambiguous and difficult to interpret (Stolper et al., 2014a; Stolper et al., 2015; Young et al., 2017). Equivalently, those tracers can also act as independent variables along with the bulk compositions in order to provide information and constrain further the global atmospheric methane budget (Haghnegahdar et al., 2017; Chung et al., 2021; Haghnegahdar et al., 2024;

Sivan et al., 2024). More information about the definitions and theory of stable and clumped isotope geochemistry can be found in Chapter 2.

#### 1.4. Thesis Overview

In this section I present the outline of this thesis. In detail, the thesis is organised in six chapters as following:

In Chapter 2, I provide the theory of clumped isotope geochemistry in CH<sub>4</sub> and the required nomenclature, and I present the sources of methane, focusing on clumped isotopic compositions. Additionally, I discuss and present the effect of different post-generation processes (mixing, oxidation, diffusion) on  $\Delta^{13}$ CH<sub>3</sub>D and  $\Delta^{12}$ CH<sub>2</sub>D<sub>2</sub> values. I also present the fundamentals of methane geochemistry focusing on the stable isotope theory and introducing key concepts such as the isotopic fractionation, the kinetic isotope effects (KIEs) and the Rayleigh distillation model. In the context of stable isotopic compositions  $\delta^{13}$ C and  $\delta$ D, I present and discuss the methane sources and sinks while introducing the methods for stable isotope measurements.

In Chapter 3, I provide a description of the methods used for the measurement and calculations of the clumped isotopic compositions of CH<sub>4</sub> in SUERC. Firstly, I introduce the methods used for the purification of the gases and the setup of the equilibration experiments needed to create the calibration standards at temperatures above 250°C. Secondly, I describe the high-resolution isotope ratio mass spectrometer Ultra 253 and the measurement setups for the three individual measurements conducted for each sample. Finally, I present the methods used for the calculation of bulk and clumped isotopic signatures, and the error propagation.

In Chapter 4, I investigate the origin of extremely He-rich natural gas in the Virginia gas field and the dominant processes taking place at the southwestern margin of Witwatersrand basin, using the clumped isotopologues of methane <sup>13</sup>CH<sub>3</sub>D and <sup>12</sup>CH<sub>2</sub>D<sub>2</sub>. In this chapter, I describe the sampling process in the Virginia gas field while I present molecular and bulk isotopic composition data along with the clumped isotopic compositions.

I present and discuss in Chapter 5 the clumped isotope data ( $\Delta_{47}$ ) for vein carbonate reservoir rocks from the in Witwatersrand basin. Using the stable isotopic compositions  $\delta^{13}$ C and  $\delta^{18}$ O, the apparent temperature  $T_{47}$ , and the findings from Chapter 4, I explore the relationship

between the carbonate and methane in the Virginia gas field. I also investigate the origin of carbon related to the calcite, and the origin of the precipitating fluid in the basin.

In Chapter 6, I present the main conclusions of this thesis, highlight the limitations of my approach and propose future work needed to understand the processes taking place in Virginia gas field. Finally, I discuss the results of my work in Chapter 4 in respect to the published data for  $\Delta^{13}$ CH<sub>3</sub>D and  $\Delta^{12}$ CH<sub>2</sub>D<sub>2</sub>.

## 2. Geochemistry of Methane

## 2.1. Chapter Overview

In this chapter I review the fundamental aspects of methane geochemistry focusing particularly on carbon and hydrogen stable isotopes. In the first sections I review the theory and definition of conventional stables isotopes of methane along with measurement methods. I discuss how the stable isotopic compositions relate to sources and sinks of CH<sub>4</sub> in nature. In a second section I introduce the theory of clumped isotopologues of methane ( $\Delta^{13}$ CH<sub>3</sub>D and  $\Delta^{12}$ CH<sub>2</sub>D<sub>2</sub>) then review the impact of mixing, diffusion and oxidation on the clumped isotopic compositions.

#### 2.2. Conventional Stable Isotopic Compositions

#### 2.2.1. Introduction

Stable isotopic compositions of carbon and hydrogen of methane have been a powerful diagnostic tool to discriminate the sources of methane and identify any secondary processes occurring in natural settings (Stahl, 1977; Schoell, 1980; Whiticar, 1999). Often these measurements are combined with the chemical composition of a gas mixture, especially by examining the relative concentrations of CO<sub>2</sub> and/or higher hydrocarbons compared to methane (Bernard et al., 1977). In addition, the stable isotopic compositions of C and H in ethane (C<sub>2</sub>H<sub>6</sub>), propane(C<sub>3</sub>H<sub>8</sub>) and butane(C<sub>4</sub>H<sub>10</sub>) can offer further insights into the origin of methane (Stahl, 1977; Sherwood Lollar et al., 2008).

While early studies by Bernard et al. (1977), Stahl (1977) and Schoell (1980) focused on understanding the origin and generation mechanisms of methane associated with petroleum reservoirs, later studies have identified the importance of methane in the atmosphere (Cicerone and Oremland, 1988; Whiticar, 1990). Studies focused on fingerprinting isotopically the atmospheric methane sources, which helped to constrain the fluxes of methane and construct the global atmospheric methane budget (Stevens and Engelkemeir, 1988; Quay et al., 1991; Lassey et al., 2007a; Thanwerdas et al., 2024; Saunois et al., 2024). However, the multiplicity of methane sources and processes in the atmosphere, marine and aquatic systems, and the subsurface often create equivocal stable isotopic signatures which are difficult to interpret without further data (Stolper, 2014a).

#### 2.2.2. Theory and Definitions

Carbon and hydrogen occur in a wide range of chemical compounds on Earth either separately (e.g. CO<sub>2</sub> or H<sub>2</sub>O) or together (CH<sub>4</sub>, C<sub>2</sub>H<sub>6</sub>, amino acids and others). Both carbon

and hydrogen have each two stable isotopes. In terrestrial systems <sup>12</sup>C is considerably more abundant than <sup>13</sup>C (<sup>13</sup>C/<sup>12</sup>C ranges typically from 0.010101 to 0.011180) while H dominates over <sup>2</sup>H, commonly known as D (deuterium) (D/H range from 0.00008567 to 0.00015576) (Hoefs, 2009).

The stable isotopic signatures of methane,  $\delta^{13}C$  and  $\delta D$ , are an expression of the contrast in isotopic ratios  $^{13}C/^{12}C$  and D/H between the sample and a standard or reference material. They are expressed in ‰ (per mil) and calculated from:

$$\delta^{13}C = \left(\frac{\binom{1^3C}{1^2C}}_{sample} - 1\right) \qquad (2.1)$$

$$\delta D = \left(\frac{\left(\frac{D}{H}\right)_{sample}}{\left(\frac{D}{H}\right)_{standard}} - 1\right) \tag{2.2}$$

Typically,  $\delta^{13}$ C is expressed against the international standard VPDB (derived from the *Belemnitella americana* from Peedee formation of South Carolina) which was first used by Urey (1951) and Craig (1957). The  $\delta D$  values are typically expressed against the international standard Vienna Standard Mean Ocean Water (VSMOW) (Hoefs, 2009). Based on measurements by Craig (1957), the isotopic ratio  $^{13}$ C/ $^{12}$ C of VPDB is at 0.011237  $\pm$  0.0000029 while a later study by Chang and Li (1990) reported a value of 0.011180  $\pm$  0.0000028 (Brand et al., 1990). The D/H ration of VSMOW was measured by Hagemann et al. (1970) and is widely accepted to be 0.00015576  $\pm$  0.0000001.

The proportion of light ( $^{12}$ C, H) and heavy isotopes ( $^{13}$ C, D) in methane can change in response to physical, chemical and biological processes, which may involve either reversible or irreversible reactions. The isotopic fractionation between two substances/phases (A and B) can be expressed by the fractionation factor  $\alpha$  using the following equation:

$$\alpha_{A-B} = \frac{R_A}{R_B} \tag{2.3}$$

R stands for the isotopic ratio of the heavy to the lighter isotope in phase A or B (e.g. D/H in water and ice). The magnitude of isotopic fractionation typically decreases as temperature increases (Hoefs, 2009).

Isotopic fractionation occurs due to the differences in chemical and physical properties which arise predominantly from the mass difference between isotopes. For example, molecules containing a heavy isotope, (for example  $^{12}\text{C-}^{13}\text{C}$ ) create stronger bonds than molecules containing two light isotopes (e.g.  $^{12}\text{C-}^{12}\text{C}$ ). Therefore, a chemical reaction will break the bonds of lighter molecules more easily (as lower dissociation energy is required) and consequently change the proportion of light-heavy isotopes in the final product/gas (Kendall and Caldwell, 1998).

There is a distinction between reversible and irreversible reactions which can create, respectively, either equilibrium fractionation or kinetic fractionation. In systems where there is exchange of isotopes between the different phases (e.g. liquid water and water vapour) or substances (e.g. H<sub>2</sub>O and H<sub>2</sub>), this leads to equilibrium distributions (Hoefs, 2009). Kinetic isotope effects (KIEs) arise when isotopic fractionation does not occur in equilibrium, usually due to different rates of reaction for different isotopes. KIEs for methane often present due to processes such as diffusion, oxidation and biologically-mediated processes like methanogenesis and methanotrophy (Valentine et al., 2003; Young et al., 2017). KIEs occur due to the different reaction rates of each isotopologue where generally the abundance of heavy isotopes is favoured in the remaining reactant (Hoefs, 2009). In general, KIEs create greater isotopic fractionation than isotope exchange (Kendall and Caldwell, 1998). Often the Rayleigh distillation model is applied in open systems to describe fractionation between two reservoirs (e.g. in the case of diffusion between the residual and diffused gases).

$$R = R_0 \times f^{a-1} \qquad (2.4)$$

In this case,  $R_0$  is the initial isotopic ratio and f is the fraction of the material remained, while  $\alpha$  is the fractionation factor introduced earlier.

#### 2.2.3. Stable Isotope Signatures of Methane

Typical  $\delta^{13}$ C values for methane from petroleum systems, coalbeds, shales, marine sediments, aquatic environments and others, range between -90 and 0% in (dominantly -50 to -30%), while  $\delta D$  ranges from -450% to -50% (dominantly -300 to -100%) (Milkov and Etiope, 2018). The relationships of stable isotopic signatures with the sources and sinks will be discussed in the next sections.

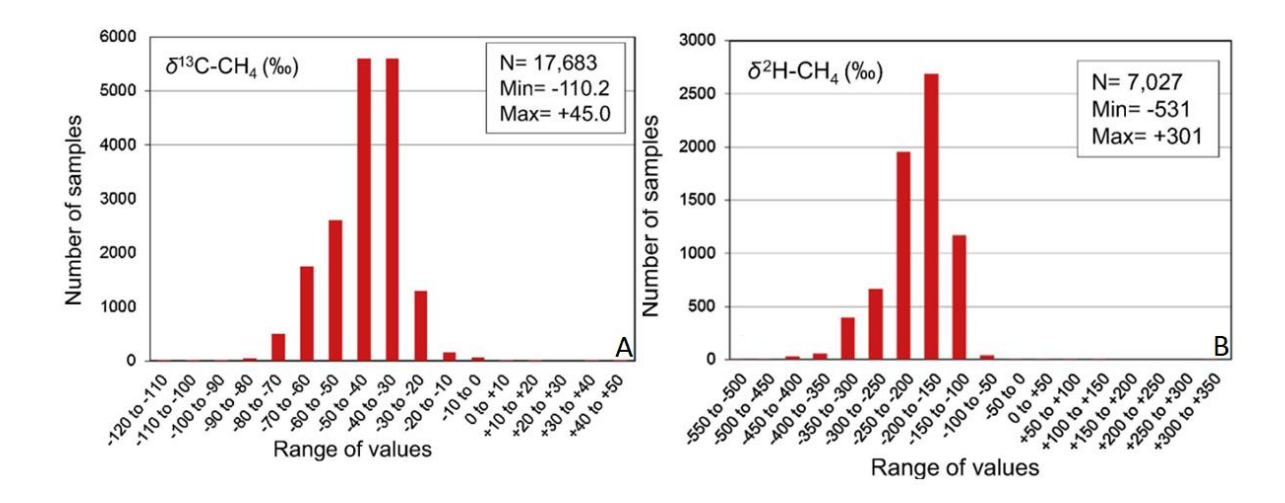


Figure 2.1: Distribution of isotopic compositions of C and H in CH<sub>4</sub>. Panel A) shows the distribution of  $\delta^{13}$ C in a compilation of data for 17,683 natural gases measured worldwide. B) shows the distribution of  $\delta$ D in compilation of data for 7,027 natural gases measured worldwide. Figures adjusted from Milkov and Etiope (2018).

The  $^{13}$ C/ $^{12}$ C and D/H ratios are the mean isotopic ratios across the ten isotopologues of CH<sub>4</sub> and for this reason  $\delta^{13}$ C and  $\delta$ D are commonly referred to as bulk isotopic compositions (Stolper et al., 2015). Therefore, we are missing information about the distribution (or partition) of the isotopes and instead we focus on the bulk ratios of  $^{13}$ C/ $^{12}$ C and D/H across all methane isotopologues. Until recently, stable isotope measurement required the conversion of CH<sub>4</sub> to CO<sub>2</sub> and H<sub>2</sub> which permanently erases the distribution of isotopes. New developments in mass spectrometry and laser spectroscopy have allowed this information to remain intact and to be measured precisely enough to be used for geochemistry and environmental science applications (Eiler et al., 2013; Ono et al., 2014; Young et al., 2016).

#### 2.2.4. Measurement Techniques

#### 2.2.4.1. Introduction

In this section, I describe the traditional and state-of-the-art measuring techniques for determining the stable isotope composition of methane along with the main methods of purification and conversion into specific analytes. The new generation of instruments are now capable of measuring the abundance of the clumped isotopologues of methane, <sup>13</sup>CH<sub>3</sub>D and <sup>12</sup>CH<sub>2</sub>D<sub>2</sub>. This thesis is only concerned with the clumped isotopologues of methane with two heavy isotopes, because the isotopologues with three heavy isotopes (or more) are extremely rare and difficult to measure with the current technology.

#### 2.2.4.2. Isotope Ratio Mass Spectrometry

Isotope ratio mass spectrometry (IRMS) is a well-established technique to quantify the relative abundance of isotopes in solid, liquid or gas samples. It is widely used in a range of sectors including forensics, medical, environmental geo- and bioscience. It is typically applied on light volatile elements (C, N, H, S, O), the noble gases (Ar, He, Ne and etc.), and other elements (e.g. K, Ca, Mg and etc.) (Bianchi and Careri, 2021).

While technological developments (such as new source materials, better optics and more stable electronics) have significantly improved the performance, stability and precision of modern isotope ratio mass spectrometers, the fundamental components do not differ from the early design of Nier (1947). These include the ion source, the magnetic sector and the ion collectors. Typically, the sample is converted into a purified gas analyte such as H<sub>2</sub>, CO<sub>2</sub>, N<sub>2</sub> or SO<sub>2</sub> (DeTata et al., 2023), and it is introduced into the mass spectrometer under vacuum conditions. The gas is expanded towards the ion source. It is ionised in the mass spectrometer source by electrons emitted by a filament (typically made from tungsten or rhenium). The ions are electrostatically accelerated and focused, while the lower-energy ions derived from the ionisation process or compounds found in the analyte gas or in the mass spectrometer are filtered out. The ion beam passes through a magnetic field, which deflects the trajectory of the beam and separates the ions according to their mass to charge ratio (m/z). Lighter molecules are deflected to a greater extent than heavier ones, resulting to trajectories with greater curvature (Figure 2.2). The ions are collected typically either by Faraday cups or electron multipliers which convert beam to the electric current. The total number of ions (N) falling onto the Faraday cup can be calculated using the following equation:

$$N = \frac{I}{e^-} \quad (2.5)$$

Where I is the electric current expressed in ampere where  $e^-$  is the elementary charge constant (1.6 × 10<sup>-19</sup> C). The electric current can be translated into counts per second (cps), which is a unit used widely in literature for reporting signal intensities in mass spectrometry. Isotope ratio mass spectrometers equipped with a multi-collector system are able to measure simultaneously different isotopic ratios of variable intensities.

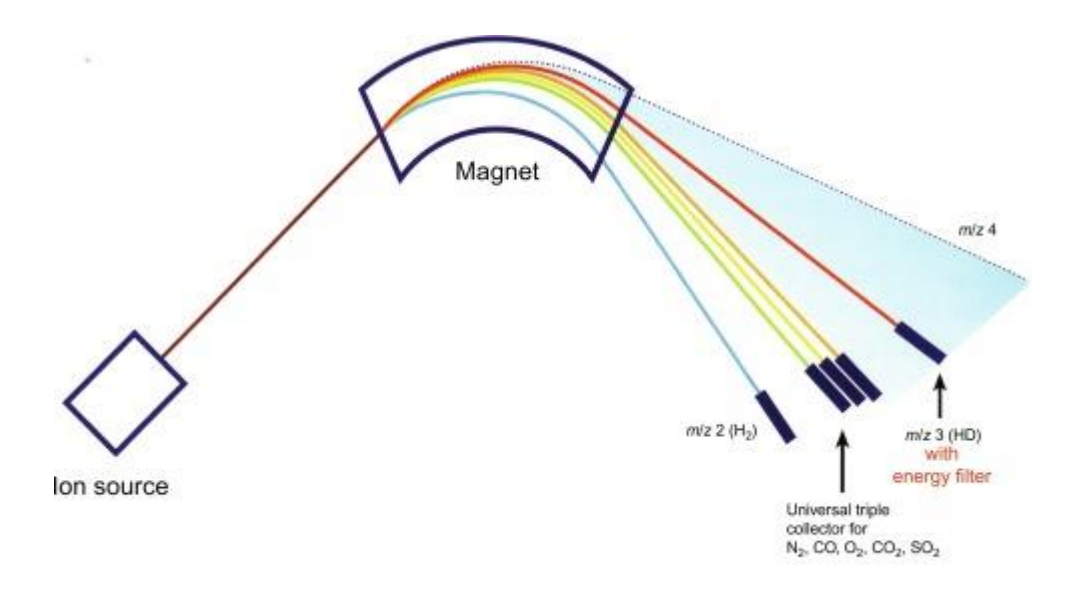


Figure 2.2: Plain schematic of hydrogen isotopologue measurement using IRMS (Kelly et al., 2018).

There are two IRMS techniques to measure the isotopic variations of carbon and hydrogen in methane. The first one, called the conventional way here, involves the quantitative transformation of methane, using a furnace within a vacuum system, into  $CO_2$  and  $H_2O$ . The  $CO_2$  is measured as described earlier in a conventional IRMS system to determine the  $^{13}C/^{12}C$  ratio of the sample and hence the  $\delta^{13}C$  of  $CH_4$  (Schoell, 1980). The  $H_2O$  is reduced into  $H_2$  by reaction with a metal at temperatures of several hundred Celsius degrees, usually with depleted U, Cr or Zn (Donelly et al., 2001). The  $H_2$  is trapped and transferred to a mass spectrometer for D/H ratio determination.

The second technique is based on the deployment of new generation mass spectrometers, known as high-resolution isotope ratio mass spectrometers (HR-IRMS) (Eiler et al., 2013; Young et al., 2016). The ability to separate peaks of the same cardinal mass allowing the measurement of methane molecules intact, and the direct measurement of (e.g.  $^{13}$ CH<sub>4</sub>/ $^{12}$ CH<sub>4</sub> and  $^{12}$ CH<sub>3</sub>D/ $^{12}$ CH<sub>4</sub> ratios) without the need for combustion or other conversion and a risk of isotopic fractionation throughout the process. The latest generation of HR-IRMS allows the clumped isotopic signatures of methane to be measured and have significantly increased the precision of  $\delta^{13}$ C and  $\delta$ D measurements significantly, by at least an order of magnitude (Dong et al., 2020). In chapter 3, I describe in more detail the IRMS and HR-IRMS instruments used for determination of stable and clumped isotopic signatures of methane.

#### 2.2.4.3. Laser Spectroscopy

Laser spectroscopy instruments utilise the absorption bands of greenhouse gases in the infrared band of the electromagnetic spectrum. The absorbance (A) of the greenhouse gas

by a laser, can be directly linked to the concentration (c) of the gas through the Beer-Lambert law:

$$A = \varepsilon \times c \times l \quad (2.6)$$

Where  $\varepsilon$  is the molar absorption coefficient and is an indication of the magnitude of absorption by a specific substance at a particular wavelength, and l is the optical path length which is connected to the geometry and design of the instrument (Cummings et al., 2011).

The development of laser spectroscopy instruments facilitated the measurements of the concentration of the atmospheric greenhouse gases, in particular  $CO_2$  and  $CH_4$  (Komhyr and Harris et al., 1977; Peterson et al., 1977; Rinsland 1988). The increasing atmospheric concentrations of greenhouse gases have driven the need to track sources. Numerous studies in the mid-1980s or early 1990s investigated the isotopic variations of carbon and oxygen in atmospheric  $CO_2$  or carbon in atmospheric  $CH_4$  (Wong, 1985; Lee and Majkowski, 1986; Becker et al., 1992). However, with low precision (~90‰ in  $\delta^{13}C$  of  $CH_4$ ) in some early cases, not sufficient to discriminate the different sources of methane (Webster and May, 1992).

The measurements of stable isotopic compositions of atmospheric CH<sub>4</sub> using laser spectroscopy pose some challenges. For instance, chemical species (e.g. H<sub>2</sub>O) or isotopologues may interfere with the laser radiation in similar absorbing line as the isotopologues of interest (Ono et al., 2014). These interferences can affect or bias the result and the precision of the measurement.

Bergamaschi et al. (1994) demonstrated the possibility of simultaneous measurements of  $\delta^{13}$ C and  $\delta D$  of atmospheric methane sources using Tunable Diode Laser Absorption Spectroscopy (TDLAS). Ono et al. (2014) using a similar technique (TILDAS- Tunable Infrared Laser Direct Absorption Spectroscopy) and based on technology developed by McManus et al. (1995), deployed an instrument for the offline measurement of the bulk isotopes ( $\delta^{13}$ C,  $\delta D$ ) and the clumped isotope  $^{13}$ CH<sub>3</sub>D (a relative abundance of 7 ppm) with improved precision (Table 2.1) but with the requirement of high-purity methane samples. Gonzalez et al. (2019), using the same instrument with the addition of another laser measured the abundance of the rare  $^{12}$ CH<sub>2</sub>D<sub>2</sub> isotopologue (0.14 ppm in air) along with the stable isotopic compositions.

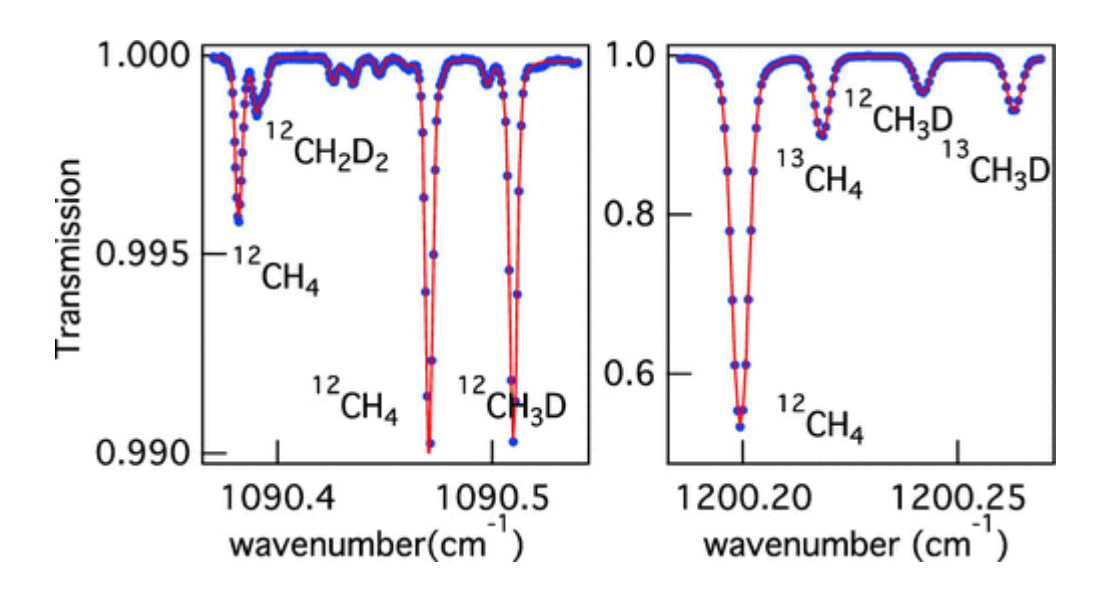


Figure 2.3: TILDAS spectra for methane isotopologue measurements. Left panel illustration shows the peaks of stable isotopologues <sup>13</sup>CH<sub>4</sub>, <sup>12</sup>CH<sub>3</sub>D and clumped isotopologue <sup>12</sup>CH<sub>2</sub>D<sub>2</sub>. Right panel illustration shows the peaks of stable isotopologues <sup>13</sup>CH<sub>4</sub>, <sup>12</sup>CH<sub>3</sub>D and clumped isotopologue <sup>13</sup>CH<sub>3</sub>D. Figure taken from Gonzalez et al. (2019).

Laser spectroscopy is a non-destructive method (Ono et al., 2014; Gonzalez et al., 2019). This means that when the measurement of the sample is completed, the sample can be measured again assuming there is a system installed to recapture the sample and reintroduce it in the measurement apparatus. As a consequence, this can result to smaller measurement uncertainties as the sample can be measured multiple times.

Another advantage of laser analysers for stable isotope measurements, is the mobility of those instruments which can measure directly atmospheric air without the need for purification. Consequently, those instruments have been used widely in field campaigns and mobile measurements (Zazzeri et al., 2017; Lowry et al., 2020; Defratyka, 2021).

Overall, IRMS is considered as a more precise method than laser spectroscopy for the measurement of the stable isotopic compositions (Bergamaschi et al., 1994; Fischer et al., 2006; Brass and Röckmann, 2010; Chen et al., 2022). Contrarily, conventional IRMS requires the conversion of CH<sub>4</sub> into CO<sub>2</sub> and only recently with the deployment of HR-IRMS instruments this is not anymore needed.

However, the new generation instruments such as TILDAS, Ultra253 and Panorama Nu are also capable of measuring the clumped isotopic compositions of methane, which was not feasible with the older generation of IRMS or laser spectroscopy, but with high-purity

requirements (Ono et al., 2014; Young et al., 2016; Dong et al, 2020). Even across the new generation of instruments HR-IRMS has been more precise than laser spectroscopy. However, recent developments in laser spectroscopy have improved precisions to reach the same ranges as HR-IRMS or better for large sample sizes (Zhang et al., 2025).

Table 2.1: List of different IRMS and laser spectroscopy instruments able to measure stable and/or clumped isotopologues of CH<sub>4</sub>, including the internal precision of each system.

Name	Туре	Clumped	Analyte	Internal	Internal
		isotopes		Precision	Precision
				δ <sup>13</sup> C (‰)	δD (‰)
VG SIRA I <sup>1</sup>	IRMS	N	CO <sub>2</sub>	0.3	-
VG	IRMS	N	H <sub>2</sub>	-	3.0
OPTIMA <sup>1</sup>					
IsoPrime <sup>2</sup>	IRMS	N	CO <sub>2</sub>	0.05	-
Delta plus	IRMS	N	$H_2$	0.07	2.3
XL <sup>3</sup>					
Ultra 253 <sup>4</sup>	HR-IRMS	Y	CH <sub>4</sub>	0.01	0.08-0.12
Panorama <sup>5</sup>	HR-IRMS	Y	CH <sub>4</sub>	0.003	0.02
TILDAS <sup>6</sup>	Laser	Y	CH <sub>4</sub>	0.03	0.04
	Spectroscopy				
QCLAS <sup>7</sup>	Laser	Y	CH <sub>4</sub>	0.03	0.01
	Spectroscopy				

<sup>&</sup>lt;sup>1</sup> Reported in Chen et al. (2022) as 1S.D, <sup>2</sup> Reported in Fischer et al. (2006) as 1S.D, <sup>3</sup> Reported in Brass and Röckmann (2010 as 1S.D <sup>4</sup> Reported in Dong et al. (2020) as 1S.E, <sup>5</sup> Reported in Young et al. (2016) as 1S.E, <sup>6</sup> Reported in Ono et al. (2014) as 1S.D, <sup>7</sup> Reported in Zhang et al. as 1S.E (2025).

## 2.2.5. Methane Sources

## 2.2.5.1. Thermogenic Methane

Thermogenic hydrocarbons are formed due to the thermal cracking of buried organic matter under a process named catagenesis. The first step involves the transformation of organic matter into kerogen (a waxy and insoluble organic substance) as a result of chemical, physical, and biological processes, along with changes in temperature and pressure over millions of years. This occurs during diagenesis. During late diagenesis or telodiagenesis,

the cracking of kerogen starts and diagenesis merges into catagenesis. Initially, at temperatures between 65 and 95°C kerogen breaks down into bitumen (a highly-viscous form of petroleum), hydrocarbons and small amount of methane (Shuai et al., 2018). At temperatures between 90 and 150°C, bitumen and kerogen will be transformed primarily into oil (oil-window) along with a with higher hydrocarbons and a higher proportion of methane compared to the initial stage. Thereafter, further thermal cracking of liquid hydrocarbons (>150 °C) results into the formation of "wet gas" which includes C<sub>2</sub>-C<sub>5</sub> hydrocarbon and CH<sub>4</sub>. Finally, an additional increase in temperature (>180 °C) will transform the remaining hydrocarbons to methane which is commonly referred as "dry gas" due to the absence of heavier hydrocarbons. Therefore, thermogenic methane can be produced at various stages of catagenesis, either during the primary cracking of the initial substrates (kerogen, bitumen), or during the secondary cracking which refers to the breakdown of oil and higher hydrocarbons. Consequently, thermogenic methane is produced typically between 65°C and 200°C (Hunt, 1996; Etiope, 2018), with recent evidence suggesting maximum temperatures up to 220°C (Stolper et al., 2014b).

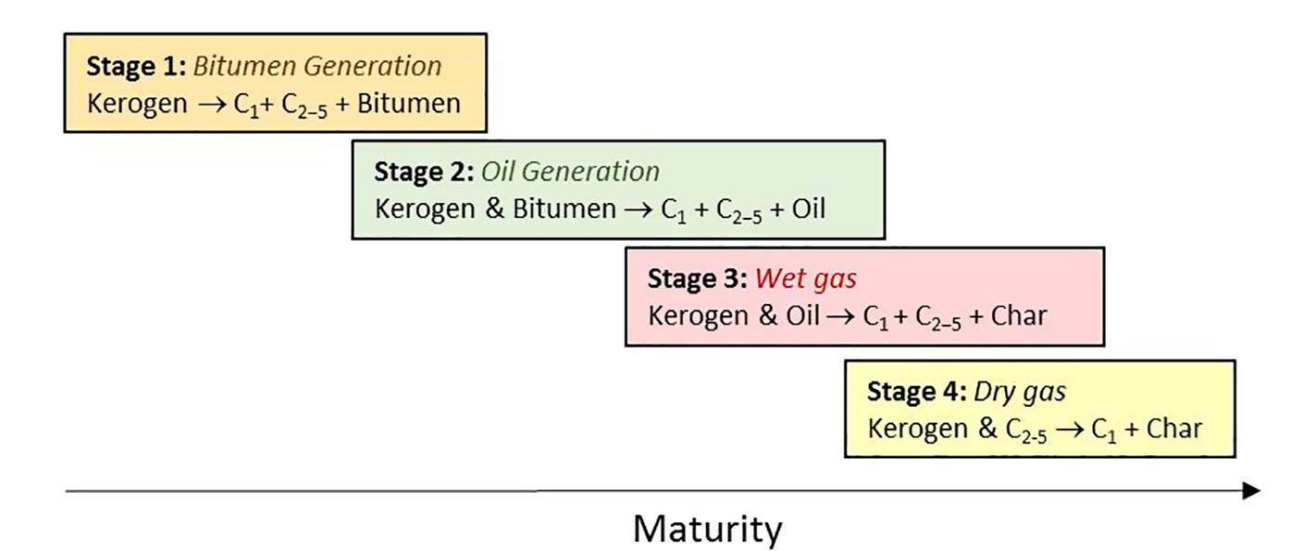


Figure 2.4: Schematic diagram describing the processes resulting to petroleum products and hydrocarbon generation through maturation of organic matter (Shuai et al., 2018).

Thermogenic methane usually is associated with petroleum systems, although its occurrence is not limited to the presence of oil. This thesis is concerned with a geological system where methane is not obviously associated with oil (see Chapter 4). Therefore, I limit this review to methane from gas only sources.

There are a few scenarios which will be analysed below where thermogenic methane is distinct and not associated with oil. For example, oil is one of the intermediate products of catagenesis and under prevailing temperatures above 150°C the gas window is reached where wet gas is produced. Further heating produces dry thermogenic gas. Although the gas in this case originates from the breakdown of oil or the same precursors as oil, the resulting thermogenic methane can be classified as non-associated gas, as the oil resources are fully exhausted during the process, with no apparent occurrence of oil in the reservoir rock. Alternatively, the occurrence of non-associated gas can be explained by considering the four different types of kerogen in sedimentary rocks, classified based on their origin and chemical composition. Kerogens consist mainly of carbon, hydrogen and oxygen in varying proportions, with smaller fractions of nitrogen and sulphur (Selley and Sonnenberg, 2023). The types of kerogen along with their characteristics can be found below:

- 1. **Type I (algal):** This type of kerogen originates from algal material deposited in lacustrine environments and is composed dominantly of lipids but includes also waxes, oils and fats. Type I kerogen is characterised by high H/C values (1.2-1.7) and low O/C (~0.06) compared to the other types of kerogens (Kandiyoti et al., 2006; Selley and Sonnenberg, 2023).
- 2. **Type II (liptinitic):** This kerogen type derives from marine organic material (algae and plankton) and is generated in sedimentary environments under reducing conditions. It is characterised by intermediate values of H/C (1-1.3) and O/C (~0.1). Typically, type II kerogens have the highest content of sulphur compared to the rest of the types.
- 3. **Type III (humic):** Type III kerogen is produced by terrestrial organic matter (mainly from plants) such as lignin, cellulose, terpenes, phenols and carbohydrates. It differentiates from Type I and Type II kerogens, as it is low in aliphatic compounds and high in aromatic compounds. It contains low H/C values (<1) and high O/C values (<0.13).
- 4. **Type IV** (inert or residual): This type of kerogen comprises of mostly inert organic matter in the form of PAHs (polycyclic aromatic hydrocarbons). It is characterised by low H/C values (<0.5) with low hydrogen content and enriched in oxygen (Othman et al., 2022). This type of kerogen will not be taken into consideration in the rest of the chapter, as it is considered as non-productive with negligible potential for oil and hydrocarbon production (Tavakoli, 2021).

Each type has different potential for oil and hydrocarbon formation (Selley and Sonneberg, 2023). For example, type I kerogen is considered as oil-prone with the biggest potential amongst the three types for liquid hydrocarbon (Kandiyoti et al, 2006). It is associated with only 3% of the global petroleum resources (Othman et al., 2022). Type II kerogens are also classified as oil-prone with potential for gaseous hydrocarbon production depending upon sufficient temperature/maturity of the organic material. Type III kerogens are considered as gas-prone with little to no potential for oil production (Selley and Sonneberg, 2023). As coal derives predominantly by type III kerogen (Burnham, 2017), coalbed methane is likely to contain a dominant component of non-associated gas, although it does exclude the possibility of oil-associated gases to be present. It is important to mention that a source rock might contain more than one type of kerogens which could be deceiving during the classification of a source rock into oil-prone or gas-prone (Tissot and Welte, 1984).

The occurrence of non-associated gases could also be attributed to the different migration pathways between thermogenic natural gas and oil. The migration of hydrocarbons in a petroleum system is controlled by buoyancy, fluid pressure gradient and capillary forces which develop in the host rock (Pang et al., 2003). The migration and accumulation of the hydrocarbons is also dependent on the geological settings of an area, as active faults and rock unconformities may act as migration pathways (England, 1994). In some petroleum systems, oil and gas tend to migrate from the source rock into the reservoir rock by primary migration. The oil and hydrocarbons accumulate within the reservoir rock assuming there is a seal which inhibits escape. The permeability and the porosity govern whether further migration (secondary migration) occurs within the reservoir rock (Chapman, 1983). The molecular size, density, and solubility of the migrating hydrocarbons also play a role. These differences in physical and chemical properties of oil and gas can affect their migration pathways and consequently the natural gas found might appear non associated with oil resources.

Oil and gas resources are categorised into conventional and unconventional depending on the permeability of the reservoir rock and whether the system requires stimulation and specific extraction methods (e.g. hydraulic fracking) (Johnson and Doré, 2010). In conventional oil and gas systems, hydrocarbons form in the source rock and migrate towards a sufficiently porous and permeable reservoir rock where they accumulate under an impermeable capping rock. Global conventional gas resources are 8.3 times smaller than the global unconventional resources (IEA, 2009; Zou, 2017). However, the production of conventional natural gas is still dominant worldwide mainly due to the low cost of extraction

and the simplicity of the process compared to unconventional gas. The process involves the vertical drilling of the cap rock to release the trapped hydrocarbons accumulated in the deeper sedimentary layers by using standard completion techniques with minimal well stimulation. Since the beginning of 21<sup>st</sup> century, the production of gas from unconventional resources has surged and in 2015 accounted for 42% of the global production of gas (Kokkinos et al., 2022). In the USA, gas production from unconventional reserves has outpaced the production from conventional wells since 2010 primarily on account of the developments in shale gas extraction (Soeder and Borglum, 2019).

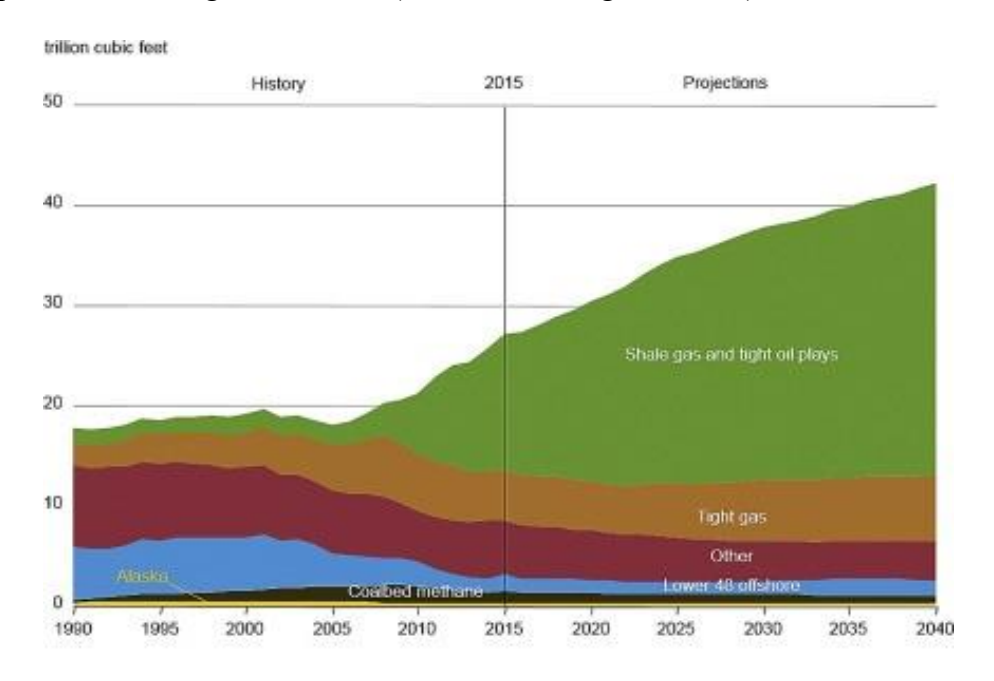


Figure 2.5: Historical and projected natural gas production from conventional and unconventional (Shale gas, Tight gas, Coalbed methane) resources in the United States of America (IEA, 2016).

Unconventional hydrocarbons are recovered directly from the source rock (no migration occurs after formation) and it requires complex extraction methods such as hydraulic fracturing (fracking) and horizontal drilling of the source rock to release economical amounts of gas (Soeder and Borglum, 2019). Fracking has been a point of controversy worldwide with numerous countries in Europe (UK, Germany, Netherlands, France, etc.) deciding to suspend or ban its utilisation for hydrocarbon extraction, due to associated adverse environmental impacts. These impacts involve fracking-induced earthquakes, greenhouse gas and air pollution emissions, land and water contamination and also excessive water usage (Cooper et al., 2016).

The general term "unconventional gas" includes reservoirs that are characterised by low permeability and low porosity. These are shale gas, tight gas, coalbed methane (CBM) and

methane hydrates. Methane hydrates usually contain gas of microbial origin (Stephenson, 2018), although the occurrence of thermogenic gas hydrates in marine environments is well-established (Sassen and Macdonald, 1994; Diaconescu et al., 2001; Dong et al., 2020; Liu et al., 2022).

According to Zou et al. (2017), the total unconventional resources worldwide are estimated at 921.9 x 10<sup>12</sup> m<sup>3</sup>, whereas Wang et al. (2016) reported it at a lower value of 826 x 10<sup>12</sup> m<sup>3</sup> with only 27% regarded as recoverable. These estimations do not account for the share of methane hydrates which are in early stages of exploration and development (Zou et al., 2017). The largest proportion of unconventional gas is found in Asia and Pacific area (29.7%), followed by North America (25.2%), former Soviet Union countries (16.8%), South America (10.5%), Middle East and North Africa (10.3%) and the rest is shared between Europe (3.8%) and Sub-Saharan African countries (3.3%) (Zou et al., 2017). More than half of the recoverable resources are found in foreland basins followed by craton basins, rift basins, passive continental margins and back-arc basins (Wang et al., 2016).

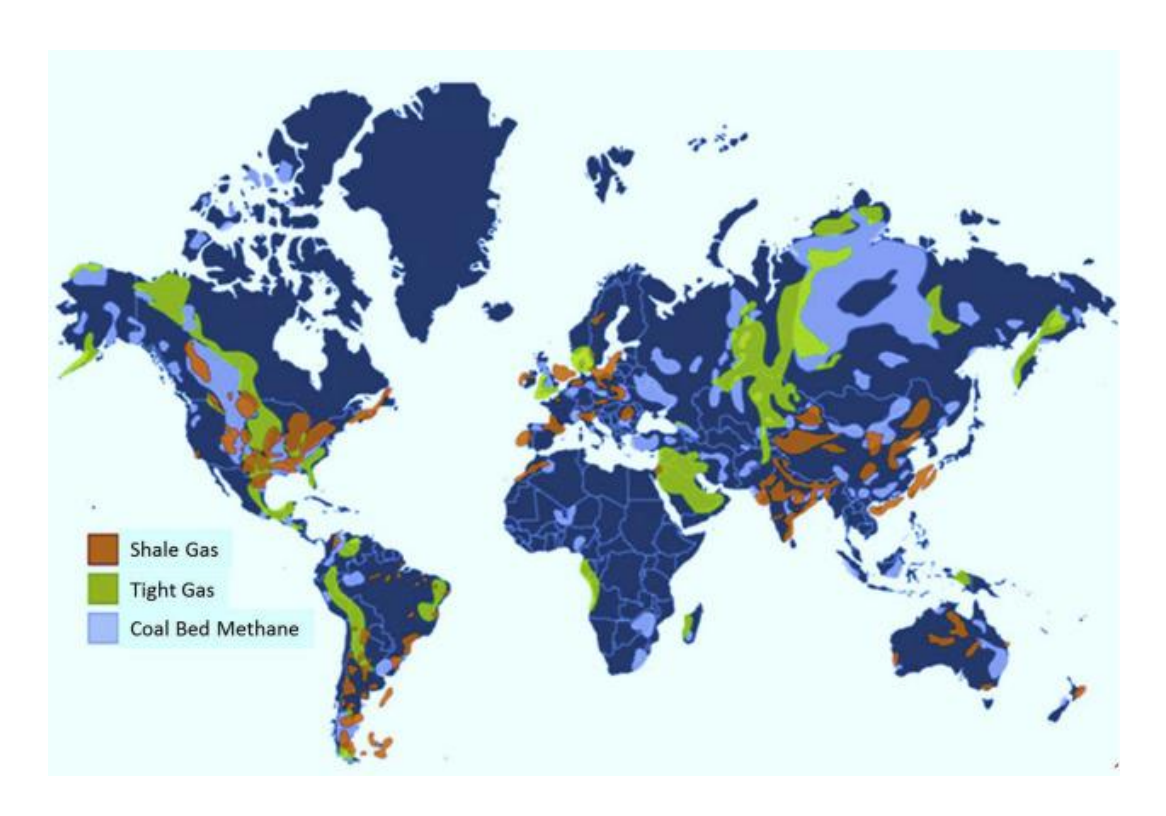


Figure 2.6: Global map of unconventional natural gas resources (Rajput and Thakur, 2016).

Shale gas is found in the subsurface trapped in shale which is a fine-grained sedimentary rock consisting of mainly clay minerals, silt minerals, carbonates, iron oxides and organic

matter typically between 1% and 20% (Varma et al., 2014). Similar to a typical conventional system, the amount and maturity of organic matter along with the type of kerogen will define the hydrocarbon potential of the shale rocks (Tisson and Welte, 1978). Shales are generally characterised by low permeability (<1000nD) and low porosity (<5%) which impedes the flow of hydrocarbons through the pores of the rock and simultaneously allow their accumulation (Goral et al., 2020).

Shale gas is the most abundant form of unconventional gas in a global scale, with estimated resources at 456.2 x 10<sup>12</sup> m<sup>3</sup> which accounts for 49.5% of the total unconventional resources (Zou, 2017). At the current state of knowledge, the largest reserves of shale gas are found at Zagros foreland basin (Middle East, Late Cretaceous to Eocene), Appalachia foreland basin (North America) and Persian Gulf foreland basin (Middle East) (Wang et al., 2016).

Tight gas is generated and accumulated in sedimentary rocks with matrix permeability typically below than 0.1 mD and less than 10% matrix porosity. Tight gas is usually found within sandstones which is a clastic sedimentary rocks composed of primarily sand-sized silicate grains, clay minerals and varying amounts of organic matter. However, tight gas reserves are not limited solely to sandstones and could also be trapped in rock formations including limestone, dolomites and siltstones (Kuuskraa, 2004).

It is the least abundant unconventional gas (excluding the methane hydrates) worldwide with estimated resources at 209.6 x  $10^{12}$  m<sup>3</sup> which accounts for 22.7% of the unconventional reserves (Zou, 2017). The largest known reserves of tight gas in the world are found in Appalachia and Alberta basins (North America).

Coalbed methane (also known as coal seam gas) is generated within coal seams or coal deposits and it can occur as a free gas in the fractures and pores of the coal, dissolved in coalbed water and chemically absorbed in the structure of the coal (Wang et al., 2016; Chen, 2021). For this reason, coal seams require stimulation in order to release the natural gas, although the permeability of the formation influences the method of stimulation. In high permeability seams (>100mD), gas is released using underreaming and cavitation methods, where at low permeability (3-20mD) formations, hydraulic fracturing is required (Zarrouk and McLean, 2019). Coalbed methane is typically found at 250 - 800 m from the surface, thus implies a lower cost of extraction (Palmer, 2010; Zarrouk and McLean, 2019).

CBM can be generated either from microbial or thermogenic processes. In the first stages of coalification (a series of biological, chemical and physical alterations that organic matter undergoes), microbial methane production is the predominant mechanism of methane

generation (Faiz and Hendry, 2006). As the burial of the coal strata progresses and the temperature rises above the optimal growth temperature of methanogens, (40°C for typical strains and above 70-80°C for thermophilic strains) methanogenic methane production is inhibited and succeeded by thermogenic processes.

Coalbed methane is the second most abundant type of unconventional natural gas with estimated resources at  $256.1 \times 10^{12}$  m<sup>3</sup> which accounts for 27.8% of the unconventional reserves (Zou, 2017). The largest proportions of CBM resources are found in the Alberta basin and Kuznetsk basin (Siberia).

Radiolytic methane (Naumenko-Dezes et al., 2022) is produced by the irradiation of organic matter by radioactive elements present in continental basins such as <sup>238</sup>U, <sup>235</sup>U, <sup>232</sup>Th, <sup>230</sup>Th, <sup>40</sup>K (and their radioactive daughters) which have been closely associated with shales (Swanson, 1961). Considerable doses ( $>10^4$  Gy) of radiation in the form of alpha particles, beta particles and gamma rays can change the properties of kerogen and increases its aromaticity and vitrinite reflectance while producing substantial amounts of light alkanes such as methane, ethane and propane (Silva et al., 2019). Even though an accurate estimation of radiolytic gas in natural gas accumulations might be challenging at present, results from laboratory experiments by Lewan et al. (1991) reported methane production of 4µmol per gram of shale (Naumenko-Dezes et al., 2022). According to Naumenko-Dezes et al. (2022), this amount of methane from radiolytic processes is 3 times lower compared to the amounts of thermogenic gas from organic matter of early maturity (<1%). This implies that in some cases (low maturity shales) the proportion of radiolytic gas can be significant (>20%), while in others (high maturity shales) thermogenic gas is even more dominant. Radiolytic gas occurs in Antrim Shale (USA), Alum Shale (Scandinavia), Colorado Group Shale (USA), New Albany Shale (USA).

### 2.2.5.2. Abiotic Methane

Abiotic production of methane differs from thermogenic and microbial pathways as they do not require the presence of organic matter to generate at least in a direct way. The term abiotic includes a wide range of mechanisms which can produce CH<sub>4</sub> under different conditions and in various geological settings. The occurrence of abiotic methane in natural settings was considered rare and controversial in the past but has gained attention in the last decades due to re-evaluation of methane sources in existing gas seeps and accumulations (Sherwood Lollar et al., 2006; Fu et al., 2007; Etiope et al., 2011; Boschetti et al., 2013; Young et al., 2017). Even though the economic significance of abiotic methane is likely limited compared to thermogenic and microbial reserves (Etiope and Sherwood Lollar, 2013), the implications

on extraterrestrial studies can be notable as it is a potential production mechanism of the Martian methane (Young et al., 2017).

An early classification of abiotic methane by Welhan et al. (1988) divided the mechanisms for methane abiogenesis into two main categories: abiotic methane could either be 1) mantlederived and characterised as primordial methane, or 2) inorganically generated at temperatures above 300-400°C in hydrothermal systems associated only with mid-ocean ridges (Etiope and Sherwood Lollar, 2013). A systematic review conducted by Potter and Konnerup-Madsen (2003) identified three major mechanisms responsible for abiotic hydrocarbon production associated with igneous rocks. According to this study, abiotic methane can be classified as mantle-derived, late-magmatic and post-magmatic. The latest and most exhaustive review by Etiope and Sherwood-Lollar (2013), argued that there at least nine processes identified as potential mechanisms for abiotic synthesis of hydrocarbons in natural systems, which can initially be distinguished into magmatic and gas-water-rock reactions. These nine mechanisms are described in brief below:

# I. Magmatic origin

- 1. **Primordial CH**<sub>4</sub>: Methane in the mantle derives from accretion of meteorites (containing CH<sub>4</sub>) during Earth's formation and has been stored since then. There is evidence of methane occurrence in several planetary bodies (Mars, Saturn, Titan, Neptune and Uranus) (Fletcher et al., 2009; Blamey et al., 2015; Webster et al., 2021) which supports the theory of CH<sub>4</sub>-bearing meteorites. However, there are doubts regarding the amount of methane carried by meteorites. In addition, due to the thermodynamic instability of CH<sub>4</sub> at extreme thermobaric conditions of the mantle, it is unlikely that methane from this origin has survived in significant amounts. At 10 to 50 GPa and 2000-3000 K methane dissociates into molecular hydrogen and carbon in the form of soot, diamond or graphite (Zerr et al., 2006). At similar pressures and moderate temperatures (1100 K), methane polymerises and produces higher alkanes (ethane, propane, butane, iso-butane) (Serovaiskii and Kutcherov, 2020).
- 2. **High-T reactions in the mantle:** Mendeleev (1877) suggested that CH<sub>4</sub> can form through a reaction between metal carbides (aluminium or beryllium) and water to produce methane and aluminium or beryllium hydroxide (Etiope and Sherwood Lollar, 2013). Although this mechanism requires highly reducing

conditions that may not be apparent in throughout the mantle (Frost and McCammon, 2008). Scott et al. (2004) proposed a different pathway where carbonates (CaCO<sub>3</sub> and FeO) are reduced under the presence of water to produce methane at between 500 and 1500 °C (Etiope and Sherwood Lollar, 2013).

$$8FeO + CaCO_3 + 2H_2O \leftrightarrow 4Fe_2O_3 + CH_4 + CaO$$
 (2.7)

3. **Respeciation of C-O-H system:** This is a late-magmatic process taking place during the crystallization of magma at temperatures below 600°C (Potter and Konnerup-Madsen, 2003). As the magmatic fluid cools down in a closed system rich in CO<sub>2</sub> and hydrogen is possible to reorganise and produce abiotic methane under the following reaction:

$$CO_2 + 2H_2O \leftrightarrow CH_4 + 2O_2$$
 (2.8)

# II. Gas-water-rock interactions

- 4. **Post-magmatic reactions:** These reactions occur when the magmatic fluid has solidified, and igneous rocks are formed. At temperatures 200°C to 500°C, reactions between water, carbon dioxide and metal oxides can lead to CH<sub>4</sub> formation under the reactions 2.7 and 2.8. These processes usually take place in geothermal systems, while the high temperatures at those environments facilitate the attainment of CH<sub>4</sub>-CO<sub>2</sub> chemical and isotopic equilibrium (Giggenbach, 1997). This supports further the occurrence of those reactions (Giggenbach, 1997; Etiope and Sherwood Lollar, 2013).
- 5. Carbonate-graphite metamorphism: Metamorphic rocks often contain graphite due to degradation of organic matter during metamorphism. When graphite coexists with C-O-H fluids at temperatures below 400°C and particularly during retrograde metamorphism, CH<sub>4</sub> formation is likely under the reaction found below (Holloway, 1984; Etiope and Sherwood Lollar, 2013).

$$Mg_3Si_4O_{10}(OH)_2 + CaCO_3 + 6C + 5H_2O \leftrightarrow 3CaMg(CO_3)_2 + 4SiO_2 + 3CH_4(2.9)$$

It is important to mention that even though this methane is produced by a solely abiotic mechanism, the graphite originates from organic matter. Therefore, in this case the term abiotic describes the mechanism of CH<sub>4</sub> formation and not the substrates taking part in this reaction (Etiope and Sherwood Lollar, 2013).

6. **Iron-carbonate decomposition:** McCollom (2003) based on laboratory experiments, proposed that siderite and water heated at temperatures of about 300 °C can react and produce predominantly CO<sub>2</sub>, H<sub>2</sub> but also alkanes.

$$3FeCO_3 + wH_2O \leftrightarrow Fe_3O_4 + xCO_2 + yCO + HCs$$
 (2.10)

This mechanism is not expected to be quantitatively significant in terms of CH<sub>4</sub>, however it may have contributed for some of the methane and carbon found in metasedimentary rocks (McCollom, 2003).

7. Carbonate methanation: Carbonate minerals (such as calcites, magnesites, siderite) at temperatures between 250°C and 800°C can react with H<sub>2</sub> molecules and produce methane under a process named carbonate methanation. This pathway involves carbonate rocks and is different from the industrial methanation which involves either CO or CO<sub>2</sub> and H<sub>2</sub> (see below) (Schmider et al., 2021). As the concentration of the available H<sub>2</sub> increases, the required temperature for carbonate decomposition decreases according to Reller et al. (1987). Additionally, the presence of metal or transition metal catalysts (such as Mg, Ca, Co, Ni, Cu, Ir, Pd) has been shown to promote the reactions under an H<sub>2</sub>-rich environment which occur either instantly or within 100 mins at 250°C temperature.

$$XCO_3 + 4H_2 \leftrightarrow CH_4 + X(OH)_2 + H_2O$$
 (2.11)   
  $(X = Ca, Mg)$    
  $FeCO_3 + 4H_2 \leftrightarrow CH_4 + FeO + 2H_2O$  (2.12)

8. **Uncatalysed CO<sub>2</sub>-reduction:** In aqueous solutions containing CO, CO<sub>2</sub> and H<sub>2</sub> at temperatures exceeding 150 °C, abiotic methane formation is possible. Seewald et al. (2006) observed rapid methane formation in aqueous solution

at 200°C as a result of CO<sub>2</sub> reduction. This methane was associated with methanol and the process does not require the presence of catalyst to occur. Following the reaction below, CO<sub>2</sub> is initially reduced to form formic acid which subsequently reduced to formaldehyde and methanol.

$$CO_2 + H_2 \rightarrow HCOOH (2.13)$$
  
 $HCOOH + H_2 - H_2O \rightarrow CH_2O (2.14)$   
 $CH_2O + H_2 \rightarrow CH_3OH (2.15)$   
 $CH_3OH + H_2 - H_2O \rightarrow CH_4 (2.16)$ 

These reactions might be particularly significant for the maintenance of microbial communities living in hydrothermal settings as the products of those reactions can serve as energy sources. However, this can occur only at temperatures sustainable for those microorganisms, below the limit of life at 122°C (Takai et al., 2008).

9. **Fischer-Tropsch reactions:** This mechanism will be given more detail, as it is widely accepted as the most common pathway for abiotic synthesis of methane (Sherwood Lollar et al., 1993; Foustoukos and Seyfried, 2004; Etiope and Sherwood Lollar, 2013). This pathway is often associated with serpentinisation of mafic and ultramafic rocks. Serpentinisation is the hydration and metamorphic transformation of minerals such as olivine and pyroxene resulting in the formation of serpentinite. Minerals formed by this process include typically nickel, chromium, iron and others. This process also releases H<sub>2</sub> molecules, which as CO or CO<sub>2</sub> are present, can lead to the formation of hydrocarbons at a wide range of temperatures between 25°C and 500°C. Methane and heavier linear hydrocarbons can be produced by catalytic hydrogenation of CO under the following process (Etiope and Sherwood Lollar, 2013):

$$nCO + 2nH_2 \leftrightarrow (CH_2)_n + H_2O$$
 (2.17)

Catalytic hydrogenation of carbon dioxide can either occur through one step methanation known as Sabatier reaction (2.18) or in two steps by converting firstly carbon dioxide to carbon monoxide in a process known as water-gas shift (reactions 2.19-2.20).

$$CO_2 + 4H_2 \leftrightarrow CH_4 + 2H_2O$$
 (2.18)  
 $CO_2 + H_2 \leftrightarrow CO + H_2O$  (2.19)  
 $CO + 3H_2 \leftrightarrow CH_4 + H_2O$  (2.20)

According to Etiope and Sherwood Lollar (2013), the occurrence of serpentinization is not a prerequisite for inorganic synthesis of abiotic methane via Fischer-Tropsch reaction, as there are other possible sources of H<sub>2</sub> in natural environments. Indeed, hydrogen could be derived from magmatic outgassing (Zgonnik, 2020), radiolysis of water in isolated environments (Sherwood Lollar et al., 2021; Karolyte et al., 2022) or cataclasis of silicate minerals at fault zones and fractured rocks (Giardini et al.,1976; Sugisaki et al.,1983; Apps and van de Kamp, 1993). Hence, there are various mechanisms plausible for H<sub>2</sub> in natural systems and subsequent synthesis of abiotic methane. Although large uncertainties remain about the rate and the degree of these processes and whether these are the limiting factors for the negligible economic significance of abiotic hydrocarbons reserves.

In industrial applications, Fischer-Tropsch reactions require the presence of a metal catalyst such as nickel, ruthenium, cobalt, iron and chromium to facilitate the process (Keunecke et al., 2024). In the case of water-gas shift reactions, the gas conversion takes place on the surface of the catalyst where the CO binds and forms a carbonyl unit which is reduced repeatedly to methylene, methyl groups and methane (McCollom and Seewald, 2007). Numerous studies have achieved abiotic synthesis of CH<sub>4</sub> via Fischer-Tropsch reactions in a controlled laboratory environment through the usage of transition metal catalysts (Foustoukos and Seyfried, 2004; McCollom and Seewald, 2007; Taran et al., 2007; Etiope and Ionescu, 2014; Young et al., 2017). These experimental studies reported rapid methane production rates from hours to days at temperatures above 200 and high pressures for Ni, Cr and Fe, and a much quicker methanation using ruthenium and rhodium catalysts (a few hours) even at room temperature and atmospheric pressure (Etiope and Sherwood Lollar, 2013). In natural settings, nickel, iron and chromium are the most abundant transition metals in ultramafic rocks such as chromitites or magnetites. Therefore, their natural occurrence can enhance abiotic CH<sub>4</sub> production.

Abiotic methane produced through Fischer-Tropsch reactions has been reported close to mid-ocean ridges such as submarine serpentinised hydrothermal fields (e.g. hydrothermal vents in Lost City and Rainbow in the Atlantic Ocean, and volcanic arcs such as the Mariana Arc in the Pacific Ocean) and land-based serpentised sites (ophiolites, peridotites massifs and igneous intrusions) in Japan (Happo), Philippines (Zambales), Oman (Samail), Turkey (Chimaera), Greece (Othrys) and Italy (Acquasanta). Abiotic methane has also been associated with crystalline rocks and fracture waters in Precambrian shields in Canada, South Africa and Scandinavia (Abrajano et al., 1990; Sherwood Lollar et al., 2006; Sherwood Lollar et al., 2008; Etiope et al., 2011; Etiope and Schoell, 2014).

#### 2.2.5.3. *Microbial CH*<sub>4</sub>

Microbial methane plays a significant role in the carbon cycle and a large contribution in atmospheric methane budget comprising up to 60% of the total emissions (Jackson et al., 2020). Microbial, or biogenic, methane is produced in a wide range of typically anoxic environments such as terrestrial, marine and freshwater systems. The production of methane known as methanogenesis is the last step of a metabolic process usually related to the degradation of organic matter performed by living organisms named as methanogens. The methanogens are single-cell organisms belonging to the domain of Archaea, commonly found within the Euryarchaeota, Crenarchaeota, Halobacterota and Thermoplasmatota phyla (Lyu et al., 2018).

There are three individual main pathways of methanogenesis: 1) hydrogenotrophic methanogenesis, 2) acetoclastic methanogenesis and 3) methylotrophic methanogenesis based on the type of the substrates utilised by the methanogenic archaea and the chemical reactions taking place.

Table 2.2: Physiological characteristics corresponding to each methanogenic order. Obtained from Angelidaki et al. (2011).

Methanogenic type	Substrates	Growth Temperature (°C)	pН
Methanosarcinales	Acetate, H <sub>2</sub> + CO <sub>2</sub> , CO, methanol, methylamines, methylmercaptopropionate, dimethylsulfide	1.0–70	4.0–10.0
Methanomicrobiales	H <sub>2</sub> + CO <sub>2</sub> , formate, ethanol,2-propanol,2- butanol,cyclopentanol	15–60	6.1–8.0
Methanobacteriales	H <sub>2</sub> + CO <sub>2</sub> , CO, formate, C <sub>1</sub> -methylated compounds	20–88	5.0-8.8
Methanococcales	$H_2 + CO_2$ , formate	<20-88	4.5–9.8
Methanopyrales	$H_2 + CO_2$	84–110	5.5–7.0
Methanocellales	$H_2 + CO_2$ , formate	25–40	6.5–7.8

The three pathways of methanogenesis are described briefly below:

1. Hydrogenotrophic methanogenesis [carbonate reduction]: Hydrogenotrophic methanogens can generate methane by reducing the available carbon dioxide usually with hydrogen, although, more rarely formate (HCOO<sup>-</sup>) or alcohols such as ethanol, propanol or 2-butanol can be used as electron donors. The following reaction describes the most common pathway of hydrogenotrophic methanogenesis (Kurth et al., 2020):

$$CO_2 + 4H_2 \rightarrow CH_4 + 2H_2O$$
 (2.21)

Hydrogenotrophic methanogens demonstrate the largest diversity across the different methanogenic orders in a wide range of temperatures (Kurth et al., 2020). Hydrogenotrophs have generally an optimal temperature of growth between 55 °C and 70 °C while some species of the methanogenic order of *Methanopyrales* can

thrive at thermophilic conditions at temperatures as high as 110 °C (Angelidaki et al., 2011; Figeac et al., 2020).

2. Acetoclastic methanogenesis [microbial fermentation]: Acetoclastic methanogenesis is one of the major pathways of methanogenesis, particularly dominant in freshwater environments and responsible for the production of biogas in anaerobic digestors (Fenchel et al., 2012). Under this pathway, acetoclastic methanogens use acetate as a substrate and convert it to methane and carbon dioxide under the following reaction:

$$CH_3COO^- + H^+ \rightarrow CH_4 + CO_2$$
 (2.22)

Acetoclastic methanogenesis is only carried out by the methanogenic order of *Methanosarcinales* and specifically from the *Methanosarcina* and *Methanosaeta* species with optimal growth temperature in the range of 25 °C to 45°C (Ma et al., 2006).

3. Methylotrophic methanogenesis: Methylotrophic methanogenesis is the least significant pathway regarding the amount of methane produced, considering the scarce availability of methanol compared to acetate, carbon dioxide and hydrogen required for the other types of methanogenesis (Conrad, 2020). However, methylotrophic methanogenesis is more common in sulfate-rich sediments (such as marine and saline environments), where sulfate-reducing bacteria are competing and binding more effectively the compounds used by hydrogenotrophic and acetoclastic methanogens (Vincent et al., 2021). Thus, methylotrophic methanogenesis is more dominant in those environments, but overall accounts for a negligible percentage of the global emissions of methane (Lyu et al., 2018).

Methylotrophic methanogenesis occurs by the methanogenic order of *Methanosarcinales* and only by one strain of *Methanobacteriales*, the *Methanosphaera Sp.*, by transforming methylated compounds such as methanol, dimethyl sulfide (DMS), methylmercaptopropionate and methylamines (Monomethylamine, Di- methylamine or Tri- methylamine) into methane under the following reactions (Angelidaki et al., 2011; Krause, 2022):

$$4CH_3OH + H^+ \rightarrow 3CH_4 + CO_2 + 2H_2O(2.23)$$

$$4CH_3NH_2 + 2H_2O \rightarrow 3CH_4 + CO_2 + 4NH_4(2.24)$$

Independently of the pathway of methanogenesis and the substrates used, all the groups of methanogenic archaea utilise the Mcr (methyl-coenzyme M reductace) enzyme which is pivotal in the last step of methanogenesis and facilitates the generation of methane (Chen, 2020).

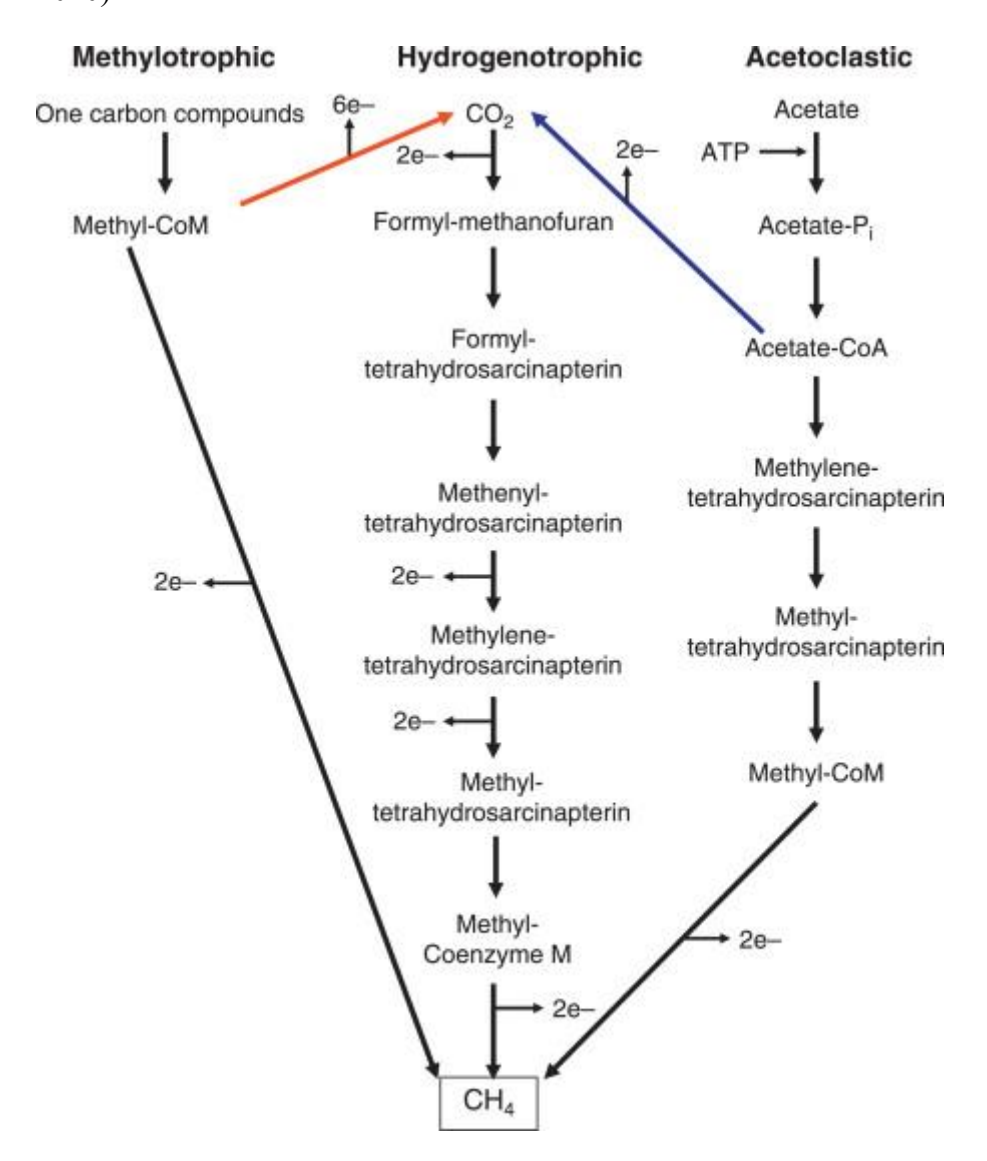


Figure 2.7: Summary of the three main pathways of methanogenesis (DasSarma et al., 2009).

Microbial methane occurs in a wide range of environments because methanogens can thrive in both oxic and anoxic environments, using different metabolic pathways and substrates for energy production. Here, I present the most significant (quantitatively) microbial sources of CH<sub>4</sub> to the atmosphere and in aquatic systems, either related to anthropogenic activities or natural processes. In this subsection, I mention the occurrence of microbial methane in gas hydrates which are a unique type of gas reservoir, while I also discuss their economic and climate importance coupled with their large global deposits.

Microbial methane emissions are the largest contributor (70%) in the global methane budget amongst the methane sources including both anthropogenic and natural emissions (Lyu et al., 2018). Microbial methane is emitted from a variety of sources and environments including wetlands, freshwater systems, rice paddies, livestock and insects, and the waste sector. Although approximately 20% of global natural gas resources are estimated to originate from microbial sources (Rice, 1993; Kotelnikova, 2002), in this section I do not account the contribution of microbial CH<sub>4</sub> associated with emissions from the fossil fuel sector.

CH<sub>4</sub> emitted by inland freshwater environments is a significant source of methane in the atmosphere, accounting for approximately 17% (112 Tg/yr) of the global emissions (Saunois et al., 2024). Methane is produced by methanogens in the sediments of lakes, ponds, rivers, streams and reservoirs and released through diffusion or ebullition (Baur et al., 2024). Methane is produced in wetlands which include as bogs, fens, marshes, swamps and others. Wetlands are the largest natural source of methane in the global methane budget, contributing 159 Tg/yr which accounts for approximately 24% of the global emissions (Saunois et al., 2024). Tropical wetlands comprise about 60% of the total wetland emissions (Murguia-Flores, 2023). Often, freshwater and wetland emissions of CH<sub>4</sub> are reported together due to the similar characteristics in terms of methane production and transport.

Rice paddies also share similar characteristics with wetlands and inland freshwater systems, although they are accounted for as anthropogenic sources. Rice paddies contribute about 4% of the total emissions (Saunois et al., 2024), with higher emissions in summer months (Meijide et al., 2011). The emissions vary as they are highly associated with the ambient temperatures, the water regime (flooded or not flooded) and the plant development stage (Meijide et al., 2011; Lee et al., 2023).

Other significant microbial sources associated with anthropogenic activities include the CH<sub>4</sub> emissions from the waste sector and the livestock. Methane emitted from landfills and sewage treatment facilities comprise about 16% of the global microbial emissions and approximately 10% of the global emissions (Lyu et al., 2018; Saunois et al., 2024). Methane is produced along with CO<sub>2</sub> and H<sub>2</sub>S in anoxic conditions during the anaerobic decomposition of organic matter found in the organic wastes of landfills and the sludge of the wastewater treatment plants.

The enteric fermentation performed by livestock is one of the largest contributors in methane emissions, accounting for 25% of the microbial emissions and approximately 15% of the

total emissions (EPA, 2021). Methanogens inhabit the rumen and intestines of animals such as cattle, sheep, goats and utilise mostly CO<sub>2</sub> and H<sub>2</sub> produced by other digestive processes, and more rarely acetate and methylamines to generate methane (Patra et al., 2017). Ruminants are not the only animals contributing to methane emissions, as methanogenic archaea living in the digestive system of termites are able to produce methane by utilising CO<sub>2</sub> and H<sub>2</sub> which are by-products of the cellulose breakdown (Zimmermann et al., 1982). The CH<sub>4</sub> emissions by termites are estimated at approximately 9-15 Tg/year which is a small amount compared to the total global emissions of 669 Tg/year (Law et al., 2024; Saunois et al., 2024).



Figure 2.8: Sources of microbial methane and their associated contributions in global microbial emissions (Lyu et al., 2018).

Natural gas hydrates are unique compounds containing ice and low-weight alkanes (dominantly CH<sub>4</sub>) and form at low temperatures (-10 to -25°C) and relatively high pressures between 3 and 30 MPa (Ruppel and Waite et al., 2020). Gas hydrates occur within 2 km below of the Earth's surface more commonly (98%) of the total gas hydrates deposits in continental slopes and rarely (2%) in polar areas, such as permafrost, lakes and tundras at depths of maximum 150 m from the surface (Kvenvolden, 1993; Jinxing et al., 2017). Even though, thermogenic gas hydrates have been discovered around the world (Gulf of Mexico, Caspian Sea, Alaska, Canada) the majority of gas hydrates originate from microbial processes dominantly by CO<sub>2</sub> reduction (Kvenvolden, 1995).

Gas hydrates have been in the spotlight of research the last decade, as they comprise at least a sixth of the Earth's methane inventory and estimated global gas deposits of 3 x  $10^{15}$  m<sup>3</sup>, more than all the unconventional gas deposits combined (Zou et al., 2013; Ruppel and Waite

et al., 2020). Consequently, they can serve as a significant energy resource in the future as the global demand of energy is expected to increase while reducing the GHG emissions (Chong et al., 2015). In contrast, as natural gas hydrates occur in marine and permafrost areas, any potential temperature increases in seawater or the atmosphere due to climate change, may perturb the stability of the hydrates and release methane into the atmosphere, and contribute to the global warming (Kvenvolden, 1993). The destabilisation of gas hydrates and the release of CH<sub>4</sub> into the atmosphere have been connected with the end of Permian period (~252 Ma), and the biggest mass extinction episode in marine and terrestrial environments in Earth's history (Brand et al., 2016).

# 2.2.6. Molecular and Isotopic Compositions

# 2.2.6.1. Thermogenic Gas

Thermogenic natural gas consists of 70-90% methane (C<sub>1</sub>) with smaller amounts (20%) of higher hydrocarbons ( $C_{2+}$ ; ethane, propane, butane and n-butane), nitrogen (0-5%), carbon dioxide (0-8%), hydrogen sulphide (0-5%), oxygen (0-0.2%) and traces of helium, neon and water vapour. The molecular composition of thermogenic gas is linked to the type of kerogen and the maturation level of the organic matter (Hunt, 1996). For instance, sapropelic kerogens (Type I and Type II) produce higher contents of C<sub>2+</sub> hydrocarbons than humic kerogen (Type III) in accordance with their higher H/C content. However, this does not necessarily translate into higher composition of C<sub>2+</sub> in the produced natural gas, as further maturation of the organic matter can lead to breakdown of the C2+ hydrocarbons and a significant increase in C<sub>1</sub>/C<sub>2+</sub> ratios. Overall, thermogenic natural gas is distinct from microbial gas based on its low C<sub>1</sub>/C<sub>2+</sub> values which can be attributed to the higher abundances of ethane, propane and butane (Bernard, 1977). A recent compilation of data by Milkov and Etiope (2018) reported  $C_1/C_{2+}$  values between 0.01 and 100,000 which overlap with those for microbial and abiotic gases. Therefore C<sub>1</sub>/C<sub>2+</sub> ratios cannot be used alone to track gas origin and further information will be required such as the kerogen type and maturation stage.

Type II kerogens are generally characterised by the highest content of sulphur compared to the other kerogen types (Aizenshtat and Amrani, 2004). H<sub>2</sub>S can be generated during the breakdown of organic matter and more precisely in late thermal maturity levels. Higher yields of CO<sub>2</sub> are expected during thermal decomposition of Type III kerogen than Type I/II, due to the higher O/C values found in humic kerogens (Hunt, 1979; Hunt, 1996). This is expected at low to medium maturation stages.

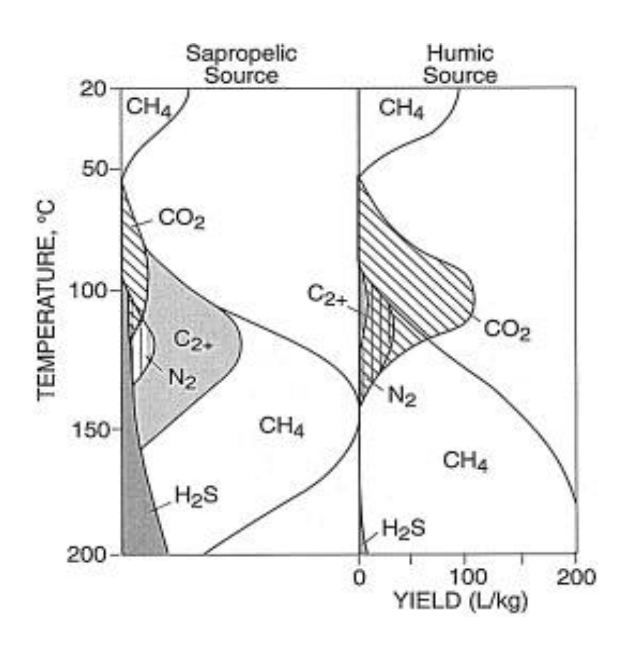


Figure 2.9: Relative proportion of generated gases during maturation of organic matter. Microbial methane can be produced initially by microbial processes at temperatures between 20-60°C in the source rock, while thermogenic methane is produced at temperatures >65 °C. Derived from Hunt (1979).

Common values of  $\delta^{13}$ C and  $\delta D$  (defined in 2.2.1 section) for thermogenic gas usually fall in a range of the isotope space, where thermogenic, microbial, and abiotic methane overlap. This overlap makes it challenging to distinguish between individual sources and mixtures (e.g., microbial-thermogenic, microbial-abiotic, or abiotic-thermogenic) based solely on isotopic composition.

Typically, the isotopic signatures of thermogenic methane in natural environments range between -50 and -20‰ for  $\delta^{13}$ C, and between -250 and -150‰ for  $\delta$ D. However, both isotopic signatures of thermogenic methane can vary largely, between -75‰ and -15‰ for  $\delta^{13}$ C, and between -350‰ and -150 ‰ for  $\delta$ D (Milkov and Etiope, 2018).

The large ranges both in  $\delta^{13}$ C and  $\delta D$  occur for a variety of reasons including the natural variability in the isotopic compositions of the substrate (organic matter/kerogen), the type of kerogen (humic vs sapropelic), the maturation stage of the source rock and post-generation processes taking place such as gas migration, oxidation, mixing and microbial cycling either within the source rock or after its accumulation in the reservoir rock (Hoeffs, 2015).

To understand the mechanisms of hydrocarbon formation through the isotopic composition of C and H, experiments have been done to reproduce the cracking of organic matter in laboratory environment. Sackett (1978) and Chung and Sackett (1979) investigated the isotopic fractionation during pyrolysis of shales and kerogen and found that  $CH_4$  produced was lower in  $\delta^{13}C$  and  $\delta D$  than the initial compound. Similarly, Sackett (1984) subjected n-

octadecane to pyrolysis at 400°C and 500°C and observed that the produced methane was lower in  $\delta^{13}$ C by 4-25% and lower in  $\delta D$  by 70-170% compared to the parent compound. Moreover, they observed that the carbon isotopic fractionation between the octadecane and the methane was decreasing with the duration of pyrolysis which agreed with the findings from previous studies (Sackett, 1978; Chung and Sackett, 1979). The isotopic signatures of thermogenic methane tend to change throughout the maturation process of the source rock. This is well-established across the literature and observed in numerous natural gas fields (Lewan, 1983; Hakami et al., 2016; Lu, 2023). Methane generated early is lower in  $\delta^{13}$ C and  $\delta D$  compared to methane generated later. This is due to unequal propensity for bond breakage depending on the isotopes of the atoms involved: During the breakdown of the kerogen, there is a preferential cleavage of  $^{12}$ C- $^{12}$ C bond (similarly for H-H), as it requires less energy to break than the  $^{12}$ C- $^{13}$ C bond (or H-D). The kerogen gets depleted in the light isotopes which increases the  $\delta^{13}$ C and  $\delta D$  values. Hence, as the maturation progresses the generated methane has higher  $\delta^{13}$ C and  $\delta D$  than the methane produced in early stages of maturation (Chung et al., 1988).

Later studies focused on understanding the breakdown of kerogen, for the different types of kerogen. For example, Clayton (1991) carried out pyrolysis experiments on different types of kerogen (type I/II vs type III) and observed that the isotopic fractionation in <sup>13</sup>C between the kerogen and the produced methane was much larger in the case of sapropelic source (type I/II) than the humic source (type III) of -17.5‰ and -1.4‰, respectively.

#### 2.2.6.2. Abiotic Gas

The relative abundance of isotopes can be used to distinguish the origin of methane and potentially indicate the formation pathway of methane (Schoell, 1980). In this section, I present the typical variations in  $\delta^{13}$ C and  $\delta D$  for abiotic methane in diverse geological environments.

Initial studies reported values for abiotic methane higher than -25% in  $\delta^{13}$ C which led to the conclusion that abiotic field in a typical ( $\delta^{13}$ C-  $\delta$ D) Schoell plot is distinct from the thermogenic and microbial fields (Etiope and Sherwood Lollar, 2013). Further study by Etiope and Schoell (2014), revealed that abiotic methane in hydrothermal and volcanic systems is isotopically distinct from methane associated with deep Precambrian crystalline rocks and fracture systems. Specifically, the  $\delta^{13}$ C ranges from -30% to -10% for methane found in volcanic and hydrothermal systems, and between -50% and -25% for methane associated with crystalline rocks (Etiope and Schoell, 2014; Etiope, 2015). Methane from those environments also differ in  $\delta$ D, however with significant overlap. Methane from

volcanic-hydrothermal systems typically vary in  $\delta D$  between -250‰ and -50‰, and -450‰ to -150‰ for methane found in deep crystalline rocks. However, abiotic methane resided within fracture systems is often mixed with microbial methane (Ward et al., 2004; Young et al., 2017; Xia and Gao, 2021; Karolyte et al., 2022) leading to lower  $\delta^{13}C$  and higher  $\delta D$ . Methane associated with serpentinised systems presents a higher variability compared to methane found in the other two environments, with  $\delta^{13}C$  to range between -37‰ and -5‰, and  $\delta D$  between -350‰ and -100‰.

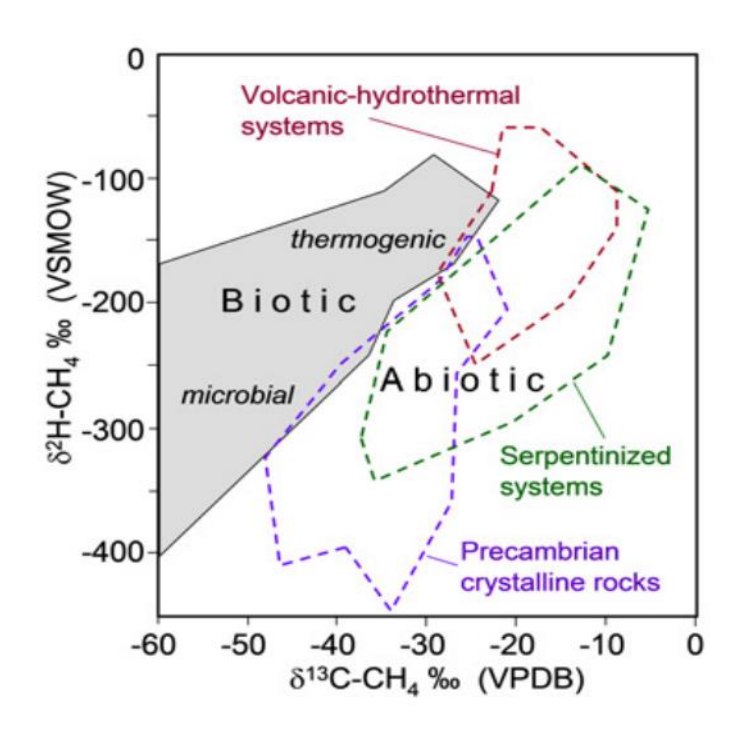


Figure 2.10:  $\delta^{13}$ C vs  $\delta^{2}$ H isotopic signatures (Schoell plot) for biotic (thermogenic and microbial) and abiotic methane found in different geological settings (Etiope and Schoell 2014).

The discrimination of abiotic methane based solely on stable isotopic and molecular compositions can be challenging. For instance, a detailed review by Milkov and Etiope (2018) on more than 20,000 samples of methane across the world, pointed out that abiotic methane has the largest variability in  $\delta^{13}$ C and  $\delta$ D, about 60 ‰ (from -50‰ to +10‰) and 400 ‰ (from -450‰ to -50‰) respectively. According to the same study,  $C_1/C_{2+}$  values might also be difficult to interpret as they spread between 0.01 and 100,000. One of the reasons of these limitations could be that abiotic methane is hardly found as a purely abiotic gas (Etiope and Sherwood Lollar, 2013), but instead is often mixed with thermogenic and microbial components in proportions either unknown or not well-constrained. Other possible explanations could be attributed to the nine different mechanisms, which can generate abiotic gas as discussed previously. Indeed, not all the pathways of abiotic methane generation are

equally plausible and volumetrically important. However, the wide range of temperatures (from 25°C in serpentinized systems to 800°C in volcanic systems), substrates (carbonate minerals, aqueous or gaseous CO<sub>2</sub>, water, metal carbides), chemical reactions, and geological settings all contribute to the variability in isotopic and molecular compositions. Importantly, the δ<sup>13</sup>C values of substrates (e.g. CO<sub>2</sub>) can also vary considerably (Wagner et al., 2018). Additionally, post-generation mechanisms such as migration, anaerobic and aerobic oxidation can also alter the isotopic signatures and complicate any effort, although this argument also applies to thermogenic and microbial methane in natural settings.

## 2.2.6.3. Microbial Gas

The chemical and isotopic composition of microbial gas is strongly associated with the metabolic pathway and the substrates used for the generation of methane, and the microorganism performing methanogenesis (Conrad, 2005). However, there are common characteristics between the microbial gases produced by the different pathways. For example, unlike thermogenic and abiotic gases which have a broad range of  $C_1/C_{2+}$  values, pure microbial gases have typically  $C_1/C_{2+}$  values above 200 due to the lack of production of alkanes other than methane (Milkov and Etiope, 2018). Therefore, the  $C_1/C_{2+}$  ratio can be an important diagnostic tool to trace microbial gas, especially when coupled with the  $\delta^{13}C$  of methane (Bernard et al., 1978).

Measurements of  $\delta^{13}$ C and  $\delta D$  have assisted with distinguishing the origin of gas across thermogenic, abiotic and microbial sources. When methane originates from microbial sources,  $\delta^{13}$ C and  $\delta$ D can potentially indicate the pathway of methanogenesis from which the microbial methane was produced (Whiticar et al., 1986). For the two most common pathways of methanogenesis, typical values of  $\delta^{13}$ C for methane produced by hydrogenotrophic methanogenesis (CO<sub>2</sub>-reduction) range between -80% and -60% and are generally lower than the typical range for acetoclastic methanogenesis which spans between -65% and -50% (Whiticar et al., 1986; Milkov and Etiope, 2018; Dong et al., 2020). This is due to the larger fractionation factor  $^{13}\alpha$  during hydrogenotrophic methanogenesis rather than acetoclastic methanogenesis (Summons et al., 1998). This larger fractionation occurs between CO<sub>2</sub> and CH<sub>4</sub>, because there are more enzymatic steps required to convert CO<sub>2</sub> into a methyl group through the hydrogenotrophic pathway compared to the acetoclastic pathway (Whiticar 1999; Conrad, 2005) (see Figure 2.7). Essentially, this means that there are more chances to fractionate <sup>13</sup>C and <sup>12</sup>C due to kinetic effects as there are more steps involved. Contrarily, methane produced by hydrogenotrophic methanogenesis usually has higher δD than methane produced by acetoclastic methanogenesis, typically between -250\% and -150\% instead of between -350‰ and -250‰, respectively (Milkov and Etiope, 2018). In hydrogenotrophic methanogenesis, the hydrogen atom is assimilated into the methane molecule from the water with a constant fractionation (Whiticar et al., 1986). On the other hand, during acetoclastic methanogenesis 3 out of 4 of the hydrogen atoms derive from the methyl group, and 1 out of 4 derive from the formation water through an intermediate reaction (Whiticar et al., 1986). Consequently, kinetic effects can occur at this step and lead overall to greater isotopic fractionation.

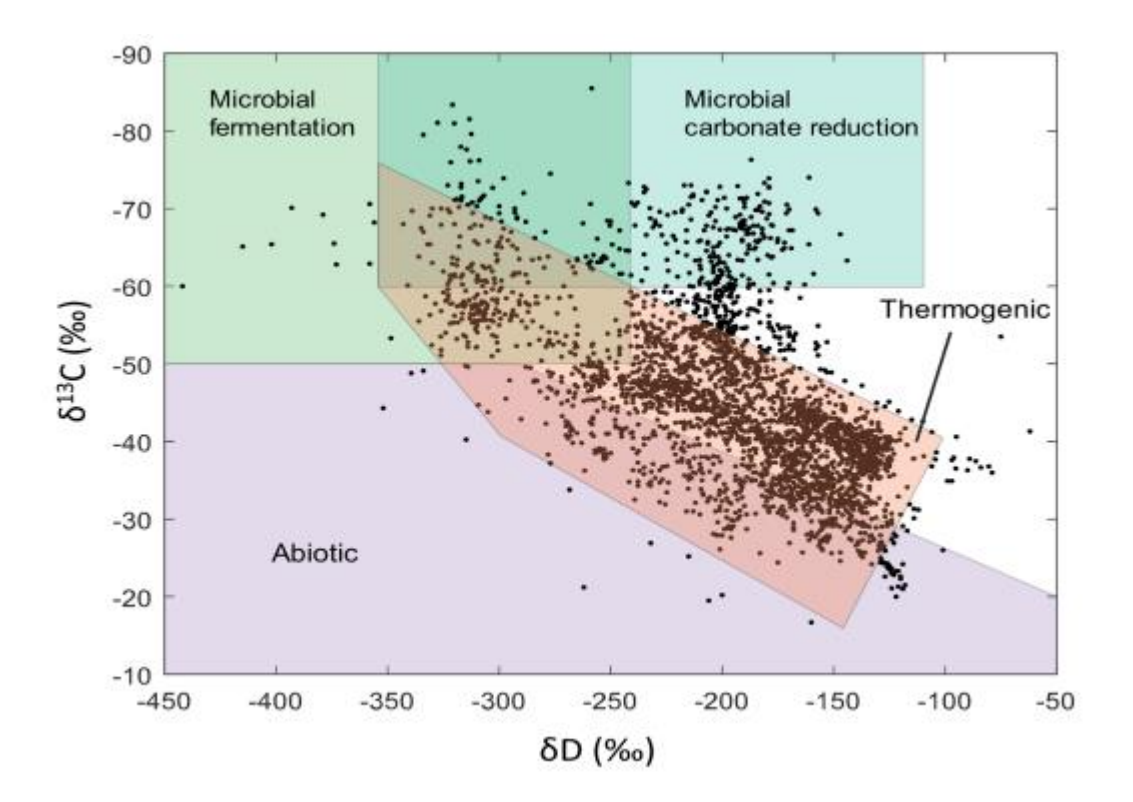


Figure 2.11:  $\delta^{13}$ C vs  $\delta D$  plot, indicating the areas for microbial fermentation [acetoclastic methanogenesis] (green), microbial carbonate reduction [hydrogenotrophic methanogenesis] (light blue), thermogenic (red) and abiotic (purple) sources (Dong et al., 2020).

# 2.2.7. Methane (CH<sub>4</sub>) Sinks

Chemical and biological processes can act to remove methane and play significant roles in the carbon cycle and the atmospheric methane budget. Chemical reactions involving radicals take place into the atmosphere, while biologically-mediated reactions occur in soils, subsurface and aquatic environments. Sink processes may create isotopic fractionation between  $^{13}\text{C}$ - $^{12}\text{C}$  and H-D and impact the isotopic signatures  $\delta^{13}\text{C}$  and  $\delta$ D of methane in natural settings (Whiticar, 1999).

## 2.2.7.1. Non-biological Processes

Chemical reactions occur in the atmosphere, particularly in the troposphere and the stratosphere. Chemical processes account for approximately 96% of the total CH<sub>4</sub> sinks (Kirsche et al., 2013). However, the sources and sinks that govern the methane atmospheric budget are subject to significant uncertainties (Kirsche et al., 2013; Saunois et al., 2024). Oxidation of CH<sub>4</sub> by OH· (hydroxyl radical) is the dominant (~90%) mechanism that consumes atmospheric methane (Saunois et al., 2024). The hydroxyl radical is also responsible for removing other greenhouse gases (CO<sub>2</sub>, HFCs) or air pollutants (CO, NO<sub>x</sub>, O<sub>3</sub>) from the atmosphere (IPCC, 2007). The initial reaction for methane oxidation is:

$$CH_4 + OH \cdot \to CH_3 \cdot + H_2O$$
 (2.25)

Subsequent chemical reactions with oxygen and other chemical species in the presence of sunlight leads to complete methane oxidation initially to CO and finally to CO<sub>2</sub> (Naik et al., 2013):

$$CO + OH \cdot \rightarrow CO_2 + H \cdot (2.26)$$

The reaction with chlorine radical (Cl·), particularly in the troposphere, removes approximately 3% of atmospheric CH4 (Allan et al., 2007; Kirsche et al., 2013; Gromov et al., 2018), although recent study suggests that it might be underestimated (van Herpen et al., 2023). This reaction takes place only within the marine boundary layer which is the part of troposphere that is in direct contact with the ocean. The Cl· derives from the NaCl contained in sea salt particles, after chemical reactions between NaCl and atmospheric species under the presence of solar radiation (Vogt et al., 1996; von Glasow, 2006; Crisp et al., 2014; Wang et al., 2019). The reaction of methane with Cl· is:

$$CH_4 + Cl \cdot \rightarrow CH_3 \cdot + HCl (2.27)$$

The reaction proceeds in a similar way as in reaction (2.26), and leads to the formation of  $CO_2$ .

While the most important sinks of methane are present within the troposphere (Ehhalt, 1974), chemical loss of methane can also occur in the stratosphere by reactions with either halogens (Cl, F), hydroxyl radical or excited oxygen atoms O(<sup>1</sup>D). While the uncertainties are large within the atmospheric models used, the hydroxyl radical reactions in stratosphere account for approximately 40% of the methane stratospheric loss, whereas reactions with halogens and atomic oxygen account for 20-35% and 25% respectively (Saunois et al., 2024). Overall,

these are not crucial for CH<sub>4</sub> destruction and only 3% of total methane loss is attributed to them in the methane atmospheric budget (Kirsche et al., 2013).

# 2.2.7.2. Biological Processes

Methanotrophs utilise methane (and other alkanes) as a substrate and produce inorganic carbon compounds (CO<sub>2</sub>, HCO<sub>3</sub><sup>-</sup>) and biomass (Tan et al., 2024). Oxidation of methane can be carried out microbially, either in aerobic and anaerobic environments, with the use of different electron acceptors such as oxygen, nitrite, nitrate, sulphur compounds and metals (e.g. Fe, Mn).

Aerobic oxidation of methane (AeOM) takes place in oxic conditions in a variety of environments including soils, marine sediments, freshwater lakes and others (Krause, 2022). AeOM performed by aerobic methanotrophs into comprises 4% of the total atmospheric methane consumption (Kirsche et al., 2013). Aerobic methanotrophs are divided into two categories; Type I methanotrophs which belong to family of *Methylococcaceae* and Type II methanotrophs correspond to *Methylocystaceae* family (Murrell, 2010). While both types of utilise the same enzyme (monooxygenase or MOO) to convert methane into methanol, they follow different pathways to convert formaldehyde into biomass (Hanson and Hanson, 1996).

Anaerobic methanotrophs (ANME) perform anaerobic oxidation of methane (AOM) under anoxic and suboxic conditions. ANME are commonly found in lake sediments, marine sediments, soils, oil-field sediments, submarine mud volcanoes, marine methane seeps, and terrestrial environments (fracture networks at deep biosphere settings) at depths even below 3 km (Lau et al., 2016; Simkus et al., 2016; Lollar et al., 2019; Dowd et al., 2022).

ANME are closely related to methanogens (similar in shape and structure), and some strains of ANME are even capable of methanogenesis in some environments (Kevorkian et al., 2020). The association of ANME with methanogens and the identification of the Mcr (*Methyl-Coenzyme M Reductase*) enzyme in methanotrophs, led to the theory that AOM can be conducted through the reverse methanogenesis pathway (Cui et al., 2015).

Overall, there are three different types of AOM dependent on the electron acceptor involved. These three types of AOM are described below:

1. **Sulphate-dependent (S-DAMO):** In this AOM type, methanotrophs using sulphate as electron acceptors and methanotrophy is coupled with sulphur oxidation performed by sulphur reducing bacteria (SRBs). AOM produces CO<sub>2</sub> and H<sub>2</sub>, where the latter is utilised by SRBs to produce bicarbonate and sulfide from the following reaction:

$$CH_4 + SO_4^{2-} \rightarrow HCO_3^- + HS^- + H_2O$$
 (2.28)

Reverse methanogenesis has not been observed in incubation experiments to date, due to poor thermodynamic yield of the reaction and inability to induce methane oxidation (Cui et al., 2015). Valentine and Reeburgh (2000) and Moran et al. (2008) proposed that methane oxidation can be achieved through reverse acetogenesis or methylogenesis. This type of AOM is commonly observed in marine sediments and freshwater environments (Ciu et al., 2015).

2. Metal-dependent (M-DAMO): In this case, AOM uses metal ions (Mn, Fe) as electron acceptors and is coupled with metal ion reduction. This type of AOM is observed in marine methane seeps and marine sediments in continental margins where there is high abundance of metal oxides (Beal et al., 2009). The exact mechanisms of metal-dependent AOM are still not completely understood but are summarised with these reactions:

$$CH_4 + 4MnO_2 + 7H^+ \rightarrow HCO_3^- + 4Mn^{2+} + 5H_2O$$
 (2.29)  
 $CH_4 + 8Fe(OH)_3 + 15H^+ \rightarrow HCO_3^- + 8Fe^{2+} + 21H_2O$  (2.30)

3. **Nitrite/Nitrate-dependent (N-DAMO):** The last known pathway for AOM was suggested by Raghoebarsing et al. (2006) and Haroon et al. (2013). In freshwater environments, AOM is accompanied by denitrification when nitrite is present. Nitrite-dependent AOM has also been associated with a newly detected bacteria type known as NC10 (He et al., 2016). In this instance, NO<sub>3</sub><sup>-</sup> is breaking down into NO and O<sub>2</sub> which are used subsequently for the AOM. A later study by Haroon et al. (2013), suggested that AOM can also be carried out when nitrate is abundant instead of nitrite. AOM in this case is performed by ANME via reverse-methanogenesis.

$$3CH_4 + 8NO_2 + 8H^+ \rightarrow 3CO_2 + 4N_2 + 10H_2O$$
 (2.31)  
 $5CH_4 + 8NO_3 + 8H^+ \rightarrow 5CO_2 + 4N_2 + 14H_2O$  (2.32)

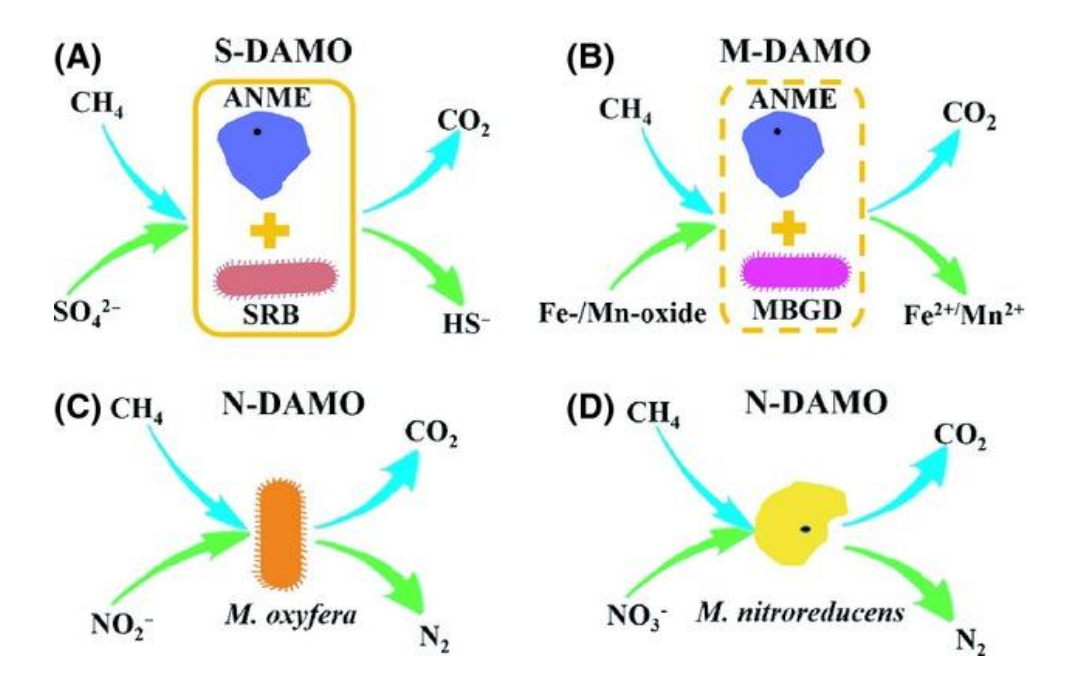


Figure 2.12: Types of AOM according to electron acceptor and microorganism involved (Cui et al., 2015).

Microbial oxidation of methane is an important sink in marine sediments where large quantities (500,000–10,000,000 Tg CH<sub>4</sub>) of methane is stored in gas hydrates (see previous subsection). Conrad (2009) estimated that without the effect of AOM, atmospheric methane concentrations would be greater by 10 to 60%.

# 2.2.7.3. Isotopic Effects

Methane oxidation either from abiotic or biotic processes increases the  $\delta^{13}$ C and  $\delta D$  of the residual methane with the isotopic shift becoming greater as the consumption of methane progresses (Krause, 2022). This occurs due to kinetic isotope effects, where the reaction rate of lighter isotopologues is faster than the heavier ones.

Multiple studies have attempted to assess the isotopic impact of sink processes either by modelling or experimental approaches (Saueresigg et al., 1995; Tyler et al., 2000; Saueresigg et al., 2001; Joelsson et al., 2014; Joelsson et al., 2015; Wang et al., 2016; Whitehill et al., 2017; Ono et al., 2021; Wegener et al., 2021; Liu et al., 2023). While there are differences in the magnitude of the isotopic enrichment, the direction of isotopic effects is well-established for the chemical oxidation of methane (Wang et al., 2016). For microbial consumption the isotopic effect varies, questions remain about whether the incubation experiments reflect accurately the natural settings and processes.

The isotopic effect of chemical reactions has been extensively studied due to the importance of chemical sink processes in the atmospheric budget of methane, especially the reaction with hydroxyl radical (Saueresigg et al., 1995; Joelsson et al., 2014). Residual methane is

progressively enriched in heavier isotopes as degradation progresses for both oxidation reactions (with OH· or Cl·). The reaction with Cl· creates a larger isotopic effect than the reaction of methane with OH· (Whitehill et al., 2017). In the following table the fractionation factors found across the scientific literature regarding the stable isotopes of carbon ( $^{13}$ C/ $^{12}$ C) and hydrogen (D/H) are summarised.

Table 2.3: Summary of fractionation factors at room temperature for methane oxidation through OH and Cl reactions. Fractionation factors are defined as in equation 2.3.

Study	α <sup>13</sup> он	$\alpha^2$ OH	α <sup>13</sup> Cl	$\alpha^2$ Cl
Whitehill et al.	$0.9939 \pm 0.0012$	$0.7494 \pm 0.0103$	$0.9415 \pm 0.0001$	$0.675 \pm 0.004$
(2017)				
Cantrell et al.	0.99462±0.0009	NM	NM	NM
(1990)				
Joelsson et al.,	NM	0.763±0.01	NM	NM
2016				
Saueresigg et	$0.996 \pm 0.0004$	0.7727±0.018	NM	NM
al., (2001)				
Feilberg et al.,	NM	NM	$0.9433 \pm 0.01$	$0.68 \pm 0.03$
(2005)				
Tyler et al.,	NM	NM	$0.94153 \pm 0.0001$	$0.6784 \pm 0.02$
(2000)				

In most cases the residual gas is progressively enriched in heavier isotopes (Holler et al., 2009; Wang et al., 2016; Wegener et al., 2021; Krause et al., 2022; Liu et al., 2023). However, the fractionation factors related to microbially-mediated oxidation of methane, either in aerobic or anaerobic environments, are less well-constrained and vary. For example, at low abundance of electron acceptors some incubation experiments showed  $\delta^{13}$ C and  $\delta D$  decreasing in the residual gas (Wegener et al., 2021; Liu et al., 2023), while in other cases one or both isotopic signatures were stable throughout the course of the experiment (Wegener et al., 2021; Liu et al., 2023). There are several assumptions about the reasons of these variations such as the type and the concentration of the electron acceptor used, the growth stage of the microbial culture, the group of the microbial culture, the rate of methanotrophy, the isotope exchange with H<sub>2</sub>O or DIC, and others (Holler et al., 2009; Wegener et al., 2021). Additionally, in the case of AOM there is also lack of knowledge about

the exact mechanisms taking place, especially in the metal and nitrite/nitrate dependent oxidation of methane (Cui et al., 2013). Variations in  $\delta^{13}$ C and  $\delta D$  have many causes, and further experimental studies are required to understand fully the impact of those processes

Whilst the list is not exhaustive, I summarise the fractionation factors measured in previous studies for AeOM and AOM.

Table 2.4: Summary of fractionation factors at room temperature for AOM and AeOM.

Study	Microbial culture	Environment	$\alpha^{13}$ ox	$\alpha^2$ ox
Holler et	ANME-2/ANME-3	Anaerobic	0.9624-	0.7604 -
al. (2009)			0.9881	0.9017
			(range)	(range)
Rasigraf	Methylomirabilis	Anaerobic	0.9708	0.7724
et al.	oxyfera			
(2012)				
Wang et	Methylococcus	Aerobic	$0.972 \pm 0.002$	$0.769 \pm 0.03$
al., 2016	capsulatus			
Wegener	Thermophilic ANME-	Anaerobic	0.9842±0.001	0.8658±0.004
et al.,	1		(high SO <sub>4</sub> )	
(2021)			1.023±0.001	
			(low SO <sub>4</sub> )	
Krause et	Methylosinus	Aerobic	0.98485 ±	0.7265 ±
al.,	trichosporium		0.00006	0.0010
(2022))				
Liu et al.,	Methanothermobacter	Anaerobic	0.9925-1.023	0.851-1.175
(2023)	marburgensis		(range)	(range)

# 2.3. Clumped Isotopes of Methane

Clumped isotope geochemistry is a rapidly developing dynamic field of isotope geochemistry concerned with the multiply-substituted isotopologues (most often called clumped isotopologues) in natural material. Most of the early studies concentrated on carbonate minerals (Ghosh, 2006; Tripati et al., 2010; Thiagarajan et al., 2011) or ethane (Taguchi et al., 2020). The development and deployment of high-resolution isotope mass spectrometers clumped isotopes determinations of CH<sub>4</sub>, N<sub>2</sub>, H<sub>2</sub>, C<sub>2</sub>H<sub>6</sub>, N<sub>2</sub>O and methyl group-bearing materials has started (Stolper et al., 2014a; Magyar et al., 2016; Young et al., 2017; Clog et al., 2018; Popa et al., 2019; Lloyd et al., 2021; Labidi and Young et al., 2022). Developments in laser spectroscopy have allowed the measurements of clumped isotopologues of N<sub>2</sub>O (Kantnerova et al., 2022), CO<sub>2</sub> (Wang et al., 2019) and CH<sub>4</sub> (Ono et al., 2014; Wang et al., 2015 and Zhang 2025).

The clumped isotopologues are the molecules of methane which bear at least two heavy isotopes, either a  $^{13}$ C and a  $^{2}$ H (deuterium) atom, such as in  $^{13}$ CH<sub>3</sub>D, or two deuterium atoms such as in  $^{12}$ CH<sub>2</sub>D<sub>2</sub>. The relative abundances of those isotopologues compared to the main isotopologue  $^{12}$ CH<sub>4</sub> are minimal (see Figure 2.13), at ppm level for  $^{13}$ CH<sub>3</sub>D and ppb level for  $^{12}$ CH<sub>2</sub>D<sub>2</sub> (Stolper et al., 2014b). Therefore, while their contribution is actually considered when measuring  $\delta^{13}$ C and  $\delta$ D using conventional IRMS, in reality is negligible compared to the abundances of  $^{13}$ CH<sub>4</sub> and  $^{12}$ CH<sub>3</sub>D. However, the addition of two independent tracers can assist with identifying the origin of methane when bulk isotopic signatures are ambiguous and fall into the overlapping areas on the  $\delta^{13}$ C and  $\delta$ D plot which are difficult to interpret. The significance of clumped isotopes of methane is not limited to providing an additional diagnostic tool, but they can potentially offer useful information into the formation conditions of methane and serve as a geothermometer (Stolper et al., 2014a; Young et al., 2017; Giunta et al., 2019).

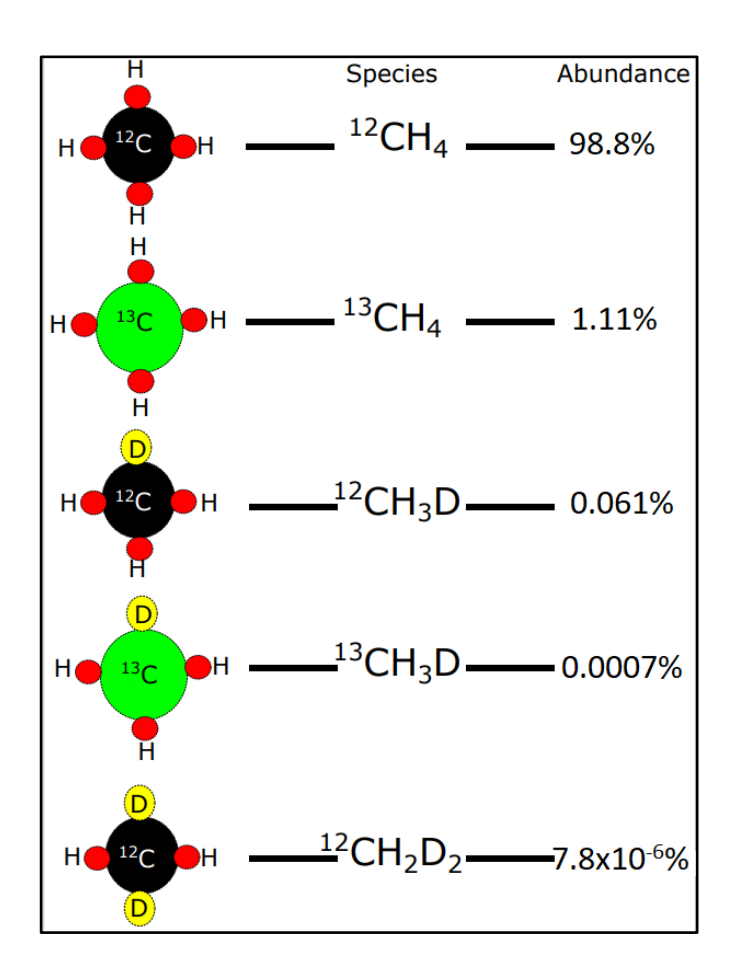


Figure 2.13: The stable isotopologues of methane and their relative abundances by assuming stochastic distribution of the isotopes and  $\delta^{13}C = \delta D = 0\%$ . Information derived from Stolper et al. (2014b).

# 2.3.1. Fundamentals

Methane isotopologues can be categorised into unsubstituted ( $^{12}\text{CH}_4$ ), singly-substituted ( $^{13}\text{CH}_4$  and  $^{12}\text{CH}_3\text{D}$ ) and multiply-substituted ( $^{13}\text{CH}_3\text{D}$ ,  $^{12}\text{CH}_2\text{D}_2$ ,  $^{12}\text{CD}_4$ ,  $^{13}\text{CH}_2\text{D}_2$ ,  $^{12}\text{CHD}_3$ ,  $^{13}\text{CHD}_3$ ,  $^{13}\text{CD}_4$ ) according to the number of heavy isotopes contained (Stolper et al., 2014a). The multiply-substituted or clumped isotopologues have unique chemical and physical properties. For instance, under thermodynamic equilibrium conditions we expect the abundance of the clumped isotopologues to decrease at increasing temperatures (Eiler, 2007). This is referred as clumping and is a consequence of the equilibrium constant in isotope exchange reactions being a temperature-dependent. For example, in the reactions below (eq. 2.33 & 2.34) at decreasing temperatures we expect increasing abundances of the clumped isotopes  $^{13}\text{CH}_3\text{D}$  and  $^{12}\text{CH}_2\text{D}_2$ .

$$^{13}CH_4 + ^{12}CH_3D \leftrightarrow ^{12}CH_4 + ^{13}CH_3D$$
 (2.33)

$$2^{12}CH_3D \leftrightarrow {}^{12}CH_4 + {}^{12}CH_2D_2$$
 (2.34)

The clumping occurs for two reasons: Firstly, there is a thermodynamic propensity towards more stable compounds as the zero point energy of clumped isotopologues is lower than singly-substituted and unsubstituted isotopologues, and secondly the enthalpies of those reactions are also temperature-dependent which affects the equilibrium distribution of the isotopologues (Eiler, 2007). At temperatures in excess of 1000°C the isotopes are expected to be randomly distributed amongst the isotopologues. This is referred as stochastic distribution and is the statistically expected distribution (Eiler, 2007). More about the calculation of stochastic distribution can be found in Chapter 3.

At thermodynamic equilibrium, the deviation of clumped isotopes from the stochastic distribution of isotopes amongst all isotopologues, can be used as proxy of formation temperature or at least re-equilibration temperature when bond-reordering occurs. These deviations are expressed in per mil (‰) and are calculated with the following equations:

$$\Delta^{13}CH_3D = \left[\frac{\left(\frac{^{13}CH_3D}{^{12}CH_4}\right)_{sample}}{\left(\frac{^{13}CH_3D}{^{12}CH_4}\right)_{stochastic}} - 1\right] (2.35)$$

$$\Delta^{12}CH_2D_2 = \left[\frac{\left(\frac{^{12}CH_2D_2}{^{12}CH_4}\right)_{sample}}{\left(\frac{^{12}CH_2D_2}{^{12}CH_4}\right)_{stochastic}} - 1\right] (2.36)$$

Initial studies on CH<sub>4</sub> clumped isotopologues (Stolper et al., 2014a; Stolper et al., 2014b; Stolper et al., 2015), reported values of the combined clumped isotope composition  $\Delta_{18}$  due to the insufficient mass resolving power to separate the  $^{13}$ CH<sub>3</sub>D and  $^{12}$ CH<sub>2</sub>D<sub>2</sub> in their measurements. In a similar way, this is defined by the following:

$$\Delta_{18} = \left[ \frac{\left( \frac{^{13}CH_3D + ^{12}CH_2D_2}{^{12}CH_4} \right)_{sample}}{\left( \frac{^{13}CH_3D + ^{12}CH_2D_2}{^{12}CH_4} \right)_{stochastic}} - 1 \right] (2.37)$$

The  $\Delta^{13}\text{CH}_3\text{D}$  and  $\Delta^{12}\text{CH}_2\text{D}_2$  (and  $\Delta_{18}$ ) are temperature-dependent at thermodynamic equilibrium. Overall, there is a good agreement between the results from the measurement of calibrated gases (see Chapter 3), and those based on calculations performed by different computational methods (Bigeleisen, Mayer, Urey model vs Path Integral Monte Carlo) in Young et al. (2017) and Eldridge et al. (2019). As a result, this agreement has helped towards the construction of a well-defined equilibrium curve in the  $\Delta^{13}\text{CH}_3\text{D}-\Delta^{12}\text{CH}_2\text{D}_2$  space, against which all measurements of natural and experimental products can be compared (Young et al., 2017; Eldridge et al., 2019; Giunta et al., 2022; Sivan et al., 2024).

# 2.3.2. Methane Sources & Clumped Isotopic Signatures

# 2.3.2.1. Thermogenic Methane

Most thermogenic gases reported to date have  $\Delta^{13}\text{CH}_3\text{D}$  and  $\Delta^{12}\text{CH}_2\text{D}_2$  values either consistent with the thermodynamic equilibrium or near the thermodynamic equilibrium curve. However,  $\Delta^{12}\text{CH}_2\text{D}_2$  in some thermogenic gases exhibit deficits compare to the thermodynamic equilibrium curve (Young et al., 2017; Jiang et al., 2024) and raises the question whether this clumped isotopic signature is associated with the mechanisms of formation or post-generation processes.

Initial pyrolysis experiments on shale and coal by Shuai et al. (2018) revealed that the combined clumped isotopic signature  $\Delta_{18}$  indicated equilibrium signatures at early-stage maturation, which was attributed to reversible exchange of hydrogen atoms during the reaction. As the maturation progressed and secondary cracking of wet hydrocarbons (C<sub>2</sub>-C<sub>5</sub>) occurred, the  $\Delta_{18}$  values shifted away from equilibrium, suggesting kinetic effects during the formation of methane from alkyl precursors. Further studies using other substrates lead to contradictory conclusions. Dong et al. (2021) explored the evolution of  $\Delta^{13}$ CH<sub>3</sub>D and  $\Delta^{12}$ CH<sub>2</sub>D<sub>2</sub> during the pyrolysis of n-octadecane (C<sub>18</sub>H<sub>38</sub>). This study reported that during the primary cracking and in the oil-window stage, the  $\Delta^{13}$ CH<sub>3</sub>D values were only slightly away from equilibrium (0.5-1‰), while  $\Delta^{12}$ CH<sub>2</sub>D<sub>2</sub> exhibited a more prominent depletion (approximately -40‰) from the expected equilibrium values at 400°C. This behaviour was

attributed to statistical effects (see the section on combinatorial effects). As maturation advanced, the  $\Delta^{12}\text{CH}_2\text{D}_2$  values increased, likely due to hydrogen isotope exchange across hydrocarbons but overall remained below the equilibrium curve. This observation agreed with the findings of later studies on natural gas systems by Xie et al. (2021) which reported that thermodynamic equilibrium is attained for  $\Delta^{12}\text{CH}_2\text{D}_2$  at 170–210 °C peak burial temperatures, and Jiang et al. (2024) which noticed disequilibrium  $\Delta^{13}\text{CH}_3\text{D}$  and  $\Delta^{12}\text{CH}_2\text{D}_2$  values for early-maturation gases.

Ultimately, the  $\Delta^{13}\text{CH}_3\text{D}$  and  $\Delta^{12}\text{CH}_2\text{D}_2$  signatures of thermogenic gases are often distinct from those of microbial and abiotic gases, as they plot closer to the thermodynamic equilibrium curve. In the past, distinguishing thermogenic gases using bulk isotopic or molecular compositions has been challenging because the expected range for thermogenic gases lies between the abiotic and microbial areas, making it difficult to identify. However, the use of  $\Delta^{13}\text{CH}_3\text{D}$  and  $\Delta^{12}\text{CH}_2\text{D}_2$  offers new potential for constraining the formation temperatures in natural environments and identify the maturation stages of organic matter (Thiagarajan et al., 2020).

### 2.3.2.2. Microbial Methane

The clumped isotopic signatures of microbial gases, either from incubation experiments or from natural settings, have been widely investigated and discussed across the literature. Initial studies reported the combined  $\Delta_{18}$  values for microbial gases from natural settings and experimental products. The microbial gases were divided as they reflected varying  $\Delta_{18}$ values, in some cases consistent with thermodynamic equilibrium and in others away from it (Stolper et al., 2014b; Stolper et al., 2015; Douglas et al., 2016). Ono et al. (2014b) and Wang et al. (2015) reported the  $\Delta^{13}$ CH<sub>3</sub>D values for microbial samples from livestock, lakes and swamps which were depleted in  $\Delta^{13}CH_3D$  and away from the expected thermodynamic equilibrium value at the formation temperature. Stolper et al. (2015) and Wang et al. (2015) suggested that those disequilibrium values arise from kinetic isotope effects and thought their magnitude to be associated with the rate of methanogenesis. In settings where methanogenesis proceeds slowly such as sedimentary environments, methane was postulated to form in internal equilibrium as the slow rate of the reaction could favour the reversibility of the reaction (Stolper et al., 2015). In contrast, in swamps, lakes or incubation experiments where there is an abundance of H<sub>2</sub>, the reaction proceeds faster which favours one side of the reaction and expresses the kinetic isotope effects (Wang et al., 2015).

The addition of  $\Delta^{12}CH_2D_2$  revealed that microbial methane is often away from equilibrium in both clumped isotopologue signatures but in some deep subsurface environments the

microbial methane is consistent with the thermodynamic isotopic equilibrium (Young et al., 2017; Ash et al., 2019; Zhang et al., 2021; Ono et al., 2022; Rhim and Ono et al., 2022; Haghnegahdar et al., 2024; Sivan et al., 2024). Young et al. (2017) proposed that, besides the rate of methanogenesis which may result to equilibrated signatures, AOM could potentially drive the clumped isotopic signatures towards equilibrium in anoxic environments such as in the deep terrestrial settings or marine sediments. While AOM can affect the clumped isotopic signatures in different ways (see oxidation paragraph in 2.3.3 section), incubation experiments by Liu et al. (2023) showed that AOM can potentially drive the  $\Delta^{13}$ CH<sub>3</sub>D and  $\Delta^{12}$ CH<sub>2</sub>D<sub>2</sub> in thermodynamic equilibrium at the environmental temperature.

To date, a substantial number of microbial samples measured derive from incubation experiments which may not be truthfully representative of methanogenesis in natural settings. The  $\Delta^{13}\text{CH}_3\text{D}$  and  $\Delta^{12}\text{CH}_2\text{D}_2$  values of these microbial gases often plot below and left of the thermodynamic equilibrium curve (see Figure 2.14), with significant differences from the equilibrium in  $\Delta^{12}\text{CH}_2\text{D}_2$ , of up to -60% (Liu et al., 2023). According to Taenzer et al. (2020), low  $\Delta^{12}\text{CH}_2\text{D}_2$  values in laboratory-produced microbial gases can arise from combinatorial effects during the formation of CH<sub>4</sub> due to pooling hydrogen atoms from different reservoirs, (in this case the methyl group and the formation water). However, the incorporation of hydrogen atoms at different enzymatic steps (with different fractionation factors) can also lead to combinatorial effects and lower  $\Delta^{12}\text{CH}_2\text{D}_2$  values (Röckmann et al., 2016; Yeung et al., 2016).

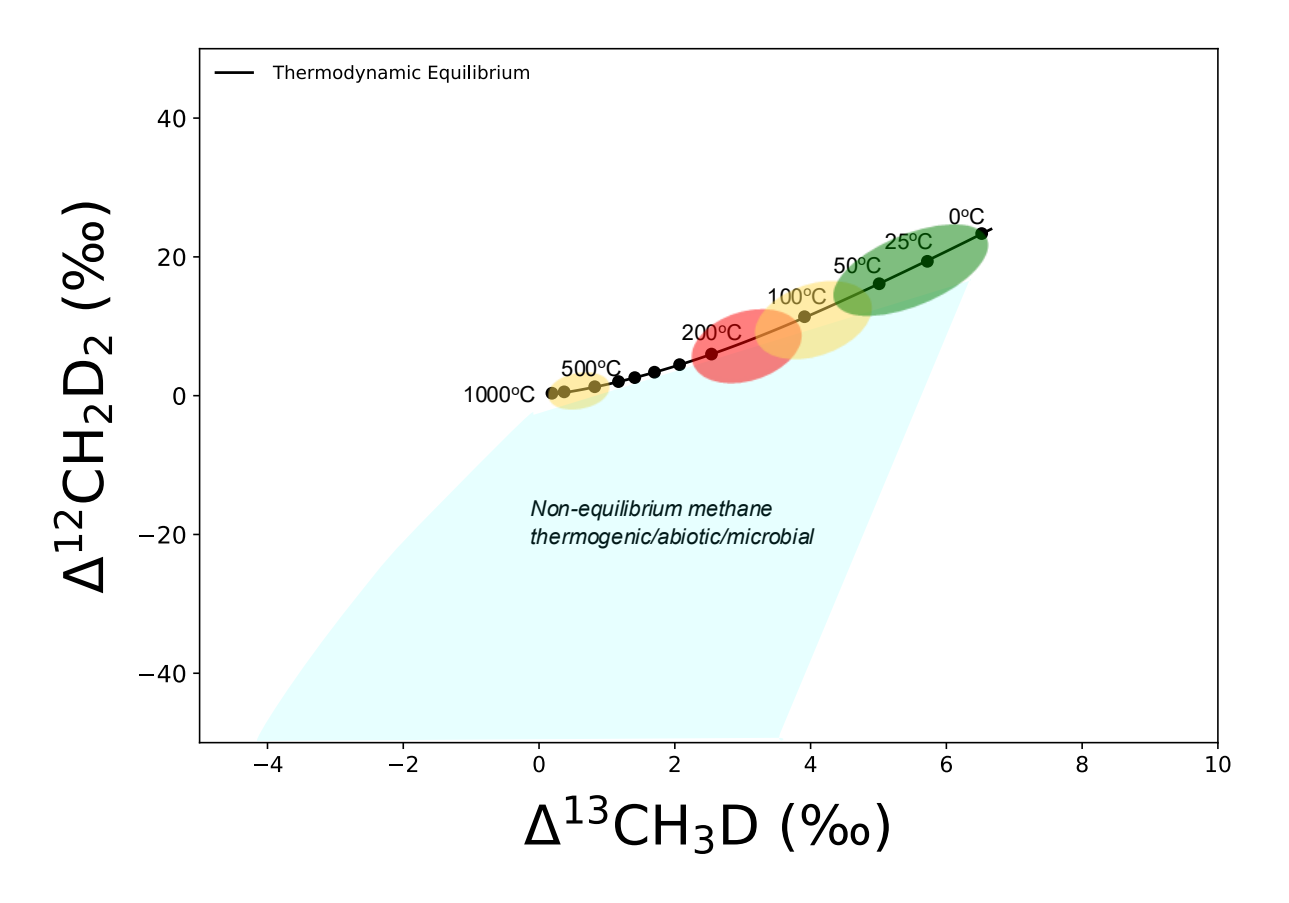


Figure 2.14: The expected defined areas in the  $\Delta^{13}\text{CH}_3\text{D}$  -  $\Delta^{12}\text{CH}_2\text{D}_2$  space when the methane produced by thermogenic (red area), abiotic (yellow area) and microbial (green area) sources fall on the thermodynamic equilibrium line. This refers to either the expected formation temperatures for each source or the experimental/natural samples already reported in literature. Plot inspired by Liu et al. (2023).

### 2.3.2.3. Abiotic Methane

Measurement of clumped isotopologues in abiotic CH<sub>4</sub> is the least reported, given the scarcity of environments where the abiotic gases dominate and the small economic significance compared to thermogenic or microbial gases (Etiope and Sherwood- Lollar, 2013). To date, there are reported values for  $\Delta^{13}$ CH<sub>3</sub>D and  $\Delta^{12}$ CH<sub>2</sub>D<sub>2</sub> for abiotic gas produced in natural settings and in laboratory environments (Young et al. 2017; Labidi et al., 2020; Nothaft et al., 2021; Labidi et al., 2024). Initially, Young et al. (2017) measured samples deriving from laboratory experiments of silane decomposition and Sabatier reaction where the majority exhibited deficits (up to 60‰) in  $\Delta^{12}$ CH<sub>2</sub>D<sub>2</sub> (ultimately larger in Sabatier reaction products than the silane experiments) and  $\Delta^{13}$ CH<sub>3</sub>D values which reflected the formation temperature of the gas. Measurements of abiotic gases associated with ophiolites in Chimaera seepage revealed  $\Delta^{13}$ CH<sub>3</sub>D and  $\Delta^{12}$ CH<sub>2</sub>D<sub>2</sub> consistent with internal equilibrium. However, measurement of abiotic gases isolated from fracture fluids and natural springs revealed  $\Delta^{13}$ CH<sub>3</sub>D values at equilibrium with small deficits in  $\Delta^{12}$ CH<sub>2</sub>D<sub>2</sub> (<10‰) (Young et

al., 2017). This study suggested that these departures from the thermodynamic equilibrium reflect quantum tunnelling effects which can influence the rates of the reaction during the assimilation of the hydrogen and deuterium atoms during the Fischer Tropsch reactions. Labidi et al. (2020) reported results for abiotic gases from hydrothermal vents and pointed out that clumped methane signatures can potentially be reset at the temperature range of the fluid. This was suggested to occur at temperatures between 65 and 360°C, with the rate of  $\Delta^{12}\text{CH}_2\text{D}_2$  re-equilibration suggested to be 2 times faster than the rate of  $\Delta^{13}\text{CH}_3\text{D}$ . A recent study by Labidi et al. (2024) investigated the clumped isotopologue signatures of methane in experimentally produced abiotic gases via Fischer-Tropsch reactions. This study observed that the  $\Delta^{13}\text{CH}_3\text{D}$  values are almost consistent with formation temperatures (typically within 1‰), while the  $\Delta^{12}\text{CH}_2\text{D}_2$  is as low as -60‰ probably due to combinatorial effects (section 2.3.3) during the formation of CH4.

Overall, reaching a consensus about the exact mechanisms of abiotic production and whether it forms in internal equilibrium is challenging, given that is often mixed with other components and due to the diverse pathways and environments of production (as discussed in section 2.2.3). Measurements of abiotic methane to date, indicate  $\Delta^{13}CH_3D$  values consistent with thermodynamic equilibrium at or close to the environmental temperatures, however with large deficits in  $\Delta^{12}CH_2D_2$ .

# 2.3.3. Isotopic Effects of Non-equilibrium Processes

Physical, chemical and biological processes can affect the fate of methane in natural environments. The effect of those processes can be identified by measuring the clumped isotopic signatures of methane  $\Delta^{13}\text{CH}_3\text{D}$  and  $\Delta^{12}\text{CH}_2\text{D}_2$  which are often driven away from the thermodynamic equilibrium curve (Haghnegahdar et al., 2017; Young et al., 2019; Giunta et al., 2021; Liu et al., 2023). In this section, we describe and model a few physical, chemical and biological processes along with a description of statistical effects able to alter the clumped isotopic compositions. More information about the calculations for mixing diffusion, and oxidation process can be found in the Appendix.

### 2.3.3.1. *Mixing*

Clumped isotopic signatures of methane  $\Delta^{13}\text{CH}_3\text{D}$  and  $\Delta^{12}\text{CH}_2\text{D}_2$  are considered useful tracers for identifying the mixing of two or more components (Young et al., 2019). This is because mixing of two gases will follow an approximately linear path in  $\delta^{13}\text{C}$  and  $\delta\text{D}$  which can potentially be resembled by multiple processes (e.g. diffusion, oxidation). However, in

the  $\Delta^{13}CH_3D$  -  $\Delta^{12}CH_2D_2$  space, the mixing of two components with different  $\delta^{13}C$  and  $\delta D$  can create non-linear arrays (Eiler, 2007; Young et al., 2016).

Understanding the mixing paths in  $\Delta^{13}\text{CH}_3\text{D}$  -  $\Delta^{12}\text{CH}_2\text{D}_2$  space is particularly important in order to decipher the origins of methane. For example, in atmospheric methane studies it can provide evidence about the main components mixed and offer information to constrain further the atmospheric methane budget (Haghnehagdar et al., 2024; Sivan et al., 2024). In natural gas systems, the origin of methane holds economic significance, as it helps determine whether the gas generation is a continuous process (and constrain the rate of production) or related to the geological past. Therefore, understanding the contribution of each component can lead to better estimations of gas resources (Zhang et al., 2020).

Below, we explore two mixing scenarios in order to demonstrate the pathways of  $\Delta^{13}CH_3D$  and  $\Delta^{12}CH_2D_2$  during the mixing process. Under the first scenario, a thermogenic gas and a microbial gas are both at thermodynamic equilibrium while they have different  $\delta^{13}C$  and  $\delta D$  and a second scenario where the thermogenic and microbial gases have different  $\delta^{13}C$  but an identical  $\delta D$  value (Figure 2.15).

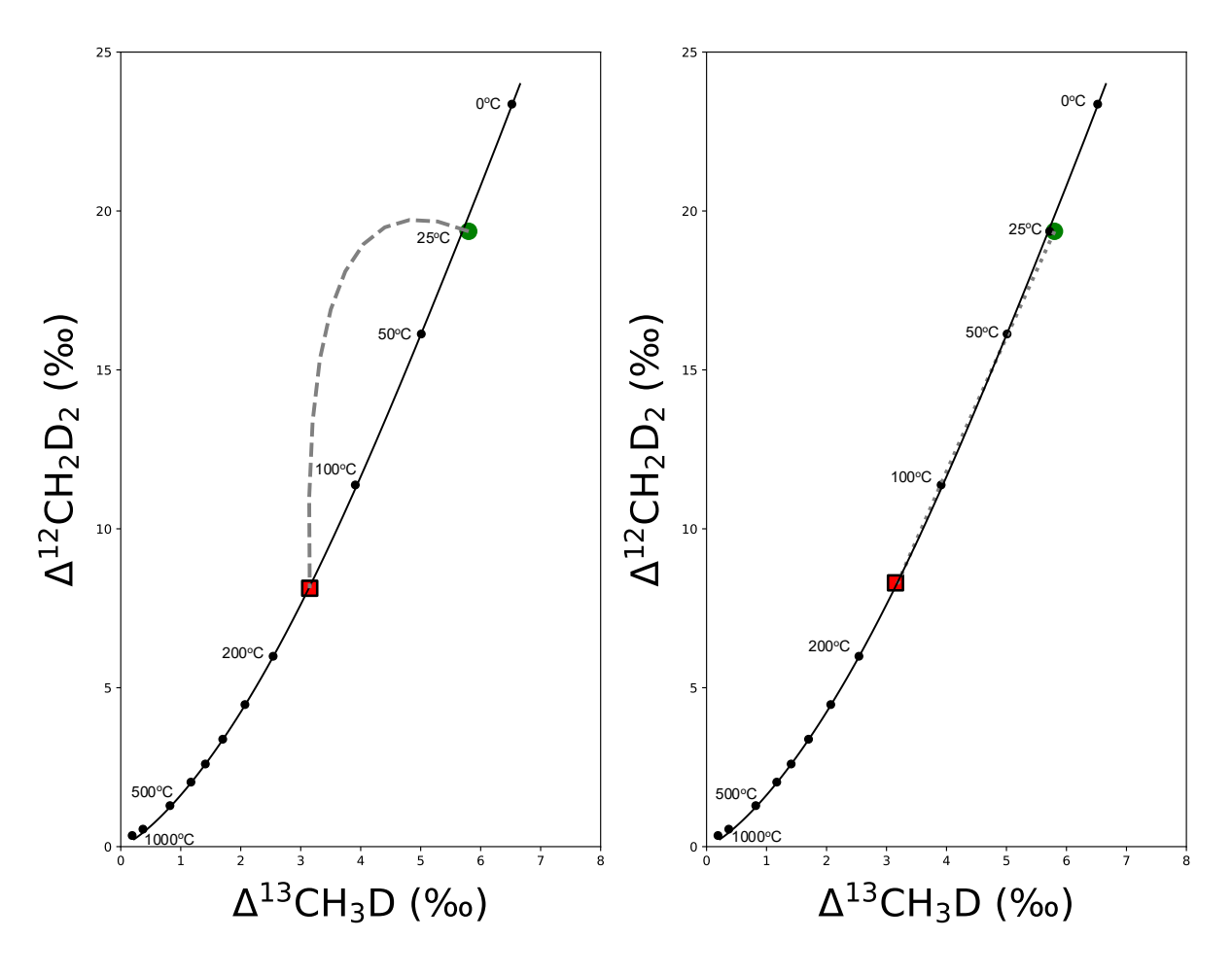


Figure 2.15: Mixing scenarios for thermogenic- microbial mixtures with in  $\Delta^{13}$ CH<sub>3</sub>D -  $\Delta^{12}$ CH<sub>2</sub>D<sub>2</sub> space a) typical mixing curve for gas mixtures with different bulk isotopic

compositions (Thermogenic:  $\delta^{13}C = -35\%$ ,  $\delta D = -220\%$ , Microbial:  $\delta^{13}C = -60\%$ ,  $\delta D = -120\%$ ) and b) mixing path for gases with identical  $\delta D$  at -220%, the mixing line nearly coincides with the thermodynamic equilibrium line .

In these examples the curvature of the mixing line is dependent on the bulk isotopic compositions. Specifically, the curvature of the mixing lines is greater when the contrast in the  $\delta^{13}$ C and  $\delta D$  of the two endmembers is larger and the curvature is less sensitive in  $\delta^{13}$ C changes and more sensitive in  $\delta D$ . In the scenario when the  $\delta D$  is identical for the thermogenic and microbial gas, the mixing path is almost perfectly linear.

### 2.3.3.2. *Diffusion*

In a system with two connected reservoirs, gases flow from the reservoir with the high gas concentration towards the other reservoir with the lower concentration. In natural gas systems, gases often migrate from the reservoir rock in the subsurface either towards a reservoir rock or to escape to the atmosphere. Therefore, diffusion can play a significant role into the fate of the natural gas (Prinzhofen and Pernaton, 1997). The occurrence of diffusion in a system can create isotopic fractionation between the residual and the escaping gases (Zhang and Krooss, 2001). We describe in the following section the assumptions taken into consideration, the calculations and the impact on bulk and clumped isotopic compositions, and the observations when diffusion is the dominating process in a system.

Previous studies by Craig and Gordon (1965), Richter et al. (2006) used the reduced masses to calculate the diffusion coefficients, and hence the fractionation factor due to diffusion. However, using more recent calculations by Bourg and Sposito (2008), the isotopic fractionation factor due to diffusive loss can be calculated from Graham's law (Lalk et al., 2022) as following:

$$\alpha = \left(\frac{m^*}{m}\right)^{-\beta} (2.38)$$

where m\* is the mass of the heavy isotopologue ( $^{13}CH_4$ ,  $^{12}CH_3D$ ,  $^{13}CH_3D$ ,  $^{12}CH_2D_2$ ) and m the of the light isotopologue ( $^{12}CH_4$ ). The parameter  $\beta$  varies between 0.5 for ideal gases and 0.25 for diffusion through water (Lalk et al., 2022).

The isotopic fractionation due to diffusive loss can be modelled assuming it is a Rayleigh process (Young et al., 2017) combined with eq. 2.4. Based on these assumptions, we can infer that isotopologues with the same cardinal mass will follow a 1-1 fractionation path.

Therefore, we expect the same impact on  $\delta^{13}C$  and  $\delta D$  (mass 17), and on  $\delta^{13}CH_3D$  and  $\delta^{12}CH_2D_2$  (mass 18). Below, we present an example where the gas is diffused from a gas reservoir through a water column and towards the atmosphere. In this case, we notice that the  $\delta^{13}C$  and  $\delta D$  values are progressively increasing (as the lighter isotopes are moving faster than the heavier ones) while the  $\Delta^{13}CH_3D$  and  $\Delta^{12}CH_2D_2$  values are decreasing. Finally, we highlight that diffusion might cause severe changes in  $\delta^{13}C$  and  $\delta D$  (%) but ultimately minor changes in  $\Delta^{13}CH_3D$  and  $\Delta^{12}CH_2D_2$  (%). This observation agrees with findings from previous studies by Giunta et al. (2021) and Lalk et al. (2022).

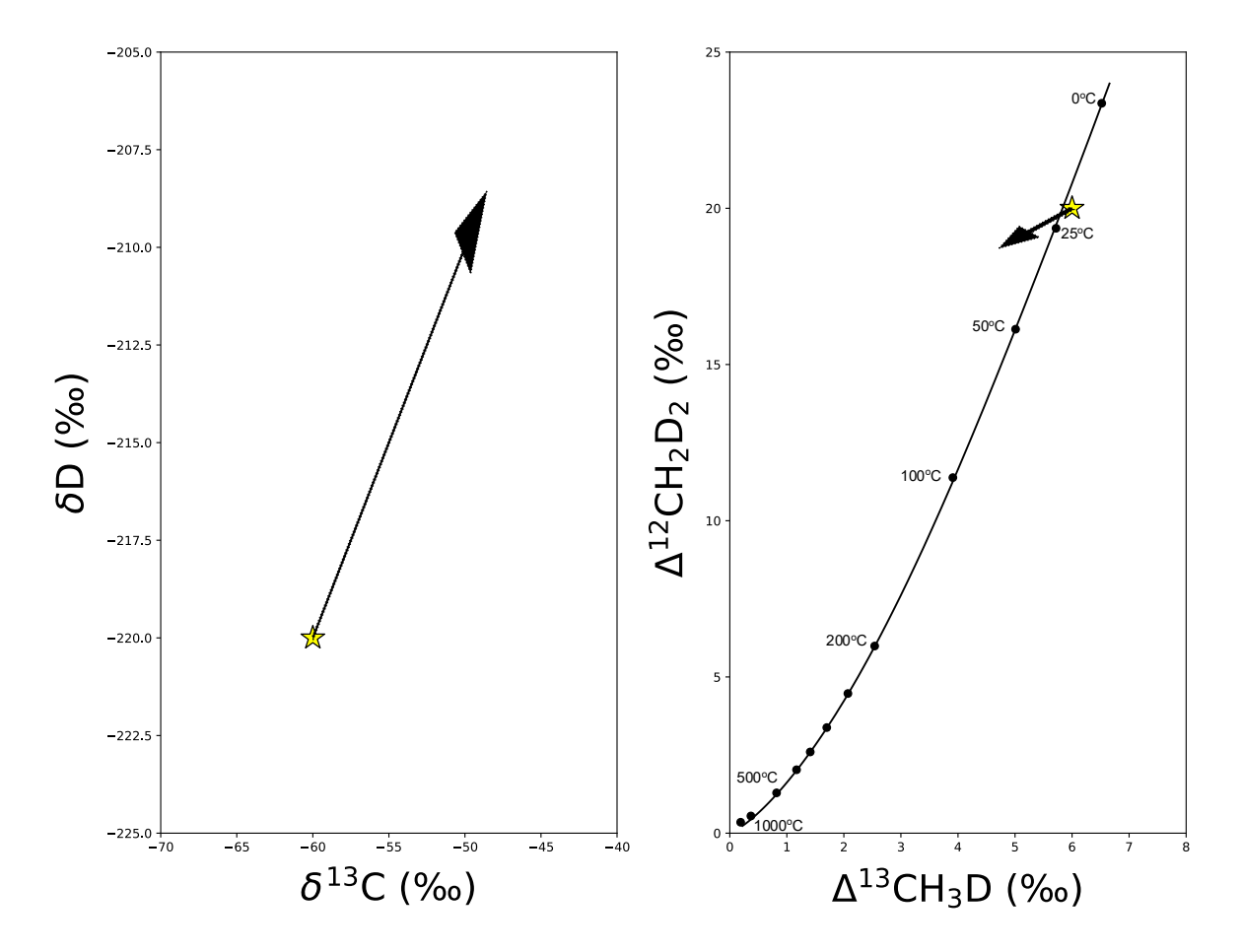


Figure 2.16: a) Modelled diffusion pathway when assuming a gas with initial bulk isotopic compositions  $\delta^{13}C = -60\%$  and  $\delta D = -220$  (shift by approximately +10% at 50% gas loss)) b) Modelled diffusion pathway in  $\Delta^{13}CH_3D - \Delta^{12}CH_2D_2$  space when assuming a gas with initial compositions  $\Delta^{13}CH_3D = 6\%$  and  $\Delta^{12}CH_2D_2 = 20\%$  (shift by approximately -0.75% at 50% gas loss). Arrowhead indicates 50% gas loss.

### 2.3.3.3. *Oxidation*

As discussed in section 2.2.4, oxidation by chemical reactions with OH and Cl radicals or via biological processes such as AeOM and AOM are the main way that methane is removed from atmosphere (Saunois et al., 2024). In this section, I explore the expected pathways for chemical or biological oxidation processes in the  $\Delta^{13}$ CH<sub>3</sub>D - $\Delta^{12}$ CH<sub>2</sub>D<sub>2</sub> space based on

findings from the literature to date and highlight that the paths exhibited in this section are not limited to the exact pathways in  $\Delta^{13}\text{CH}_3\text{D}$  and  $\Delta^{12}\text{CH}_2\text{D}_2$ . However, they represent the consensus amongst different studies. The reader is referred to the Appendix where I present using Monte Carlo simulations that the pathways are immensely sensitive to small changes in fractionation factors.

### 2.3.3.4. Oxidation by Cl and OH

Given the significance of the reactions between methane and OH or Cl radicals in the atmosphere and the marine boundary layer, it is important to thoroughly understand the impact of these reactions on the clumped isotopic signatures Δ¹³CH₃D and Δ¹²CH₂D₂. This is particularly relevant for studies which focus on constraining the atmospheric methane budget through the clumped isotopic signatures, as this information can provide insights into the contributions of the atmospheric methane sources and sinks (Haghnegahdar et al., 2017; Haghnegahdar et al., 2024; Sivan et al., 2024). Haghnegahdar et al. (2017) used ab initio calculations and reported the KIEs related to methane oxidation by OH and Cl radicals. Those were in good agreement with previous studies either by modelling or experimental setups for both clumped isotopologues (Joelsson et al., 2014; Sauer et al., 2015; Joelsson et al., 2016).

Overall, the impact of Cl reaction on  $\Delta^{13}\text{CH}_3\text{D}$  and  $\Delta^{12}\text{CH}_2\text{D}_2$  is more severe compared to reactions with OH radical (Fig 2.17). For example, at 90% oxidation (10% of the initial gas remain) the  $\Delta^{13}\text{CH}_3\text{D}$  and  $\Delta^{12}\text{CH}_2\text{D}_2$  of the residue has decreased by 6.8‰ and by 81‰, while at the same conditions the reaction with OH results to decreases of 1.3‰ and 13‰, respectively. Therefore, the magnitude of the isotopic fractionation is considerably larger in  $\Delta^{12}\text{CH}_2\text{D}_2$  than  $\Delta^{13}\text{CH}_3\text{D}$  for OH and Cl sink reactions. The fractionation factors are summarised in the Table 2.5 below.

Table 2.5: Summary of fractionation factors at room temperature for methane oxidation through OH and Cl reactions.

Isotopologue	CH <sub>4</sub> + OH·	CH <sub>4</sub> +Cl·
<sup>13</sup> CH₃D	$\alpha = \{0.74 \text{ to } 0.752\}$	$\alpha = \{0.625 \text{ to } 0.685\}$
$^{12}CH_2D_2$	$\alpha = \{0.52 \text{ to } 0.552\}$	$\alpha = \{0.3413 \text{ to } 0.714\}$

In the Appendix, I present evidence that the slope and direction of these processes are in fact very sensitive even at small changes of the KIEs figures, well below the reported uncertainty. As an example, we investigate the case of OH reaction given its significance as the dominant atmospheric sink. Overall, we emphasize the need for deeper investigation of the impact of those reactions in the  $\Delta^{13}\text{CH}_3D$  -  $\Delta^{12}\text{CH}_2D_2$  space as there is a lack of experimental studies to date.

### 2.3.3.5. Aerobic Oxidation of Methane (AeOM)

Two studies concerning the impact of AeOM on both clumped isotopic compositions of methane in incubation experiments. The findings of these studies are in good agreement with each other, in terms of fractionation factors values and understanding the critical parameters affecting the pathways of Δ¹³CH₃D and Δ¹²CH₂D₂ due to AeOM (Krause et al., 2022; Li et al., 2024). In a closed system with negligible production of CH<sub>4</sub>, we expect a decrease both in  $\Delta^{13}$ CH<sub>3</sub>D and  $\Delta^{12}$ CH<sub>2</sub>D<sub>2</sub> which is demonstrated in the figure below (Figure 2.17) (Krause et al., 2022). Potentially, AeOM in those systems can mimic the clumped isotopic compositions produced by methanogenesis which are often below and left from the equilibrium curve at Δ¹³CH₃D and Δ¹²CH₂D₂ (Young et al., 2017; Giunta et al., 2019; Wang et al., 2023; Haghnegahdar et al., 2024; Sivan et al., 2024). However, this is depending on the initial clumped isotopic signatures of the gas. Contrarily, in a closed system with an equal production and oxidation of CH<sub>4</sub>, the produced pathways by AeOM are distinct with extreme increases in  $\Delta^{12}$ CH<sub>2</sub>D<sub>2</sub> (even beyond 100%) and often less significant increases in  $\Delta^{13}$ CH<sub>3</sub>D, typically less than 3% (Krause et al., 2022; Li et al., 2024) (see Figure 2.17). The exact pathway was suggested to be sensitive to the Damköhler number (the ratio between the oxidation rate and the cross-membrane methane transport rate) and overall controlled by reservoir effects (Li et al., 2024). In open systems and in steady-state conditions, the impact of AeOM on  $\Delta^{13}$ CH<sub>3</sub>D and  $\Delta^{12}$ CH<sub>2</sub>D<sub>2</sub> was similar to the previous example, but largely dependent on the ratio between the oxidation rate and advection rate ( $\varphi$ ) and less dependent on the Damköhler number (Li et al., 2024). Therefore, in specific settings (open systems or closed systems with high Damköhler number, Da ≈1) the clumped AeOM can be easily traced by the clumped isotopic signatures of methane.

Therefore, the impact of AeOM on  $\Delta^{13}CH_3D$  and  $\Delta^{12}CH_2D_2$  for the residual gas is variable and strongly dependent on the system of interest and parameters such as the production and oxidation rate of CH<sub>4</sub> and others (Krause et al., 2022).

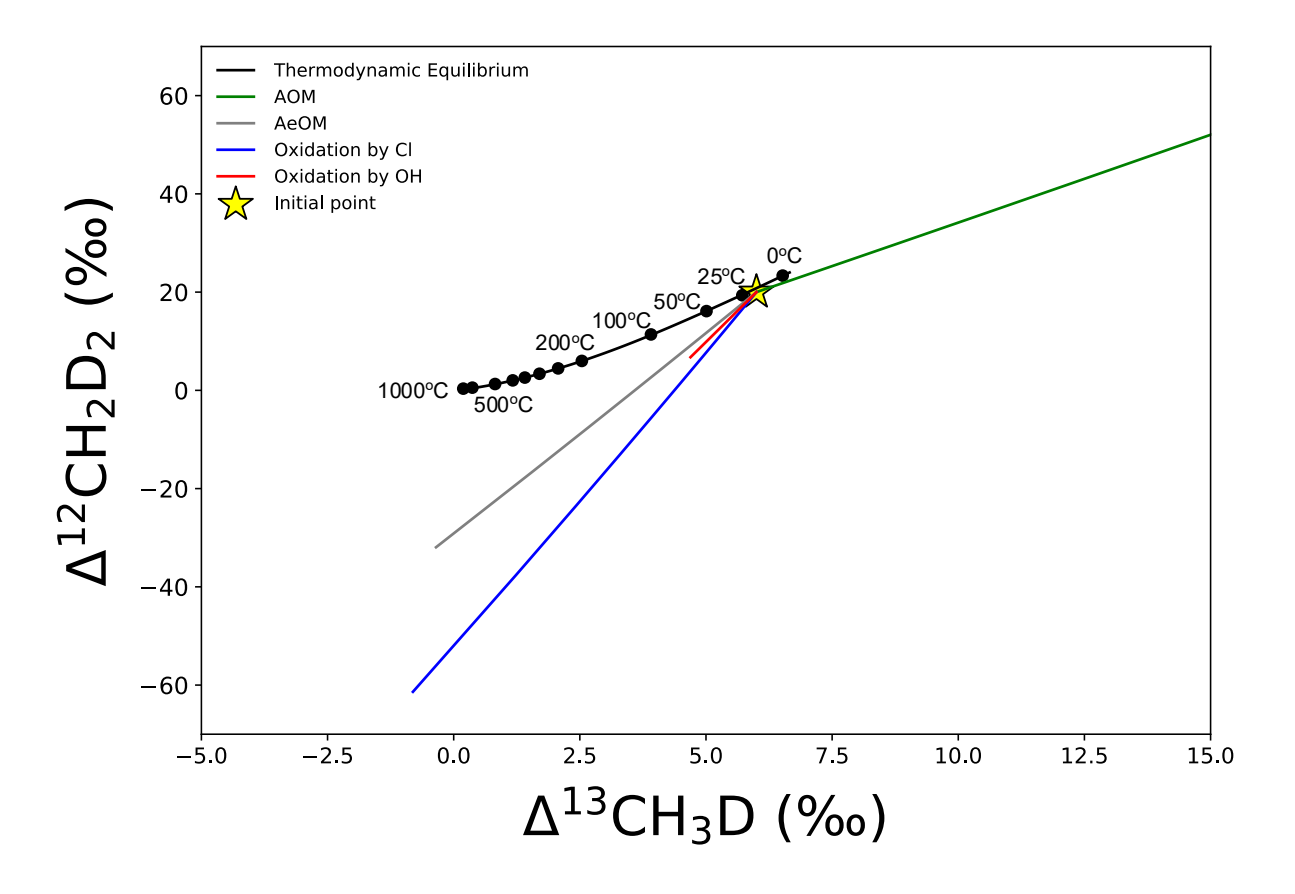


Figure 2.17: Oxidation paths for Anaerobic oxidation of methane – green line (AOM) (Liu et al., 2023), Aerobic oxidation of methane – grey line (AeOM- in closed system) (Krause et al., 2022), oxidation by Cl and OH radicals (Haghnehagdar et al., 2017), when assuming a gas with initial compositions  $\Delta^{13}$ CH<sub>3</sub>D = 6‰  $\Delta^{12}$ CH<sub>2</sub>D<sub>2</sub> = 20‰ in a single reservoir of methane (closed-system).

### 2.3.3.6. Anaerobic Oxidation of Methane (AOM)

The impact of AOM on  $\Delta^{13}\text{CH}_3D$  and  $\Delta^{12}\text{CH}_2D_2$  signatures is not fully-understood and can potentially reflect either kinetic isotope effects or internal thermodynamic equilibrium (Young et al., 2017; Ash et al., 2019; Ono et al., 2021; Giunta et al., 2022; Liu et al., 2023). Initial studies by Stolper et al. (2015), Wang et al. (2016) and Young et al. (2017) observed that microbial methane can be either in internal equilibrium or away from the equilibrium line and was suggested to be affected by the rate of methanogenesis or reset as a result of AOM. Field observations by Ash et al. (2019) and Giunta et al. (2022) were inconsistent with a single behaviour for the isotopic effect of AOM on clumped isotopic compositions. Ash et al. (2019) observed that methane sampled from marine sediments was approaching the thermodynamic equilibrium in  $\Delta^{12}\text{CH}_2D_2$  and reached thermodynamic equilibrium at approximately  $8^{\circ}\text{C}$  in  $\Delta^{13}\text{CH}_3D$  with increasing depth where AOM was expected to be active. In contrast, Giunta et al. (2022) reported measurements of clumped isotopic compositions for CH<sub>4</sub> samples from the Black Sea sediments, with significantly enriched  $\Delta^{13}\text{CH}_3D$  and

 $\Delta^{12}$ CH<sub>2</sub>D<sub>2</sub> at 15.7 ‰ and 74.6‰, respectively. These extreme values were speculated to arise by kinetic isotope effects during AOM through almost irreversible reactions.

A study by Liu et al. (2023), focused on investigating the effect of AOM on the clumped isotopologues of methane by conducting incubation experiments using sediment slurries from marine environments and fracture fluids. In this study, both pathways for AOM were detected where Liu et al. (2023) distinguished them into equilibrium-driven AOM and kinetically-driven AOM. The former one was hypothesised to occur in the deep subsurface and environments with low thermodynamic drive, and catalysed by the Mcr enzyme which promotes isotope exchange in the first step of AOM (reaction 2.39), while the latter one was suggested to occur when the reaction (2.39) is completely irreversible and approximates a Rayleigh process. Liu et al. (2023) constructed a reaction network of isotopologues in order to model the impact of AOM on the clumped isotopic signatures. An important parameter of this model is the reversibility  $(\varphi)$ , which is the ratio of the reverse rate constant to the forward rate constant of the following reaction which is believed to be the most reversible:

$$CH_4 \leftrightarrow CH_3 + H$$
 (2.39)

When the reversibility  $\varphi$  approaches 0, AOM is kinetically driven and the impact of AOM is similar to the example in Figure 2.17. If the reversibility  $\varphi$  approaches value 1, the AOM is equilibrium-driven and it drives both clumped isotopic signatures onto the thermodynamic equilibrium curve.

Overall, the clumped isotopic signatures of methane can be useful tracers of the AOM especially when the reaction is completely irreversible, as the simultaneous increase at this magnitude in  $\Delta^{13}$ CH<sub>3</sub>D and  $\Delta^{12}$ CH<sub>2</sub>D<sub>2</sub> cannot be caused by other processes (Figure 2.17).

### 2.3.3.7. Combinatorial Effects

Combinatorial effects (also called statistical effects) can generate molecules depleted in clumped isotopologues compared to stochastic distribution and below the equilibrium curve in multiple isotopic species such as CH<sub>4</sub>, O<sub>2</sub>, N<sub>2</sub> and others (Yeung et al., 2015; Röckmann et al., 2016; Yeung et al., 2016, Taenzer et al., 2020). These effects occur during the formation of a molecule when the atoms derive from distinct isotopic pools or are incorporated into the molecule by a different process with distinctive isotopic fractionation for the two (or more) atoms in the final molecule (Yeung et al., 2016). Combinatorial effects are shown to occur mostly during biological processes or during chemical kinetic isotope effect related to bond-formation and bond- rupture (Yeung et al., 2016). Combinatorial effects are present when two rare isotopes of the same element occur in the same molecule

(e.g. D-D in CH<sub>4</sub>, N-N in N<sub>2</sub>, O-O in O<sub>2</sub>) and may create significant departures from the stochastic distribution while the magnitude is largely dependent on the isotopic fractionation between the isotopic pool and the final molecule (Yeung et al., 2016; Röckmann et al., 2016).

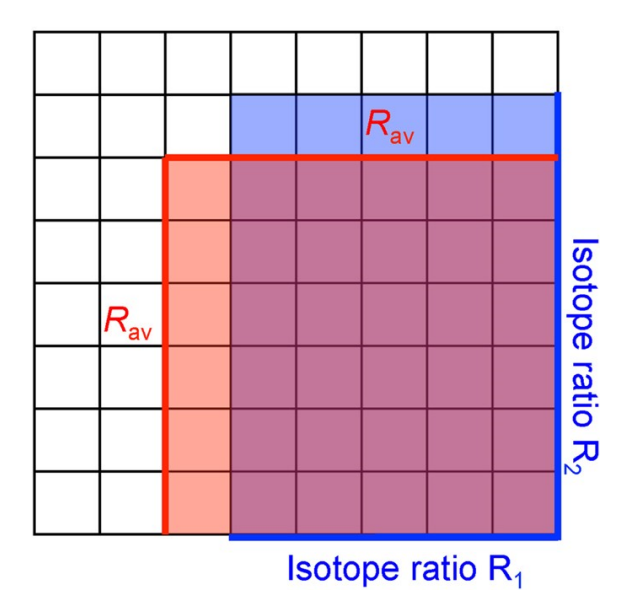


Figure 2.18: Geometric representation of statistical clumped isotope compositions. Derived from Röckmann et al., 2016.

In the simplest form, when two atoms of the same element are combined in a molecule and their isotopic ratio are  $R_1$  and  $R_2$ , the expected stochastic ratio ( $R_{stochastic}$ ) can be calculated simply as the product of those ratios (Röckmann et al., 2016):

$$R_{stochastic} = R_1 \times R_2$$
 (2.40)

However, these two atoms are indistinguishable from each other within the molecule, and we are unable to measure separately the isotopic ratio of each one. Therefore, we make an approximation that stochastic distribution ( $R_{ap,stochastic}$ ) of the isotopologue is simply the average ratio of those two atoms:

$$R_{ap,stochastic} = \left(\frac{R_1 + R_2}{2}\right)^2 \qquad (2.41)$$

The statistical clumped isotopic signature attributed on those differences in the general form can be written as following (Röckmann et al., 2016):

$$\Delta = \frac{R_{stochastic}}{R_{ap,stochastic}} = \left(\frac{geometric\ mean}{arithmetic\ mean}\right)^{n} - 1 \qquad (2.42)$$

Where n, represents the number of atoms with different isotopic ratios.

By combining eq. 2.40, 2.41, 2.42, the clumped isotopic signature  $\Delta$  due to combinatorial effects, is equal to:

$$\Delta = \frac{R_{stochastic}}{R_{ap,stochastic}} = -\frac{(R_1 - R_2)^2}{(R_1 + R_2)^2}$$
 (2.43)

From eq. 2.43, we obtain that the  $\Delta$  value can only be zero when  $R_1 = R_2$ , otherwise in case  $R_1 \neq R_2$  the  $\Delta$  always takes a negative value. It is significant to highlight that this anti-clumping signature is not dependent on the absolute values of the ratios, but instead it depends only on the difference/contrast of the ratios of those two atoms (Röckmann et al., 2016; Yeung et al., 2016).

In CH<sub>4</sub>, combinatorial effects can potentially affect the clumped isotopic signature of  $\Delta^{12}\text{CH}_2\text{D}_2$ , which contains the D-D bond (Yeung et al., 2016; Young et al., 2017). Due to the strong disequilibrium signatures in  $\Delta^{12}\text{CH}_2\text{D}_2$  (up to -60‰) measured for microbial and abiotic methane, combinatorial effects were suspected to contribute at least partially at those departures from thermodynamic equilibrium, possibly in conjunction with kinetic isotope effects (Young et al., 2017). Taenzer et al. (2020) proved that combinatorial effects can influence the  $\Delta^{12}\text{CH}_2\text{D}_2$  in methanogenesis experiments, when the three hydrogen atoms are donated by the methyl group and one can be obtained by the water medium. Contrarily, those effects are unexpected during abiotic methane formation as the differences in fractionation factors during hydrogen addition steps are not expected to be significant at those temperatures (Young et al., 2017).

Overall, combinatorial effects can alter the clumped isotopic signatures of CH<sub>4</sub> and should be considered when interpreting clumped isotopic data, particularly when negative  $\Delta^{12}\text{CH}_2\text{D}_2$  values are reported.

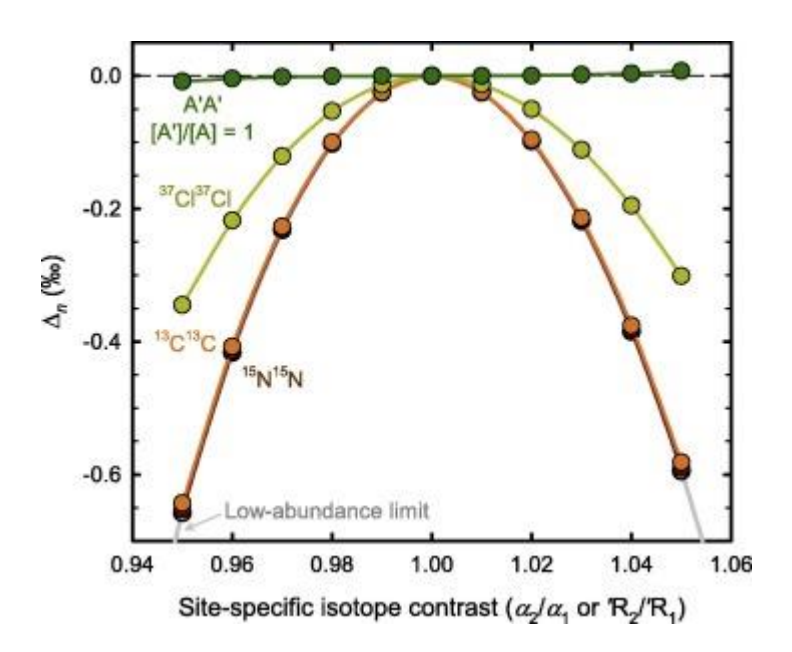


Figure 2.19: The impact of combinatorial effects due to the isotopic contrast between two molecules (examples are given for the clumping of carbon, nitrogen and chlorine heavy isotopes). Figure taken from Yeung (2016).

In this thesis, I will describe the methodology developed in SUERC for the measurement of clumped isotopes of CH<sub>4</sub>, while I present an application of clumped isotopes on CH<sub>4</sub> collected from natural settings. While methane is the main focus of this thesis, bulk (<sup>18</sup>O and <sup>13</sup>C) and clumped isotopes have been measured in carbonate veins from natural settings in order to assess any potential relationship between methane and carbonates veins.

# 3. Analytical methods

# 3.1 Overview

In this chapter I provide a full description of the instrumentation and analytical methodologies developed during tis PhD. This includes information about the procedure for the purification of natural gas samples, a description of the experiments concerning the equilibrated methane samples, a description of the 253 Ultra mass spectrometer, the measurement procedures, the validation of the purification and equilibration processes and finally the data processing undertaken to generate the final bulk isotopic signatures ( $\delta^{13}$ C and  $\delta$ D) and the clumped isotopic signatures ( $\Delta^{13}$ CH<sub>3</sub>D and  $\Delta^{12}$ CH<sub>2</sub>D<sub>2</sub>).

# 3.2 Purification and Preparation of Methane

### 3.2.1 Purification

Prior to the introduction of a methane sample into the mass spectrometer and the isotopic analysis, the sample must undergo purification to restrict any interferences during the measurement by contaminants (Stolper et al., 2014a; Eldridge et al, 2019). Essentially, we take advantage of the different condensation temperatures of gases based on their partial pressures, for gases found commonly in natural gas mixtures (Stolper et al., 2014a). The condensation or release of the gases from a cryostat to the vacuum line is monitored using two pressure gauges (Edwards WRG S14.5, Edwards Pirani APG-100XM).

Initially, the sample is released towards the headspace of a Janis closed-cycle cryostat cooled with liquid He. I allowed an equilibration time of 15 mins to ensure complete capture of methane in the cryostat (initially held at 20K). At 20K, only He and H<sub>2</sub> are non-condensable, and they are evacuated at the end of the equilibration time using either a scroll pump (Edwards nXDS6i) or turbomolecular pump (Pfeiffer HiCube 80) depending on pressure range, which are both attached to the back of the line (see Figure 3.2). Subsequently, I increased the temperature to 45K and wait for 5 minutes to release N<sub>2</sub> and O<sub>2</sub> which are pumped away. I heated the cryostat at 75K to release CH<sub>4</sub> and other non-condensable gases trapped within the methane molecules. As a high purity (>99%) of methane for the isotopic analysis is required, I conducted several cycles (typically 3-5) between 75K to 45K to ensure complete removal of O<sub>2</sub> and N<sub>2</sub>. The cycles between 75K and 45K are necessary to release and quantitatively remove N<sub>2</sub> and O<sub>2</sub> molecules that could have been trapped amongst the abundant CH<sub>4</sub> molecules.

Before trapping the gas, the 5A molecular sieves (6-8 pellets) are enclosed within a 6 mm (outer diameter) borosilicate/quartz glass tube. The molecular sieves are flamed for 30 minutes under vacuum in order to remove any gases (mostly N<sub>2</sub>, O<sub>2</sub>, H<sub>2</sub>O) adsorbed onto the surface of the molecular sieves during their storage and exposure to atmospheric air. The purified methane gas is captured in a glass sample tube filled with the molecular sieves, cooled to -196°C with liquid nitrogen for 5 minutes or until the vacuum line pressure has stabilised. The glass tube is sealed using a H<sub>2</sub>-CH<sub>4</sub> mixture-oxygen flame torch. The setup for methane purification and trapping is shown in Figures 3.1 and 3.2.

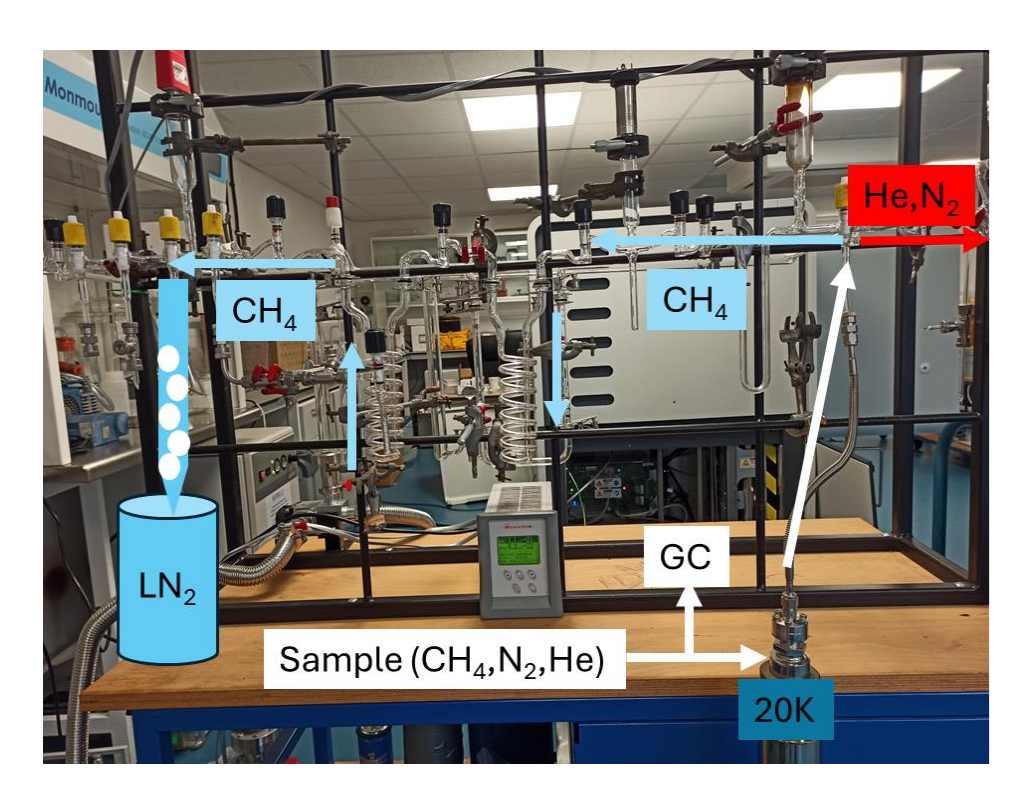


Figure 3.1: Photograph of the vacuum apparatus and procedures used for handling and purifying CH<sub>4</sub>-contained samples. Red colour indicates the removal of gases using vacuum pumps. GC refers to the injection point for a gas syringe in order to sample gas for major gas composition analysis using gas chromatography.

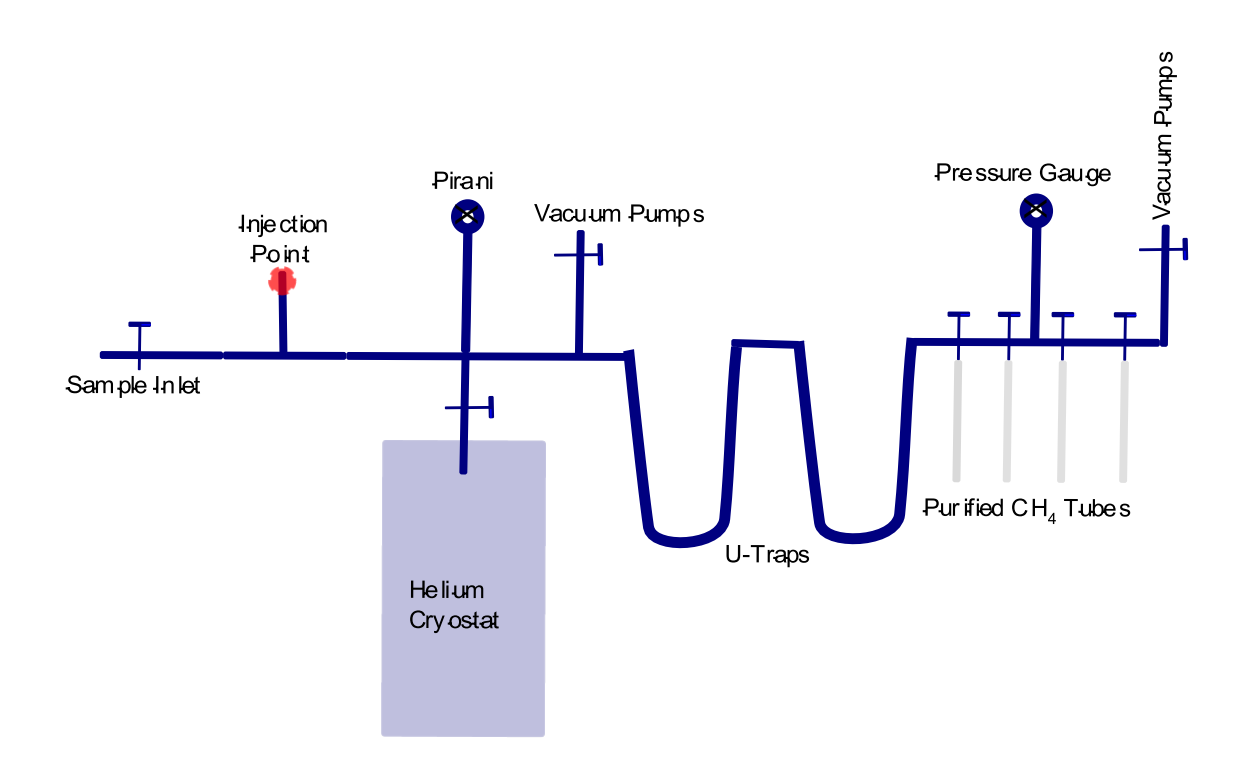


Figure 3.2: Diagram of the vacuum apparatus and inlet used for handling and purifying CH<sub>4</sub>-contained samples. Red circle depicts the injection point for a gas syringe to measure major gas compositions. A Pirani gauge and a pressure gauge are used to monitor the pressure at different points in the vacuum line.

### 3.2.2 Preparation

The sample tube containing the CH<sub>4</sub> trapped onto the molecular sieves is inserted into a tube cracker connected to the dual-inlet of the mass spectrometer. The molecular sieves are heated at 150°C using an external heater for 1h to release all the CH<sub>4</sub>. The heaters are required to be in contact with the tube containing the molecular sieves throughout the process, as previous experiments have shown a consistent C isotopic fractionation of approximately 0.5‰. The tube cracker, the fittings and the dual-inlet are evacuated using the mass spectrometer pumps for approximately 5-10 minutes to remove air. The methane is then expanded into the bellows of the mass spectrometer by cracking the glass tube which along a pre-established score. The bellows are compressed and expanded from 0 to 100% of the possible volume over the course of 2 minutes, which serves to mix the gas and erase any isotopic gradient that may have developed as a result of the initial expansion and temperature gradient, following the protocols established by Stolper et al. (2014a). The gas sample is then introduced into the mass spectrometer through a capillary.

# 3.3 Equilibrated Gases

# 3.3.1 Introduction

The lack of internationally accepted standards (approved by NBS or IAEA) for the measurements of the clumped isotopes of methane, or of community-wide standards similarly to clumped isotopes in carbonates (see Chapter 5) (Bernasconi et al., 2018), raises the need to prepare equilibrated aliquots in the laboratory. In comparison to the carbonate standards for clumped isotopes which are in solid phase, the distribution, shipping and storage of standards in gas phase such as those for methane clumped isotopologues, would be more challenging due to physical effects (e.g. diffusion) which can cause isotopic fractionation. Therefore, it is more practical to create internal standards in the laboratory, potentially at the expense of standardisation and reproducibility across laboratories.

These clumped isotope standards are needed to determine the clumped isotopic compositions of the working gas in SUERC and subsequently can be used as an anchor points of our measurements. My methodology for the experimentally equilibrated gases in SUERC follows established methods developed and reported in earlier studies by Stolper et al. (2014), Young et al. (2016), Wang et al. (2019), and Eldridge et al. (2019).

In theory, the methane isotopologues are expected to attain internal equilibrium, allowing to anchor measurements to a calibration of the clumped isotope geothermometer and check the accuracy of the mass spectrometer over the long term (Stolper et al., 2014a).

It is needed to create experimental products with an isotopic distribution reflecting thermodynamic equilibrium at known temperatures. This is achieved by enabling the isotope exchange between the isotopologues of methane (reactions 3.1 & 3.2), which is promoted by a catalyst at a given temperature. However, the heating temperature should be in a range where no or little methane loss takes place, as observed by Stolper et al. (2014a) at temperatures below 500°C. The usage of a suitable catalyst activates the C-H bonds as previous equilibration experiments have shown in H<sub>2</sub>-CH<sub>4</sub> and CO<sub>2</sub>-CH<sub>4</sub> systems (Horibe and Craig, 1995; Horita, 2001; Stolper et al., 2014a).

$$^{13}CH_4 + ^{12}CH_3D \leftrightarrow ^{12}CH_4 + ^{13}CH_3D$$
 (3.1)  
 $2^{12}CH_3D \leftrightarrow ^{12}CH_4 + ^{12}CH_2D_2$  (3.2)

Two procedures were used for the equilibration of gases from 1 to 500°C using two different catalysts (Eldridge et al., 2019). A nickel-based catalyst was used for 250°C to 500°C (Stolper et al. 2014a), while for the 0 to 200°C a γ-Al<sub>2</sub>O<sub>3</sub> catalyst was used (Wang et al.,

2019; Eldridge et al., 2019). (Wang et al., 2019; Eldridge et al., 2019). For completion reasons I describe both equilibration methods. However, it should be mentioned that all the measurements conducted in this thesis only have used calibration within 250-500°C, while for the low temperature range (0-200°C) I had only participated in the designing and conceptualisation of the experimental setup. I organise the following section into two parts, each for the specific temperature range

# 3.3.2 High-temperature Experiments

Firstly, 20mg of nickel-based powder (~66% nickel on silica—alumina, Alfa Aesar) are added into a quartz tube with 5A molecular sieves (6-8 pellets), and subsequently the tube is stuffed with glass wool (Sigma Aldrich) which prevents the nickel powder from moving across the tube. This is more evident when the tube is evacuated, or the gas expanded across the vacuum line. The tube is attached to the vacuum line and under vacuum (Figure 3.2), while this time the molecular sieves and the catalyst are heated with the flame torch to remove any contaminants. An aliquot of the working gas (high-purity methane) is expanded towards a tube and is trapped onto the molecular sieves by immersing the tube into a container topped with liquid nitrogen. Once the gas is secured and the glass tube flame-sealed, the tube is transferred to the middle of a box furnace. There, it is heated for specific duration (Table 3.1) at the targeted temperature in order to achieve full equilibration. Once the glass tube is removed from the box furnace, it is quenched with compressed air to prevent partial isotope exchange during cooldown, although any effect should be negligible and beyond analytical precision as the tubes and their content reach ambient temperature in a few minutes at most. The equilibrated methane sample is now loaded through the tubecracker into the vacuum line, to purify and isolate the CH<sub>4</sub> from the contaminants (i.e. H<sub>2</sub>) produced during the heating process (subsection 3.2 purification).

Table 3.1: List of equilibrated samples prepared in SUERC and reported in Eldridge et al. (2019), including temperature and duration of heating.

Temperature (°C)	Catalyst used	Heating Duration <sup>a</sup>	Heating Duration <sup>b</sup>
		(hours)	(hours)
500	Ni	~3	1-4
400	Ni	~5	4-6
350	Ni	~10-11	9-12
300	Ni	~50	24-65
250	Ni	~120	72-184
165.4	γ-Al <sub>2</sub> O <sub>3</sub>	-	6.5-8.5
127.8	γ-Al <sub>2</sub> O <sub>3</sub>	-	23-25.5
75.7	γ-Al <sub>2</sub> O <sub>3</sub>	-	233-288
50.5	γ-Al <sub>2</sub> O <sub>3</sub>	-	292-478.5
25	γ-Al <sub>2</sub> O <sub>3</sub>	-	551-622
1.2	γ-Al <sub>2</sub> O <sub>3</sub>	-	503.5-816

**a**: Heating duration for the equilibration experiments conducted at SUERC. **b**: Heating duration for the equilibration experiments as reported in Eldridge et al. (2019).

### 3.3.3 Low-temperature Experiments

This set of experiments is more demanding as the catalyst ( $\gamma$ -Al<sub>2</sub>O<sub>3</sub>) requires significant activation before it can be used for equilibration of the gas (Eldridge et al., 2019). The usage of  $\gamma$ -Al<sub>2</sub>O<sub>3</sub> was first proposed by Wang et al. (2019), while Eldridge et al. (2019) developed the technique and optimised the workflow for the equilibrated experiments at this temperature range.

Pellets of  $\gamma$ -Al<sub>2</sub>O<sub>3</sub> (~10 pellets; ~0.25 g) were loaded into quartz tube and heated under vacuum to for 20-30 minutes with the flame torch to remove any adsorbed gases. Subsequently, the pellets were heated at 550°C for 5 hours in the presence of O<sub>2</sub>, and for a further 12-14 hours at the same temperature under vacuum. The pellets can be either used directly for the equilibration experiment or stored under vacuum by sealing the tube.

Twenty pellets (0.5 g) of activated catalyst were used to absorb approximately 30 mL of high purity methane in an evacuated glass vial before the heating/cooling. The gas is sampled through the septum cap to monitor the state of equilibration during the heating or cooling process. The glass vial was transferred into a refrigerator, water bath or heating device depending on the desirable equilibration temperature (Table 3.1). Once the equilibration is

achieved, the equilibrated sample was expanded into the vacuum line and trapped on the cryostat to proceed with the purification/preparation process as described earlier.

# 3.4 Mass Spectrometer-Ultra 253

The Thermo Fisher Scientific Ultra 253, hereafter Ultra, is a high-resolution gas-source isotope ratio mass spectrometer designed to resolve peaks of interest from isobaric species (Eiler et al., 2013). This capability was unfeasible with the older generation of gas source dual-inlet isotope ratio mass spectrometers, which were only able to distinguish peaks formed at the collector by ion beams with m/z at least 1 amu apart (Stolper et al., 2014a). Additionally, previous methods required the chemical conversion of CH<sub>4</sub> into CO<sub>2</sub> and H<sub>2</sub>O to measure  $\delta^{13}$ C and  $\delta$ D due to low resolution. Instead, high-resolution mass spectrometers such as Ultra can resolve sufficiently the peaks from  $^{13}CH_4^+$  and  $^{12}CH_3D^+$  (both at m/z ~ 17) to determine the  $\delta^{13}$ C and  $\delta D$  of a sample, without the need of combustion or pyrolysis. More importantly, the improvements in instrument resolution, sensitivity and stability (Eiler et al., 2013; Young et al., 2016), has allowed the measurement of the rare doubly-substituted isotopologues of methane at m/z 18 (Stolper et al., 2014a; 2014b; 2015; Young et al., 2017). These are particularly challenging measurements to conduct since those peaks are considerably close to each other (3 milli amu or hereafter mamu), and close to peaks from either naturally abundant species such as water (~30 mamu), and products of reactions in the ion source (\frac{13}{CH\_5}^+ and \frac{12}{CH\_4D}^+) at mass 18 (1-2 mamu). As discussed earlier in Chapter 2. the clumped isotopic compositions  $\Delta^{13}CH_3D$  and  $\Delta^{12}CH_2D_2$  may provide further information into the generation mechanisms and the origin of the natural gas (Thiagarajan et al., 2020), or act as an independent tracer for constraining further the atmospheric methane budget (Haghnegahdar et al., 2017; Haghnegahdar et al., 2024; Sivan et al., 2024).

The description of the Ultra has been firstly reported by Eiler et al. (2013), which thoroughly described a prototype version of the Ultra based in Caltech. My description will also include information from Stolper et al. (2014a), Dong et al. (2020), and observations after our collective experience in SUERC and collaboration with the manufacturer, Thermo Fisher Scientific. The Ultra consists of six major components which are all critical from the generation of the ion beam until the measurement of the ions into the detector array. These components are the dual-inlet and the changeover block, the ion source, the electrostatic analyser (ESA), the magnetic sector, the transfer optics elements, and the detector array (Figure 3.3).

The gas is stored in the compressible bellows of the dual-inlet, which allows the pressure to be equal for both the standard and sample gases. A series of pneumatic valves, named as changeover block is responsible for the constant flow of the gas into the ion source. The capillary crimps determine the flow rate from the bellows and need to be balanced. The flow can be adjusted by compressing the bellows up to a source pressure limit of  $2.5 \times 10^{-7}$  mbar. This limit minimises the abundance of ionisation adducts which can affect or bias the measurement. Operating at source pressures above  $2.5 \times 10^{-7}$  mbar can cause source arcing which will result to signal instabilities and may damage to the instrument.

The ion source is an electron-impact ionisation similar to a Nier-type source (Eiler et al., 2013). A metal source filament emits electrons which collide with the gas molecules in order to create ions. The produced ions are then accelerated at 10keV which produces an ion beam, which passes through a mechanical aperture (slit) of three possible widths (250  $\mu$ m, 16 $\mu$ m, 5  $\mu$ m). The selection of the width is crucial as a smaller entrance slit width will reduce sensitivity (as the transmission of the ions will be smaller) but will result to increased resolutions due to reduced dispersion of the ion beam (Eiler et al., 2013). Based on the slit width, the Ultra operates in three easily selectable modes on Qtegra: low-resolution (250  $\mu$ m slit width), medium-resolution (16  $\mu$ m slit width), and high-resolution (5  $\mu$ m slit width). In full transmission (low resolution mode), the proportion of gas molecules entering the source relative to the ions produced and detected (the ion yield) is approximately 1200:1 for CO<sub>2</sub> (Dong et al., 2020). This ratio declines with reducing transmission in medium and high-resolution modes by approximately 15-fold and 50-fold, respectively, compared to the low-resolution mode.

After passing through the entrance slit the ion beam is focused by a quadrupole lens, then sent through an ESA which uses an electric field to filter out low and high energy ions. Before entering the magnetic sector, the ion beam is accelerated at 10 keV and further focused to improve resolution by a set of accelerating lenses with focusing and rotating quadrupoles, including an aperture lens (Dong et al., 2020). The use of the aperture lens is optional and results in lower sensitivity by ~66% (HR+ mode). The ions are separated based on m/z using a magnetic field created by a 520 kg magnet of 23 cm radius. The ion beams are focused through another focusing quadrupole before entering the detection system.

The collector array consists of eight movable detector positions and one in the central position which is fixed. The eight cups are evenly distributed at the low and high mass relative to the central detector, with the L4, L3, L2, L1 detectors on the low mass side, and the H4, H3, H2, H1 detectors on the high mass side. The entrance slit of the collector varies across the detector array and can be chosen depending on the peak of interest and the required resolution. For example, all the collectors have an entry slit width of 800µm, except the

central collector of 1mm, the collector L4 of 1.3mm, and H4 collector of 40µm. Besides the central cup, some of the collectors (L3, L1, H1, H3) are moveable using a motorised trolley while the rest are pushed around or dragged, as the collectors are mount in pairs with set distance to each other (Eiler et al., 2013). The high mass positions (H2, H3, H4) are equipped with a Faraday cup and an electron multiplier, with the central cup to have additionally a large size secondary electron multiplier (SEM). Similarly, the high-mass positions are equipped with smaller scale secondary electron multipliers, known as CDDs (Compact Discrete Dynode) whose performance is crucial for our measurements (Sections 3.5.2 – 3.5.4). The performance of CDDs is important because they offer minimal contributions (<0.1 counts per second or cps) from other sources of errors besides the counting statistics error, such as the dark noise (referring to the noise when there are no incident ions moving towards the detector) and noise related to the ion-scattering within the detector array (Dong et al., 2020). However, CDDs are particularly sensitive and non-linear to higher current intensities (>10<sup>6</sup> cps) and exposure beyond this limit might shorten substantially the longevity of the CDDs.

All Faraday cups are interconnected with signal amplifiers ranging from  $10^7$  to  $10^{12} \Omega$  (Eiler et al., 2013) which can be selected according to the target signal intensity. The array of Faraday cups of varying slit widths, amplifiers and CDDs allows to measure simultaneously signals over many magnitudes of signal intensity. In the case of methane isotopologue measurements, this varies with source pressure, tuning parameters and operating modes but typically ranges from  $1.5 \times 10^9$  cps for  $^{12}\text{CH}_4^+$  to 100 cps for  $^{12}\text{CH}_2\text{D}_2^+$  in HR mode and  $1.5 \times 10^{-7}$  mbar source pressure (see sections below).

The Ultra is typically operated at ultra-high vacuum conditions ( $<10^{-8}$  mbar). This is achieved using 5 turbomolecular pumps (Pfeiffer HiCube 80) backed by a scroll-type pump (Edwards nXDS6i), and two ion pumps. Two turbomolecular pump the dual-inlet system (one for each dual-inlet), and three turbomolecular pumps are between the source and ESA section, where the pressure is monitored by pressure gauges. One ion pump is located between the ESA and the magnetic sector, and the other one between the magnet and the detector array (Eiler et al., 2013). Typical baseline pressures within the system (without gas flow), range between 1 x  $10^{-8}$  and 1 x  $10^{-9}$  mbar for the ion source and ESA section, and 2 to 3 x  $10^{-9}$  mbar for the detector housing. The vacuum pumps for the preparation line and the mass spectrometer are oil-free, as hydrocarbon contamination could affect the background levels of the instrument.

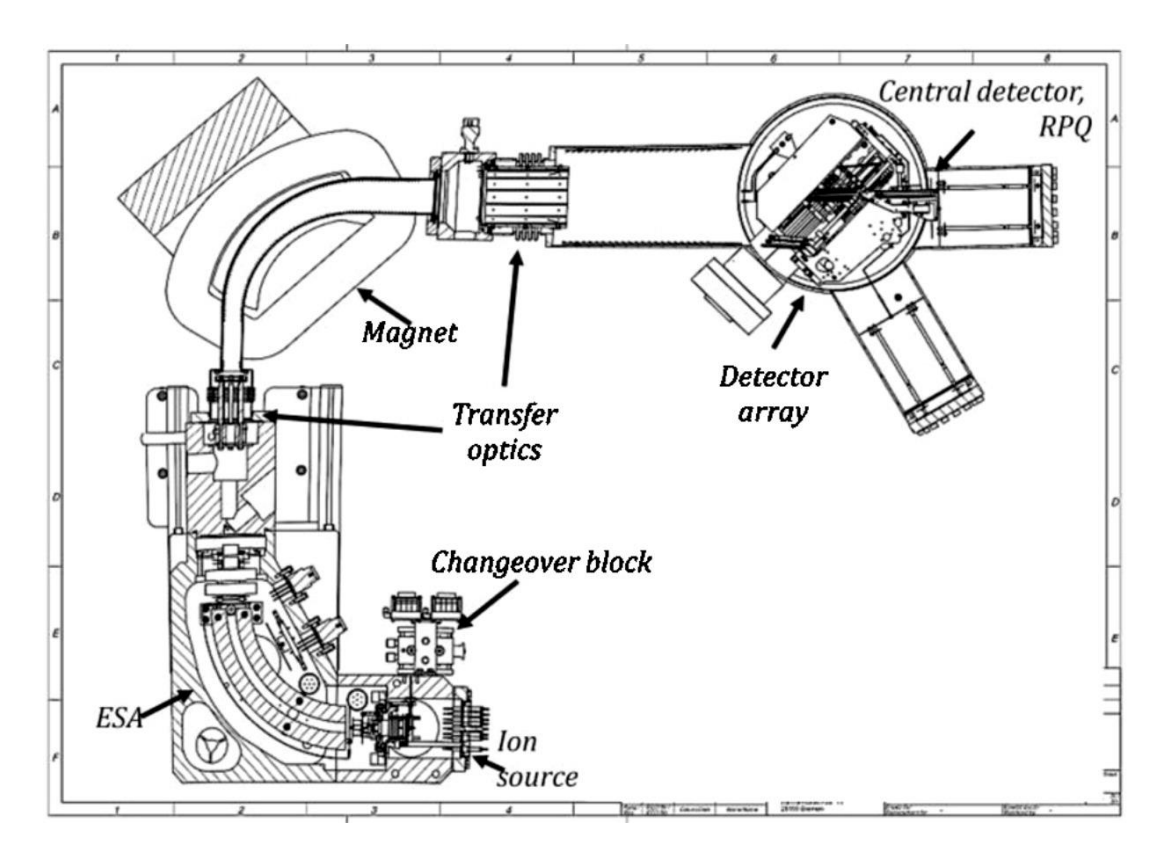


Figure 3.3: Schematic depiction of the main components of the Ultra including the ion source, the electrostatic analyser (ESA), the transfer optics before and after the magnetic section, and finally the detector array consisting of 9 collectors.

The Ultra has been installed in 2015 at the Clumped isotope laboratory in SUERC (Figure 3.4) and has been used with a diverse array of analytes in order to answer questions in a variety of scientific fields such as geology, geochemistry, atmospheric science and others. The Ultra is mainly used to measure methane isotopologues for samples deriving from natural gas systems (as is in this thesis) and atmospheric methane (Houston et al., 2024), the clumped isotopes and <sup>17</sup>O in carbonaceous meteorites (Clog et al., 2024), and of the isotopic composition of helium has been measured in experimental products. Care is required when switching from one analyte to another (e.g. CH<sub>4</sub> to CO<sub>2</sub>), as the source chemistry and conditions change and the optimal settings for one analyte/measurement might not correspond to optimal or sufficient settings for another measurement.



Figure 3.4: Photograph of the Ultra 253 hosted in the Clumped Isotope laboratory at SUERC.

The terms of resolution and mass resolving power are often used interchangeably in literature. According to Murray (2022), *resolution* describes the ability to resolve two peaks from each other. Based on Dempster (1918), this can be defined as the smallest possible difference  $(\Delta(m/z))$  between two peaks, where each peak can be measured discretely (10% valley definition), divided by m/z (Murray, 2022). Contrarily, *mass resolving power* (m/ $\Delta$ m) can be used as a quantitative term to demonstrate the ability of a mass spectrometer to separate two peaks. The  $\Delta$ m is the beam width, or the  $\Delta$ m associated with the leading edge of the peak as the beam enters the cup (5-95% flank definition) (Figure 3.5) (Murray, 2022).

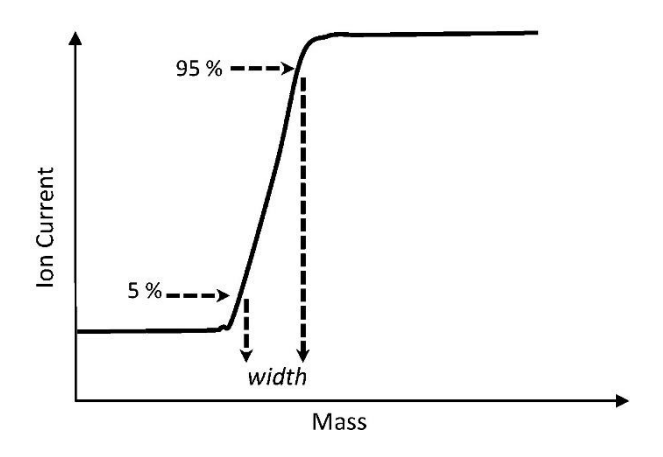


Figure 3.5: Illustration of the definition for the calculation of mass resolving power  $m/\Delta m$  (Eiler et al., 2013). Qtegra software provides the calculation for either mass side (relatively to the peak) automatically after a magnet scan.

The SUERC Ultra can consistently reach a mass resolving power of 28,000 in HR mode (MRP, 5-95% edge definition), and up to 45,000 in HR+ mode but typically operating between 39,000 and 43,000. These MRP were determined by magnet scans using collector H4. Typically for the central cup at low resolution mode the optimised MRP does not exceed 5,000, while in medium-resolution mode the MRP is up to 18,000, and in HR mode it is up to 25,000.

### 3.5 Methane Measurements

# 3.5.1 Preliminary Checks

Before setting up for measurements, we usually conduct some checks to monitor the state of the Ultra and ensure the quality of the measurements. A few of those checks include the state of the pumping system and the pressure levels across the different sections of the Ultra. Using the pressure gauges at the source, the ESA, and multi-collector array we can verify if the pumps are functional and if the background and the pressures in the mass spectrometer are within the expected range. Other checks include monitoring the background signal from species that can be often found in the mass spectrometer from atmospheric air introduction or from previous measurements of another analyte. The detected signals typically correspond to the presence of gases such as N<sub>2</sub>, O<sub>2</sub>, H<sub>2</sub>O and CO<sub>2</sub>. This is particularly important for our measurements as abnormal abundances (abundances above the long term monitored values) of those gases would create scattered ions, change the instrument fractionation, and increase the background levels which all can affect the results of our measurements. Finally, we monitor the sensitivity of the instrument and the state of the high-resolution slit, usually by checking the intensity ratios in low resolution and medium resolution modes against the high-resolution modes. If significant shifts from the expected values are detected, we either substitute the high resolution slit for a new one (which happens on average every 6-9 months) or make further investigations into the conditions of the source and the filament. All those checks mentioned, are conducted in a daily basis and an archive is kept for future reference.

The relative measurement position for a target peak varies depending on the occurrence of neighbouring species, either from naturally occurring species or species produced during the ionisation process in the source of the mass spectrometer (adducts). Those occurrences can distort the approximately Gaussian shape of a single peak. However, our aim is to measure on a part of the beam where any interference is minimal and any magnet drifts or peak position shifts during the measurement will not affect the data substantially (e.g. measuring off peak). For the peaks of interest, we identify two possible measuring positions:

- 1. Peaks of interest which are first or last at a given cardinal mass, are measured on a flat feature on either end of a composite peak shape. In this case, the peak is only partially resolved and the measuring position is described as the "shoulder" of the peak. Examples of those cases are the peaks of <sup>12</sup>CH<sub>4</sub><sup>+</sup>, <sup>13</sup>CH<sub>4</sub><sup>+</sup>, <sup>13</sup>CH<sub>3</sub>D<sup>+</sup>, and for those measurements a high mass resolving power is required to observe the peak shoulder (Figure 3.6).
- 2. In other cases, the peak is surrounded by other peaks and cannot be measured on the shoulder of the composite peak. This requires high resolution and by using the fine collector H4 this is achieved by clipping the beam. In this way, we can separate fully or partially the peak of interest from the other peaks at the same cardinal mass, with or without contribution from the neighbouring peaks. Examples of those peaks where the H4 collector is used, are the <sup>12</sup>CH<sub>3</sub>D<sup>+</sup> and <sup>12</sup>CH<sub>2</sub>D<sub>2</sub><sup>+</sup> (Figures 3.7 & 3.8).

To determine the bulk and clumped isotopic compositions of carbon and hydrogen in a methane sample, three individual measurements are required to quantify the relative abundance of 5 isotopologues at mass 16, 17 and 18 amu. During the first measurement, the relative abundances of  $^{13}\text{CH}_4^+/^{12}\text{CH}_4^+$  and  $^{13}\text{CH}_3\text{D}^+/^{12}\text{CH}_4^+$  are measured simultaneously in order to quantify the isotopic signatures of  $\delta^{13}\text{C}$  and  $\delta^{13}\text{CH}_3\text{D}$  between the sample and our working gas. The second measurement is required to determine the relative abundance of  $^{12}\text{CH}_2\text{D}_2^+/^{12}\text{CH}_4^+$  to determine the  $\delta^{12}\text{CH}_2\text{D}_2$ . This is the most challenging measurement given the low natural abundance of this CH<sub>4</sub> isotopologue (resulting to low signal intensity of only  $\sim 100$  cps), the presence of neighbouring ionisation adducts ( $^{13}\text{CH}_5^+$  and  $^{12}\text{CH}_4\text{D}^+$ ), and the presence of the clumped isotope  $^{13}\text{CH}_3\text{D}^+$  at the same cardinal mass at 18 amu (Figure 3.7). Finally, over the third measurement we measure the ratio of  $^{12}\text{CH}_3\text{D}^+$  to  $^{12}\text{CH}_4^+$  to calculate the  $\delta$ D. The limiting factor of this measurement is the narrow flat plateau of the  $^{12}\text{CH}_3\text{D}$  feature which typically varies between 0.4-0.8 mamu.

For all measurements, we wish the position of the collectors to allow simultaneous integration of the peaks of interest with no or minimum interference from neighbouring peaks (see sections 3.5.2 - 3.5.4).

For each methane sample, the total measurement time is about 20-25 hours (assuming sufficient sample size of 70 µmol). This includes the time to optimise the settings and set up the measurement. The tuning time for optimal conditions usually varies and highly depends on the state of the instrument (e.g. after a baking procedure), whether other analytes have been introduced into the source (e.g. CO<sub>2</sub>), and the time passed from the last tuning of the instrument as natural drifts are expected over time. Typically, no more than 30 minutes to 1

hour is required for tuning and setting up an individual measurement, and other procedures which will be explained into the further subsections. Hence, the sample throughput of the Ultra is one methane sample per day from the moment the sample has been introduced into the bellows of the Ultra.

Table 3.2: Overview of CH<sub>4</sub> isotopologues measurements using the SUERC 253 Ultra. The rarest isotopologues for each measurement are <sup>13</sup>CH<sub>3</sub>D<sup>+</sup> for the first measurement, <sup>12</sup>CH<sub>2</sub>D<sub>2</sub><sup>+</sup> for the second measurement and <sup>12</sup>CH<sub>3</sub>D<sup>+</sup> for the third measurement.

Isotopologues measured	Isotopic signatures calculated	Mode	Source pressure (mbar)	Signal rarest isotopologue (cps)	Measurement time (h)
<sup>12</sup> CH <sub>4</sub> , <sup>13</sup> CH <sub>4</sub> , <sup>13</sup> CH <sub>3</sub> D	$\delta^{13}$ C,	HR+	2x10 <sup>-7</sup>	4,000-6,000	~5
	$\Delta^{13}$ CH <sub>3</sub> D				
<sup>12</sup> CH <sub>4</sub> , <sup>12</sup> CH <sub>2</sub> D <sub>2</sub>	$\Delta^{12}CH_2D_2$	HR	1.5x10 <sup>-7</sup>	90-120	~10-13
<sup>12</sup> CH <sub>4</sub> , <sup>12</sup> CH <sub>3</sub> D	δD	HR+	9x10 <sup>-8</sup>	100,000-	~5-7
				130,000	

# 3.5.2 Measurement of $\delta^{13}$ C & $\delta^{13}$ CH<sub>3</sub>D

This measurement is needed to determine simultaneously the  $\delta^{13}C$  and  $\delta^{13}CH_3D$  of a sample against the working gas. The measurement requires HR<sup>+</sup> mode because the flat portion of  $^{13}CH_3D^+$  shoulder appears sloped in HR mode and adds noise on the measurement. The L4, L2 and H2 collectors are oriented to align  $^{12}CH_4^+$ ,  $^{13}CH_4^+$  and  $^{13}CH_3D^+$  peaks. The most abundant isotopologue  $^{12}CH_4^+$  (typical 6.5 - 8.5 x  $10^8$  cps at 2 x  $10^{-7}$  mbar source pressure) is measured on L4 collector using a Faraday cup with a  $10^{10}\,\Omega$  amplifier. The second most abundant isotopologue  $^{13}CH_4^+$  (1 – 2 x  $10^7$  cps) is measured on L2 Faraday cup using a  $10^{11}\Omega$  amplifier. The clumped isotopologue  $^{13}CH_3D^+$  (4,000-6,000 cps) is measured on H2 CDD collector (800  $\mu$ m entry slit) using a  $10^{12}\,\Omega$  amplifier.

The measurement is organised into 8 cycles, each including 10 repetitions of standard-sample bracketing of 60 integrations lasting 1.05s each, which allows us to investigate for drifts or outliers. For the precise measurement and calculation of the bulk and clumped isotopic composition we need sufficient information about the background levels (see 3.4.2). A background measurement is conducted with gas flowing into the source by shifting the measuring position by 50 mamu. The background intensities are measured both for the sample and the standard gas, after the completion of the 8 measuring cycles and organised

into 1 cycle with identical number of integrations and integration time. The total measurement time ( $\sim$ 5h) leads to precisions of typically 0.01‰  $\delta^{13}$ C for and 0.30-0.35‰ for  $\delta^{13}$ CH<sub>3</sub>D (1 standard error). The measurement precision of the  $\delta^{13}$ CH<sub>3</sub>D measurement is routinely equal to the counting statistics limit and rarely exceeds it by up to 1.2 times.

For this measurement, we require beforehand a flat portion of approximately 1 mamu on the  $^{13}\text{CH}_3\text{D}$  peak in order to ensure that the measurement is not drifting off-peak, resulting in peak addition, e.g.  $^{13}\text{CH}_3\text{D}^+ + ^{13}\text{CH}_5^+$  or drifting off the shoulder of the peak, resulting in signal loss. The centre position is determined once for each cycle after the automated pressure balance and before the first measurement of the working gas (in a standard working gas- sample-working gas bracketting), only on the standard bellow and using the H2CDD collector by monitoring the centre of the  $^{13}\text{CH}_3\text{D}^+$ - $^{13}\text{CH}_5^+$  peak. The measurement position is defined by applying a constant offset on the centre position of the peak. Generally the peak centre determination for this measurement is less frequent than for the  $\delta D$  and  $\delta^{12}\text{CH}_2D_2$  because a wide collector H2 (800 µm) is used. Therefore, typical drifts during the measurement of  $^{13}\text{CH}_3D^+$  do not affect the signal intensity. Where drift is detected we apply a filtering method to remove outliers (Section 3.6.2).

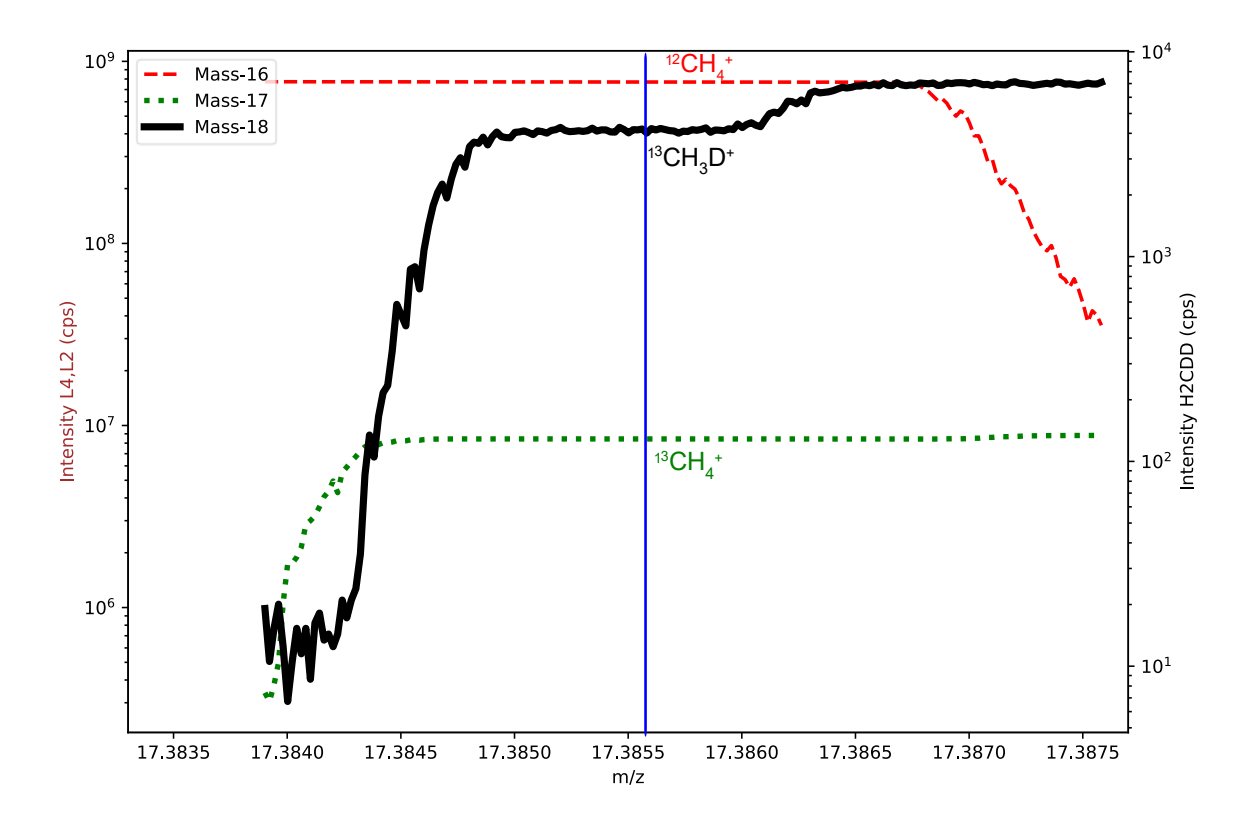


Figure 3.6: Peak scan for the measurement of <sup>12</sup>CH<sub>4</sub><sup>+</sup>, <sup>13</sup>CH<sub>4</sub><sup>+</sup>, <sup>13</sup>CH<sub>3</sub>D<sup>+</sup> using collectors L4, L2, H2CDD (all in log-scale), respectively. Blue vertical line indicates approximately the position of measurement.

# 3.5.3 Measurement of δ<sup>12</sup>CH<sub>2</sub>D<sub>2</sub>

The measurement of  $\delta^{12}\text{CH}_2\text{D}_2$  is performed in HR mode using collectors L4 Faraday cup (using  $10^{10}\,\Omega$  amplifier) on  $^{12}\text{CH}_4^+$  beam (typical intensities 1-1.4 x  $10^9$  cps at 1.5 x  $10^{-7}$  mbar source pressure) and the H4 CDD (0.04 mm entry slit width) on  $^{12}\text{CH}_2\text{D}_2^+$  beam (typically 100 cps). The narrow collector slit is required to resolve the  $^{12}\text{CH}_2\text{D}_2^+$  from the other isobaric species. The high relative abundances (compared to the  $^{12}\text{CH}_2\text{D}_2^+$  intensity) of clumped isotopologue  $^{13}\text{CH}_3\text{D}^+$  and ionisation adduct  $^{13}\text{CH}_5^+$  (~2000 cps), along with their proximity to the  $^{12}\text{CH}_2\text{D}_2^+$  peak create a contribution on the position where the  $^{12}\text{CH}_2\text{D}_2^+$  signal is measured. To overcome this peak-tailing effect, this contribution is corrected (see section 3.6.2).

The measurement is performed over 18 cycles, each including 10 repeats of the standard-sample bracket with 60 integrations of 1.05 seconds each. The background is measured with the same parameters as the sample/standard after a magnet jump of +100 mamu away of the measurement mass point in the end of the measurement. Using this measurement procedure, we achieve typically 1.5 - 2‰ for  $\delta^{12}$ CH<sub>2</sub>D<sub>2</sub> (12-13 hours measurement), which is routinely 1 - 1.2 times the counting statistics limit. This is similar to data reported by other laboratories equipped with an Ultra (Eldridge et al., 2019; Dong et al., 2020; Wang et al., 2023).

For setting up this measurement and optimising the MRP and peak shape the steps were followed:

- 1. I optimise the MRP (approximately 28,000 MRP is required for this measurement) and the peak shape on H<sub>2</sub>O peak due to the close proximity to the <sup>12</sup>CH<sub>2</sub>D<sub>2+</sub> peak (same cardinal mass and approximately -0.03 amu away from the <sup>12</sup>CH<sub>2</sub>D<sub>2</sub>+ peak), but in absence of neighbouring peaks.
- 2. Focus settings are tuned for intensities as close to zero as possible on the right side of the tail of <sup>13</sup>CH<sub>5</sub><sup>+</sup> peak, to minimise the contribution on the <sup>12</sup>CH<sub>2</sub>D<sub>2</sub><sup>+</sup>.
- 3. The height of the valley between <sup>13</sup>CH<sub>3</sub>D<sup>+</sup>-<sup>13</sup>CH<sub>5</sub><sup>+</sup> and <sup>12</sup>CH<sub>2</sub>D<sub>2</sub><sup>+</sup>-<sup>12</sup>CH<sub>4</sub>D<sup>+</sup> is an indicator of high resolution and minimum interference of the adjacent peaks on the <sup>12</sup>CH<sub>2</sub>D<sub>2</sub><sup>+</sup> signal. This is optimised by adjusting the focus settings of the Ultra.

As with the  $\delta D$  measurement, the small width of the H4 collector slit and possible drifts in the relative position of ion beam- collector require systematically and before every acquisition (either sample or standard), to verify the peak position for the measurement. This is performed using the H4 CDD on the  $^{13}CH_5^+$  peak. When the peak centre fails (given the

small width of the peak in addition to interferences on the peak shape from the  $^{13}\text{CH}_3\text{D}^+$  and  $^{12}\text{CH}_2\text{D}_2^+$  peaks) or if we measure away from the correct position, the acquisition is removed during the data processing. This is normally resolved with a simple  $3\sigma$  filtering and does not require an approach that is more sophisticated than for the  $\delta D$  determination (Eldridge et al., 2019). Usually, this data filtering approach improves the final precision by approximately 0.2-0.3‰. This is smaller than the precision of the measurement (1.5-2.0‰), but ultimately significant for the final precision of the measurement.

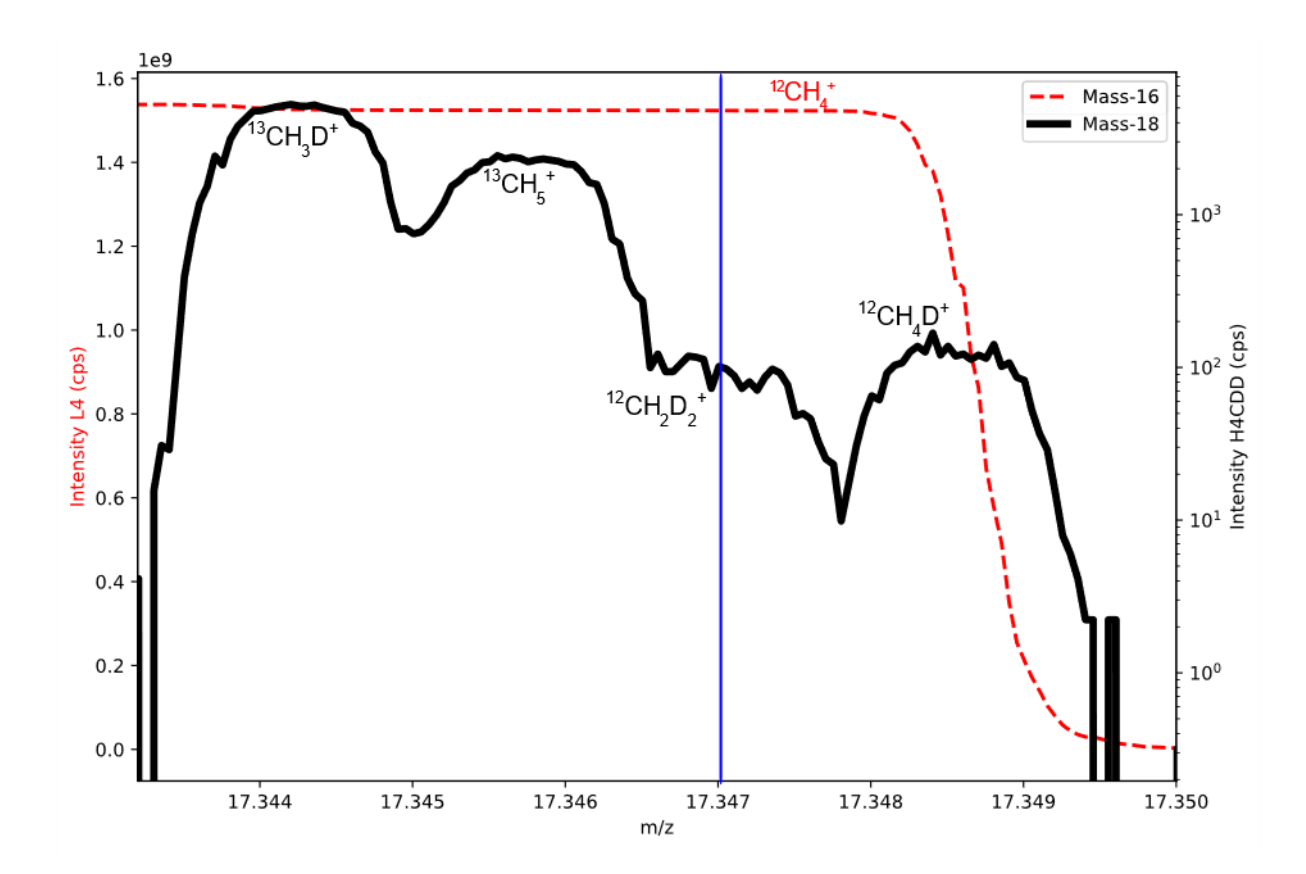


Figure 3.7: Peak scan for the measurement of <sup>12</sup>CH<sub>4</sub><sup>+</sup> and <sup>12</sup>CH<sub>2</sub>D<sub>2</sub><sup>+</sup> using collectors L4 and H4CDD (in log-scale), respectively. We require the "valleys" between <sup>13</sup>CH<sub>3</sub>D<sup>+</sup> and <sup>13</sup>CH<sub>5</sub><sup>+</sup>, <sup>12</sup>CH<sub>2</sub>D<sub>2</sub><sup>+</sup> and <sup>12</sup>CH<sub>4</sub>D<sup>+</sup> to be as close to zero as possible to ensure sufficient peak separation, and a flat peak for <sup>12</sup>CH<sub>2</sub>D<sub>2</sub><sup>+</sup> to minimise the measurement error. Blue vertical line indicates approximately the position of measurement.

### 3.5.4 Measurement of δD

The  $\delta D$  measurement is performed in HR<sup>+</sup> mode using collector L2 Faraday cup for the main beam  $^{12}\text{CH}_4^+$  using a  $10^{10}\,\Omega$  amplifier (typical intensities 2-4 x  $10^8$  cps at 9 x  $10^{-8}$  mbar source pressure), and the  $^{12}\text{CH}_3D^+$  beam (typically100,000-120,000 cps) on the H4 collector CDD (0.04 mm slit width). This allows resolution of  $^{12}\text{CH}_3D^+$  from the adjacent peaks (the ionisation adduct,  $^{12}\text{CH}_5^+$  and the abundant methane peak of  $^{13}\text{CH}_4^+$  (see Figure 3.8).

The measurement includes a standard-sample bracketing which is performed 10 times over 10 cycles overall. For each acquisition, we perform 75 integrations in a low integration time of 0.52 seconds. Background intensities are measured by performing a magnet jump at +0.1 amu away from the measurement mass position with the gas flowing at the end of the measuring cycles. One cycle of the background is measured for the standard and the sample gases with the same integration time and number of integrations as the measurement. Typically, precision of 0.1-0.12‰ is achieved, which is comparable to other laboratories (Eldridge et al., 2019; Zhang et al., 2021; Wang et al., 2023; Sivan et al., 2024).

This measurement requires a minimum 42,000 MRP (5-95%) and a flat plateau of about 0.5 mamu. A narrower flat portion of the peak increases the chances of drifting off-peak which considering the small width of the collector slit is probable I the course of the measurement (7 hours) if no peak centre correction is done. To avoid that we determine the precise peak position (using H4 CDD collector on the <sup>12</sup>CH<sub>3</sub>D<sup>+</sup> peak) before every acquisition either for the standard or sample gas.

The precision of this measurement may be up to 1.5 times above the expected counting statistics limit, which implies other sources of noise during the measurement. This occurs due to the high signal intensity of this peak (>100,000 cps), and the drifts resulting from the suboptimal relative positioning of the collector (possibly related to temperature fluctuations observed in other labs, see Wang et al., 2023). Therefore, we apply the data filtering techniques suggested by Eldridge et al. (2019) based on the z-score of each ratio measured (Section 3.6.2). The data filtering typically improves the internal precision of this measurement by less than 20% (Section 3.6.2).

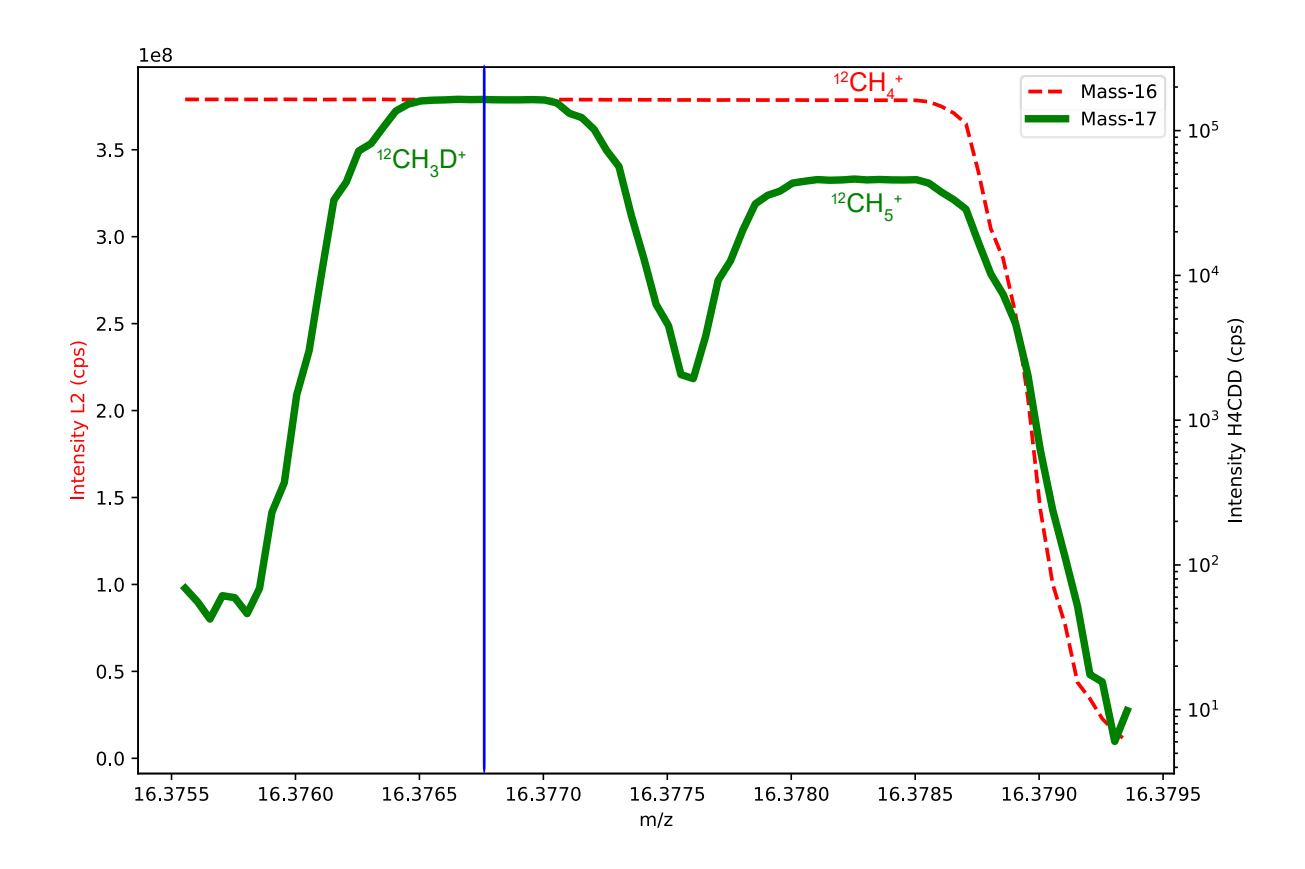


Figure 3.8: Peak scan for the measurement of <sup>12</sup>CH<sub>4</sub><sup>+</sup> and <sup>12</sup>CH<sub>3</sub>D<sup>+</sup> using collectors L2 and H4CDD (in log-scale), respectively. Blue vertical line indicates approximately the position of measurement.

# 3.6 Data Processing

# 3.6.1. Validation of Methods

### 3.6.1.1. Purification

Isotopic fractionation can arise from physical or chemical processes during the handling, capture, release and purification processes of the samples in the laboratory. A study by Stolper et al. (2014a) reported a fractionation of 0.1‰ and 0.5‰ for  $\delta^{13}$ C and  $\delta D$ , respectively. The isotopic fractionation was attributed to gas handling and release of the gases from the molecular sieves. However, no shift was apparent in the clumped isotopic compositions. The methods employed here are similar to those suggested by Stolper et al. (2014a), and we quantify isotopic fractionation related to those processes.

My initial tests included measurements of the working gas stored in a glass container in the lab against aliquots of that same gas that underwent capture and release from the molecular sieves. Initial results showed a considerable isotopic fractionation of 0.5% in  $\delta^{13}$ C, which was attributed to the heating and the release of the gas from the molecular sieves (Section 3.2). Once this was resolved by keeping the heaters on throughout the release of the gas into

the dual inlet, the isotopic fractionation in  $\delta^{13}$ C was negligible and within the analytical error (0.01‰). Generally, we use the  $\delta^{13}$ C as a proxy to detect those isotopic fractionations due to the intense signal and the high precision of the measurement in a short amount of measuring time (<20 mins). The measured values observed for the rest of the bulk and clumped isotopic signatures were within the analytical error of those measurements.

Further checks included the purification process used through the cryogenic system. The gas from the container was compared to a gas aliquot which went through the purification as described in Section 3.2. The results did not reveal any isotopic fractionation associated with the purification process for all the measurements conducted.

# 3.6.1.2. Equilibration Experiments

The equilibration experiments are required to determine the clumped isotopic compositions,  $\Delta^{13}\text{CH}_3\text{D}$  and  $\Delta^{12}\text{CH}_2\text{D}_2$ , of the working gas which are initially unknown. This is an important step to report our samples relative to the absolute thermodynamic reference frame and for laboratory intercomparison (Chapter 2 for details). The calibration process is also useful to determine the precision of the measurements and monitor the long-term performance and precision of the Ultra (Stolper et al., 2015).

Initially the equilibrated gases were measured against the working gas and reported against the working gas reference. In this case, the clumped isotopic compositions of the working gas are assumed to be 0% ( $\Delta^{13}$ CH<sub>3</sub>D<sub>wg</sub> =  $\Delta^{12}$ CH<sub>2</sub>D<sub>2wg</sub> = 0%). Using a least square regression between the measured values against theoretical values (e.g. based on calibration equations reported by Young et al. (2017) and Eldridge et al., (2019)), the clumped isotopic compositions of the gas can be determined. Using the intercept of this equation, the two clumped isotopic compositions can be inferred in the absolute reference frame. The details of the calculations can be found in Section 3.6.2.

The results from the equilibrated experiments conducted in SUERC are reported in the figure below (Figure 3.9). This calibration process is ongoing and conducted especially during the measurements of a set of natural and experimental products. The results demonstrate that the equilibration of the gases has been successful in the temperature range 250-500°C, as all the gases reported below are within 1 standard error from the heating/equilibration temperature. Besides the successful equilibration process, the precision enables us to distinguish gases of different formation temperatures provided their clumped isotope compositions reflect thermodynamic equilibrium. Typical precisions of 0.35% for  $\Delta^{13}$ CH<sub>3</sub>D and 2.0% for  $\Delta^{12}$ CH<sub>2</sub>D<sub>2</sub> correspond to +22°C/-20°C and +34°C/-27°C, respectively, at 120°C.

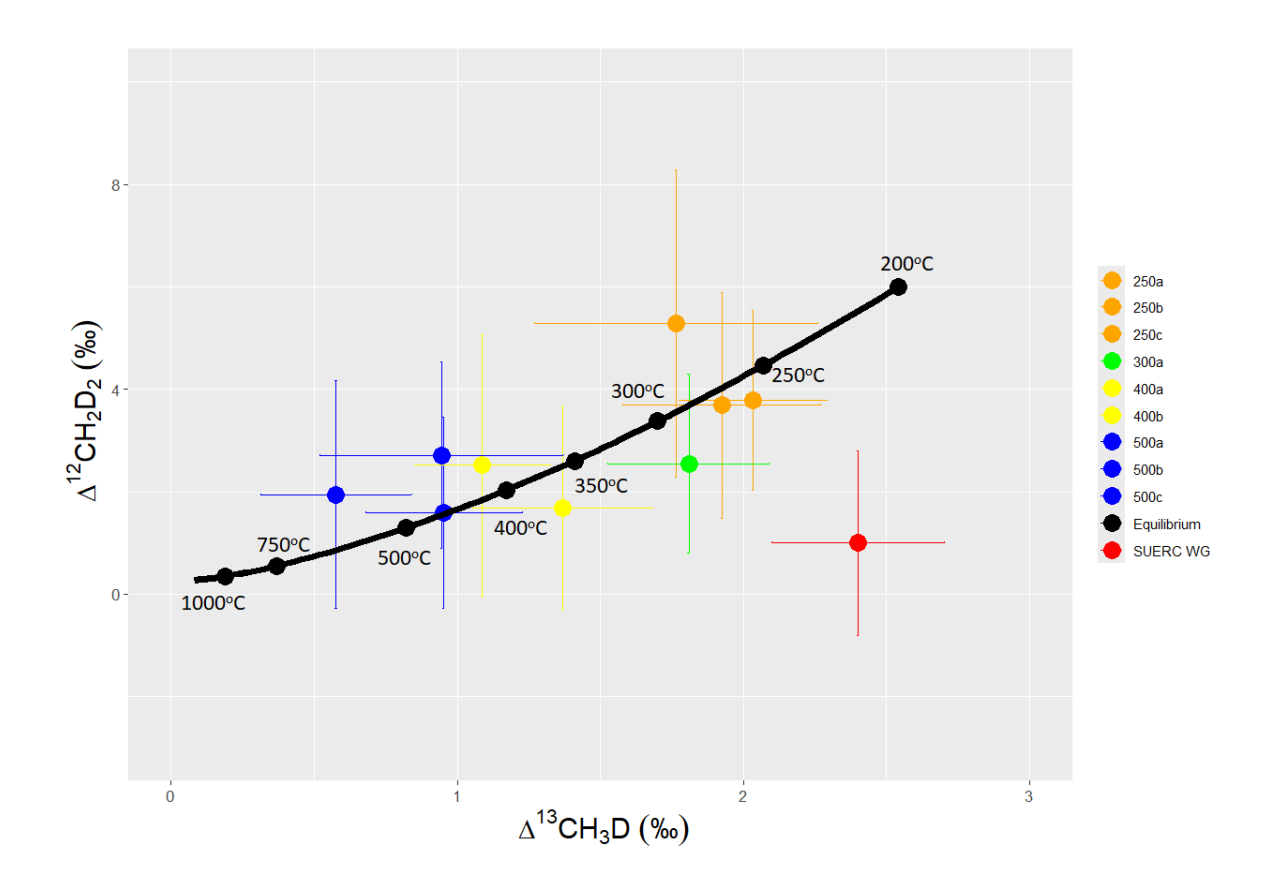


Figure 3.9: Results for the equilibrated gases produced and measured in SUERC. The results are reported against the absolute thermodynamic reference frame. Error bars refer to 1 S.E. These equilibration experiments covered the temperature range from 250°C to 500°C. Every point is a separately prepared and equilibrated aliquot of gas.

The equilibration experiments yield  $\Delta^{13}\text{CH}_3\text{D} = 2.4\%$  (± 0.3%) and  $\Delta^{12}\text{CH}_2\text{D}_2 = 1.0\%$  (± 1.8%) for the working gas, against the absolute reference frame. This plots below the thermodynamic equilibrium curve. As those values do not reflect an internal isotopic equilibrium, the apparent temperatures would be dissimilar. Based on the temperatures derived from the clumped isotopic compositions, the apparent temperatures would be at approximately 220°C and 450°C for  $\Delta^{13}\text{CH}_3\text{D}$  and  $\Delta^{12}\text{CH}_2\text{D}_2$ , respectively.

The clumped isotopic composition of the working gas determined from these experiments is used for the calculation of the isotopic composition of natural samples (Chapter 4). However, the calibration experiments need to be extended to 0 to 250°C in order to establish long term reproducibility.

## 3.6.2. Calculation of Isotopic Compositions

#### 3.6.2.1. Bulk Isotopic Compositions

The measurement of the bulk isotopic compositions of the working gas allows the calculation the  $\delta^{13}C$  and  $\delta D$  of methane samples against the international standards VPDB and VSMOW. For the measurement of the bulk isotopic signatures of the SUERC working gas conventional methods have been used: chemical transformation and isotope ratio mass spectrometry using  $CO_2$  and  $H_2$  as analytes. More information about the conventional mass spectrometry methods I used can be found in the Appendix. The isotopic analysis yielded results of  $\delta^{13}C$  = -42.1 (VPDB) ( $\pm$  0.1‰) and  $\delta D$  = -184.4‰ ( $\pm$  5‰) (VSMOW) . Therefore, those values are used as a calibrated anchor point to calculate and convert differences between samples and working gas measured in the Ultra into the international reference frames. The linearity of the Ultra is established due to measurements reported by Stolper et al.(2014a); Zhang et al., (2021); Sivan et al., (2024), and measurements of different bulk isotopic compositions conducted in SUERC.

In order to calculate precisely the bulk isotopic signatures, we need to determine the levels of the background signal. This is possible as background signal intensity are recorded before the end of any measurement (3.5.2-3.5.4). This is important as scattered ions or ions from other species (e.g. NH<sub>3</sub><sup>+</sup>) can contribute to the signal. For both measurements the procedure for background removal is similar; background levels are measured in each bellow (sample and working gas) at the end of eash measurement. The intensities measured are averaged for each bellow and deducted from the relevant signal intensity.

Subsequently, the data quality is evaluated to detect and filter any outliers. Typically, for the  $\delta^{13}$ C no filtering approaches are needed due to the wide collector and flat-topped peak used for this measurement. Therefore, even if any typical drifts in peak position occur during the measurement this will not correspond to any critical signal loss, and thus to outliers. However, for the  $\delta D$  calculation we use a specific filtering approach as mentioned in previous sections (Section 3.5.4), due to the narrow collector used in combination with the high intensity of this peak. This approach for filtering the  $\delta D$  data was first described and used by Eldridge et al. (2019) and is based on the evaluation of each sub-integration using the z-score (the number of standard deviations away from the mean value). The z-score in this case for the number of sub-integrations (n) can be calculated with the following equation:

$$z = \sqrt{2} \times erf^{-1} \left( 1 - \frac{1}{n} \right) \quad (3.1)$$

Where  $erf^{-1}$  is the inverse error function erf, which can be given by the following equation:

$$\operatorname{erf}(z) = \frac{2}{\sqrt{\pi}} \int_{0}^{z} e^{-t^{2}} dt$$
 (3.2)

In order to apply the filtering, we evaluate the ratio for each sub-integration ( $R_i$ ) in comparison to the third maximum ratio in the distribution ( $R_{3rd,max}$ ), which was used as a compromise by Eldridge et al. (2019) between detecting successfully the outliers and minimising the amount of data points falsely detected as outliers. The difference between the  $R_{3rd,max}$  and the  $R_i$  is divided by the expected standard deviation ( $\sigma_{CS}$ ) from the counting statistics and from other sources of error. As for this measurement we use a CDD ion counter, and assume that the Johnson-Nyquist noise and the dark noise are negligible. Therefore, in this scenario we consider the counting statistics to be the only source of noise.

$$\frac{R_{3rd,max} - R_i}{\sigma_{CS}} \ge 2 \times z \tag{3.3}$$

Using equations 3.1 and 3.2, we expect any ratio for each sub-integration that fulfil the following condition to be considered as an outlier (Eldridge et al., 2019):

$$R_i \le R_{3rd,max} - 2 \times \sqrt{2} \times erf^{-1} \left( 1 - \frac{1}{n} \right) \times \frac{\sqrt{i_{12CH3D} \times t_i}}{i_{12CH4}}$$
 (3.4)

The terms  $i_{12CH3D}$  and  $i_{12CH4}$  are referring to the intensities of  $^{12}\text{CH}_3\text{D}$  and  $^{12}\text{CH}_4$  in counts per second (cps), while  $t_i$  is the integration time and n the number of integrations.

According to Eldridge et al. (2019), this data filtering approach improves the internal precision for their instrument of approximately 25%. However, in SUERC our data suggest significant but more moderate improvements of 10-20%, possibly due to the use of the CDD instead of the Faraday cup for this measurement. Essentially, the CDD provides lower noise compared to the Faraday cup.

The calculation of  $\delta^{13}$ C and  $\delta D$  is based on the general forms of equations 2.1 & 2.2 (Chapter 2). Previous measurements by Stolper et al. (2014a) and Eldridge et al. (2019) account for signal contribution of  $^{13}$ CH<sub>3</sub><sup>+</sup> and  $^{12}$ CH<sub>2</sub>D<sup>+</sup> onto the signal of  $^{12}$ CH<sub>4</sub><sup>+</sup>, which requires "fragmentation" corrections. As the mass resolving power of the SUERC instrument is sufficient to measure on the shoulder of the m/z=16 peak this correction is not required. Instead, the  $\delta^{13}$ C and  $\delta D$  have been calculated using the following equations:

$$^{13}R_{sample} = (\frac{\delta^{13}C_{sample}}{1000} + 1) \times ^{13}R_{wg} (3.5)$$

$$\delta^{13}C = \left( \left( \frac{{}^{13}R_{sample}}{{}^{13}R_{VPDB}} \right) - 1 \right) (3.6)$$

Where  ${}^{13}R_{VPDB} = 0.01118$  (Chang and Li, 1990), and  ${}^{13}R_{sample}$  is the  ${}^{13}C/{}^{12}C$  ratio of the sample (defined as the measured  ${}^{13}CH_4^+/{}^{12}CH_4^+$  ratio).

While the equations for the calculation of  $\delta D$  can be found below:

$$^{2}R_{sample} = (\frac{\delta D_{sample}}{1000} + 1) \times {^{2}R_{wg}}$$
 (3.7)

$$\delta D = \left( \left( \frac{{}^{2}R_{sample}}{{}^{2}R_{VSMOW}} \right) - 1 \right)$$
 (3.8)

In this case,  ${}^2R_{VSMOW} = 0.00015576$  (Xie et al., 2018), and  ${}^2R_{sample}$  is the D/H ratio of the sample (defined as the measured  ${}^{12}\text{CH}_3\text{D}^+/{}^{12}\text{CH}_4^+$  ratio).

Both  $^{13}R_{wg}$  and  $^2R_{wg}$  are the calibrated ratios for the working gas, as calculated for the SUERC gas with  $\delta^{13}C = -42.1\%$  (VPDB) and  $\delta D = -184.4\%$  (VSMOW). All bulk isotopic compositions are expressed in permil (‰).

#### 3.6.2.2. Clumped isotopic compositions

Using the results of the equilibration experiments (3.6.1) the clumped isotopic composition of sample can be calculated. For any further calculations hereafter, I use the values calculated for the working gas,  $\Delta^{13}\text{CH}_3\text{D}_{wg} = 2.4\%$  ( $\pm$  0.3%) and  $\Delta^{12}\text{CH}_2\text{D}_{2wg} = 1.0\%$  ( $\pm$  1.8%), against the absolute thermodynamic frame.

The background measurements are described in sections 3.5.2 - 3.5.4 along with the measurements of the clumped isotopologues. As for the bulk isotopic compositions, the background signal is measured for each detector away from any peaks and for both gases measured (sample and working gas). Then the measured background signal is deducted from the signal measured from each isotopologue of interest and for each gas.

In this case, we do not perform a sophisticated filtering as previously described for the  $\delta D$  measurement, even when  $^{12}CH_2D_2^+$  is measured by the narrow H4 detector used for the  $^{12}CH_3D^+$ . Using the filtering approach for the  $^{12}CH_2D_2^+$  measurement, based on z-score, only removes a small fraction of data (<0.2%), which does not result to significantly higher precision. This finding agrees with the figures reported in Eldridge et al. (2019). Instead, we use both for  $\delta^{13}CH_3D$  and  $\delta^{12}CH_2D_2$  measurement, a simple filter by flagging any data falling

beyond  $3\sigma$  (standard deviation)away from the average value as outliers. This improves the final precision by less than 10% and 10-20% for the  $\delta^{13}CH_3D$  and  $\delta^{12}CH_2D_2$  measurements, respectively.

Because the peak of  $^{12}\text{CH}_2\text{D}_2^+$  is not fully resolved from the adjacent peaks of  $^{13}\text{CH}_3\text{D}^+$  and  $^{13}\text{CH}_5^+$  (Figure 3.7), we need to apply corrections to account for the signal contribution from those peaks (known as "tailing effect"). For this reason, initially the tailing of the  $^{13}\text{CH}_3\text{D}^+$  and  $^{13}\text{CH}_5^+$  was monitored before every measurement of the  $\delta^{12}\text{CH}_2\text{D}_2$ . We assess the tailing by magnet scans where we monitor the position of the  $^{13}\text{CH}_3\text{D}^+$  and  $^{13}\text{CH}_5^+$  peaks relatively to the  $^{12}\text{CH}_2\text{D}_2^+$  peak. Typically, the  $^{13}\text{CH}_3\text{D}^+$  and  $^{13}\text{CH}_5^+$  peaks are located approximately -  $0.003 \pm 0.0003$  amu and - $0.0013 \pm 0.0002$  amu from the measurement position for  $^{12}\text{CH}_2\text{D}_2^+$ . Additionally, the signal intensities of  $^{13}\text{CH}_3\text{D}^+$ ,  $^{13}\text{CH}_5^+$  and  $^{12}\text{CH}_2\text{D}_2^+$  peaks are monitored, including also the background intensity (off-peak) at +0.1 amu from the  $^{12}\text{CH}_2\text{D}_2^+$ . All values are noted, as the background signal of  $^{12}\text{CH}_2\text{D}_2^+$  consists of three terms:

$$b_T = b_{off-peak} + b_{13CH3D} + b_{13CH5}$$
 (3.9)

The first term  $b_T$  refers to the total background,  $b_{off-peak}$  corresponds to the signal at +0.1 amu from the peak, the second and third term  $b_{13CH3D}$  and  $b_{13CH5}$  refer to the to the tailing signal contributions by  $^{13}\text{CH}_3\text{D}^+$  and  $^{13}\text{CH}_5^+$ .

The  $H_2^{16}O^+$  peak is located at approximately -0.3 amu from the  $^{13}CH_3D^+$ ,  $^{13}CH_5^+$  and  $^{12}CH_2D_2^+$  peaks. It used as a model (as all the peaks should have a similar shape) of a fully resolved peak shape. In this case, we monitor the intensity of the  $H_2^{16}O^+$  peak and the intensities away from the centre of the peak, at distances equal to those between  $^{12}CH_2D_2^+$  and  $^{13}CH_3D^+$  or  $^{13}CH_5^+$ . Those are used to calculate the tailing contribution from each adjacent peak:

$$b_{13CH3D} = (i_{13CH3D} - b_{off-peak}) \times tf_{13CH3D}$$
 (3.10)

$$b_{13CH5} == (i_{13CH5} - b_{off-peak}) \times t f_{13CH5} \quad (3.11)$$

Where the tailing factors  $tf_{13CH3D}$  and  $tf_{13CH5}$  can be calculated from the following equation using the intensities measured at the water peak:

$$tf_x = \frac{i_{tail} - b_{off-peak}}{i_{H20} - b_{off-peak}} \quad (3.12)$$

Where the  $i_{tail}$  corresponds to the intensities measured at the tail of  $H_2^{16}O^+$  beam (each correspond to either  $^{13}CH_3D^+$  or  $^{13}CH_5^+$  according to the distance measured), while the  $i_{H20}$  to the intensity measured at the peak of the water beam.

This correction scheme was firstly outlined by Xie et al. (2019) and described thoroughly by Eldridge et al. (2019). The total tailing background calculated in the SUERC Ultra typically varies from 0.4 to 0.6 cps, which is 0.4 to 0.6% of the 100 cps signal intensity of <sup>12</sup>CH<sub>2</sub>D<sub>2</sub><sup>+</sup>. The tailing background has been monitored over the measurement period (~2 months) of natural samples and experimental products and has been consistent within the range reported (Chapter 4). A flow chart describing the data processing required for each measurement can be found in the Appendix.

The clumped isotopic signatures are expressed compared to the stochastic distribution (equations 2.35 & 2.36), we need first to calculate the ratios of the stochastic distribution for any sample:

$$^{13CH3D}R_{sample,stoch} = 4 \times ^{13}R_{sample} \times ^{2}R_{sample}$$
 (3.13)  
$$^{12CH2D2}R_{sample,stoch} = 6 \times (^{2}R_{sample})^{2}$$
 (3.14)

Where the numbers 4 and 6 correspond to the 4 and 6 isotope configurations which are possible for each isotopologue. Combining equations 2.35, 2.36, 3.13 and 3.14 results in:

$$\Delta^{13}CH_3D = 1000 \times \left[ \frac{{}^{13CH3D}R_{sample}}{4 \times {}^{13}R_{sample} \times {}^{2}R_{sample}} - 1 \right] (3.15)$$

$$\Delta^{12}CH_2D_2 = 1000 \times \left[ \frac{{}^{12CH2D2}R_{sample}}{6 \times ({}^{2}R_{sample})^{2}} - 1 \right] (3.16)$$

The terms  $^{13CH3D}R_{sample}$  and  $^{12CH2D2}R_{sample}$  can be calculated using the following:

$$^{13CH3D}R_{sample} = \left(\frac{\delta^{13}CH_3D}{1000} + 1\right) \times ^{13CH3D}R_{wg}$$
 (3.17)

$$^{12CH2D2}R_{sample} = \left(\frac{\delta^{12}CH_2D_2}{1000} + 1\right) \times ^{12CH2D2}R_{wg}$$
 (3.18)

While the quantities  $^{13CH3D}R_{wg}$  and  $^{12CH2D2}R_{wg}$  can be calculated from the clumped isotopic composition of the working gas (in the absolute thermodynamic frame) which is known from the equilibration experiments, and the stochastic distribution of the working gas.

## 3.6.3. Error Propagation

In order to constrain the error of the clumped isotopic compositions  $\Delta^{13}\text{CH}_3\text{D}$  and  $\Delta^{12}\text{CH}_2\text{D}_2$ , we need to consider the uncertainties for each measurement. For example, the bulk isotopic compositions are used to calculate the stochastic distribution (Section 3.6.2), and hence the clumped isotopic signatures. Therefore, the uncertainties of those measurements contribute to the error of the clumped isotopic signatures.

There are different approaches used in isotope geochemistry to propagate the errors of the isotopic compositions of interest. An analytical deterministic approach considers the uncertainty for each variable which is transferred over the calculations to propagate the uncertainty of the quantity of interest (McGraw-Hill, 2003; Stefan and Trappitsch, 2023). In the general form, the variance for a quantity of interest X, is a function of the variances of the input variables f,g,h:

$$\sigma_X^2 = (\frac{\partial X}{\partial f})^2 \times \sigma_f^2 + (\frac{\partial X}{\partial g})^2 \times \sigma_g^2 + \dots + 2\left(\frac{\partial X}{\partial f}\right) \left(\frac{\partial X}{\partial g}\right) \times \sigma_{fg} + \dots \quad (3.x)$$

Therefore, to propagate the errors for the isotopic composition of interest with this method we would need to solve the partial derivatives. Although this approach can produce accurate results, it can be complex and time consuming to use. For this reason, I have adopted a an approach based on a of Monte Carlo simulation for error propagation of geochemical quantities (Anderson 1976). The simulation is a probabilistic model which uses random sampling of variables to predict possible outcomes. They have been used widely in isotope geochemistry for error propagation of isotopic signatures as it is considered an effective, versatile and simple approach (Skrzypek et al., 2010; Lloyd et al., 2021; Stephan and Trappitsch, 2023).

For our application, we use the uncertainties of our mass spectrometry measurements to calculate the uncertainties in the clumped isotopic compositions. The Monte Carlo simulation requires the definition of a probability distribution where the random numbers will be drawn from, to run the simulation. In this aspect, I choose a Gaussian distribution for each variable as we expect all the possible values for a single variable to be equally probable (within uncertainty). I run 10<sup>5</sup> iterations, using the mean value for each measured variable

and the standard error of the measurement. For each set we calculate the resulting clumped isotope compositions, and then we can examine their distribution, and report their average and standard deviation. Similar approaches have been used for the clumped isotopic compositions of methane by Eldridge et al. (2019) and clumped isotopic composition of methyl groups by Lloyd et al. (2021).

The calculation of the bulk and clumped isotopic compositions follows a similar framework described in the previous section (see section 3.6.2). For the error propagation of the bulk isotopic compositions the Monte Carlo simulations for the isotopic compositions measured against the working gas using the standard error of the measurement, and the bulk isotopic compositions using the equations (3.5) and (3.7) are calculated. The mean value of the distribution is calculated, while the propagated error is expressed as the standard error of the distribution. The final calculated errors for both  $\delta^{13}$ C and  $\delta$ D are usually 0.01-0.03% and 0.1-0.12%, respectively. Typically, the calculated propagated error for the bulk isotopic compositions is almost identical (within 1%) to the standard error of the measurement. This is expected as the bulk isotopic compositions are only dependent on the result of the measurement and not affected by other variables.

The error propagation for the clumped isotopic compositions is achieved by running Monte Carlo simulations around the measured mean values of  $\delta^{13}CH_3D$  and  $\delta^{12}CH_2D_2$ , considering the standard error of those measurements and the uncertainties for the bulk measurements as calculated from the Monte Carlo simulation. The clumped isotopic compositions are calculated by equations 3.15 and 3.16 and the stochastic distributions used are calculated using the distributions calculated for the bulk isotopic ratios from the Monte Carlo simulations. The final calculated errors for both  $\Delta^{13}CH_3D$  and  $\Delta^{12}CH_2D_2$ , usually do not exceed the measurement internal precision ( $\delta^{13}CH_3D$  and  $\delta^{12}CH_2D_2$ , respectively) by more than 10-20%. The propagated error, usually, for each measurement is ~0.3% for and ~2.0% for  $\Delta^{13}CH_3D$  and  $\Delta^{12}CH_2D_2$ , respectively.

# 4. Origin of Methane in Virginia gas field

## 4.1 Introduction

Methane is a potent greenhouse gas produced by natural processes and anthropogenic activities, present in the atmosphere, subsurface, marine environments and freshwater systems (Kirsche et al., 2013; Saunois et al., 2024). Ambient atmospheric methane concentrations reached 1932 ppb in 2024 (Lan et al., 2024), which is approximately 2.6 times higher than pre-industrial levels (Saunois et al., 2024). Methane is also the main constituent of natural gas, a fossil fuel projected to be in the energy mixture even beyond 2100 under certain scenarios (Dubey et al., 2023). Natural gas is also expected key-role in energy transition through reforming into H<sub>2</sub>, a carbon-neutral energy source (Zhang et al., 2024).

In sedimentary environments, methane is often produced along with oil and gaseous alkanes (ethane, propane, butane and etc) by the thermal decomposition of organic matter. In other settings, CH<sub>4</sub> production is closely associated to H<sub>2</sub> produced through abiotic processes either due to water-rock interactions (e.g serpentisation) or the presence of radiolytic elements (U, Th, K) (Karolyte et al., 2022; Warr et al., 2022; Etiope, 2023). The occurrence of these elements leads to production and potentially to accumulation of noble gases, mainly helium and argon (Greene et al., 2008; Warr et al., 2018). Specifically, helium is an important and rare commodity which is used across several industries from high semiconductor manufacturing or MRI machines, and its supply had undergone several shortages in the last twenty years (Kornbluth, 2022; Siddhantakar et al., 2023).

Due to the environmental and commercial significance of methane and its close association with hydrocarbons, hydrogen and noble gases, it is important to understand the processes which govern the generation, modification and destruction of methane in subsurface accumulations. The carbon and hydrogen stable isotopic compositions of methane (reported as δ<sup>13</sup>C and δD) have been valuable tools to discriminate the origin of the gas and identify post-generation processes (Schoell, 1980; Whiticar et al., 1999; Milkov and Etiope, 2018). Recent developments in mass spectrometry and laser spectroscopy (Eiler et al., 2013; Ono et al., 2014; Young et al., 2017) have allowed the measurement of the abundances of clumped isotopologues (<sup>13</sup>CH<sub>3</sub>D and <sup>12</sup>CH<sub>2</sub>D<sub>2</sub>) which not only offer additional dimensions for source fingerprinting, but also may provide insights into the formation or re-equilibration temperature of methane (Stolper et al., 2015; Wang et al., 2015; Douglas et al., 2017; Young et al., 2017; Giunta et al., 2019; Giunta et al., 2021, Lalk et al., 2022; Labidi et al., 2024).

In this study, I investigate the origin of gas residing within an interconnected and extended fracture network in the southwestern margin (Virginia gas field) of the Witwatersrand basin which overlies the Archean Kaapvaal Craton (Karolyte et al., 2022). The gases have been sampled from the surface, compared to previous studies in this basin which sampled from the mining environments at depths of 800m or deeper (Ward et al., 2004; Sherwood Lollar et al., 2006; Young et al., 2017).

The occurrence of carbon seams and shale led early studies to suggest that methane should be primarily of thermogenic origin with possible addition of coalbed gas from the Karoo and/or mantle-derived abiotic methane (Cook,1998). More recent studies using molecular and isotopic compositions on samples collected in gold mines across the basin, concluded that multiple methane sources occur across the basin (Ward et al., 2004; Sherwood Lollar et al., 2006; Young et al., 2017).

Regional differences in molecular and isotopic composition of gases have been identified across the Witwatersrand Basin. Gas samples from the southwestern (Beatrix, Masimong) and eastern (Evander, Middelbult) mines have generally lower  $\delta^{13}$ C, higher  $\delta$ D and higher C<sub>1</sub>/C<sub>2+</sub> (methane to heavier hydrocarbon ratio) values compared to samples from the northern mines (Kloof, Driefontein, Mponeng, Tau Tona). This suggests that methane in the southwestern and eastern areas is primarily microbial in origin, with a varying but not wellconstrained contribution from either thermogenic or abiotic sources (Ward et al., 2004). In contrast, the northern mines exhibit isotopic signatures and gas compositions more consistent with predominantly abiotic (Fischer-Tropsch-derived) or thermogenic methane, with a smaller microbial contribution that is more apparent in Driefontein mine. Takai et al. (2001), Onstott et al. (2006), Ward et al. (2004), Lau et al. (2016), Magnabosco et al. (2016) and Simkus et al. (2016) studied the microbial communities living in the fracture fluids in Tau Tona, Driefontein and Beatrix mines. These studies identified methanogens (Methanosarcina mazei, Methanosarcina barkeri, Methanobacterium) which can produce methane through the hydrogenotrophic pathway (CO<sub>2</sub> reduction). Simkus et al. (2016) also reported metagenomic and isotopic data confirming the detection of anaerobic methanotrophic archaea, which consume methane as an energy source. Lau et al. (2016) proposed that a whole microbial ecosystem, dominated by sulphur-oxidising denitrifiers, is sustained by methane produced by methanogens and consumed by AOM (anaerobic oxidation of methane) coupled with sulphur reduction. The most recent study by Karolyte et al. (2022) proposed a model that explains the occurrence of gases (mainly He, CH<sub>4</sub>, N<sub>2</sub>) in Virginia gas field, where radioactivity drives the <sup>4</sup>He production through alpha decay while radiolysis produces H<sub>2</sub> which is utilised by methanogens.

In this study, I measure the chemical composition of gases collected at surface wells in the Virginia gas field and the bulk and clumped isotopic compositions of the methane in these gases. The clumped isotopic compositions of CH<sub>4</sub> can differentiate abiotic and microbial gases from thermogenic (Young et al., 2017). Using those tools, I aim to identify the origin of methane in Virginia gas field and constrain the dominant processes within the system.

# 4.2 Geological Context

## 4.2.1 Geology

The Witwatersrand Basin is a large Archean, intracratonic basin filled with volcanosedimentary rocks that overlie a 3.1 Ga-old granitic basement. The Dominion group (3.09 Ga) sits on the basement and consists of sedimentary and volcanic rocks extremely rich in radiogenic uranium (425 to 563 ppm) and thorium (30-40 ppm) (Shango Solutions, 2020). The Witwatersrand Supergroup overlies the Dominion and is sub-divided based on depositional characteristics, into the West Rand Group (2.9 Ga) and the overlying Central Rand Group (2.78 Ga) (Ward et al., 2004). The West Rand Group has a maximum thickness of 5,150 m and is composed of shale, quartzites, sands, argilites with a maximum depth at 7,500 m. The Central Rand Group is mainly composed of quartzites and conglomerates with minor shale and volcanic layers that reach a maximum thickness of 2,900m. The Central Rand Group conglomerates are characterised by high-Au and U contents. The overlying Ventersdorp Supergroup (2.7 Ga) is a mafic volcanic sequence, comprised of tholeitic flood basalt and thinner layers of sandstone (Coward et al., 1995). Between the Ventersdorp Supergroup and the Transvaal Supergroup (2-2.5 Ga) lies the Black Reef which is a quartzite deposit rich in organic matter. The Transvaal Supergroup consists of a thick dolomitic unit and clastic sedimentary rocks (Omar et al., 2003). The Carboniferous Karoo sediments and volcanic rocks (200 Ma) are present in the east and south sections of Witwatersrand Basin (Onstott et al., 2006).

#### 4.2.2 Methane in Witwatersrand

The Witwatersrand basin has been widely studied due to gold, platinum, diamond and uranium exploitation (Kenan and Chirenje, 2016; Cook, 1998). Mining activities started in 1886 in mines such as Mponeng, Kloof, Tau Tona, Driefontein, Evander, Beatrix and Masimong which are amongst the deepest in the world, expanding eventually to as low as 4000 meters below surface level. During the mining activities, methane was detected and

was often the cause of explosions within the mines (Cook, 1998). Those gases were also significantly enriched in helium compared to typical natural gas (Hugo, 1963). Gases emanate towards the surface from dykes, fissures and faults in Witwatersrand basin, and have varying molecular compositions in this area, ranging from almost pure methane (up to 99%) to exceptionally helium-rich (up to 21%) (Ward et al., 2004; Sherwood Lollar et al., 2006; Karolyte el al., 2022), considerably higher than the economic threshold of helium exploitation at 0.1% (Danabalan et al., 2022).

It is important to highlight that this system is atypical and different from conventional (e.g oil and gas fields) and many unconventional gas systems (like shale gas or coalbed methane). For example, there is no obvious source rock in the basin compared to a typical natural gas system, although there is sporadically distributed carbonaceous matter throughout the basin in the form of carbon seams and solid bitumen nodules (Spangenberg and Frimmel, 2001). Additionally, there is no reservoir rock which is often observed in an oil and gas field and the gases reside within fractures, faults and dykes (Mkhabela and Manzi, 2017). The cap rock is believed to be the tillite and dolerites at the base of Karoo Supergroup, which have allowed the gases to accumulate over millions of years. (Lippmann et al., 2003).

#### 4.3 Methods

# 4.3.1 Gas Sampling

I collected gas samples from the Virginia gas field in October 2022 in collaboration with Renergen. Renergen produces liquified natural gas and helium at southwest Witwatersrand basin near the towns of Welkom, Virginia and Theunissen by drilling into fractures, dykes/sills running from west to the east, and faults running from north to south. I collected samples from 12 different surface wells typically extending at depths 300-700m. 11 of those wells are cased (equipped for production) and classified as "blowers" or production wells. Well 2190 is the only uncased and non-production well sampled. It is a simple borehole from which gas emanates into the atmosphere. Typical gas flow rates range from 500,000 to 6,000,000 L/day. These wells were selected to reflect different geological settings (faults, dykes and sills) and the potentially distinct methane sources that might be present, based on the more than a decade experience of Renergen exploration phase and previous research findings (Ward et al., 2004; Sherwood Lollar et al., 2006, Karolyte et al., 2022). Samples were collected in refrigeration-type Cu tubes (60-70cm long, 3/8" inner diameter) attached to a metal rack (aluminium or stainless steel). Both sides of the tube were well-connected with plastic hoses using a pair of adjustable clips to avoid contamination by atmospheric air. The gas was allowed to flush the tubes for 5 to 10 mins, then both ends were simultaneously closed with metal clamps to seal the tubes. The sampling method is described in detail in Gyore et al. (2015). The samples were then transferred to SUERC (Scottish Universities Environmental Research Centre) where all the subsequent analyses were conducted.

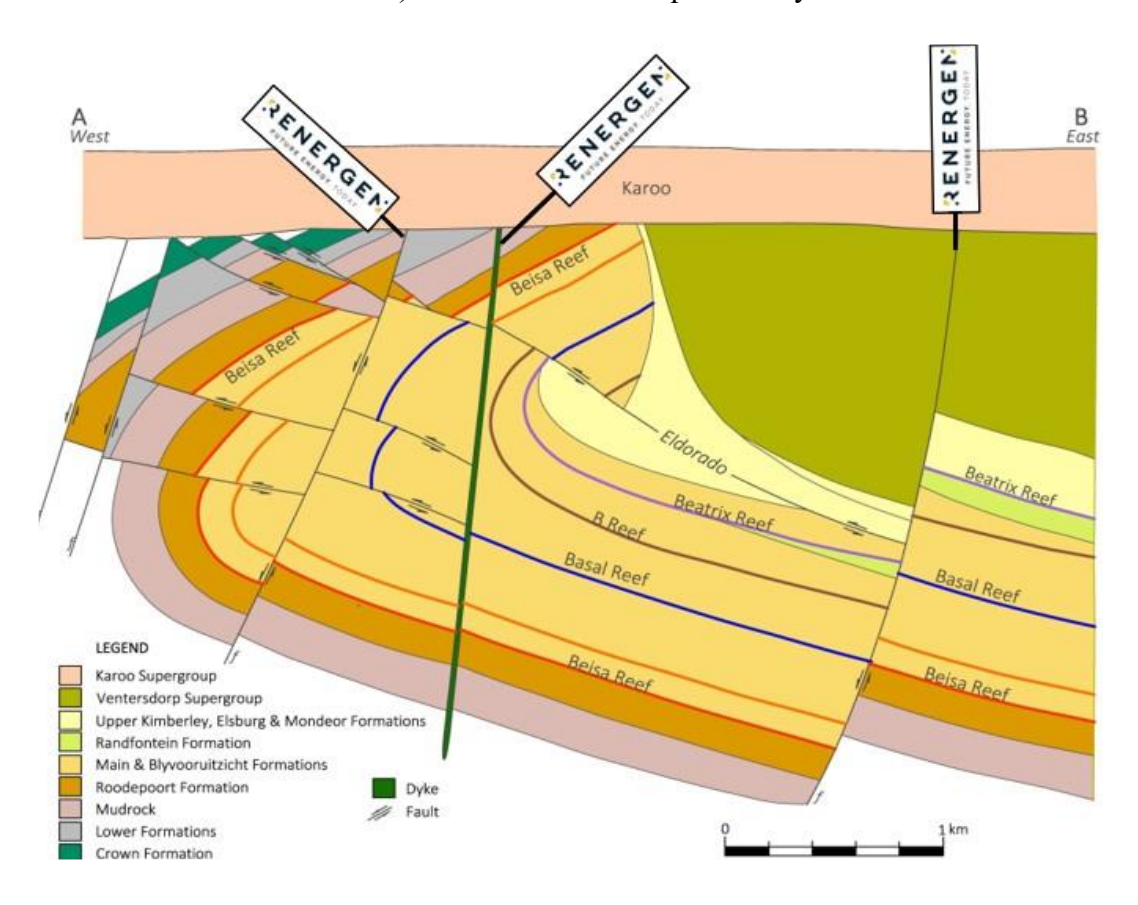


Figure 4.1: Cross-section of wells sampled in Virginia gas field. Figure modified from Turner et al. (2016).

## 4.3.2 Laboratory Methods

For this chapter, I measured the molecular and isotopic composition of the fracture gases. The molecular compositions of the gases were measured using a gas chromatograph. The GC system (Hewlett Packard 5890) has been described in Chen et al. (2019), Chen et al. (2022) and in the Appendix of this thesis.

As a first step, I connected the Cu tubes to the vacuum line, evacuated the connections (connecting the sampling tube to the main line) until the vacuum was approaching the baseline <2.0E-05 mbar. Then, I opened the tube, expanding the gas in a volume equipped with a rubber septum port and waited a minimum of 2 minutes. I sampled through the septum using a gas-tight SGE 100µL syringe (gas was secured with a push-pull valve) and the gas was injected into the GC system. The GC system is using a He-carrier gas and hence, is unable to detect any potential He content found in the gas mixture.

After the gas composition measurement, the gas was expanded towards the headspace of the cryogenic system. The purification of the gases, and the measurement of bulk and clumped isotopic composition proceeded using the methods described in Chapter 3.

# 4.4 Results

## 4.4.1 Gas Compositions

I measured gas compositions for the fracture gases sampled in Virginia gas field. My findings agree with previous studies in adjacent wells and local mines, concluding that these gases are dominated by methane (Ward et al., 2004; Simkus et al., 2016; Karolyte et al., 2022). Previous studies near or within the Virginia gas field, have suggested that the gases are a mixture of three major components: CH<sub>4</sub>, N<sub>2</sub>, He (not measured in this study) followed by traces of CO<sub>2</sub> and C<sub>2+</sub> (Ward et al., 2004; Karolyte et al., 2022).

My measurements show that methane is dominating the gas mixture, with concentrations ranging from 78.9% to 96.4% (average 92.1%). N<sub>2</sub> concentrations range from 3.4% to 21.1% with an average value of 7.6%. CO<sub>2</sub> contents vary between 0% and 0.42% with an average value of 0.08%. All samples, except P15 well, contain C<sub>2</sub>H<sub>6</sub> with average value of 0.17% and maximum value of 0.52%. Only in one sample (EX01 well) C<sub>3</sub>H<sub>8</sub> was detected, with no detection of C<sub>4</sub>H<sub>10</sub> across our dataset.

While the precise quantification of He was not attempted in this study, during the purification of the sample I was able to verify semi-quantitatively its contribution to the gas mixture as it did not condense at 20K during the sample clean-up (see Chapter 2).

Table 4.1: Gas compositions measured for Virginia gas samples. Values normalised to 100%.

Sample	CH <sub>4</sub> (%)	N <sub>2</sub> (%)	CO-	C <sub>1</sub> /C <sub>2+</sub>	He(%)*
			2(%)		
P15	78.90	21.10	-	7890	-
MDR01	93.04	3.67	0.07	1922.4	3.2
СЗРО	94.45	3.73	0.09	873.5	1.7
R2D2	94.63	3.84	0.19	871.6	1.3
NEA02	77.70	10.20	0.08	883	12.0
SPG3	88.66	7.43	0.33	437.5	3.5
EX01	94.03	3.32	0.32	281.9	2.2
PO7	82.77	14.30	0.60	162.4	2.0
ST23	93.18	4.29	0.17	433.5	2.3
HDR01	91.68	6.59	0.19	775.6	1.5
2190A	92.89	7	0	844.4	-

<sup>\*</sup> concentrations are reported based on long-term measurements provided by Renergen and were not conducted in SUERC.

# **4.4.2** Molecular and Isotopic Compositions

Gases from the Virginia gas field exhibit significant variations both in  $\delta^{13}$ C -CH<sub>4</sub> and C<sub>1</sub>/C<sub>2+</sub>. The  $\delta^{13}$ C values of methane range from -41.2‰ to -58.8‰ (against VPDB) and they generally are in good agreement with data from adjacent wells (Figure 4.2) and overlapping with data in the local mines (Ward et al., 2004; Simkus et al., 2016; Young et al., 2017). The C<sub>1</sub>/C<sub>2+</sub> values vary between 162 and 7890 which are in the same range as gases collected from the local gold mines (Beatrix, Masimong, Merriespruit) between 1km and 2km below the surface.

In Figure 4.2, a few measured samples fell within or close the microbial area, whilst the majority of samples fell in the area between the microbial and the abiotic or thermogenic fields. Samples from Virginia are typically distinct in  $\delta^{13}C$  and  $C_1/C_{2+}$  from gases collected at other Witwatersrand mines. Those gases generally plot either in the thermogenic or abiotic field in the  $\delta^{13}C$  vs  $C_1/C_{2+}$  plot (Ward et al., 2004; Sherwood Lollar et al., 2006; Simkus et al., 2016; Nisson et al., 2023).

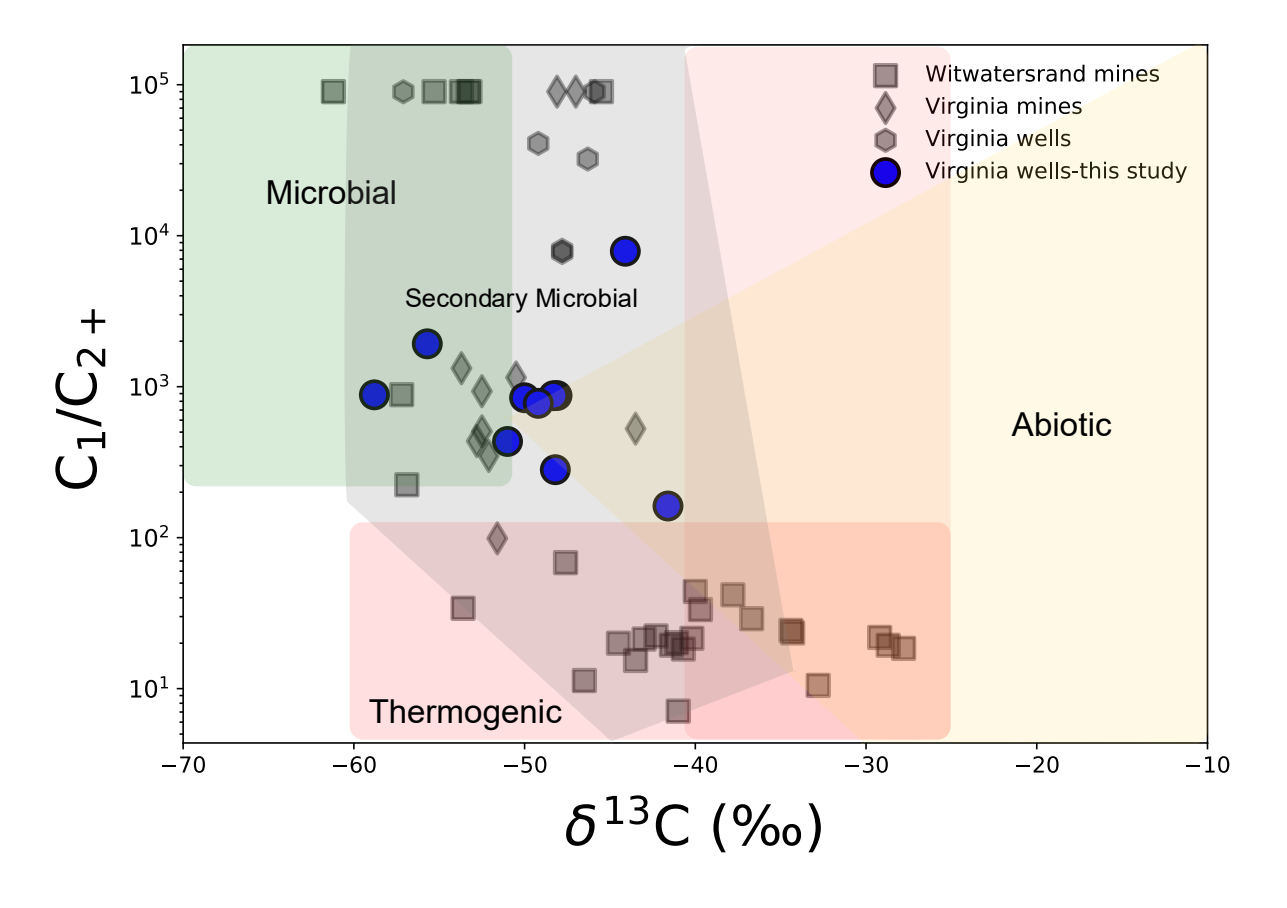


Figure 4.2:  $\delta^{13}$ C (reported against VPDB), against the ratio of abundances (C<sub>1</sub>/C<sub>2+</sub>) of methane (C<sub>1</sub>) and higher hydrocarbons such as ethane, propane, butane (C<sub>2+</sub>). This is a compilation of data from this study (blue dots), data from Karolyte et al., (2022) (navy dots) for Virginia wells, data from local gold mines (Virginia mines) such as Beatrix, Masimong, Merriespruit from Ward et al., (2004) and Simkus et al. (2016) (grey diamonds), and data from Witwatersrand coal and gold mines such as Evander, Middelbult, Driefontein, Kloof, Mponeng, Tau Tona, Moab Khotsong from Ward et al. (2004), Sherwood Lollar et al. (2006), Simkus et al. (2016), Nisson et al. (2023) (grey squares) Samples with C<sub>1</sub>/C<sub>2+</sub> above 100,000, have been capped at this value. The microbial (dark green), thermogenic (red) and abiotic (yellow) areas are designed based on review by Milkov and Etiope (2018).

The  $\delta D$  values of methane shows limited variation from -215% to -226% (against VSMOW), which is relatively small given the large range of  $\delta D$  of methane across the Witwatersrand basin from -180% to -420% (Ward et al., 2004; Sherwood Lollar et al., 2006; Simkus et al., 2016; Young et al., 2017; Nisson et al., 2023). The  $\delta D$  values measured in this study are in good accordance with the values reported by Karolyte et al. (2022), ranging from -217% to -231%. While the well gases have a similar  $\delta^{13}C$  range with those measured for local mines, the  $\delta D$  values differ. The  $\delta D$  values of methane collected from local mines in Virginia, are typically between -180% and -200% with an average value of -196% which is 26% higher than the average value of well gases (~-222%).

Overall, the Virginia well and mine samples are falling between the microbial carbonate reduction (hydrogenotrophic methanogenesis) and the thermogenic/abiotic genetic fields (Figure 4.3). All the Virginia gases differ from the samples analysed from the deeper Witwatersrand mines which are generally higher in  $\delta^{13}$ C (-28‰ to -42‰) and considerably lower in  $\delta$ D (-250‰ to -420‰). These gases are falling in the abiotic and thermogenic genetic fields in the  $\delta$ D-  $\delta^{13}$ C plot (Ward et al., 2004; Sherwood Lollar et al., 2006; Simkus et al., 2016; Young et al., 2017; Nisson et al., 2023).

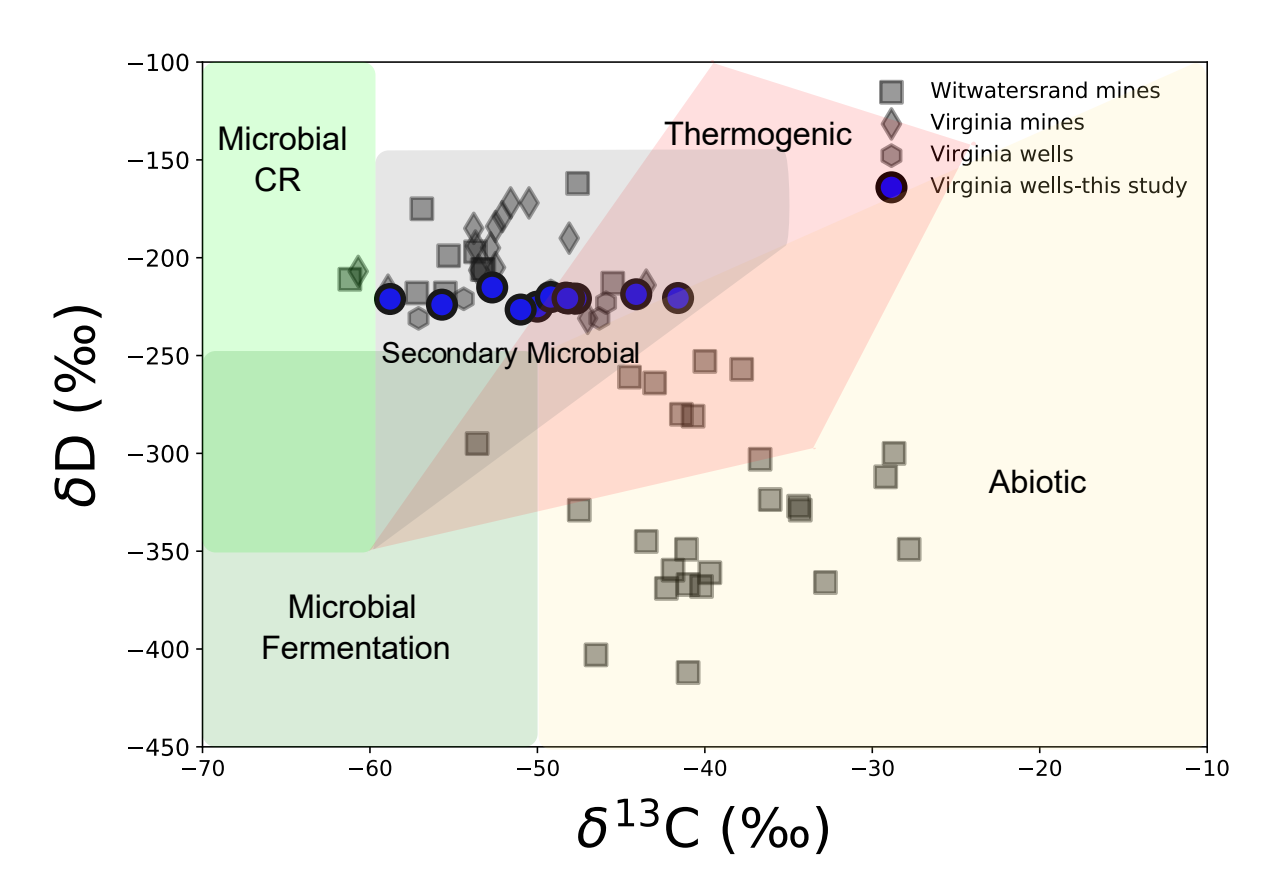


Figure 4.3:  $\delta^{13}$ C (reported against VPDB) versus the isotopic composition of hydrogen in methane,  $\delta D$  (reported against VSMOW). Symbols and fields derived from same sources as in Figure 4.2.

## 4.4.3 Clumped Isotopic compositions

Samples from the Virginia gas field display a significant variability in  $\Delta^{13}$ CH<sub>3</sub>D from 6.7% to 13.6% (1s.e ~0.35). This range is one of the widest reported in natural settings to date. The majority of samples are within analytical uncertainty from each other at approximately ~7% and three samples above 8% (8.5-13.6%) in  $\Delta^{13}$ CH<sub>3</sub>D. A relatively small variability is observed in  $\Delta^{12}$ CH<sub>2</sub>D<sub>2</sub> from 6.8% to 20.8% (1s.e ~2.0%), where most data points fell within 1s.e from ~11%, except for a single point at 20.8% and one at 6.8% (Figure 4.4).

Typically, the  $\Delta^{13}$ CH<sub>3</sub>D ranges in natural settings and laboratory experiments from -5‰ to 7‰ (rarely up to 15‰, Giunta et al., 2019) and exhibits overall smaller variation than  $\Delta^{12}$ -

CH<sub>2</sub>D<sub>2</sub> which can range from -40‰ to 40‰ (Young et al., 2017; Liu et al., 2023; Sivan et al., 2024), and in specific cases above 60‰ (Giunta et al., 2019).

All data points from the Virginia gas field are below and to the right of the thermodynamic equilibrium curve. In previous studies microbial, thermogenic and abiotic gases plot either on the thermodynamic equilibrium curve or depleted in  $\Delta^{12}\text{CH}_2\text{D}_2$  compared to the equilibrium curve. In most cases, microbial and abiotic gases display larger offsets from equilibrium for  $\Delta^{12}\text{CH}_2\text{D}_2$  than for  $\Delta^{13}\text{CH}_3\text{D}$  (Young et al., 2017; Giunta et al., 2019; Giunta et al., 2020; Sivan et al., 2024). Contrarily, thermogenic gases are often on or close to the equilibrium line, although that it is possibly dependent on the maturation stage of the gas (Dong et al., 2021). Consequently, the greater part of the Virginia gases falls away from the "traditional" source areas based on previous data plotted in the  $\Delta^{12}\text{CH}_2\text{D}_2$  vs  $\Delta^{13}\text{CH}_3\text{D}$  space.

Young et al. (2017) measured gases collected from the gold mines of the wider Witwatersrand basin, which all exhibited disequilibrium signatures. This study included data points from local mines (Beatrix and Masimong) and other Witwatersrand mines such as Kloof and Tau Tona located at the north margin of the basin. Well gases from Virginia were completely distinct in  $\Delta^{12}\text{CH}_2\text{D}_2$  and  $\Delta^{13}\text{CH}_3\text{D}$  from the gases collected from the northern mines (Figure 4.4). The gases from Virginia wells are similar to the ones from local Virginia mines in most cases, with four samples falling within 2 S.E from the values reported in Young et al. (2017).

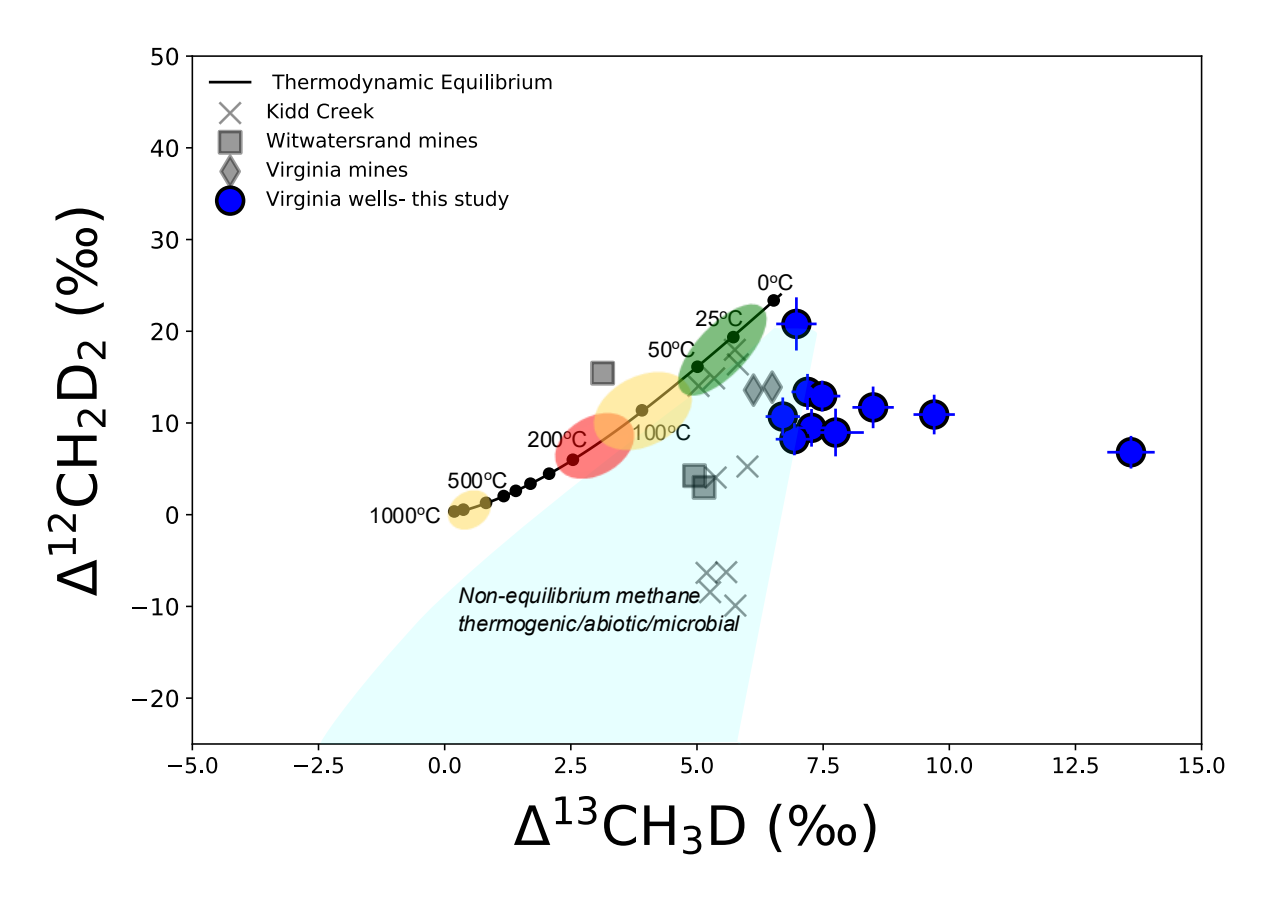


Figure 4.4: Clumped isotopic compositions (Δ¹³CH₃D vs Δ¹²CH₂D₂) for gases from this study (Virginia wells- blue dots), samples from Virginia mines (Beatrix and Masimongorange squares) and Witwatersrand mines (Kloof, Tau Tona- grey squares) reported in Young et al. (2017). Microbial (green), low temperature abiotic (yellow), thermogenic (red) areas are plotted based on previous studies (Young et al., 2017). Microbial area plotted based on mesophiles and thermophiles temperature range (15°C-65°C). Abiotic methane area refers to low temperature methanation by Fischer- Tropsch reactions typically below 120 °C (Etiope, 2013).

#### 4.5 Discussion

In this section, I am presenting and discussing physical, chemical and biological processes that are potentially able to explain the results reported in this study, taking into consideration the prevailing geological and environmental conditions of the area of interest.

# 4.5.1 Temporal Evolution of δ<sup>13</sup>C

Several studies have measured the stable isotopic composition of methane along with the molecular composition of the gases sampled close or within the Virginia gas field (Ward et al., 2004; Simkus et al., 2016; Karolyte et al., 2022). I sampled three wells where two of those are identical to a previous study (Karolyte et al., 2022) and one has been previously measured in SUERC (with a different method) on behalf of Renergen. In all instances, the

 $\delta D$  values reported in this study are within error of the previous measurements (Table 4.2). In contrast, I observed differences in the  $\delta^{13}C$  and  $C_1/C_{2+}$  values measured.

Across the three common boreholes sampled,  $\delta^{13}C$  in this study were systematically lower, with a difference ranging from 0.4‰ in borehole EX01 to 6.1‰ in ST23. An earlier study by Simkus et al. (2016) had identified differences in geochemical parameters (concentrations of alkanes, DOC,  $\Delta^{14}_{DIC}$  value and isotopic composition of H<sub>2</sub>O) over the course of a year, attributed to variations in the geochemical characteristics of the fracture fluid, and secondarily affected by the adjacent mining activities and changes in the microbial activity. The differences in  $\delta^{13}C$  and  $\Delta^{14}_{DIC}$  observed could indicate a varying carbon source or differences occurring within the microbial communities (Simkus et al., 2016). Additionally, I observed that the  $C_1/C_{2+}$  values measured in this study are significantly lower than those reported in Karolyte et al. (2022). For example, the average  $C_1/C_{2+}$  value of our study is of 1493, while Karolyte et al. (2022) reported average  $C_1/C_{2+}$  of 44737. Overall, my data are in a good agreement with the values reported in Ward et al. (2004), with an average  $C_1/C_{2+}$  of 665 for fluids sampled from the adjacent mines of the Virginia area.

While the exact reason of these discrepancies might be difficult to pinpoint precisely, these could occur due to the aforementioned geochemical variations and/or sampling and analytical artifacts. Indeed, our study differs in methodology from the previous ones, as I sampled free-phase gas compared to the fracture fluids sampled in Ward et al. (2004) and Karolyte et al. (2022). Differences in solubility in water across the alkanes could affect the  $C_1/C_{2+}$  values, but the fact that our data lie in the middle of the range reported in the mentioned studies suggests that is unlikely to be the main reason.

Table 4.2: Intercomparison of the molecular and stable isotopic compositions measured for the wells in Virginia from this study, Karolyte et al. (2022) and using conventional IRMS in SUERC.

Borehole	This study	Karolyte et al.	Renergen/SUERC*
		(2022)	
NEA02	$\delta^{13}C = -58.8\%$	NM	$\delta^{13}C = -54.4\%$
	$\delta D = -221.1\%$		$\delta D = -221\%$
	$C_1/C_{2+} = 883$		$C_1/C_{2+} = NM$
ST23	$\delta^{13}C = -51\%$	$\delta^{13}$ C= -45.9‰	NM
	$\delta D = -226.5\%$	δD= -223‰	
	$C_1/C_{2+} = 433.5$	$C_1/C_2 = 89832$	
EX01	$\delta^{13}C = -48.2\%$	$\delta^{13}$ C= -47.8‰	NM
	$\delta D = -220.8\%$	δD= -223‰	
	$C_1/C_{2+}=281.9$	$C_1/C_{2+}=8010$	

NM: Not Measured

#### 4.5.2 Diffusion

Physical processes such as diffusion can alter the bulk and clumped isotopic compositions of methane. In the Virginia gas field, gases can migrate from the subsurface towards the surface through faults, fractures and dykes which act as conduits (Manzi et al., 2012). Karolyte et al. (2022) identified the impact of diffusive loss (preferential loss of He over CH<sub>4</sub>-N<sub>2</sub>) for a few samples collected from the Virginia gas field. I evaluate the effects of diffusion on the relative abundances of methane isotopologues, considering both diffused gas from a larger subsurface reservoir and residual gas affected by previous diffusive loss.

Diffusive loss creates mass fractionation by favouring the abundance of light isotopologues in the diffused gas, while the abundance of heavy isotopologues increases in the residual gas. As a result, I expect a decrease in  $\delta^{13}$ C,  $\delta D$  of the diffused gas, but an increase in  $\Delta^{13}$ CH<sub>3</sub>D and  $\Delta^{12}$ CH<sub>2</sub>D<sub>2</sub> (and vice versa for the residual gas) (Young et al., 2017; Giunta et al., 2021; Lalk et al., 2022). The impact of diffusion on each isotopologue depends only on the molecular masses of the isotopologue and the main component (e.g. water) which the gas is diffusing through. Hence, I expect a 1:1 isotopic fractionation between  $^{13}$ CH<sub>4</sub>- $^{12}$ CH<sub>3</sub>D and  $^{13}$ CH<sub>3</sub>D -  $^{12}$ CH<sub>2</sub>D<sub>2</sub>, as they have the same cardinal mass (17/16, 18/16). An example of a diffusion scenario can be found detailed in Chapter 2.

I calculate the expected variations in bulk and clumped isotopic compositions for both diffused and residual gas, with starting compositions at both end of the  $\delta^{13}$ C range observed

<sup>\*</sup> Unpublished data for measurements conducted in SUERC in 2020 using conventional IRMS with methods described in Chen et al. (2022). Gas sampled from NEA02 was sampled in an identical method as in this study.

in our samples (Figure 4.5). A 50% diffusive loss results in an increase of approximately 10‰ in  $\delta^{13}$ C and  $\delta D$  for the residual gas and an equal decrease for the diffused gas. The opposite fractionation trend is displayed in  $\Delta^{12}CH_2D_2$  and  $\Delta^{13}CH_3D$ , but with only a much smaller 0.55‰ increase/decrease. Considering that Virginia gases exhibit a small range of 10‰ in  $\delta D$  with a variation of 17‰ in  $\delta^{13}C$ , diffusion is unable to account for the large variation in  $\Delta^{13}CH_3D$  (~7‰). This is also supported by general lack of agreement between  $\delta^{13}C$  and  $\delta D$  which should be observed if diffusion at play, as a 1:1 fractionation path is expected. In theory, diffusion could account for smaller variations in in bulk and clumped isotopic compositions, however, it is unlikely to be a dominant process in the current system.

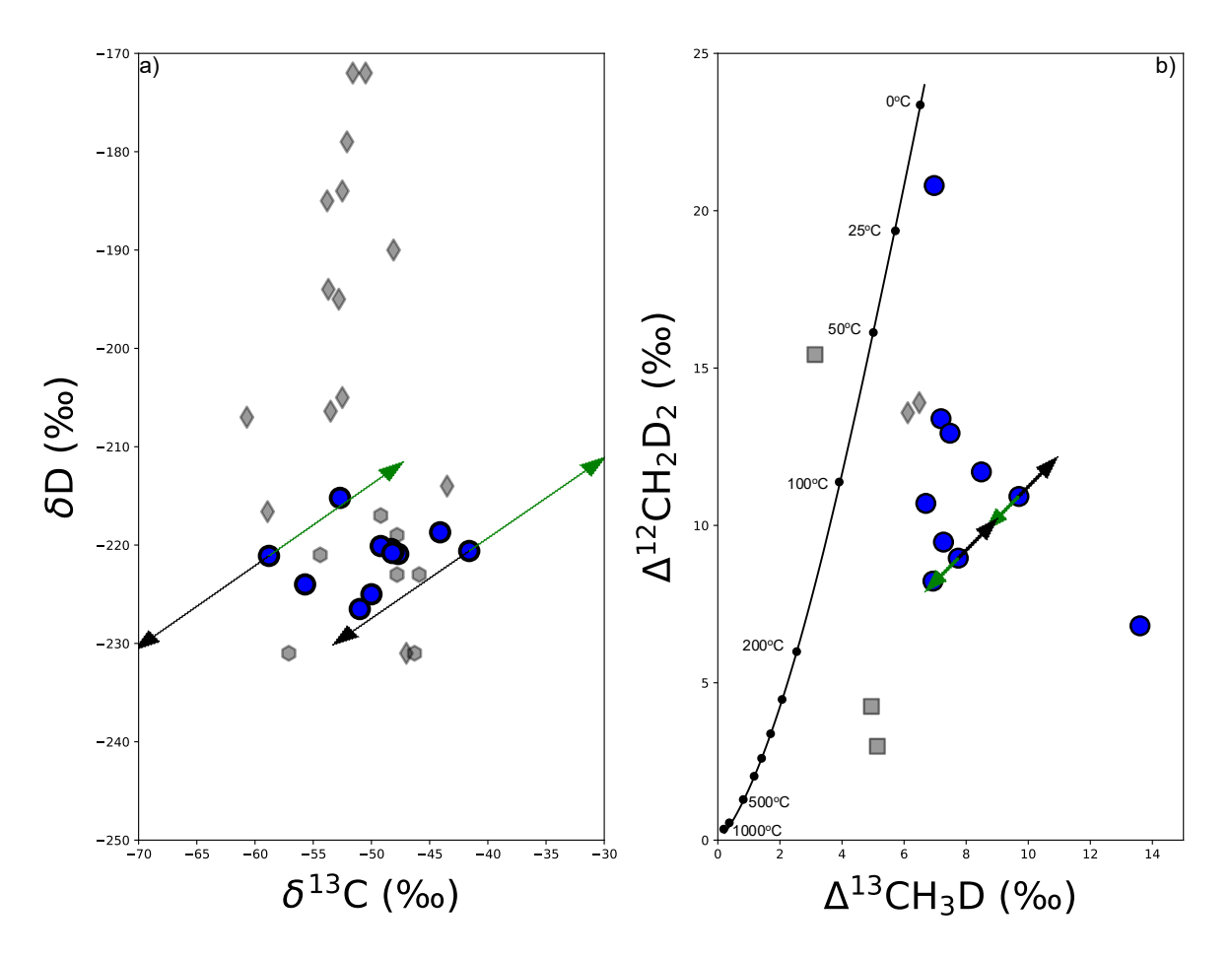


Figure 4.5: Diffusion scenarios considering the isotopic fractionation in bulk and clumped isotopic compositions. Green arrow displays the diffusion trend for the residual gas, while black arrow displays the trend for the diffused gas. All diffusive scenarios are calculated using Graham's law and  $\beta=0.25$  (diffusion through water column). Arrow head's pointing at expected isotopic fractionation trend and indicates 50% loss. Symbols as in Figure 4.2.

# 4.5.3 Isotope Exchange with H<sub>2</sub>O

Methane isotopologues can exchange carbon and hydrogen atoms when in contact with other chemical species found in the subsurface. At geological timescales, CH<sub>4</sub> and H<sub>2</sub>O can

exchange hydrogen atoms with or without the presence of a catalyst in sedimentary and hydrothermal systems (Turner et al., 2022). At temperatures below 120°C, isotope exchange between methane-water (without a catalyst present) requires billions of years (Turner et al., 2022).

Given the small variation of  $\delta D$  and  $\Delta^{12}CH_2D_2$  of the Virginia gases along with the age of the geological formations (>2.0 Ga), one could argue that methane and water have reached isotopic equilibrium over this timescales. I assess this scenario by plotting the clumped isotopologues against the fractionation between methane and water.

The apparent temperatures calculated from  $\Delta^{13}CH_3D$  are below 0°C, and the isotopic contrast (E) between CH4 and H2O indicate disequilibrium between methane and the associated water, as they are not compatible with equilibrium for that isotopologue (Figure 4.6a). In contrast, the Virginia gases fall close on at the isotopic equilibrium curve in the  $\Delta^{12}CH_2D_2$  vs  $\epsilon$  (the isotopic contrast between methane and water) plot. The data could indicate isotopic equilibrium between methane and water at approximately 120°C, which is considerably higher than the current temperatures of 25-30°C at 1km below the ground (Onstott et al., 2007). This may have been possible at the geological past during the cooling of the basin (Nisson et al., 2023). However, I postulate that the Virginia data fall on the equilibrium line coincidentally and not as a result of equilibration between methane and water for two reasons. Firstly, the clumped isotopic compositions demonstrate internal disequilibrium and could not have attained external equilibrium (with H<sub>2</sub>O) when internal equilibrium is not achieved. One could argue that the re-equilibration is taking place at different rates for each clumped isotopologue, however this would require a substantially higher re-equilibration rate for  $\Delta^{12}CH_2D_2$  which is at equilibrium with water compared to the rate for  $\Delta^{13}$ CH<sub>3</sub>D which is far from equilibrium. There is no supporting evidence for such a contrast and given that the isotopic and molecular compositions indicate a dominant microbial origin of the methane, this is unlikely to occur at this temperature range considering the limit of life at 122°C (Patra et al., 2018).

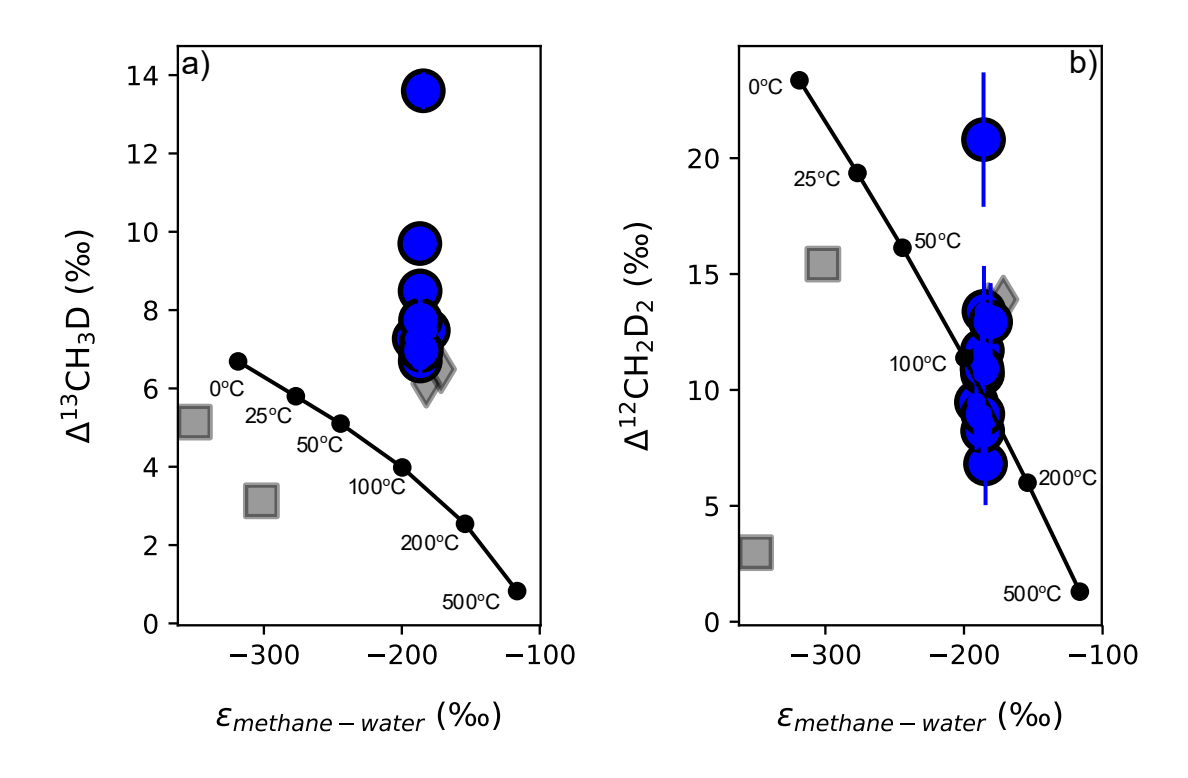


Figure 4.6:  $\Delta^{13}\text{CH}_3D$  and  $\Delta^{12}\text{CH}_2D_2$  plotted vs the fractionation between methane and associated formation waters. This fractionation is reported as  $\epsilon_{\text{methane-water}}$  ( $\epsilon_{\text{methane-water}}$  = (D/H)<sub>methane/</sub>(D/H)<sub>water</sub> - 1). The equilibrium curve is calculated using Horibe and Craig (1995) calibration. No water samples were collected in this study, calculations based on an average value for data reported in Warr et al. (2021) and  $\delta D_{\text{water}}$  = -42‰. Symbols as in Figure 4.1.

#### **4.5.4** Mixing

Bulk and clumped isotopic data, for the gases collected from Virginia gas field, are compatible with more than one sources of methane. In the  $\delta D$  vs  $\delta^{13}C$  and  $C_1/C_{2+}$  vs  $\delta^{13}C$  plots, data falling between the microbial area (hydrogenotrophic methanogenesis) and the thermogenic- abiotic areas are often considered to be the result of mixing (Figure 4.7). According to Milkov and Etiope (2018), this is also the expected range of  $C_1/C_{2+}$ ,  $\delta D$  and  $\delta^{13}C$  for secondary microbial gas (Figure 4.7).

Previous studies in Virginia mines have concluded that the gas is primarily microbial, with a variable contribution from an abiotic endmember (Ward et al., 2004; Simkus et al., 2016; Young et al., 2017), although Karolyte et al. (2022) suggested that the abiotic methane contribution is almost negligible. Ward et al. (2004) suggested that microbial methane is associated with palaeometeoric waters at relatively shallow depths (<2km), while abiotic methane results from rock-water interactions taking place in deeper depths, carried to the surface by hypersaline fluids through an extended and interconnected fracture system. The abiotic endmember was suggested to be identical to the dominant abiotic endmember found

in the wider Witwatersrand area (e.g. Tau Tona, Driefontein, Mponeng mines) at depths of more than 3km. Contrarily, previous studies by Cook (1998) and England et al. (2002), proposed that methane is of thermogenic origin and deriving from the thermal decomposition of the shales found within the Witwatersrand Supergroup. This was based on oil and methane co-occurrence found within fluid inclusions (Drennan and Robb, 2006).

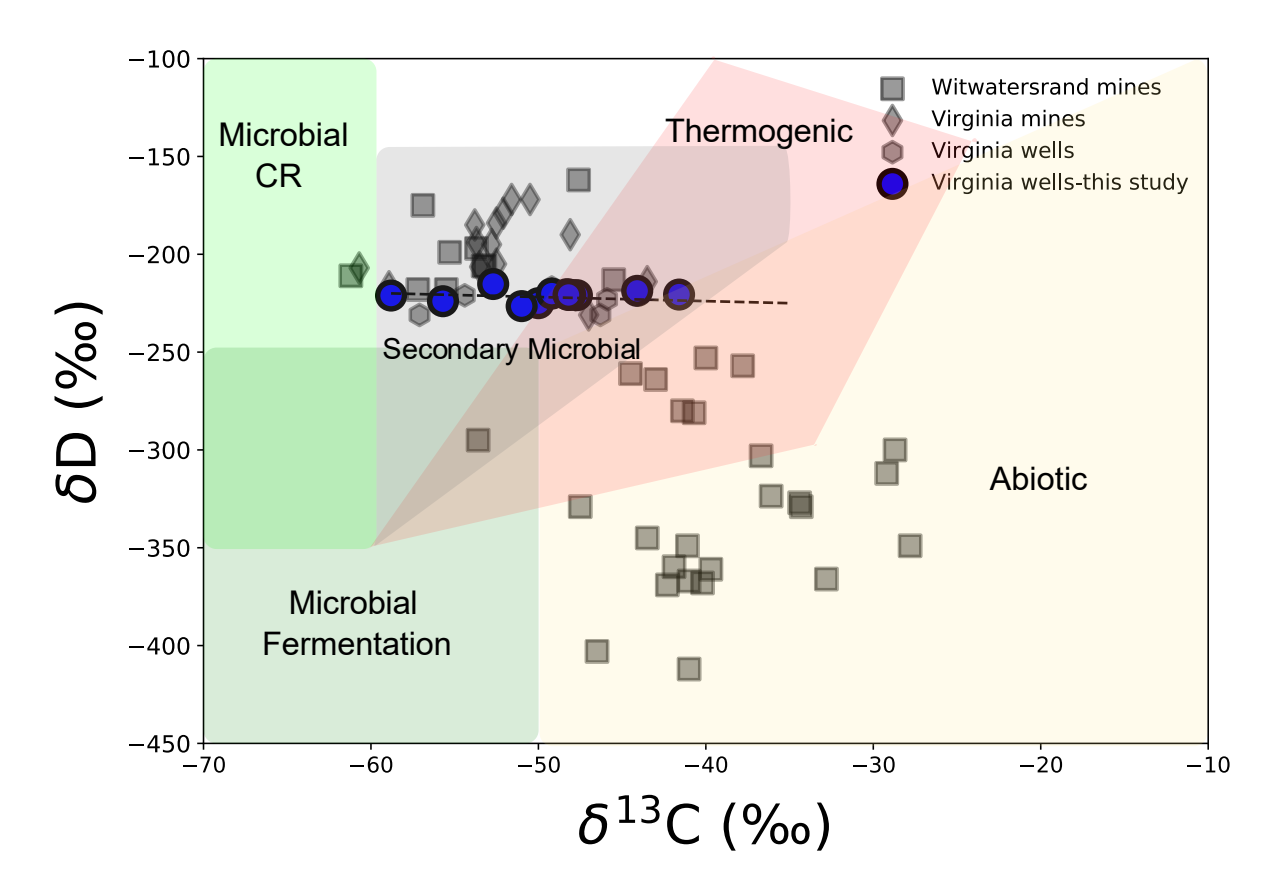


Figure 4.7:  $\delta^{13}$ C (reported against VPDB) versus the isotopic composition of hydrogen in methane,  $\delta D$  (reported against VSMOW). Dashed line indicates the mixing trend proposed.

As discussed in Chapter 2, microbial and low-T abiotic methane often typically have clumped isotope compositions that are not reflecting thermodynamic equilibrium, plotting below the thermodynamic equilibrium curve, with some exceptions (Young et al., 2017; Labidi et al., 2020; Labidi et al., 2024; Sivan et al., 2024). Methane in thermogenic gas however plots on or close to equilibrium at the temperature of methane formation (Young et al., 2017; Thiagarajan et al., 2020). For the microbial methane, the substrate availability and the rate of methanogenesis have been identified as parameters which can affect the bulk and clumped isotopic compositions (Stolper et al., 2015; Ono et al., 2022). In a deep-subsurface environment, such as in Virginia gas field settings, a microbial endmember on or near the equilibrium line at approximately 25-30°C is expected (as the rate of methanogenesis is likely slow with higher degree of reversibility), in contrast to the disequilibrium signatures

found for methane collected in pond and lakes or incubation experiments (where methane production proceeds faster) (Stolper et al., 2015; Young et al., 2017; Wang et al., 2023; Sivan et al., 2024). For the thermogenic endmember, I have considered the findings from Young et al. (2017) for the Kloof gold mine, where CH<sub>4</sub> appeared to be largely thermogenic at approximately 150°C. Given the limited data on abiotic gas in subterranean environments, I use the gases measured at Kidd Creek mine in the Canadian Shield as the best available example of low-temperature abiotic gas for our end-member composition (Sherwood Lollar et al., 2002; Young et al., 2017). In fact, both the Canadian Shield and the Witwatersrand basin are of Archaean age with an extensive network of fractures in the subsurface.

Overall, I conclude that most of the Virginia gases fall closest to the mixing line between the abiotic endmember away from equilibrium and a microbial endmember plotting on the equilibrium curve. The microbial gas appears to be the dominant source in a proportion approximately 70%-30% in most samples. It is important also to note that despite the previous studies by Cook (1998), England et al. (2002), Drennan and Robb (2006), the clumped isotopes suggest a negligible contribution from thermogenic methane.

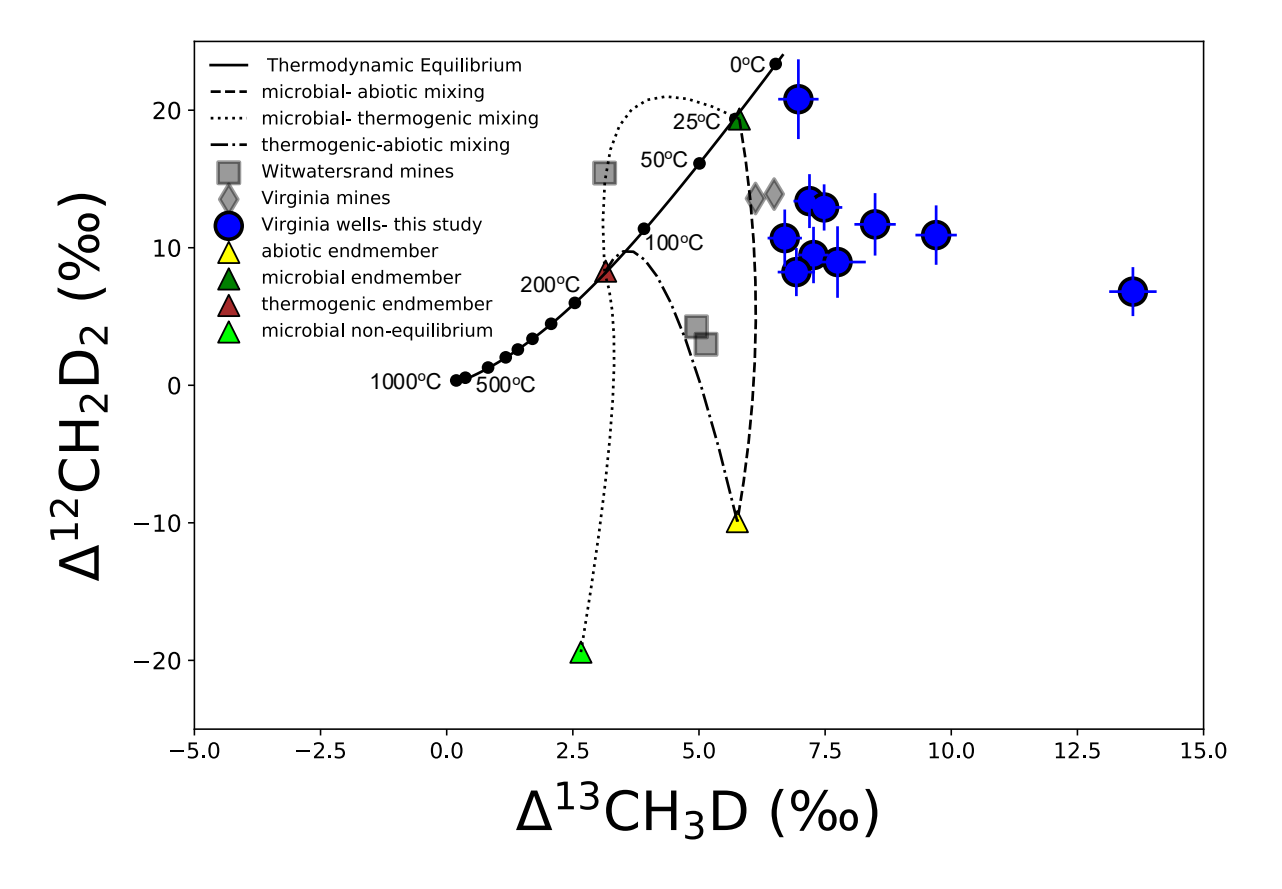


Figure 4.8:  $\Delta^{13}$ CH<sub>3</sub>D vs  $\Delta^{12}$ CH<sub>2</sub>D<sub>2</sub> plot including the mixing lines amongst thermogenic ( $\delta^{13}$ C = -36.1‰,  $\delta$ D = -323.6‰), microbial at equilibrium ( $\delta^{13}$ C = -58.8‰,  $\delta$ D = -220‰), microbial out of equilibrium ( $\delta^{13}$ C = -58.8‰,  $\delta$ D = -220‰), and abiotic ( $\delta^{13}$ C = -35‰,  $\delta$ D = -225‰) endmembers. Clumped isotopic compositions based on the findings by Young et al. (2017) for Kloof mine (thermogenic), Birchtree mine (microbial at

equilibrium), Methanococcus thermolithotrophicus (microbial out of equilibrium), Kidd Creek mine (abiotic). Bulk isotopic compositions from microbial and abiotic endmembers derived from this study.

## 4.5.5 Anaerobic Oxidation of Methane (AOM)

The anaerobic oxidation of CH<sub>4</sub> is another process able to alter the bulk and clumped isotopic compositions of this gas (Ash et al., 2019, Ono et al., 2020; Giunta et al., 2022 ;Liu et al., 2023). Anaerobic methanotrophy is a microbially-mediated process which is performed by methanotrophic archaea (ANME) (Leu et al., 2020). Microbial communities of methanotrophs have been detected in diverse environments such as marine sediments, lacustrine settings, hydrothermal systems and deep terrestrial sediments (Iversen and Jorgensen, 1985; Segarra et al., 2015; Wankel et al., 2012; Lollar et al., 2019; Nishimura et al., 2023).

Methanotrophic communities have been identified across the Witwatersrand basin and specifically, in fluids collected from fault and fracture systems within the gold mining environments at depths beyond 1kmbls (Magnabosco et al., 2014; Simkus et al., 2016; Lau et al., 2016). In those systems, anaerobic methanotrophs comprise only a small percentage (~0.1%) of the microbial communities which are dominated by sulphur reducing bacteria and sulphur oxidizers (Lau et al., 2016). Similar figures are reported for the proportion of ANME in fluids from mining environments (Beatrix mine) within the Virginia gas area at approximately 0.1-0.2% of the total microbial communities (Simkus et al., 2016).

Culture experiments have been used to understand the effect of AOM on methane isotopologues, which is largely controlled by kinetics as lighter isotopes react faster than the heavy ones (Ono et al., 2021; Wegener et al., 2021). This implies that methane processed by anaerobic methanotrophs is progressively enriched in  $^{13}$ C and D. However, this is not always the case as in settings with low electron acceptor availability ( $SO_4^{2-}$ ,  $NO_3^{-}$ ,  $NO_2^{-}$ , etc.), where AOM may deplete the residual gas in heavy isotopes or even not affect the abundance of bulk isotopes depending on the experiment or environmental parameters (Wegener et al., 2021; Liu et al., 2023). Both experimental and natural studies of AOM have shown that  $\Delta^{13}$ CH<sub>3</sub>D and  $\Delta^{12}$ CH<sub>2</sub>D<sub>2</sub> increase simultaneously, not depending on the electron acceptor availability (Giunta et al., 2021; Ono et al., 2021; Giunta et al., 2022; Liu et al., 2023). However, a different trend was identified by Liu et al. (2023) when conducting incubation experiments using fracture fluids from deep biosphere settings from the Beatrix mine in the Virginia gas field. In this incubation experiment by Liu et al. (2023), AOM increased the

 $\Delta^{13}$ CH<sub>3</sub>D value of the residual methane (by 3‰) with limited influence on  $\Delta^{12}$ CH<sub>2</sub>D<sub>2</sub> values and was believed to drive the clumped isotopic signatures towards thermodynamic equilibrium at the reaction/culture temperature, without significant impacts on  $\delta^{13}$ C and  $\delta$ D values (Appendix). This was attributed to potential reversibility of the first step of the reaction, catalysed by the Mcr enzyme, and promoting isotope exchange during the first step of AOM. Liu et al. (2023) constructed a model including only the first step of AOM, believed to be the most reversible, and the concentrations of the 12 isotopologues involved in this reaction.

I apply this model to the data collected in this study, to explore if the variations observed in clumped isotopic signatures are compatible with the effects of AOM. I use the same parameters ( $\phi = 2 \times 10^{-6}$ ) as the ones used in Liu et al. (2023). I identify two possible scenarios:

1. Liu et al. (2023) proposed that methane in Virginia gas field (Beatrix mine) is abiotically produced with initial clumped isotopic composition at or near thermodynamic equilibrium at 200 °C. The equilibrium or near equilibrium Δ¹³CH₃D and Δ¹²CH₂D₂ is erased temporarily by AOM as isotopes are redistributed amongst isotopologues, which results in clumped signatures at thermodynamic equilibrium but this time at the current environmental temperatures approximately at 25-30°C. During the AOM the clumped isotopic compositions exhibit non-equilibrium values. With the proposed parameter (φ), this cannot explain the whole variation in Δ¹³CH₃D observed in this dataset (Figure 4.9). However, by changing the φ parameter and assume one with a smaller degree of reversibility (φ = 5 x 10⁻²) this scenario can be plausible and could explain the variation in our dataset.

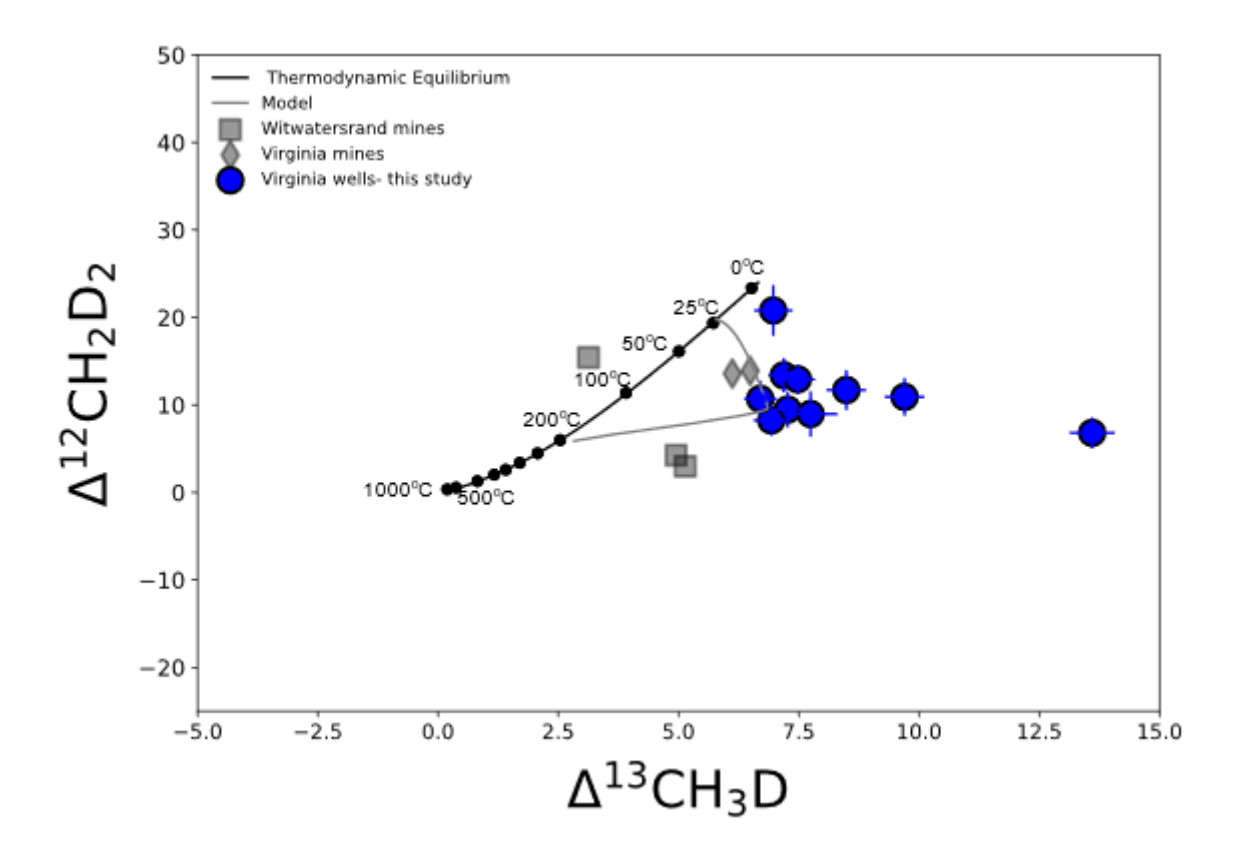


Figure 4.9: Clumped isotopic compositions in Witwatersrand with AOM model. ~1% methane consumption.

2. While the previous scenario cannot be excluded completely, the molecular ( $C_1/C_{2+}\sim1000$ ) and isotopic data ( $\delta^{13}C\sim-60\%$ ) along with previous studies (Ward et al., 2004; Simkus et al., 2016; Karolyte et al., 2022) indicate rather a significant microbial component. This time, I run the model with a starting point set on the mixing curve between microbial and abiotic endmembers as suggested in section 4.5.4. In this case, the model produces the following results:

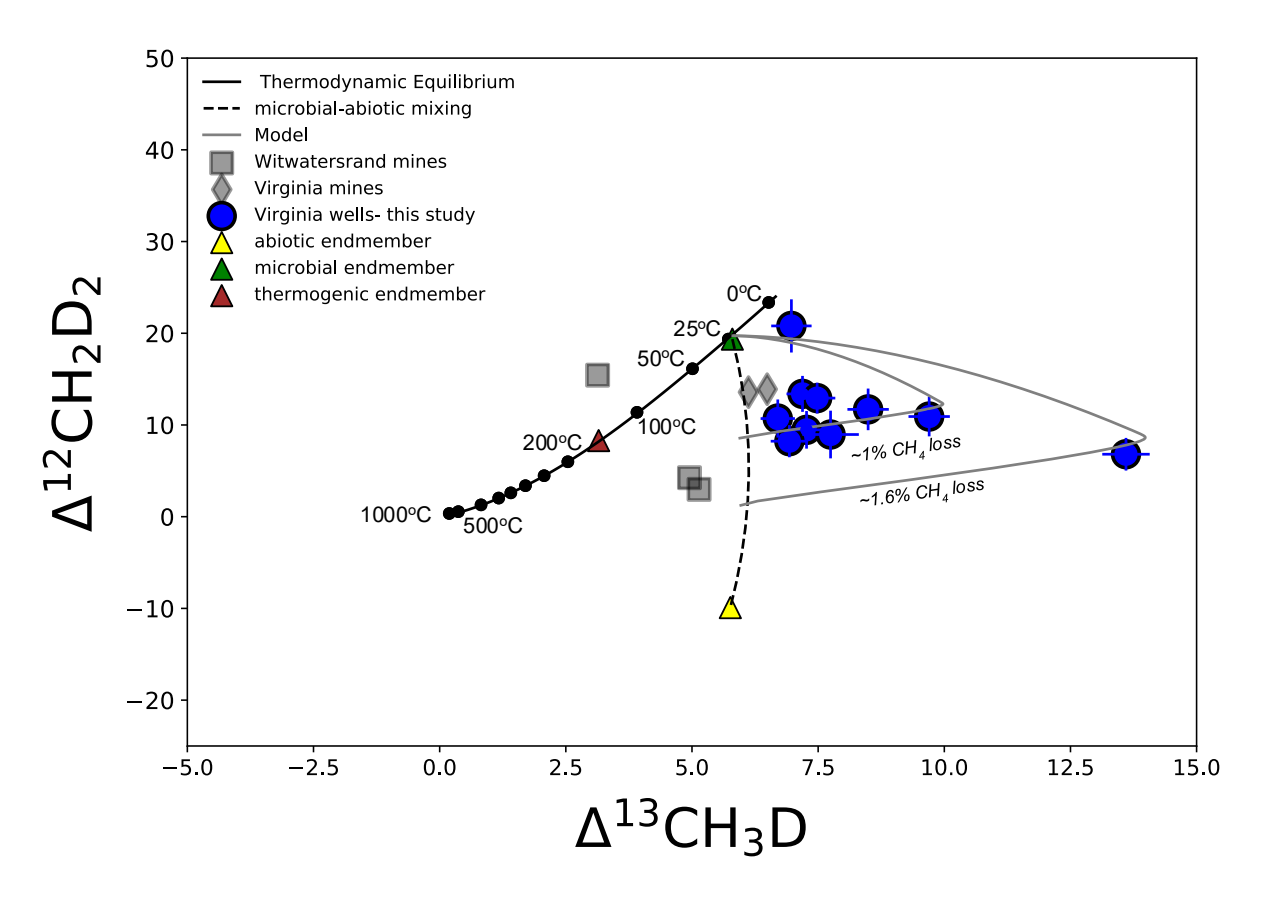


Figure 4.10: Clumped isotopic compositions in Witwatersrand with AOM model. Paths indicate the two scenarios of 1 and 1.6% methane loss due to AOM.

Under this scenario, the  $\Delta^{13}\text{CH}_3\text{D}$  is increasing initially up to approximately 9.7% (3.5% away from the starting point) with little variation in  $\Delta^{12}\text{CH}_2\text{D}_2$ . Subsequently,  $\Delta^{13}\text{CH}_3\text{D}$  is decreasing while  $\Delta^{12}\text{CH}_2\text{D}_2$  is increasing, both towards the thermodynamic equilibrium curve at 25°C (environmental temperature chosen for this scenario, corresponding to 1km below ground level). Most of the samples agree with this interpretation, however there is some variability in  $\Delta^{13}\text{CH}_3\text{D}$  and  $\Delta^{12}\text{CH}_2\text{D}_2$  values not fully consistent with the expected trend from AOM. For example, the sample from well-P15 has the highest  $\Delta^{13}\text{CH}_3\text{D}$  is not compatible with the previous scenario. For this sample, it can be assumed that it is either a result of mixing between a dominant abiotic component (which drives it lower in  $\Delta^{12}\text{CH}_2\text{D}_2$ ) with a minor microbial component, and AOM with different degree of reversibility ( $\phi = 5 \text{ x}$   $10^{-7}$ ) and higher CH<sub>4</sub> or an unknown methane source or process not previously identified.

#### **4.5.6 Model**

In this section, I present a conceptual model of the basin and the related processes taking place, based on findings from this study and previous studies by Omar et al., (2003), Karolyte

et al. (2022). Radiolytic elements, found in high abundances in the Dominion and Witwatersrand Supergroups, undergo radioactive decay which produces <sup>4</sup>He (via alpha decay) and H<sub>2</sub> through radiolysis of the fracture water. Abiotic methane is likely produced by Fischer-Tropsch reactions and associated with the 2.0-2.3 Ga hydrothermal fluid (Ward et al., 2004), which is transported to the surface along with He and H<sub>2</sub> within the fracture fluids. In the geological period before the deposition of the Karoo rock layers, the gases migrated along the fractures and were released into the atmosphere when the rock porosity allowed (Karolyte et al., 2022). This resulted into gas losses, with preferential loss of H<sub>2</sub> and He compared to CH<sub>4</sub> due to their smaller molecular mass (Gilfillan and Stuart, 2020). At that time, methanogenesis is unlikely to have contributed substantially to the methane production because of the high thermal gradient and prevailing temperatures, above the limit of life (122°C) at approximately 70Ma (Omar et al., 2003).

In the post-Karoo period, the tillites and dolerites of Dwyka and Ecca groups of the Karoo sediments acted as a cap-rock and prevented gas escape into the atmosphere, which allowed long-term accumulation over geological periods (Lippmann- Pipke, 2003). While in the northern margin of Witwatersrand basin, the H2 concentrations are exceptionally high in some cases (>10%), the H<sub>2</sub> concentrations in Virginia are often below the detection limit in most wells and mines (Ward et al., 2004). Studies by Ward et al. (2004) and Sherwood Lollar et al. (2006) identified an inverse correlation between  $H_2$  concentrations and  $\delta^{13}C$ , and proposed a scenario where methanogens utilise the radiolytic H<sub>2</sub> and produce microbial CH<sub>4</sub> depleted in <sup>13</sup>C. This microbial CH<sub>4</sub> is mixed within the fractures with the abiotically produced methane at proportions approximately 70:30, however no contribution from thermogenic CH<sub>4</sub> is observed based on the isotopic and molecular compositions. The  $\Delta^{13}$ CH<sub>3</sub>D and  $\Delta^{12}$ CH<sub>2</sub>D<sub>2</sub> indicate that methanotrophy is taking place in the basin, consuming approximately 1-1.6% of the accumulated CH<sub>4</sub>. The results highlight the importance of methanogenesis and methanotrophy as key processes in the deep subsurface, as they are thought to sustain an oligotrophic microbial community dominated by sulphur oxidizing microbes (Lau et al., 2016).

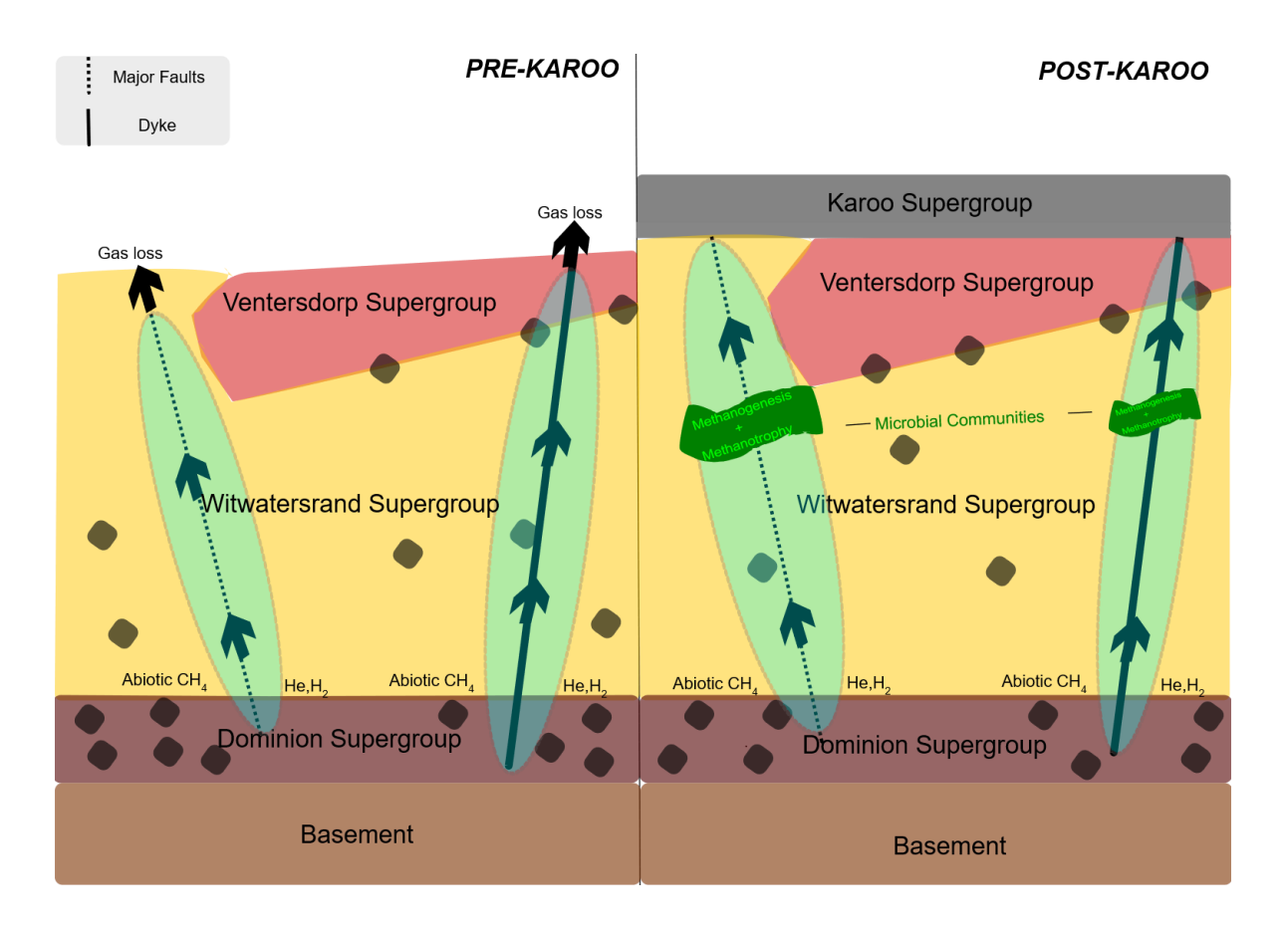


Figure 4.11: Schematic of the conceptual model including the geology and the processes taking place within the basin. Blue circled areas symbolise the fracture fluid. Black polygons depict the radiolytic elements (U, Th, K).

# 4.6. Conclusions

In this chapter I have measured the molecular and isotopic compositions to determine the origin of gases in the Virginia gas field and identify the dominant processes in the subsurface. My results indicate a mixture of two sources, a dominant microbial component (~70%) with a smaller contribution from abiotic methane (30%). In contrast to previous studies (Cook, 1998), there is no evidence of a significant thermogenic contribution and if present, is likely at minor amounts. Methane cycling takes place in the basin with methanotrophy consuming less than 1.6% of the accumulated CH<sub>4</sub>. This results in Δ<sup>13</sup>CH<sub>3</sub>D values above 7‰, which are higher than the typical values for methane in natural settings (Wang et al., 2015; Young et al., 2017; Thiagarajan et al., 2020; Mangenot et al., 2021; Nothaft et al., 2021; Sivan et al., 2024). These findings shed light on deep subsurface processes and highlights the importance of clumped isotopes to identify those processes and distinguish the origin of methane at similar geological settings.

# 5. Origin of Carbonate in the Virginia Gas Field Reservoir Rocks

#### 5.1. Introduction

Carbonate rocks are amongst the most common sedimentary rocks. In the Earth's crust, 90 % of carbonate rocks consist of calcite (CaCO<sub>3</sub>) and dolomite (CaMg(CO<sub>3</sub>)<sub>2</sub>), substantially higher than 10-15 wt. % found in sedimentary rocks (Dietzel, 2011). However, other minerals may be present either in carbonate or sedimentary rocks such as aragonites, magnesites, siderites and others (Pansu and Gaytheyrou, 2006).

Carbonates can form in a variety of environments such as the oceans, in freshwater systems, in soils or in the Earth's crust. The formation of carbonates occurs due to different processes associated with living organisms or abiotic processes (Pansu and Gautheyrou, 2006). In oceans, accumulation of carbonate-rich material from shells, foraminifera, algae can lead to the formation of carbonate rocks such as limestone in the sediments. Alternatively, formation of carbonates can occur by precipitation of dissolved inorganic carbon (DIC). This DIC can derive from dissolution of atmospheric CO<sub>2</sub> in water either in seawater or freshwater. This results to the formation of carbonic acid, which can breakdown into bicarbonate ions (HCO<sub>3</sub><sup>-</sup>) and carbonate ions (CO<sub>3</sub><sup>2</sup>-). Due to the abundance of Ca<sup>2+</sup> in ocean water, solid carbonates can form under the following reaction:

$$Ca^{2+} + CO_3^{2-} \leftrightarrow CaCO_3$$
 (5.1)

Carbonates also form in freshwater systems and terrestrial environments including caves and soils. Carbonates veins in rocks are an indication of hydrothermal fluid circulation (Pagel et al., 2018; MacDonald et al., 2019).

In sedimentary and marine environments, carbonates may be associated with methane, through biological processes. Under anaerobic conditions methanotrophs can convert CH<sub>4</sub> into bicarbonate ions under the following (Budai et al., 2002; Lloyd et al., 2016; Mizuno et al., 2023):

$$CH_4 + SO_4^{2-} \leftrightarrow HCO_3^- + HS^- + H_2O$$
 (5.2)

The DIC produced from the methane can then lead to carbonate precipitation (Castanier et al., 1999; Akam et al., 2020).

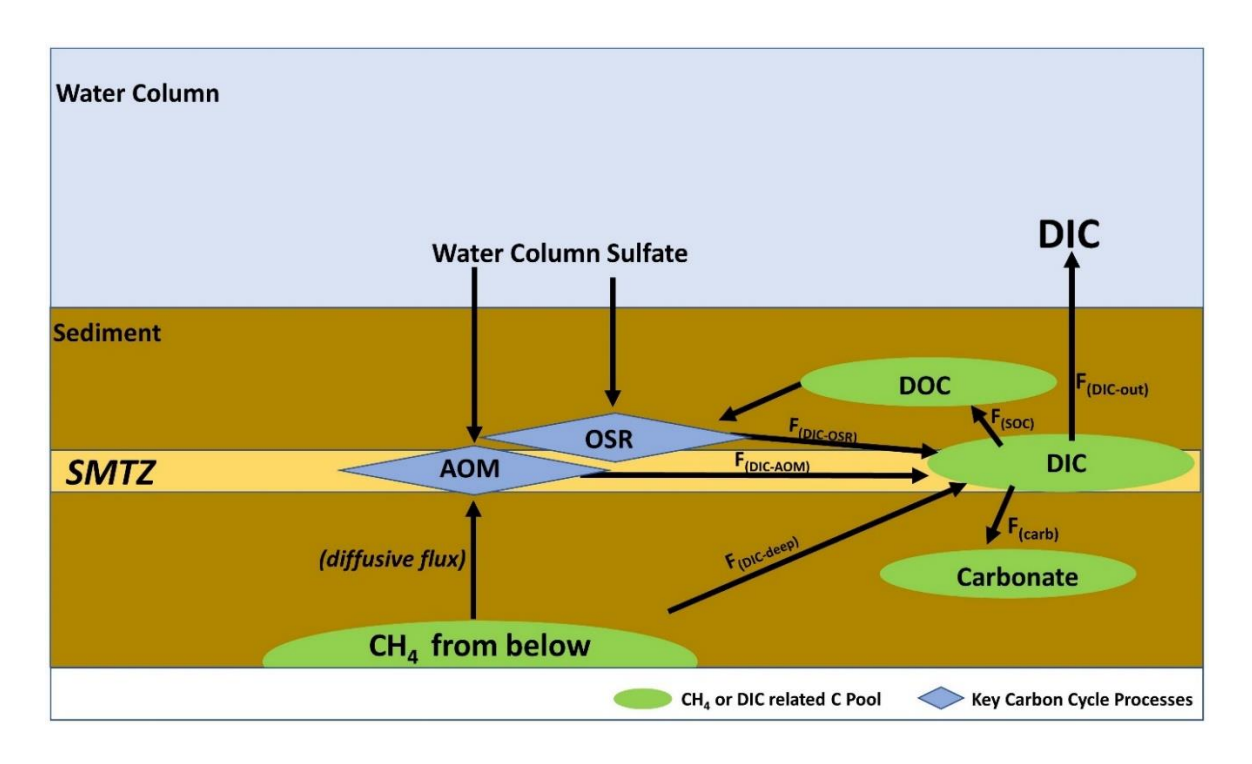


Figure 5.1: Diagram of carbon cycle and carbonate formation through the AOM in the sediments of a shallow marine environment (Akam et al., 2020).

Since the mid- $20^{th}$  century, the carbon and oxygen isotope composition of carbonates have been used to understand the origin of carbon (Urey, 1951; Hayes, Craig, 1953), constrain paleoclimates and paleoenvironments (Hui et al., 2013) and the source of ore fluids (Barker and Dipple, 2019). However, using the  $\delta^{18}O$  of the carbonates to determine formation temperatures requires assumptions about the oxygen isotopic composition of the precipitating fluid, which can be challenging (Gregory, 1991; Jaffrés et al., 2007). Technological developments in the last 20 years have allowed the determination of the abundance of doubly-substituted isotopologues such as  $^{13}C^{18}O^{16}O$  in carbonates (Ghosh et al., 2006a; Ghosh et al., 2006b, Guo and Eiler, 2007). The clumped isotope tracers can be used to determine carbonate formation temperatures, without requiring assumptions regarding the isotopic composition of the fluid (Eiler, 2007; Stolper et al., 2018). However, at temperatures above 150°C the clumped isotopes in carbonates can be reset by solid-state bond reordering (Passey and Henkes, 2012; Stolper and Eiler, 2015; Lloyd et al., 2018).

Previous studies have used the  $\delta^{13}$ C and  $\delta^{18}$ O to investigate the source of the carbonates and the fluids from which they precipitated in the Witwatersrand basin (Beukes et al., 1990; Bau et al., 1999; Boice et al., 2003; Ward et al., 2004; Zhao et al., 2006; Frauenstein et al., 2009; Jaguin et al., 2010; Warr et al., 2021; Nisson et al., 2023). These studies have argued in favour of multiple sources of carbon in the basin, suggesting also the occurrence of two

different fluids in the fracture system either originating within the basin or infiltrating the fracture zones from the surface (Jaguin et al., 2010; Nisson et al., 2023).

In this chapter I report measurements of the stable and clumped isotope compositions ( $\Delta_{47}$ ) of carbonate (n = 14) from quartz-calcite veins in the Witwatersrand basin. All samples are from a single core taken from the production area of the Virginia gas field (see Chapter 4). The  $\Delta_{47}$  measurements coupled with the  $\delta^{13}$ C and  $\delta^{18}$ O of the calcites allow us to:

- I. Reconstruct the temperature of calcite deposition and connect them with the geological events that took place in the basin.
- II. Investigate the source(s) of carbon contributing to the DIC.
- III. Constrain the oxygen isotopic composition of the precipitating fluid and indicate the origin of the fluid.
- IV. Assess the potential relationship between the calcites and the methane resources found within the Virginia gas field.

I provide the context on the systematics of the  $\delta^{13}$ C and  $\delta^{18}$ O in carbonates for interpretation of the results. This is followed by a description of the methods used for sampling, the geology of the Virginia gas field and the petrography of the quartz-calcite veins, supported by data provided by the field geologists of Renergen, the company exploiting the gas field. Finally, I describe the analytical methods and data processing used.

# 5.2. Nomenclature & Stable Isotopes

#### 5.2.1. Introduction

The isotopic signatures  $\delta^{13}$ C and  $\delta^{18}$ O in carbonates are measured after dissolution in phosphoric acid, which produces  $CO_2$  for analysis (Section 5.5). The  $\delta^{13}$ C is expressed in per mil (‰) against the Vienna Peedee Belemnite standard (VPDB), and the definition can be found in Chapter 2. In carbonates the  $\delta^{13}$ C (against VPDB) varies largely in terrestrial systems between approximately -125‰ and +40‰ values with both extreme values usually associated with biological processes (Budai et al., 2002; Drake et al., 2015).

Here, I present the equation for the calculation of  $\delta^{18}O$  which is expressed in per mil and against the internation standard VPDB (0%).

$$\delta^{18}O_{VPDB} = \left(\frac{\binom{180}{160}}{\binom{180}{160}}_{sample} - 1\right)$$
 (5.3)

The  $\delta^{18}$ O (against VPDB) in terrestrial carbonates typically varies between 0‰ and -25‰ (Grossman, 1998; Zhuo et al., 2019). For water or fluids measurements, generally the  $\delta^{18}$ O is relative to the international standard VSMOW (Vienna Standard Mean Ocean Water) (IUPAC, 1994) instead. Using the following equation from Brand et al. (2014) and Kim et al. (2015), we can convert the  $\delta^{18}$ O values in VPDB scale to  $\delta^{18}$ O in VSMOW:

$$\delta^{18}O_{VSMOW} = 1.03092 \times \delta^{18}O_{VPDB} + 30.92$$
 (5.4)

This equation can be calculated using the  $^{18}\text{O}/^{16}\text{O}$  ratios for VPDB and VSMOWs, where  $^{18}\text{R}_{\text{VPDB}} = 0.00206716068$  and  $^{18}\text{R}_{\text{VSMOW}} = 0.0020052$  (Yurimoto, 2017; Srivastava and Verkouteren, 2018).

# **5.2.2.** Carbon Isotopes

The typical variations in  $\delta^{13}$ C values in nature range from -60‰ to +5‰ depending on the formation mechanisms (e.g biotic or abiotic), the environment (e.g marine, terrestrial or freshwater), the isotopic composition of the substrates utilised, the chemical species (CO<sub>2</sub>, CH<sub>4</sub>, carbonates), and the prevailing conditions during formation (e.g temperature). The  $\delta^{13}$ C of carbonates varies from approximately -125‰ to +40‰, while typical values range from -25‰ to +5‰. The extreme positive values of  $\delta^{13}$ C are associated with methanogenesis (Budai et al., 2002; Lloyd et al., 2016), while the extreme negative values of  $\delta^{13}$ C originate from interactions between DIC and the anaerobic oxidation of methane (Drake et al., 2015; Lloyd et al., 2016; Mizuno et al., 2023).

Carbonate minerals can be found in diverse environments such as marine, terrestrial and freshwater systems, which creates a potential for  $\delta^{13}$ C differences due to utilisation of diverse carbon pools and the different prevailing conditions and processes. Marine carbonates exhibit a relatively narrow range of  $\delta^{13}$ C values, whereas carbonates derived from freshwater and terrestrial environments exhibit larger variations (Wagner et al., 2018). This overlap can make it challenging to identify the source of carbon. Most often, marine carbonates exhibit

 $\delta^{13}$ C values which are significantly higher and distinct compared to those for freshwater and terrestrial systems. The  $\delta^{13}$ C of marine carbonates range typically from -5‰ to 5‰ and is largely controlled on the  $\delta^{13}$ C of the bicarbonate of the ocean which shows small variability (Zeebe and Wolf-Gladrow, 2001; Hoefs, 2015). However, geological events known as "carbon isotope events" have caused in the geological past either negative or positive excursions (<5‰) in  $\delta^{13}$ C of carbonates lasting typically between thousands of years to a few million years (Kump and Arthur, 1999; Vervoort et al., 2019). Additionally, increases in  $\delta^{13}$ C are associated with interglacial periods and the deposition of organic matter enriched in  $^{13}$ C (Shields and Veizer, 2002) or connected to the activity of methanogenic communities (Hayes and Waldbauer, 2006; Hoefs, 2016).

The  $\delta^{13}$ C of terrestrial and freshwater carbonates is largely dependent on the isotopic composition of the dissolved inorganic carbon (DIC) in the precipitating fluid (Candy et al., 2011). However, the  $\delta^{13}$ C of freshwater carbonates can depend also on past and current climate and seasonal trends, the temperature of the water, the biological activity within the system, and the age of the ecosystem (Hoefs, 2015). Nevertheless, the  $\delta^{13}$ C of freshwater carbonates typically falls between -15‰ and +5‰ (Tucker and Wright et al., 1990; Hoefs, 2015; Graniero et al., 2021). In terrestrial environments, carbonates inherit their carbon from atmospheric CO<sub>2</sub> or from CO<sub>2</sub> produced by soil respiration. The  $\delta^{13}$ C of carbonates depends on many factors, but more importantly on the isotopic composition of the source of carbon (Candy et al., 2011). The isotopic composition of atmospheric CO<sub>2</sub> varies typically from -10‰ to -8‰ and differs from the isotopic composition of CO<sub>2</sub> from soil respiration (-29‰ to -24‰), which is produced by microbial processes and vegetation (Pataki et al., 2003). Terrestrial carbonates exhibit a  $\delta^{13}$ C range from -15‰ to 0‰ (Wagner et al., 2018).

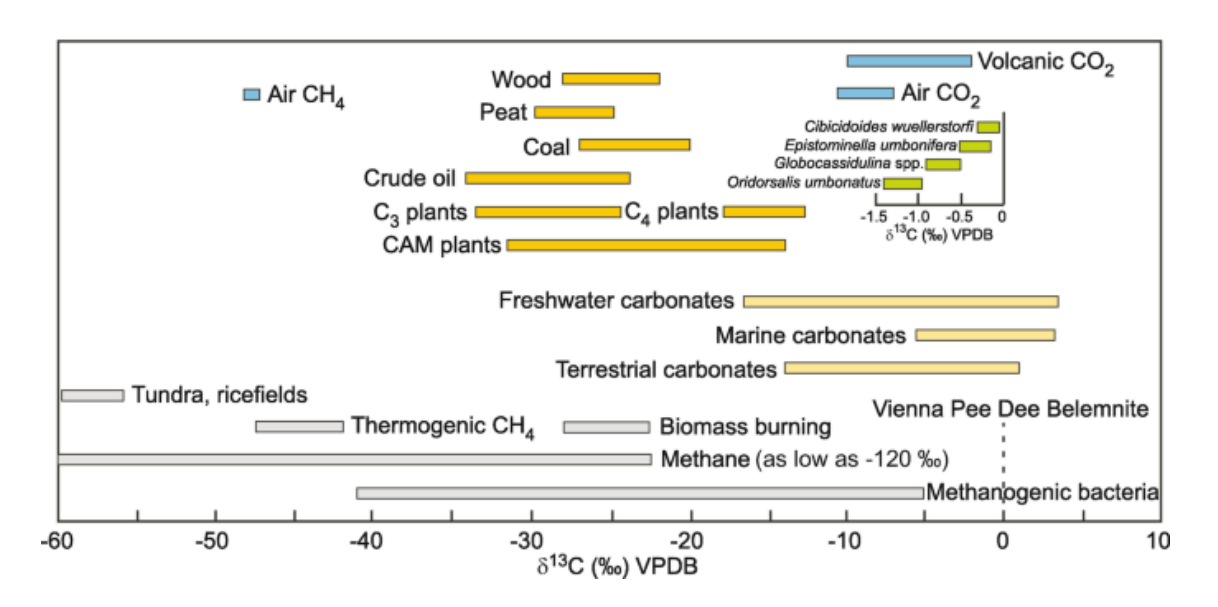


Figure 5.2: Variations in  $\delta^{13}$ C (against VPDB) for carbon-bearing compounds in natural environments (Wagner et al., 2018).

#### 5.2.3. Oxygen Isotopes

The  $\delta^{18}$ O values of water and minerals range from -50‰ for freshwater from ice shelves to +40‰ for atmospheric CO<sub>2</sub> (against VSMOW) or equivalently from -78‰ to 9‰ against VPDB (Grossman, 1998). The  $\delta^{18}$ O from atmospheric CO<sub>2</sub> exhibits small interannual variabilities, typically below 2‰, related to the carbon and hydrological cycles, and varies with latitude due to climate patterns (Welp et al., 2011). In addition, the  $\delta^{18}$ O of atmospheric CO<sub>2</sub> is often altered locally by isotopic exchange with H<sub>2</sub>O mainly through vegetation, other biological processes, and anthropogenic activities (Luz and Barkan, 2011; Schumacher et al., 2011; Ishidoya et al., 2025).

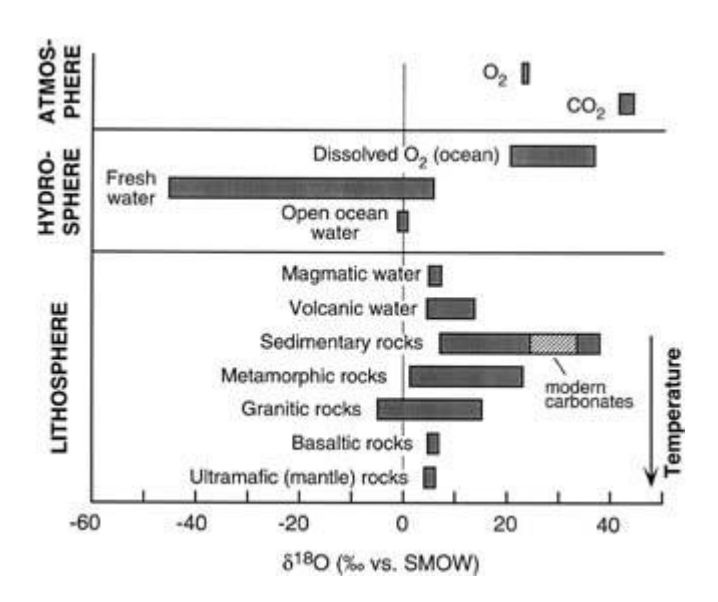


Figure 5.3: Typical variations of  $\delta^{18}$ O (against SMOW) for materials from natural environments within the atmosphere, hydrosphere and lithosphere (Grossman, 1998).

The  $\delta^{18}$ O values of carbonates reflect the isotopic composition of the water from which they precipitate, as oxygen atoms in carbonate originate from the DIC (primarily bicarbonate), which exchanges oxygen isotopes with the fluid (Urey, 1951). Additionally, the  $\delta^{18}$ O of carbonate is temperature-dependent due to isotope fractionation between carbonate and water during precipitation (Epstein et al., 1951; Watkins et al., 2014). The isotopic composition of oxygen in carbonates has been used for decades as a tool to infer paleotemperatures from ancient oceans or other systems (Urey et al., 1951). For example, if the isotopic composition of oxygen is known in both carbonates and the fluid, the temperature of precipitation can be calculated assuming isotopic equilibrium. Early studies by O'Neil et al. (1969) calculated the fractionation factor between carbonates and water, which was modified later by Friedman and O'Neil (1977) as follows:

$$\alpha_{carb-H2O}^{18} = e^{(2.78 \times \frac{1000}{T^2} - 0.00289)}$$
 (5.6)

Recent calibrations take into account acid fractionation and updated values for the isotopic ratio in reference materials (Kim & O'Neil, 1997; Kim et al., 2007, 2015), and lead to the following equation for the fractionation factor between calcite-water (Bajnai, 2023):

$$\alpha_{cal-H2O}^{18} = e^{(18.04 \times \frac{1}{T} - 0.03218)}$$
 (5.7)

The isotopic signature of carbonates in natural systems exhibit significant variability due to the diverse fluids found in marine, freshwater and terrestrial systems and the range of formation temperatures. For example, marine carbonates  $\delta^{18}\text{O}_{\text{VPDB}}$  values typically range between - 2‰ and 2‰ (Östlund et al., 1987), and are controlled by seawater temperature and  $\delta^{18}\text{O}$  value, both of which can vary due to global and local effects such as the mixing of oceans, variations in the volume of ice shelves and salinity (Delaygue, 2009). Freshwater carbonate  $\delta^{18}\text{O}$  values often range from -4‰ to -10‰. However, local effects (mean residence time, temperature, biological activity, etc), can lead to the formation of freshwater carbonates significantly outside of this range, between -50‰ and +5‰ (Grossmann et al., 1998; Hoefs, 2015). In terrestrial systems, the  $\delta^{18}\text{O}$  of the carbonates usually vary from -10‰ to 0‰, and depends on the origin of the precipitating fluid, possible interactions with oxygen-bearing minerals in the crust and the temperature during precipitation (Grossman, 1998; Budai et al., 2002).

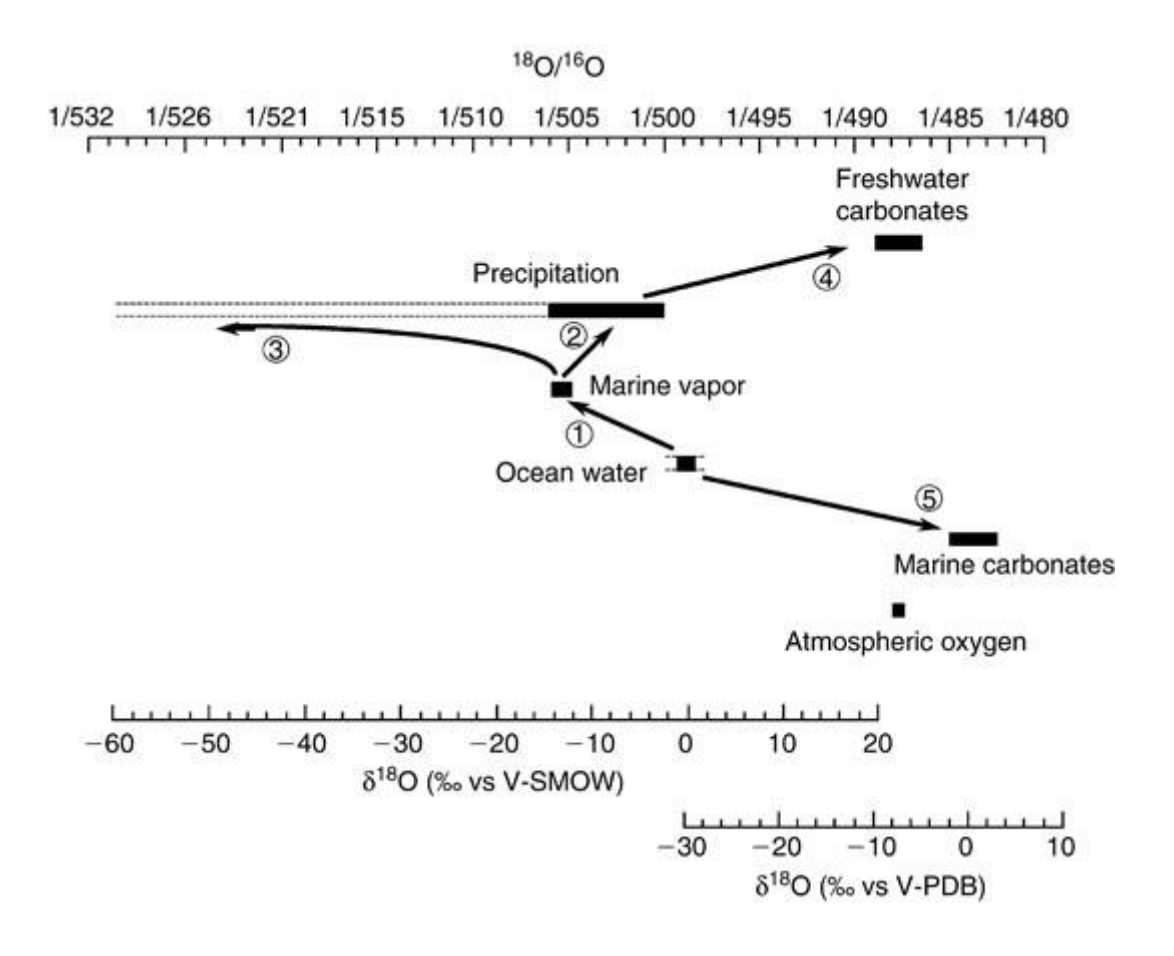


Figure 5.4: Variations of  $\delta^{18}O$  (against SMOW & VPDB) for materials from natural systems. Arrows and numbers indicate sources and processes (Delaygue, 2009).

# **5.3.** Clumped Isotope Thermometry

Since the early 2000s, reliable measurements of multiply-substituted isotopologues in CO<sub>2</sub> derived from carbonates have been feasible with a precision sufficient for geochemistry applications (Gosh et al., 2006a; Schauble et al., 2006; Huntington and Petersen et al., 2023). These measurements do not only offer an extra tracer for investigating any processes after the formation and deposition of the calcites but most importantly, they reveal the growth temperature of the calcites without the need to make assumptions on the  $\delta^{18}$ O of the fluid from which the carbonate precipitated. Instead, the temperature of the carbonate precipitation is estimated through the relative abundance of isotopologues, including  $^{13}$ C<sup>18</sup>O<sup>16</sup>O, as isotopologues bearing several heavy isotopes are, at equilibrium, more abundant at lower temperatures (Gosh et al.,2006a; Schauble et al., 2006; Eiler, 2007). Consequently, using the formation temperature and the  $\delta^{18}$ O of the carbonate it is possible to calculate the  $\delta^{18}$ O of the precipitating fluid (Nooitgedacht et al., 2021).

The clumped isotopic signature  $\Delta_{47}$  is expressed in per mil (‰). The abundance of multiply substituted isotopologues is compared to the abundance expected for a random distribution of isotopes amongst isotopologues (the stochastic distribution, see Chapter 2). Although there are 2 other isotopologues of  $CO_2$  ( $^{12}C^{17}O^{18}O$  and  $^{13}C^{17}O_2$ ) with a cardinal mass of 47 (Eiler, 2007), they are only minor components and in practice we are only concerned with variation in  $^{13}C^{18}O^{16}O$ , leading to the simplified equation:

$$\Delta_{47} \approx \left(\frac{\left(\frac{^{13}C^{18}O^{16}O}{^{12}C^{16}O^{16}O}\right)_{sample}}{\left(\frac{^{13}C^{18}O^{16}O}{^{12}C^{16}O^{16}O}\right)_{stochastic}} - 1\right) (5.8)$$

Technological improvements in isotope ratio mass spectrometry (IRMS) have allowed the measurement of an additional clumped isotopologue, the  $^{12}C^{18}O^{18}O$  (Fiebig et al., 2019).  $\Delta_{48}$  values are calculated neglecting minor isotopologues as follows (Eiler, 2007):

$$\Delta_{48} \approx \left(\frac{\left(\frac{^{12}C^{18}O^{18}O}{^{12}C^{16}O^{16}O}\right)_{sample}}{\left(\frac{^{12}C^{18}O^{18}O}{^{12}C^{16}O^{16}O}\right)_{stochastic}} - 1\right) (5.9)$$

The simultaneous measurement of  $\Delta_{47}$  and  $\Delta_{48}$  can improve significantly the identification of kinetic processes which may not be obvious using only  $\Delta_{47}$  (Bajnai et al., 2020). This is equivalent to the studies measuring only the  $\Delta^{13}\text{CH}_3\text{D}$  or the combined clumped isotopic signature  $\Delta_{18}$  of CH<sub>4</sub> (Stolper et al., 2015; Wang et al., 2015), where most of the samples initially reflecting thermodynamic equilibrium or falling close to the expected formation temperature. Considering all  $\Delta^{12}\text{CH}_2\text{D}_2$  analyses, kinetic isotope effects were more easily identified and linked to specific process or processes (Young et al., 2017; Giunta et al., 2021; Hagnegahdar et al., 2024; Sivan et al., 2024).

#### 5.4. Witwatersrand Basin

The geology of Witwatersrand basin has been discussed in Chapter 4, therefore I will briefly mention the existing lithologies and focus on the sequences of interest in the context of the calcites. The Witwatersrand Basin is an Archean intracratonic basin with a basement consisting of granite and greenstones (3.1 Ga), succeeded by the volcano-sedimentary rocks of the Dominion Group (3.08 Ga). The Dominion Group is followed by the Witwatersrand Supergroup (2.9 Ga) which includes the West Rand Group (2.9 Ga) and the Central Rand (2.8 Ga) (Tucker et al., 2016). Above the Witwatersrand Supergroup are the volcanic rocks of the Ventersdorp Supegroup (2.7 Ga) with minor amounts of sedimentary rocks such as rudites and arenites (Visser and Grobler, 1985). Across the Witwatersrand basin, the Ventersdorp consists of three main groups: the Paiel Group, the Platberg Group, and the Klipriviersberg Group (Van Der Westhuizen et al., 1991). In particular, this study is concerned only with the Klipriviersberg Group where the calcites were sampled, while the other mentioned lithographies did not occur in the core sampled. The Klipriviersberg Group is made of tholeiitic lavas and komatiites, covering over 30,000 km<sup>2</sup> with a thickness of 1,500–2,000m (Van Der Westhuizen et al., 1991). Particularly in the Virginia gas field at the southwestern section of Witwatersrand basin, the greater part of the Transvaal Supergroup (~2.4 Ga) consisting primarily by dolomites and limestones, has been eroded (Ward et al., 2004). The Ventersdorp Supegroup is typically overlaid by the Karoo Supergroup (200 Ma) which consists of shales with minor dolerites, sandstones and tillites.

#### 5.5. Methods

# 5.5.1. Sampling

The calcites were sampled in September 2023 from a core retrieved from the production area of Virginia gas field (see Appendix). The core was drilled along a fracture at an angle of 50° (from vertical) in April 2021 during gas exploration operations at well-P12. The studied core

extends from the surface down to 417 m below ground level and overlies the andesitic lavas of Ventersdorp Supergroup which are found at depths from 417 m and beyond, down to 993 m below ground level. Quartz-calcite veins occur within the Klipriviersberg Group of the Ventersdorp Supergroup. Signs of healed fractures are apparent in the core. Throughout the core, the calcites are typically fine grained and filling vugs within the fractures. The veins filling varies within the core from approximately 3 cm (Sample 5) to a ~2 m (Sample 9) at most (Figure 5.5). Overall, 14 samples were collected from the Klipriviersberg Group at depths from 476 to 935 m.



Figure 5.5: Quartz-calcite vein sampled of approximately 16cm thickness The Klipriviersberg lavas are noted.

The vein material was powdered using a handheld drill to separate the calcite hand-picked from the quartz and the volcanic host rock. Additional treatment is not necessary at this stage of sample preparation, as silicate contaminants do not react with acid and do not yield significant amount of CO<sub>2</sub> that would affect the isotopic measurements.

#### 5.5.2. Stable and Clumped Isotope Measurements

#### 5.5.2.1. Carbon Dioxide Extraction

The calcite samples were loaded into a manually operated acid digestion and CO<sub>2</sub> purification vacuum line at the Clumped isotope laboratory at SUERC. The methods have been described previously in McCormick et al. (2023). Three to five mg of calcite powder were weighed and loaded in a small glass container that is then introduced into the vacuum line. Each sample was pumped to remove the atmospheric gases while moisture was trapped on cryogenic traps, before the sample is dropped into an acid bath (>103% H<sub>3</sub>PO<sub>4</sub>) heated at 90°C. The reaction proceeds for 10-15 minutes under the following:

$$CaCO_3 + 2H^+ \rightarrow 2Ca^{2+} + CO_2 + H_2O$$
 (5.10)

The CO<sub>2</sub> was trapped continuously in a spiral-shaped glass trap cooled with liquid nitrogen. A spiral trap cooled by an isopropanol-dry ice bath is placed between the acid reaction vessel and the liquid nitrogen-cooled trap, in order to separate water from CO<sub>2</sub>. A freeze-thaw cycle (the sample is heated and released, and subsequently trapped using liquid N<sub>2</sub>) is performed to release and remove any contaminants trapped within the frozen CO<sub>2</sub> molecules, which are then extracted by a vacuum pump. These steps are essential for removing the residual water vapour, and minimising the exchange of O between water and CO<sub>2</sub>, which results in isotopic fractionation (Affek et al., 2013). Unwanted isotopic exchange can change the original clumped isotopic signature ( $\Delta_{47}$ ) and, consequently, the apparent temperature of the sample (Swart et al., 2019; Bernasconi et al., 2021). The CO<sub>2</sub> is then transferred to a cold-finger held at liquid nitrogen temperature (-196°C). The cold-finger is connected to a Baratron© pressure gauge in a known volume. Once the CO<sub>2</sub> is fully trapped, the liquid nitrogen bath is replaced with a water bath at room temperature (21 ± 1°C) in order to release the CO<sub>2</sub> to allow determination of the absolute amount. The CO<sub>2</sub> is then passed into a helium stream towards the inlet of the gas chromatograph through a Hayesep Q column (3.05 m length and

1/8 inch outer diameter) held at 40°C. This step is necessary for further purification of the sample mainly removing nitrous oxides, N<sub>2</sub>, sulfur-bearing gases, hydrocarbons, and requires approximately 16 mins before introduction into the bellow of the mass spectrometer.

#### 5.5.2.2. Isotopic Analysis

The isotopic composition of the CO2 was determined by a Thermo Fisher MAT 253 gas source isotope ratio mass spectrometer. The gases are expanded into the mass spectrometer using adjustable bellows of the dual-inlet system in order to achieve the optimum beam intensity (operating at 16 V at m/z 44). The mass spectrometer is equipped with a set of six Faraday cups that detect simultaneously the ion beams of m/z = 44 ( $^{12}C^{16}O^{16}O^{+}$ ), 45  $(^{13}C^{16}O^{16}O^{+} + ^{12}C^{17}O^{16}O^{+})$ , 46  $(^{12}C^{18}O^{16}O^{+} + ^{13}C^{17}O^{16}O^{+} + ^{12}C^{17}O^{17}O^{+})$ , 47  $(^{13}C^{18}O^{16}O^{+})$ and 48 ( $^{12}C^{18}O^{18}O^{+}$ ). While the measurement of mass 48 (typically  $\sim$  40 ppm) and the corresponding clumped isotopic composition  $\Delta_{48}$  are now feasible at high precision with a new generation of mass spectrometers (Fiebig et al., 2019), the  $\Delta_{48}$  value is used as an indicator of contamination (e.g. hydrocarbons) as suggested by Huntington et al. (2009). Measurements of  $\Delta_{48}$  with sufficient precision for geochemical investigation is not possible with the SUERC instrument due to scattered ions from the major CO<sub>2</sub> peak at m/z =44 (Bernasconi et al., 2013). The ions from the major beam at m/z 44 are deflected within the mass spectrometer, creating secondary electrons and resulting in a negative baseline on the faraday cups measuring at m/z 45 to 48 (Swart, 2021) that depends on the intensity of the main ion beam and is referred to as a pressure baseline. Consequently, the CO<sub>2</sub> isotopologues measured at m/z 45, 46, 47 and 48 require pressure baseline (PBL) corrections. These corrections improve significantly the stability and precision of  $\Delta_{47}$  and  $\Delta_{48}$  measurements (He et al., 2012; Bernasconi et al., 2013; Swart., 2021).

For each sample, the isotopic signatures  $\delta^{13}$ C,  $\delta^{18}$ O,  $\Delta_{47}$  are measured, while the  $\Delta_{47}$  can be used to calculate the apparent formation temperature for the calcite sample. The measurements are carried out in 7 blocks each consisting of 6 acquisitions with a 26 seconds integration time. The typical measurement time of one sample is approximately 2 hours. Usually, 2 to 4 samples can be analysed per day after running a minimum of 2 calibration standards. In this study, the ETH carbonate reference standards were used for calibration (see in 5.5.3).

# 5.5.3. Data Processing

In order to determine precisely the isotopic compositions (and ultimately the  $T_{47}$ ) of samples, a series of calculations is required. The isotopic composition of the samples was measured relative to a reference gas of known isotopic compositions which allows the  $\delta^{13}$ C and  $\delta^{18}$ O

to be expressed directly against VPDB and VSMOW respectively. We use the updated IUPAC values for the  $^{13}\text{C}/^{12}\text{C}$  ratio in VPDB (0.011180), the  $^{17}\text{O}/^{16}\text{O}$  (0.038475) and the  $^{18}\text{O}/^{16}\text{O}$  in VSMOW (0.0020052), and the parameter  $\lambda$  describing  $^{18}\text{O}/^{17}\text{O}$  fractionations (0.528) (Daëron et al., 2016; Petersen et al., 2019).

Finally, we need to determine the final  $\Delta_{47}$  in the absolute reference frame (see Chapter 2). This is because we need to infer the  $\Delta_{47}$  of the standard gas used, observe the magnitude and/or variations of scale compression effects through the time, and validate that our PBL corrections are adequate. Four solid carbonate standard materials (ETH1, ETH2, ETH3, ETH4) are used to construct an empirical transfer function (ETF) from the measured  $\Delta_{47}$  against the working gas to  $\Delta_{47}$  values in the absolute reference frame as proposed in Bernasconi et al. (2021). The ETF is essentially a linear regression between the raw  $\Delta_{47}$  measured by a specific instrument against the accepted  $\Delta_{47}$  values in the absolute reference frame (Kocken et al.,2019). The slope and the intercept of the linear regression is then used to calculate the final  $\Delta_{47}$ .

I applied corrections on the standard and sample  $\Delta_{47}$  data to take into account a rising trend of  $\Delta_{47}$  values during the measurement period observed when measuring any of the ETH standards. This can occur due to subtle variations in the instrument fractionation over time. More detailed information on the correction scheme can be found in the Appendix.

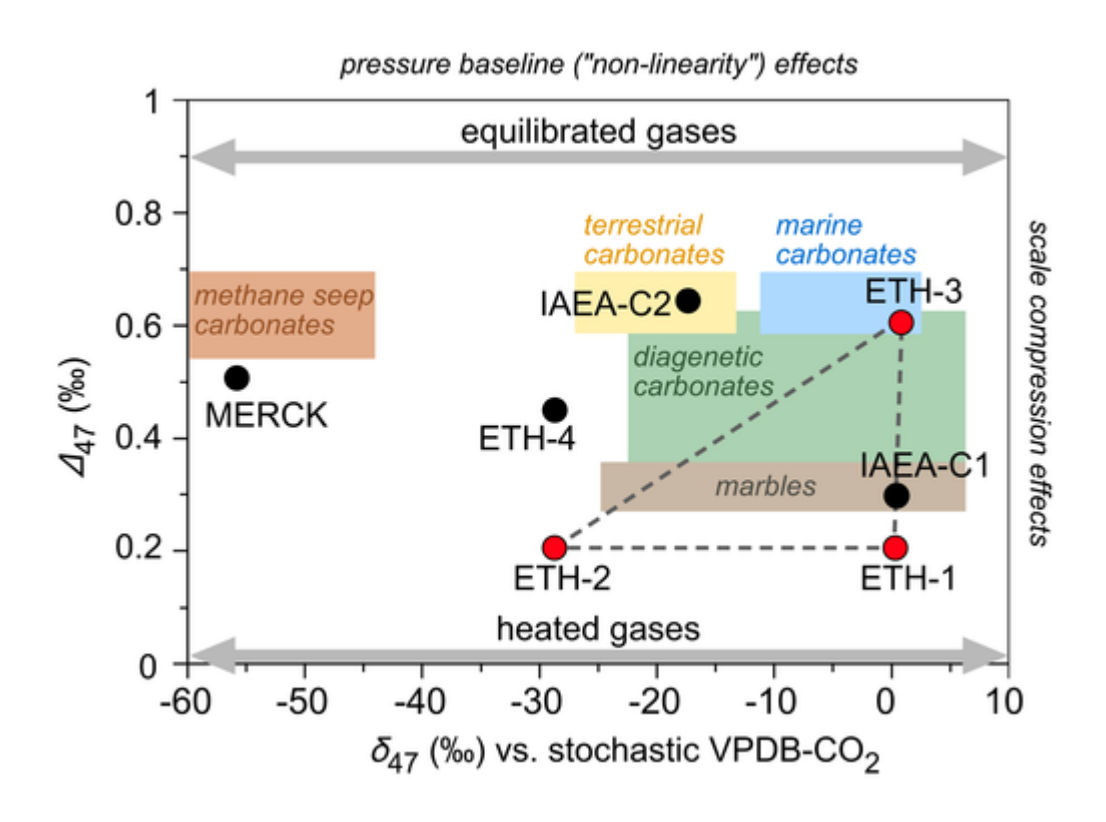


Figure 5.6: The  $\delta_{47}$  (difference between a sample and a heated gas at 1000°C) against  $\Delta_{47}$  values expressed in permil (‰) of the carbonate standards (ETH1 to ETH4) in comparison to natural and synthetic carbonate samples (Bernasconi et al., 2021).

The apparent formation temperature from the reprojected  $\Delta_{47}$  value (using the mean value after at least three replicates) can be calculated using the following equation derived from Anderson et al. (2021) for an acid reaction temperature of 90°C:

$$\Delta_{47(I-CDES90^{\circ}C)} = 0.0390 (\pm 0.0004) \times \frac{10^{6}}{T^{2}} + 0.153 (\pm 0.004)$$
 (5.11)

The analytical uncertainty on  $\Delta_{47}$  is calculated by selecting the greatest standard deviation of the  $\Delta_{47}$  for the ETH standards and amongst the replicates of each sample, and dividing it by the square root of the number of replicates (Drummond, 2021). Typically, each sample is analysed three times.

## 5.6. Results

## 5.6.1. $\delta^{13}$ C and $\delta^{18}$ O

The isotopic signatures of  $\delta^{13}$ C and  $\delta^{18}$ O for calcites collected from the Virginia gas field display a range of approximately 7.5‰ and 4.5‰ (Figure 5.7), respectively. The  $\delta^{13}$ C (vs VDPB) varies across the dataset from -9.06‰ for Sample-5 (depth 623.1 m) to -1.57‰ measured for Sample-13 (depth 899.6 m). The  $\delta^{18}$ O (vs VPDB) varies to a smaller extent than  $\delta^{13}$ C, with the lowest value at -21.72‰ measured for Sample-11 (depth 779 m) and the highest value at -17.16‰ for Sample-7 (depth 716.1 m) .

The values overlap previous measurements for vein calcites from the Ventersdorp sequence (Fig 5.7).  $\delta^{13}$ C measurements of vein calcite from the Virginia area reported by Jaguin et al. (2010) range from -9.4‰ to -3‰ while  $\delta^{18}$ O varied from -22.2‰ to -21.2‰. Calcite veins from the gold mines of Orkney and Evander are in the same range in  $\delta^{13}$ C, but in average lower in  $\delta^{18}$ O. However, calcite veins from the Moab Khotsong mine are consistently lower in  $\delta^{13}$ C with an average value of -9.85‰ and in a similar range to Virginia gas field in  $\delta^{18}$ O.

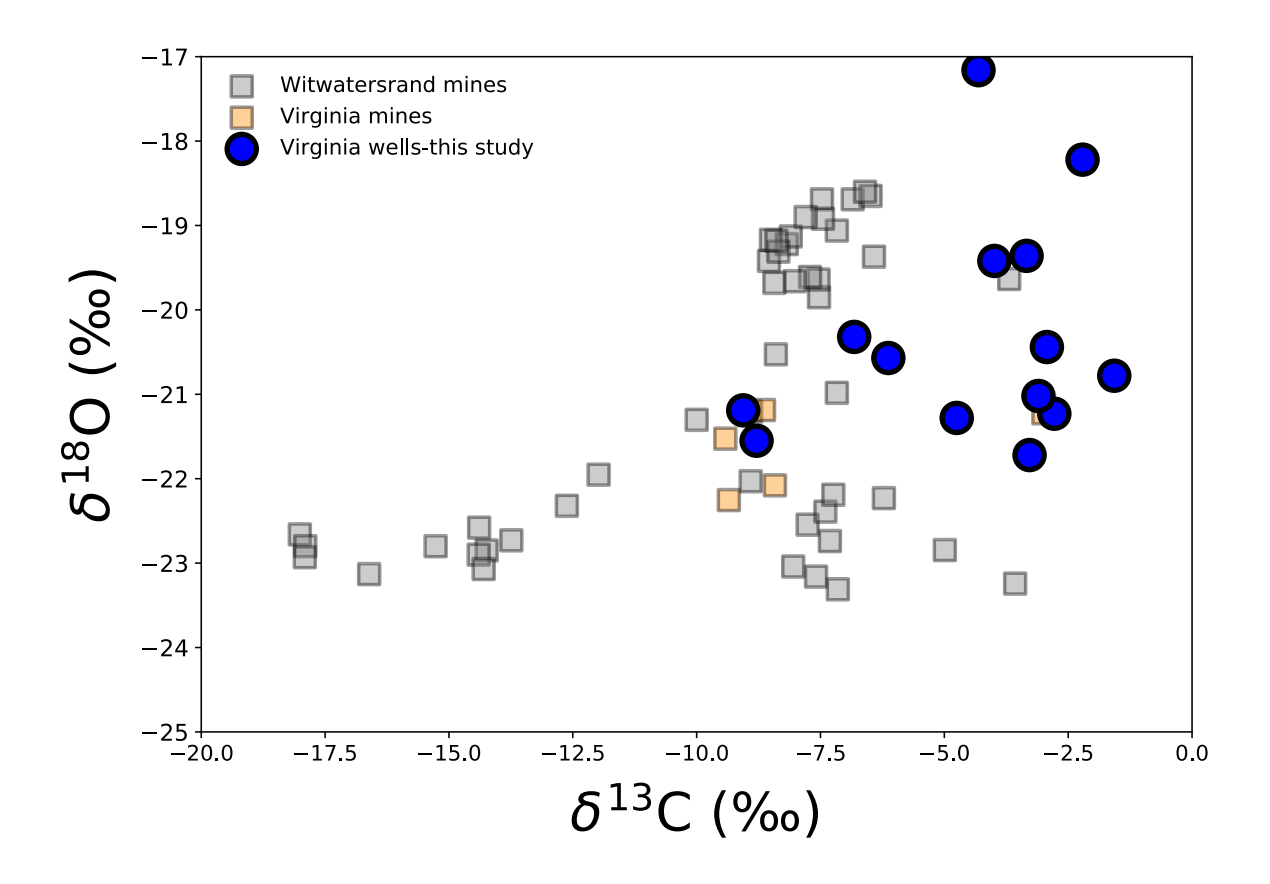


Figure 5.7:  $\delta^{13}$ C vs  $\delta^{18}$ O values of calcite veins from the Witwatersrand basin. Blue circles from this study, orange squares from Jaguin et al. (2010) for Masimong mine, grey squares for other Witwatersrand mines from Jaguin et al. (2010) and Nisson et al. (2023) for other Witwatersrand mines (Moab Khotsong, Orkney, Evander).

## 5.6.2. $\Delta_{47}$ and Apparent Temperatures

The  $\Delta_{47}$  values of the calcites range from 0.32 to 0.50‰, with an average analytical uncertainty of  $\pm$  0.012‰. This is the first reported dataset of the clumped isotopic signatures in any carbonates from the Witwatersrand basin, therefore the measurements cannot be compared with previous studies across the area. Using eq. (5.8) the apparent temperatures (T<sub>47</sub>) of the Virginia calcites has been determined (Figure 5.8 & 5.9).

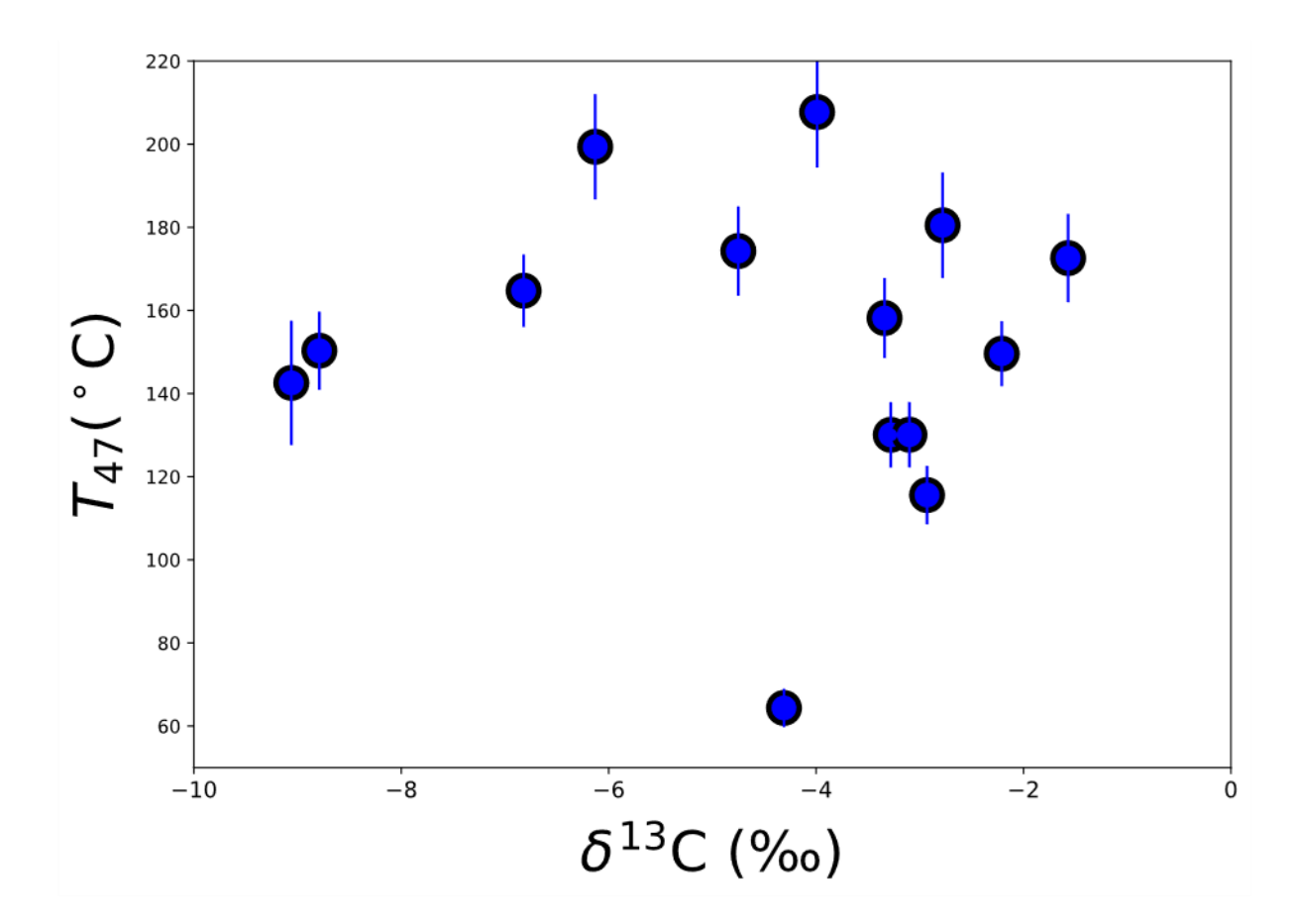


Figure 5.8:  $\delta^{13}$ C vs T<sub>47</sub> values for the calcites sampled in Virginia gas field.

The apparent temperatures for the calcites range from  $64 \pm 6$  °C to  $208 \pm 13$  °C (the uncertainties in temperature are increasing at increasing temperatures). The majority of samples (9 out of 14) yielding temperatures between 120 and 180°C. With the exception of two samples all are within error from the range of fluid inclusion homogenisation temperatures (130-200°C) from the Orkney mine (at the northwestern section of the Witwatersrand basin) and Virginia/Welkom (Jaguin et al. 2010).

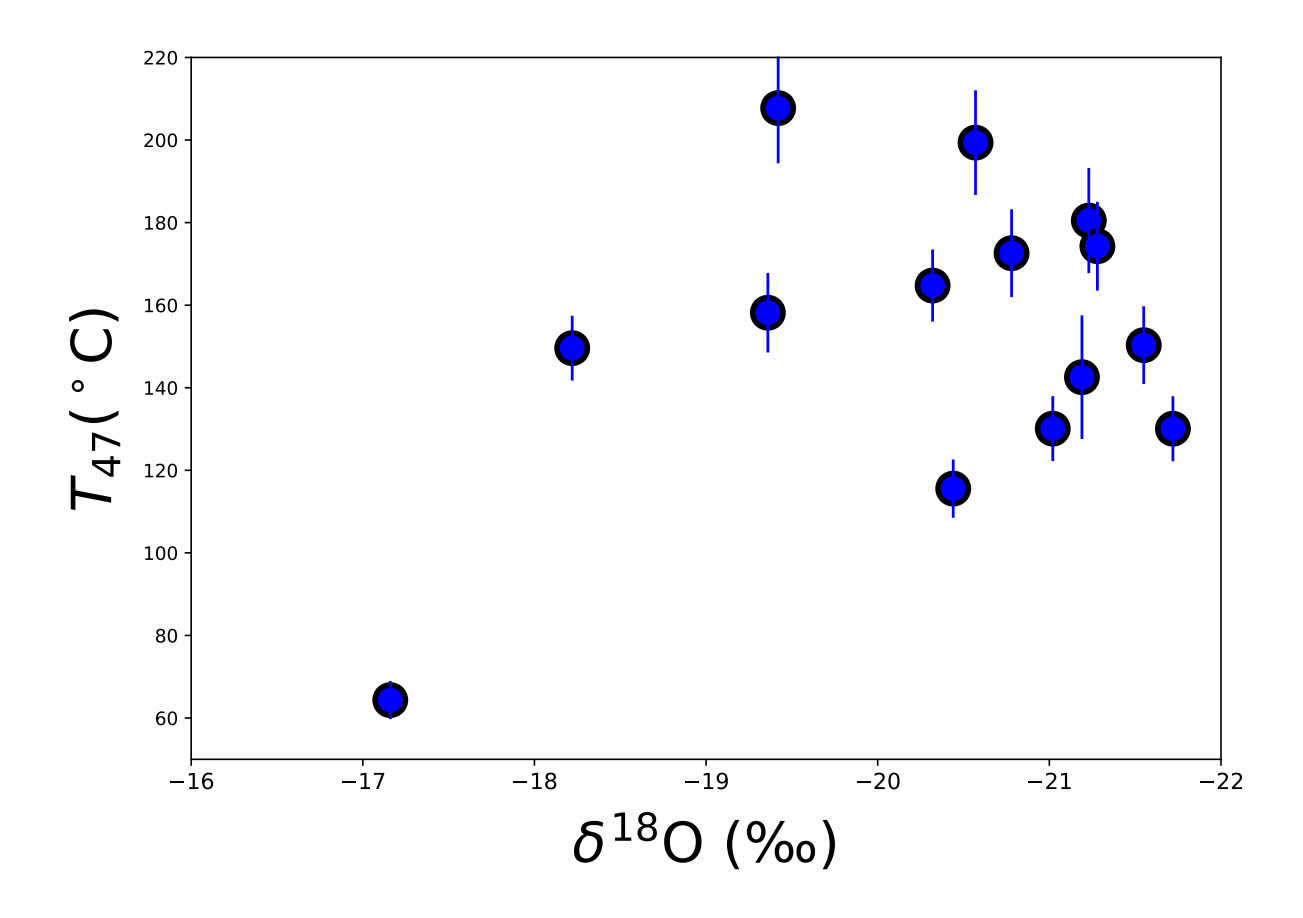


Figure 5.9:  $\delta^{18}$ O vs T<sub>47</sub> values for the calcites sampled in Virginia gas field.

# 5.7. Discussion

In this section, I discuss the results of this study in comparison to the previous research findings on the origin of carbon in calcites in the basin. I also use the  $T_{47}$  and the  $\delta^{18}O$  of the calcites to constrain the origin and isotopic characteristics of the precipitation fluid. Finally, I evaluate the potential relationship between methane and calcites, as observed in other sedimentary basins and fracture systems(Budai et al., 2002; Drake et al., 2015; Lloyd et al., 2016; Nooitgedacht et al., 2021; Mizuno et al., 2023).

### 5.7.1. Thermal History of the Witwatersrand Basin

The thermal history of Witwatersrand basin holds significance not just for understanding the geological history of the region but also has economic importance given the abundant gold, uranium and helium deposits (Tucker et al, 2016), as well as the formation and accumulation of light hydrocarbons found across the basin (Ward et al., 2004; Sherwood Lollar et al., 2006). In this section, we consider how the  $T_{47}$  determinations provide insights into the thermal history of the basin.

The Witwatersrand basin has undergone several metamorphic, hydrothermal, magmatic and tectonic events (Frimmel et al., 1999; Frimmel et al., 2002; Omar et al., 2003; Tucker et al., 2016). The principal events are the early and late syn-depositional deformation events that occurred during the deposition of the Central Rand Group (2.9-2.7 Ga), the uplift of the basin due to regional compression (~2.8 Ga) and the deposition of Ventersdorp Supergroup (2.7 Ga), which all resulted into the creation of a network of faults. Due to the magmatic origin of the Ventersdorp Supergroup, the burial of underlying rocks, and the associated hydrothermal activity, the temperature in the basin was significantly increased. This occurred due to the thinning of the crust during rifting, which allowed the heat flow from the mantle.

Dykes and sills related to the Ventersdorp deposition allowed hydrothermal fluids to circulate within the basin and are associated with small scale remobilisation of the gold (Drennan and Robb, 2006; Tucker et al., 2016). A post-Transvaal age deformation event is associated with the impact of Vredefort meteorite (2.02 Ga) which caused an uplift in the central region of the basin and caused at least two metamorphic events (McCarthy et al., 1986; Tucker et al., 2016). The emplacement of the Bushveld Complex at 2.05 Ga is associated with an increase of the thermal gradient of 20°C/km in the Witwatersrand basin (Jaguin et al., 2010; Tucker et al., 2016). The intrusion of Bushveld had a significant impact on the temperature evolution and fluid circulation in the northern margin of the basin (Frimmel, 1997) with limited thermal impact on the southwestern section of the basin (Tucker et al., 2016).

The heat produced by radioactive decay of U in the reef rocks, with average concentrations across the basin at least four times higher than in the Earth's crust (Krauskopf, 1979; Frimmel, 1997), cannot be ignored. According to Jones (1988), this is likely the reason for the high heat flux at Witwatersrand basin compared to other Archean age basins (Frimmel, 1997).

Ultimately, the Witwatersrand basin has experienced cooling from a maximum temperature during in the Central Rand Group at approximately 350± 50°C at the peak of metamorphism after the deposition of the Transvaal Supegroup (2.06 Ga)(Fuchs et al., 2021). The Vredefort meteorite impact (~2.02 Ga) caused the infiltration of hydrothermal fluids in the basin (Frimmel, 1997), and a heat shock with temperatures exceeding 700°C in the centre of the dome and below 400°C at the margins of the basin (Gibson et al., 1998). The current basin temperatures range from 20 to 60°C, with a current average thermal gradient of about 10°C/km for the last 30 Myr (Omar et al., 2003; Nisson et al., 2023). The temperature in the Central Rand Group was above 120°C at approximately 422 Ma, cooling associated with

erosion events at ~120 Ma and ~90 Ma, drove the temperature to drop at a rate of approximately 1.4°C/Ma (Omar et al., 2003).

The apparent temperatures from the clumped isotopic compositions  $\Delta_{47}$  suggest several events of calcite precipitation with temperatures ranging between 64 and 200°C, . However, at temperatures above 150°C and over geological timescales, clumped isotopes can be reset by bond reordering (Stolper and Eiler, 2015). Thus, in this case, the new apparent temperatures either reflect the temperature of the newly attained equilibrium or a temperature altered compared to the original formation temperature, but without reaching equilibrium (Henkes et al., 2014; Stolper and Eiler, 2015; Lloyd et al., 2018). Therefore, it is important to understand whether the apparent temperatures reflect the formation or the resetting temperature of the calcites in veins.

Fluid inclusions in quartz-calcite veins from the Witwatersrand Supergroup, the Ventersdorp Contact Reef, the Ventersdorp Supergroup (i.e. same stratigraphic sequence as the samples from this study) (Frimmel et al., 1999; Drennan and Robb, 2006; Jaguin et al., 2010) are classified based of fluid inclusion-type (i.e. shape and fluid phases) inferring the occurrence of at least 4 different fluids (Frimmel et al., 1999; Drennan and Robb, 2006; Jaguin et al., 2010). In Virginia two main water-dominant fluid systems are present in the fluid inclusions, one related with high-CO<sub>2</sub> concentration along with variable amounts of CH<sub>4</sub>, N<sub>2</sub> and ethane, and one rich in KCl and NaCl (Frimmel et al., 1999). Fluid inclusions exhibit homogenisation temperatures of between 115 and 199°C (Jaguin et al., 2010), in good agreement with temperatures reported by Frimmel et al. (1999) who reported homogenisation temperatures at approximately 135°C for both types of fluid inclusions. T<sub>47</sub> from calcite clumped isotopes (13 out of 14 samples) are consistent with this temperature ranges, suggesting that quartz-calcite vein formation occurred at similar conditions. In the absence of other explanations, the CO<sub>2</sub>-rich fluid in the fluid inclusions should be related to the fluids from which the calcite precipitated. Therefore, I propose that the apparent temperatures likely reflect formation temperatures for the calcites, deriving from at least one precipitating fluid rich in CO<sub>2</sub> at a similar temperature (115-200°C) after the Vredefort impact. Additionally, even assuming the extreme thermal gradient of 20°C/km suggested after the Bushveld Complex emplacement, this would suggest that the surrounding rocks were considerably cooler than the fluid, and significantly lower than the 150°C which is required for bond reordering for calcites (Lloyd et al., 2017). Consequently, hereafter we use the apparent temperatures T<sub>47</sub> as formation temperature of the calcite veins and discuss on this basis.

Overall, the data confirm that the basin has experience warmer temperatures in the geological past spanning based on the T<sub>47</sub> of the calcites spanning between 65°C and 200°C. Certainly, the calcites deposited in different prevailing conditions than the current, however due to the of lack of geochronological data it is challenging to pinpoint specific events of fluid circulation and exact geological periods for the calcite deposition.

### 5.7.2. Origin of Carbon

The  $\delta^{13}$ C of the calcites provide constraints on the source of carbon (Candy et al., 2011). the calcite  $\delta^{13}$ C range -9.0% to -1.5% may be due to one or more processes occurring over the geological history of the Witwatersrand basin. We discuss below the different possibilities which could have driven the variability in the  $\delta^{13}$ C of the calcites.

## 5.7.2.1. Temperature Effects

Because the calcites have variable T<sub>47</sub>, this could potentially have an impact on the fractionation factor between the DIC of the fluid and the calcite, and consequently the  $\delta^{13}$ C of the calcite. The fractionation between DIC and calcite increases with decreasing temperature (Criss, 1991). However, given the lack of relationship between the  $\delta^{13}$ C and the formation temperatures (Figure 5.8), it is unlikely that the variation in precipitation temperature controls the fluid  $\delta^{13}$ C. The cooling of the basin and the decreasing environmental temperatures within the fracture system could have an impact on  $\delta^{13}$ C. The magnitude of temperature change is likely smaller than the observed variations in this study as shown by previous studies on the magnitude of the fractionation factor and its variations with temperature. For example, an experimental study by Romanek et al. (1992) showed a difference in the enrichment factor for CO<sub>2</sub> and calcite of approximately 3.5% between 10°C and 40°C. Further, the fractionation factor between bicarbonate ions in water and precipitated calcite exhibited no temperature dependence in the range 10-40°C (Romanek et al., 1992). These experiments were conducted in a temperature range (10-40 °C) outside of the T<sub>47</sub> range in this study, but we would expect smaller fractionation magnitudes at higher T.

In summary, I propose that if any temperature effect has affected the  $\delta^{13}$ C of the calcites is probably smaller than the 3.5% reported by Romanek et al. (1992), and ultimately does not explain the full range of  $\delta^{13}$ C reported. Hence, other reasons for the observed variation in  $\delta^{13}$ C should be explored.

#### 5.7.2.2. Multiple Sources of Carbon

Previous studies of the  $\delta^{13}$ C of the DIC of deep mine fluids (Nisson et al., 2023) and the  $\delta^{13}$ C of the in the Ventersdorp Supergroup (Jaguin et al., 2010; Nisson et al., 2023) have proposed that two or more carbon sources were present within the Witwatersrand basin.

Previous studies by Onstott et al. (2006), Slater et al. (2006), Simkus et al. (2016) reported extreme variations in DIC  $\delta^{13}$ C of fracture fluids isolated from Witwatersrand basin mines, ranging from -42‰ to +12‰. In the Virginia area the  $\delta^{13}$ C is -42‰ to -2.1‰ which is a significantly wider spread than the range of calcite  $\delta^{13}$ C. Simkus et al. (2016) argued that the lowest value (-42‰) is a result of anaerobic oxidation of microbial CH<sub>4</sub> (AOM), which decreases the  $\delta^{13}$ C by adding carbon  $^{13}$ C-poor into the DIC pool.

The wide range in calcite  $\delta^{13}$ C from the Welkom/Virginia, Evander and Orkney areas led Jaguin et al. (2010) to propose two different carbon sources. A lower  $\delta^{13}$ C (<-10‰ VPDB) source is probably associated with the organic matter found throughout the basin (Parnell et al., 1996; Gray et al., 1998; England et al., 2002; Drennan and Robb, 2006), and a higher  $\delta^{13}$ C (~-3‰) carbon source is associated with marine carbonates. Both Jaguin et al. (2010) and Nisson et al. (2023) discussed how this endmember could have either originated directly from Precambrian seawater or a fluid that inherited a DIC high in  $\delta^{13}$ C, after interaction with marine carbonates possibly from the overlying Transvaal Supergroup.

The  $\delta^{13}$ C results from this study are comparable to the results from Jaguin et al. (2010) for the Virginia area and consistent ultimately with the occurrence of two carbon sources The endmember with high  $\delta^{13}$ C is probably of marine origin.  $\delta^{13}$ C values around 0‰ are typical for a marine endmember, which are significantly enriched in  $^{13}$ C compared to magmatic or atmospheric sources (Wagner et al., 2018). There are two possible sources for low  $\delta^{13}$ C carbon:

- 1. Input from the oxidation of organic matter in Witwatersrand Supergroup or the Ventersdorp Contact Reef (VCR).
- 2. Inputs from microbial methane ( $\delta^{13}$ C ~-50% or lower) processed by AOM to form CO<sub>2</sub>, that then dissolved and added to the DIC pool.

The second scenario might be plausible because methanotrophic communities have been identified across the basin (Simkus et al., 2016; Lau et al., 2016; Liu et al., 2023). AOM can drive the  $\delta^{13}$ C of the DIC to values as low as -42‰, as observed by Simkus et al. (2016) and Lau et al. (2016). The produced CO<sub>2</sub> is typically enriched by 5-15‰ relative to methane, based on the fractionation factors displayed in Chapter 2 and reported in previous studies

(Holler et al., 2009; Wegener et al., 2021; Liu et al., 2023). However, this scenario is unlikely since the majority of calcites have precipitated at temperatures exceeding the limit of life even for hyperthermophilic communities, which can survive at temperatures up to 122°C (Takai et al., 2008). An alternative explanation would require the DIC from AOM to have been generated at shallower depths, where lower temperatures could have allowed microbial activity. Even taking into account the greater thermal gradient (18°C/km) in the geological past (Omar et al., 2003), this would still require extreme temperatures for microbial activities. Therefore, the contribution of AOM into the DIC is considered unlikely under these conditions and more likely in the modern environment.

Consequently, it is likely that the lowest in  $\delta^{13}$ C derives from the organic matter that is widely present in the Ventersdorp contact reef (VCR) and the Witwatersrand Supergroup. The  $\delta^{13}$ C from the organic matter across the Witwatersrand varies between approximately -30‰ and -22‰ (Spangenberg and Frimmel, 2001), while the  $\delta^{13}$ C of the organic matter from beyond the Virginia area was at the higher end of this range (Hoefs and Schidlowski, 1967). The CO<sub>2</sub> produced by the thermal oxidation of organic matter should be moderately enriched in  $^{13}$ C compared to the initial organic matter, at approximately 1 to 5‰ (Andresen et al., 1994). Therefore, the CO<sub>2</sub> produced from the organic matter in the Witwatersrand Supegroup should have an initial isotopic composition between -21‰ to -17‰. Using the fractionation factor for CaCO<sub>3(s)</sub>-CO<sub>2(g)</sub> reported by Emrich et al. (1970) and Romanek et al. (1992), the expected  $\delta^{13}$ C of carbonates should be between -14‰ to -10‰. Similarly, based on the fractionation factor for CaCO<sub>3(s)</sub>-HCO<sub>3</sub>, the  $\delta^{13}$ C of the DIC should be in the range of -15 to -11‰.

The high- $\delta^{13}$ C endmember was proposed to be of marine origin from an unknown source(Jaguin et al. 2010). that the absence of marine carbonates in the upper Witwatersrand Supergroup and throughout the Ventersdorp Supergroup leads to the suggestion that it originates eitheras seawater trapped within the deposition of the West Rand (Frimmel, 2019; Nisson et al., 2023), or in a downward migrating fluid that has dissolved marine carbonates from the Transvaal Supergroup. Given the long tectonic activity in Witwatersrand basin resulting into the uplift of the basin (Coward et al., 1995; Mkhabela and Manzi, 2017), the erosion and weathering of Transvaal Supergroup in Virginia area and the eastern section of the basin (Ward et al., 2004), and the occurrence of dykes and thrust faults across the basin (Winter, 1995), either source for the marine endmember is possible. The marine endmember proposed in this study with  $\delta^{13}$ C at approximately -1.5‰, is compatible with the range of  $\delta^{13}$ C (-3 to 0‰) for the Transvaal limestones (Beukes et al., 1990; Bau et al., 1999;

Frauenstein et al., 2009). Therefore, I suggest that the marine endmember likely originates from the Transvaal limestones and was transported within the fracture system from a fluid entering the fracture system and was migrating downwards.

Based on the values calculated for both endmembers, estimations can be made regarding the contribution of each source into the carbon pool where calcites precipitated. For the endmember associated with the organic matter, I use the lower value in the range (-14‰) provided because both calibrations from Emrich et al. (1970) and Romanek et al. (1992) are in a range of temperatures (10-60°C) considerably below than the precipitation temperatures of the calcites. For this reason, the fractionation factor for  $CaCO_{3(s)}$ - $CO_{2(g)}$  should be lower due to the higher prevailing temperatures, and the  $\delta^{13}C$  of the calcite closer to the lower end of the range. Hence, I conclude that based on those assigned values for each endmember the maximum contribution of the source of carbon associated with the organic matter should be at maximum 40% at the sample with the lowest  $\delta^{13}C$  (~ -9.0‰) and 0% at the sample with the highest  $\delta^{13}C$  (~ -1.5‰).

# 5.7.3. Isotopic Constraints on the Precipitating Fluid

In this section, I provide constraints related to the oxygen isotopic composition in the precipitating fluid, calculated using the  $T_{47}$  and  $\delta^{18}O$  values of the calcite from equation 5.5 (Kim and O'Neil, 1997; Bajnai, 2023). In addition, I compare the values inferred to the values of the  $\delta^{18}O$  reported in literature for the fracture fluids across the Witwatersrand basin or other Precambrian basins.

#### 5.7.3.1. Fluid $\delta^{18}$ O

The  $\delta^{18}O_{fluid}$  of the fluid ranges between -8.1± 0.7‰ for calcite with the lowest precipitation temperature ( $T_{47} = 64^{\circ}C$ ) to 5.5±1.0 ‰ for the calcite with the highest precipitation temperature ( $T_{47} = 207^{\circ}C$ ). These values cover a larger range than the reported values in Warr et al. (2021) for the current fracture fluids in Virginia area which range between -8.7‰ to -4.4‰. Based on that and the precipitation temperatures of the calcites calculated, it could be argued that only a small fraction of the calcites in the veins is associated with the current fluid and that the majority of the calcites have either originated from a different fluid and/or that the fluid has been submitted to alterations over geological timescales (Nisson et al., 2023). The latter can be supported by the long residence times (from 0.77 to 136 Ma) calculated and reported by Lippmann et al. (2003) and Heard et al. (2018) using noble gas residence times. The residence times for fracture fluids sampled within or close to the Virginia gas field were the highest across the basin, ranging between 39 to 136Ma and at least an order of magnitude higher than the other samples and localities.

The maximum  $\delta^{18}O_{fluid}$  value is compatible with the range of hydrothermal fluids (typically from 3‰ to 15‰, Kerrich and Ludden, 2000; Grove and Harris et al.,2010; Warr et al., 2021; Nisson et al., 2023). This is in agreement with findings from other studies which proposed the circulation of hydrothermal fluids within the basin (Frimmel et al., 1999). The origin of hydrothermal fluids is important to understand in the basin as hydrothermal events are often associated with the mineralisation and/or mobilisation of the gold (Tucker et al., 2016). Frimmel et al. (1999) suggested, based on fluid inclusions from the reefs and veins in the VCR, that the circulating fluid could be either of metamorphic origin, having acquired its characteristics after interacting with the rocks in the Ventersdorp Supergroup, or of meteoric origin after acquiring the DIC from the limestones of the Transvaal Supergroup as it descended from the surface to the bottom of the basin through fractures.

Zhao et al. (2004), based on measurements of oxygen isotopes in quartz and calcites veins in the VCR, suggested that these veins are a result of the circulation of a hydrothermal fluid, while Drennan and Robb (2006) and Jaguin et al. (2010) proposed a mixture of hydrothermal and meteoric fluids. Finally, Nisson et al. (2023) suggested contributions from Precambrian seawater.

Based on the  $\delta^{18}O_{\text{fluid}}$  coupled with the apparent temperatures  $T_{47}$ , I suggest that the circulating fracture fluid in Virginia is likely the result of mixing between a hydrothermal and meteoric water which infiltrated the fracture system from the surface. For the hydrothermal endmember, I assume that it is identical to the endmember with the highest  $\delta^{18}O_{\text{fluid}}$  (5.5%) at 200°C. This temperature is significantly lower than the postulated temperature (350°C) of the hydrothermal fluid in the basin (Gray et al., 1998; Fuchs et al., 2021), however the fluid has likely undergone cooling before the Karoo deposition. It is challenging to constrain the  $\delta^{18}O_{fluid}$  of the meteoric component as other processes are taking place concurrently with the mixture of the two fluids. For example, the cooling of the basin, along with the exchange of oxygen between the fluid and the O-bearing host rocks, tends to lower the fluid  $\delta^{18}O$  (Warr et al., 2021). Therefore, it would be risky to assume that the sample which yields the lowest  $\delta^{18}$ O for the fluid is the potential meteoric endmember as it is likely affected by the cooling of the basin and has exchanged oxygen atoms with the surrounding minerals (Jaguin et al., 2010), considering also the long residence and circulation time within the fractures over millions of years (Lippmann et al., 2003; Heard et al., 2018). Both isotopic exchange and cooling could have also altered the  $\delta^{18}$ O of the hydrothermal endmember and should be considered when constraining the fluid endmembers.

Nevertheless, I attempt to give some constraints on the palaeometeoric water endmember based on the results and previous studies. According to Heard et al. (2018), the majority of fracture water samples from the Witwatersrand basin exhibit values close to the modern local meteoric water from Pretoria with  $\delta^{18}\text{O}\sim-3\%$ , while samples from the Virginia gas field are on the GMWL (Global Water Meteoric Line) but considerably enriched in  $^{18}\text{O}$  from the meteoric water in Pretoria. Instead, Heard et al. (2018) pointed out that fracture water from Virginia is isotopically similar to the meteoric water from the Lesotho Highlands (-7.5%  $\leq \delta^{18}\text{O} \leq -5.5\%$ ), and concluded that could be due to an identical hydrological regime occurring in the Lesotho Highlands, compatible also with the long residence times observed in Welkom area. However, the majority of the calcites we sampled indicate fluids substantially higher in  $\delta^{18}\text{O}$  (-4% to 6%) which deposited either at different conditions and/or from a different fluid.

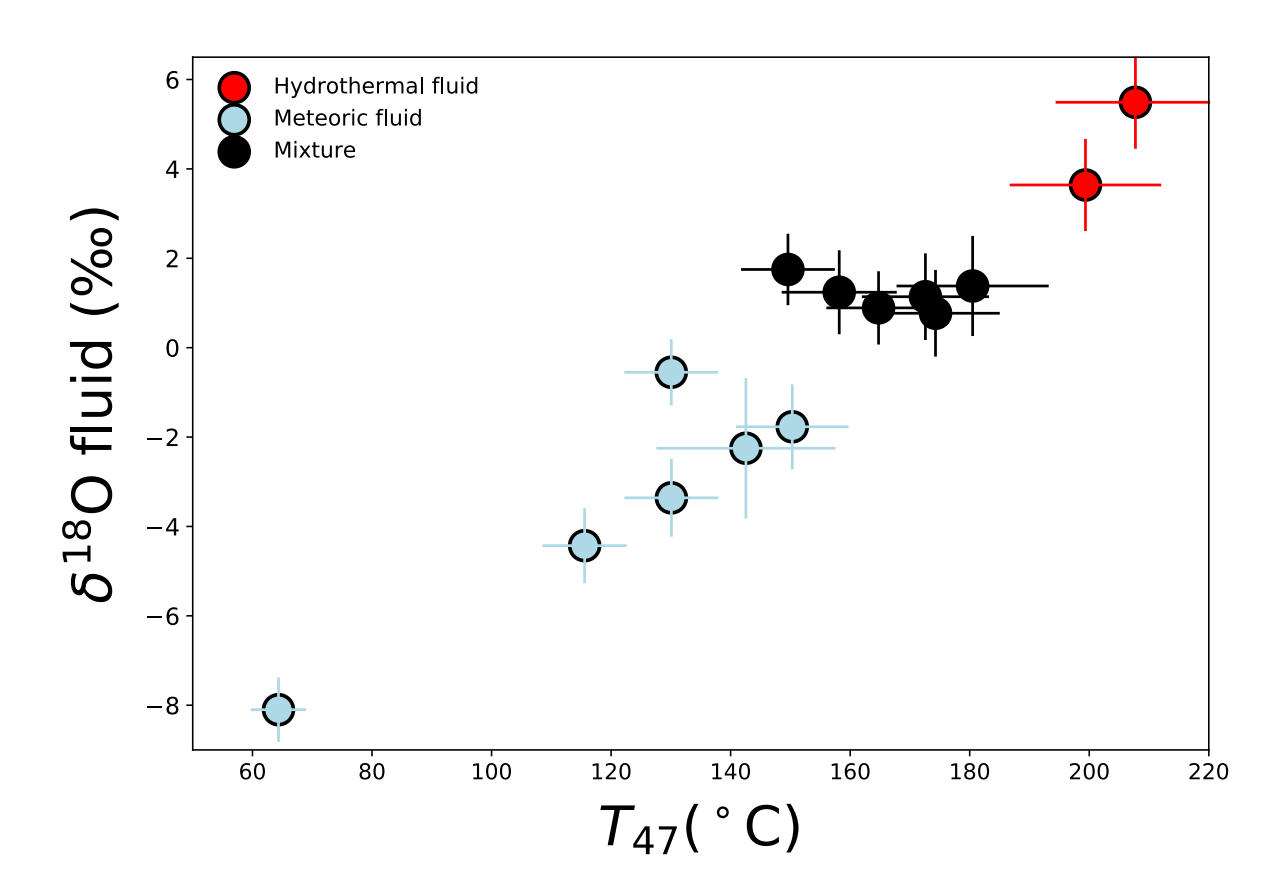


Figure 5.10: T<sub>47</sub> vs  $\delta^{18}O$  (VSMOW) of the fluids proposed to occur within the fracture system.

The dataset indicates the mixing of two fluids: a hydrothermal fluid with  $\delta^{18}O$  at approximately 6% and the palaeometeoric water at maximum -4%. This range is higher

than the range of  $\delta^{18}$ O reported in Heard et al. (2018). It is important to highlight that there is no strong evidence to support that the modern meteoric fluid should necessarily have a similar isotopic composition with the palaeometeoric fluid which entered the basin especially when it has been resided in the fracture system over millions of years (Heard et al., 2018). Finally, in the absence of hydrogen isotopic data for the fracture fluids some trends or processes could be ambiguous to interpret or identify.

The contribution of each endmember can be calculated based on the  $\delta^{18}O$  of the two endmembers. For the palaeometeoric endmember, I did not consider the sample at ~65°C as it is either affected by low temperature isotope exchange of oxygen atoms between the fluid and rock minerals (Warr et al., 2021), or associated with the modern meteoric water in the basin given the  $\delta^{18}O$  and the precipitation temperature. For the calculations, I will assume that the rest of the samples are not affected by those processes. Consequently, for the samples between 0% and 2% assumed to be a result of mixing, a contribution of approximately 50% for each endmember is calculated, with an uncertainty of 10% considering the error in the  $\delta^{18}O$  of the fluid of approximately 1%. Additional uncertainties can arise from the assignment of the endmembers, due to the potential isotope exchange between the fluid and the host rocks.

Using the formation temperatures and the oxygen isotopes of the calcites I can constrain the characteristics of past fluids associated with the calcite deposition. This fluid is a mixture of hydrothermal fluid with a palaeometeoric water that entered the basin and is distinct from the modern fracture fluid measured by Ward et al. (2004) and Heard et al. (2018). This scenario is also internally consistent with the proposed origin of carbon, assuming the upward moving hydrothermal fluid has transported the DIC associated with the organic matter found in the sedimentary rocks of Witwatersrand Supergroup, and the palaeometeoric water has been moving downwards in the basin and transported the DIC associated with the Transvaal limestones into the faults.

# 5.7.4. Calcite-CH<sub>4</sub> Relationship

In sedimentary environments, the carbon in calcites and CH<sub>4</sub> can originate from the same source and/or formation or post-formation processes involving the calcites or CH<sub>4</sub> can affect the isotopic composition of DIC (Budai et al., 2002). As a result, either of these compounds can buffer the isotopic composition of the other. When the carbon in the DIC pool results from biological processes that can produce either distinctly extreme negative or positive  $\delta^{13}$ C values which are unlikely to result from other processes (Budai et al., 2002; Drake et al., 2015; Lloyd et al., 2016; Mizuno et al., 2023). As CH<sub>4</sub> is the dominant gaseous species within

the fracture fluids in the Virginia gas field and of great economic significance (Ward et al, 2004; Karolyte et al., 2022; Chapter 4), it is important to explore potential relationships with other carbon-bearing compounds in the fracture system such as the calcites. In theory, there are (at least) three potential ways for calcites-CH<sub>4</sub> to associated:

- I. The calcites are deposited after or during the methane formation and derive directly from the DIC affected by methanogenesis or produced by methanotrophy (see Chapter 4).
- II. CH<sub>4</sub> was generated after the deposition of calcites, either abiotically (e.g. Fischer-Tropsch reactions) or via methanogenesis, from the same DIC which produced the calcites.
- III. Calcites-DIC and CH<sub>4</sub> have no cogenetic link, however they have been transported within the fracture system by a common fluid.

These mechanisms are non-mutually exclusive and may overlap. For example, if the DIC and abiotic CH<sub>4</sub> were carried from the same circulating fluid, younger CH<sub>4</sub> could potentially form under favourable conditions either by abiotic or microbial processes over geological timescales.

Based on findings from Chapter 4 and previous studies (Ward et al., 2004; Simkus et al., 2016; Karolyte et al., 2022), methanogenesis is the dominant process of methane generation in Virginia, with smaller but significant amounts of abiotic methane (mean ~30%). Anaerobic methanotrophs actively consume a small fraction of the methane within the fractures, however the produced CO<sub>2</sub> mainly occurs in the liquid phase and typically below 0.5% in free gas phase (see Chapter 4). Therefore, the isotopic composition of carbon in DIC could have been affected by those processes, in a similar way as those observed in fracture-filling calcites in some sedimentary environments (Budai et al., 2002).

While Simkus et al. (2016) have reported  $\delta^{13}C_{DIC}$  in fracture fluids from Virginia consistent with DIC derived from methanotrophy (down to -42‰), the  $\delta^{13}C$  of calcites measured in this study are either not affected by AOM or only affected to a small degree, because even the lowest value (-9‰) of  $\delta^{13}C$  in calcites is considerably higher than the lowest reported  $\delta^{13}C_{DIC}$  (Simkus et al. 2016). Additionally, all but one of the T<sub>47</sub> are above the threshold of life at 122 °C (Takai et al., 2008), where no biological processes are expected to be active as even hypethermophilic microorganisms would not survive (Omar et al., 2003). This suggests that calcites were unlikely to have been deposited after

or during the generation of the methane currently present in the fractures of the basin and affected by microbial cycling(Chapter 4). Sample 7 ( $T_{47} = 64^{\circ}$ C) is the only one which could have been affected indirectly by microbial cycling of CH<sub>4</sub> as at this temperature both methanogenesis and methanotrophy can be active. Its  $\delta^{13}$ C (~-4.3%) does not, however indicate any obvious input from these processes.

Instead, a combination of scenarios II and III is more likely but overall difficult to constrain quantitatively with the current data. Two types of fluid inclusions have been isolated from the Witwatersrand Supergroup and VCR in Virginia area, one aqueous type of high salinity rich in CO<sub>2</sub>, with variable amounts of CH<sub>4</sub>, and one aqueous type with low salinity (Frimmel et al., 1999; Drennan and Robb, 2006; Jaguin et al., 2010). Therefore, CH<sub>4</sub> and DIC have coexisted in the same fluid, in support of mechanism III suggested. However, it is not clear whether there is a direct cogenetic relationship between calcites and methane. In addition, both types of fluid inclusions have homogenisation temperatures at approximately 135°C (Frimmel et al., 1999; Jaguin et al., 2010), consistent with the apparent temperatures for most calcites sampled. This suggests that DIC and abiotic CH<sub>4</sub> could have been transported from the same fluid which was circulating through the fractures and elevated towards the surface until the deposition of the calcites, while abiotic methane either diffused away if the system was open or remained within the fracture. However, there is a possibility that the methane collected from this study is not associated with the methane found in the fluid inclusions, as for example the elevated temperatures in the basin could have facilitated the production of thermogenic methane.

Because microbial CH<sub>4</sub> is the dominant component in the fracture fluid compared to the abiotic methane, it is important to discuss potential origins of the DIC involved. After 75 Ma, when the temperature dropped below 120°C (Omar et al., 2003), methanogens may have utilized DIC from three potential sources; the pre-existing DIC in the fracture system derived from the oxidation of organic matter and transported by the hydrothermal fluids, the DIC associated with the Transvaal limestones and carried by the paleometeoric fluids, or a mixture of both.

There is no clear association between the calcites and the methane sampled and measured in Chapter 4. In fact, the majority of the methane accumulated in the fractures has likely been produced after the calcite deposition. If any relationship exists between those two phases of carbon in Virginia, this would be between the calcites and the abiotic methane which is only in a minor component in the gas mixture (Ward et al. (2004); Karolyte et

al., (2022); Chapter 4 of this work). Future studies the isotopic composition of carbon in DIC and CH<sub>4</sub> in fluid inclusions could reveal or reject the potential association proposed based on the expected fractionation between DIC-CH<sub>4</sub> within the homogenisation temperature range.

#### 5.8. Conclusions

The calcite veins have precipitated at temperatures between 65 to 220°C in the fracture system of Virginia gas field. This is a clear indication that those calcites have precipitated at diverse conditions, different from those prevailing at the basin the last million years. Using radiometric techniques such as U-Pb dating on the calcites could improve our understanding of the basin and point out events related to the precipitation of the calcites, such as the infiltration of the hydrothermal and meteoric fluids or the Vredefort meteorite impact. The  $\delta^{13}$ C and  $\delta^{18}$ O values suggest two distinct carbon sources and a mixture of different fluids circulating in the basin. The paleometeoric fluid (low in  $\delta^{18}$ O) has circulated in the basin and transported DIC of marine origin (high in  $\delta^{13}$ C), possibly derived from the Transvaal limestones. The hydrothermal fluid (high in  $\delta^{18}$ O) has ascended from the sedimentary rocks of Witwatersrand Supergroup or deeper carrying DIC associated with oxidation of organic matter. The calcites have no direct connection to the microbial methane as they do not precipitate from the CO<sub>2</sub> produced by the AOM. This can be supported by the differences in  $\delta^{13}$ C and the precipitation temperatures of the calcites, where the majority is higher than the limit of life at 122°C.

# 6. Conclusions

#### 6.1. Overview

In this chapter, I summarise the key contributions of this thesis concerning the method development and scientific findings. In addition, I discuss the limitations and advantages of my approach and suggest further steps where applicable.

## **6.1.1.** Analytical Developments

A significant part of this work has been devoted to method development, in order to measure precisely and accurately the clumped isotopic compositions of CH<sub>4</sub> in the Clumped Isotope laboratory of SUERC. Before introduction into the dual-inlet of the mass spectrometer, any gas mixture is required to be purified. To purify methane and achieve the required purity (>99.9%), I used a cryostat and developed, optimised and tested purification methods to remove other gaseous species often found in natural gas mixtures. In addition, I have designed and conducted equilibration experiments in order to produce equilibrated aliquots of CH<sub>4</sub>. These equilibrated aliquots can be used as anchor points and report the samples measured in SUERC into the thermodynamic reference frame.

I have developed and validated mass spectrometry methods for the measurement of bulk and clumped isotopic compositions of methane using a high-resolution mass spectrometer, the ThermoFisher MAT Ultra. Due to variations in the performance of the Ultras across laboratories (Eldridge et al., 2019; Mangenot et al., 2021; Zhang et al., 2021; Wang et al., 2023; Sivan et al., 2024), the methods cannot be directly used. Therefore, it has been necessary to adapt and optimise the methods based on the performance of the Ultra hosted at SUERC. The SUERC Ultra consistently achieves mass resolving powers of up to 42,000 in HR+ mode and 28,000 in HR mode, which differs from the performance reported by other laboratories (>45k in HR+ and ~30k in HR mode). For this reason, background corrections and frequent peak position determination were implemented to ensure optimal accuracy and reproducibility of the data measured in SUERC. Using a size sample of 70  $\mu$ mol and after a total measurement time of 20-25 hours, the SUERC Ultra can achieve internal precisions of 0.01‰, 0.12‰, 0.3‰ and 1.5-2.0‰ for the measurements of  $\delta^{13}$ C,  $\delta$ D,  $\delta^{13}$ CH<sub>3</sub>D and  $\delta^{12}$ CH<sub>2</sub>D<sub>2</sub>, respectively.

I have also developed and applied tools for data processing to filter out outliers, propagate errors, and calculate the final values for the bulk and clumped isotopic signatures of CH<sub>4</sub>. All the techniques and tools developed through this work are now part of routine measurements in the Clumped Isotope laboratory of SUERC.

Future developments should include the testing of the cryogenic method for purification at different amounts of CH<sub>4</sub>. The method has been tested in the Virginia gases where the methane amounts ranged from 77% to 99%, and the equilibrated gases while are mainly consisting of methane. However, it will be valuable to test the purification method in gas mixtures with lower percentages of CH<sub>4</sub> (<50%). Other developments could include the automation of the cryostat and the vacuum line to accelerate the purification process and hence the throughput of samples. Another way to increase throughput of samples in the laboratory, it is to fully automate the measurement methodology using the Qtegra software and run all measurements subsequently. This will reduce the time between the measurements, however it is indeed a very challenging task, as it requires very stable conditions for the mass spectrometer.

## 6.1.2. Methane in Virginia Gas Field

I used measurements of the bulk and clumped isotopologues of methane in gas samples from the Virginia gas field in South Africa to understand the origin of methane. This gas accumulation is a world-class helium deposit. The helium content of the gas ranges from 1 to 12%, substantially higher than the economic limit of He recovery at 0.1% (Danabalan et al., 2022). The gas mixture is largely dominated by CH<sub>4</sub> (70-90%) but its origin is not well constrained. Gas samples have been collected in a fieldwork campaign in Virginia gas field in October 2022 at the southwestern section of Witwatersrand basin. Based on molecular and isotopic compositions, I concluded that the origin of methane in those samples is a mixture of microbial and abiotic sources, with a negligible at best thermogenic contribution. The results are consistent with a mixing model between a microbial endmember at the thermodynamic equilibrium curve at 25°C and an abiotic endmember with a deficit in  $\Delta^{12}$ CH<sub>2</sub>D<sub>2</sub> of approximately -10% from the thermodynamic equilibrium curve. Based on the clumped isotopic compositions of methane, I have identified the re-processing of CH<sub>4</sub> through the anaerobic oxidation of methane (AOM), which was not apparent with only the bulk isotopic compositions. Using a model for the effect of reprocessing methane by AOM, developed by Liu et al. (2024), my data indicate a CH<sub>4</sub> consumption by methanotrophic communities of maximum 1-2% of the methane accumulation.

Those findings have allowed the revision of the prevailing model suggested by Karolyte et al. (2022), under which radioactive decay is the main process that produces He (via alpha decay) and H<sub>2</sub> (via radiolysis of water), where the latter one is utilised by methanogens to produce CH<sub>4</sub>. Given the lack of H<sub>2</sub> (assuming it is all converted into methane by methanogenesis), there should be a correlation between the proportion of microbial methane

(indicated by lower  $\delta^{13}$ C) and He. However, a clear association between helium content and  $\delta^{13}$ C of the gases is not observed (Appendix). Therefore, either the radiolysis is not the main driver for CH<sub>4</sub> production as previously thought, or the CH<sub>4</sub>-He relationship has changed over geological time due to physical, chemical or biologically-mediated processes.

The study of the gases in Virginia gas field and in the wider Witwatersrand basin, can be used as an analogue to identify "atypical" gas fields worldwide, with a potential for helium reserves of substantial economic and strategic significance.

## 6.1.3. Calcites in Virginia Gas Field

Methane is the most dominant gas in the gas mixture of Virginia, with only traces (<0.4%) of CO<sub>2</sub> measured in the gas mix. However, calcites veins are present in a fracture network, where the gases reside over millions of years in some cases (Lippmann et al., 2003). The studies of calcite veins have been useful to understand the carbon cycle in geological systems, while they often interact with methane (Shemesh et al., 1992; Mizuno et al., 2023). In this thesis, I utilise the  $\delta^{13}$ C,  $\delta^{18}$ O, and  $\Delta_{47}$  of calcites in order to understand the origin of carbon, the origin of the precipitating fluid in the basin, and investigate if any association occurs between the CH<sub>4</sub> and the calcite in the Virginia gas field.

The apparent temperatures derived from  $\Delta_{47}$  indicate a wide range from approximately 65 to 220°C and suggest several precipitation events for the calcites at temperatures well above those prevailing at the basin in the last million years. Those temperatures are in good agreement with homogenisation temperatures from fluid inclusions studied by Jaguin et al. (2010) and Frimmel et al. (1999) in the Virginia gas field and the wider Witwatersrand basin. Thus, the apparent temperatures are expected to be growth temperatures of the calcites and not a result of bond reording. Additional measurements, such as U-Pb dating could provide constraints on the age of precipitation for the calcites. This can potentially pinpoint the geological events responsible for the DIC-bearing fluid circulation and the calcite precipitation.

The  $\delta^{13}$ C values suggest two sources of carbon in the Virginia gas field. The endmember high in  $\delta^{13}$ C (-1.5‰) is consistent with a marine origin, possibly associated with the marine carbonates from the eroded Transvaal Supegroup in the SW section of the Witwatersrand. The lower in  $\delta^{13}$ C endmember (<-9‰) is consistent with a source of carbon associated with the oxidation of organic matter.

Based on the oxygen isotopic composition and the formation temperatures of the calcites, I identified two distinct fluids responsible for the formation of the calcites in the Virginia gas

field. The data suggest a mixture of two fluids, one higher in  $\delta^{18}O$  (>3‰) consistent with a hydrothermal origin, and one lower in  $\delta^{18}O$  of palaeometeoric origin which is isotopically distinct from the modern meteoric fluid measured previously. Hence, I conclude that the fluid circulation within the fractures is a mixture of two isotopically distinct fluids of different temperatures associated with different geological events or periods.

Considering the precipitation temperatures and the isotopic compositions of carbon in calcites and CH<sub>4</sub> (from Chapter 4), no clear relationship is observed between the calcite veins and CH<sub>4</sub>. Given that the majority of the CH<sub>4</sub> in the Virginia gas field is of microbial origin, and that microbes cannot survive at high temperatures (beyond 122°C) at which many of the calcites formed, methane was generated after the events leading to calcite precipitation. However, two possible scenarios can be considered; either CH<sub>4</sub> was produced (abiotically or microbially) from the same DIC pool from which calcites have formed, or there is no cogenetic link between calcites-CH<sub>4</sub> and they have simply been transported from the same fluid circulating within the fracture system. Understanding better the relationships between DIC, calcites and methane will provide a better understanding of the geochemical evolution of the Witwatersrand basin.

# **Appendices**

# Appendix I: Calculations of isotopic signatures for nonequilibrium processes

## **Mixing**

In this example, f is the fraction of gas A with bulk isotopic signatures  $\delta D_A$ ,  $\delta^{13}C_A$ , while gas B has a fraction of 1-f with bulk isotopic signatures  $\delta D_B$ ,  $\delta^{13}C_B$ :

$$\delta D_{mix} = \delta D_A \times f + \delta D_B \times (1 - f)$$
  
$$\delta^{13} C_{mix} = \delta^{13} C_A \times f + \delta^{13} C_B \times (1 - f)$$

Similarly, the ratio of abundances between the mass-18 (<sup>13</sup>CH<sub>3</sub>D or <sup>12</sup>CH<sub>2</sub>D<sub>2</sub>) and <sup>12</sup>CH<sub>4</sub> of clumped isotopologues should follow this linear relationship:

$$[R^{^{13}CH_3D}]_{mix} = [R^{^{13}CH_3D}]_A \times f + [R^{^{13}CH_3D}]_B \times (1 - f)$$
$$[R^{^{12}CH_2D_2}]_{mix} = [R^{^{12}CH_2D_2}]_A \times f + [R^{^{12}CH_2D_2}]_B \times (1 - f)$$

However, when calculating the clumped isotope signatures  $\Delta^{13}CH_3D$  or  $\Delta^{12}CH_2D_2$  of the mixed gas, the stochastic distribution of the mixing gas follows the equations below:

$$[R^{^{13}CH_3D}]_{mix,stoch} = 4 \times [^{13}C]_{mix} \times [H]_{mix}^3 \times [D]_{mix}$$
$$[R^{^{12}CH_2D_2}]_{mix,stoch} = 6 \times [^{12}C]_{mix} \times [H]_{mix}^2 \times [D]_{mix}^2$$

Using equations 2.35 & 2.36, the  $\Delta^{13}CH_3D$  and  $\Delta^{12}CH_2D_2$  of the mixing product can be calculated, assuming the prior calculation of the abundances for each isotope.

#### **Diffusion/Oxidation**

The calculations for diffusion and oxidation require the prior knowledge of the fractionation factors. For the diffusion, the fractionation factor is calculated through equation 2.38, while for oxidation some values can be found in Table 2.5 (obtained from the literature). Once, those are known the Rayleigh distillation model can be used as in equation 2.4. For the residual gas, the actual abundances of <sup>13</sup>CH<sub>3</sub>D or <sup>12</sup>CH<sub>2</sub>D<sub>2</sub> can be calculated as:

$$[^{13}CH_3D]_{residual} = [R^{^{13}CH_3D}]_{initial} \times (f^{a_{13}CH_3D-1}) \times [^{12}CH_4]_{residual}$$

$$[^{12}CH_2D_2]_{residual} = [R^{^{12}CH_2D_2}]_{initial} \times (f^{a_{12}CH_2D_2-1}) \times [^{12}CH_4]_{residual}$$

Once those are calculated along with the new stochastic distributions, the  $\Delta^{13}CH_3D$  and  $\Delta^{12}CH_2D_2$  of the residual gas can be calculated as a function of the fraction of the gas left.

# **Appendix II: Monte Carlo Simulations**

In this section, I investigated the robustness of modelling predictions for methane sink pathways. Using Monte Carlo simulations (n=100), I explore the impact of small changes in the fractionation factors on  $\Delta^{13}CH_3D$  and  $\Delta^{12}CH_2D_2$ . Three different scenarios are explored below.

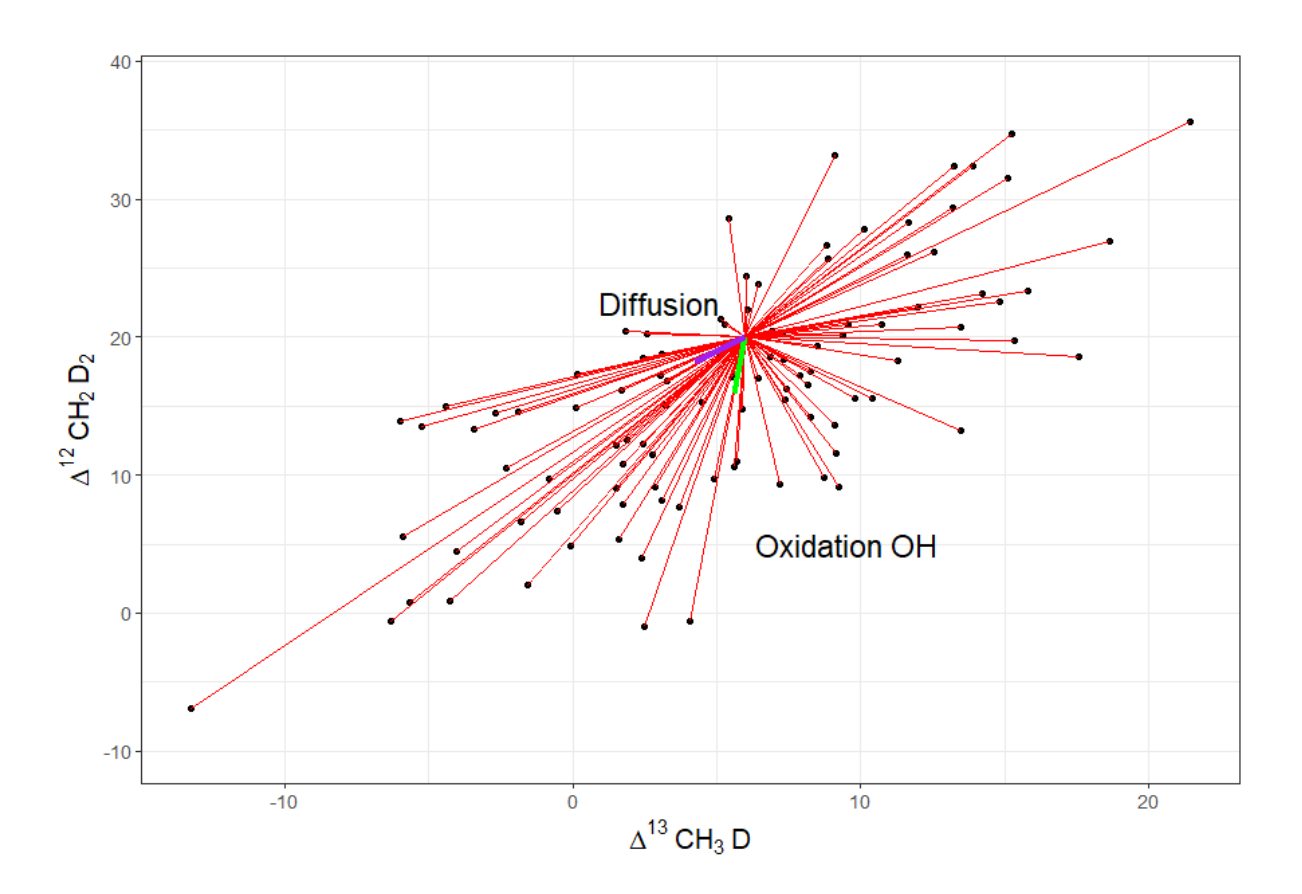


Figure 1: Monte Carlo simulation assuming a random error on the KIEs for OH oxidation at the last significant digit given. Diffusion trend indicated with purple line, OH oxidation pathway indicated with green line for the KIEs reported in Haghnegahdar et al. (2017). Black dot indicated 50% gas loss.

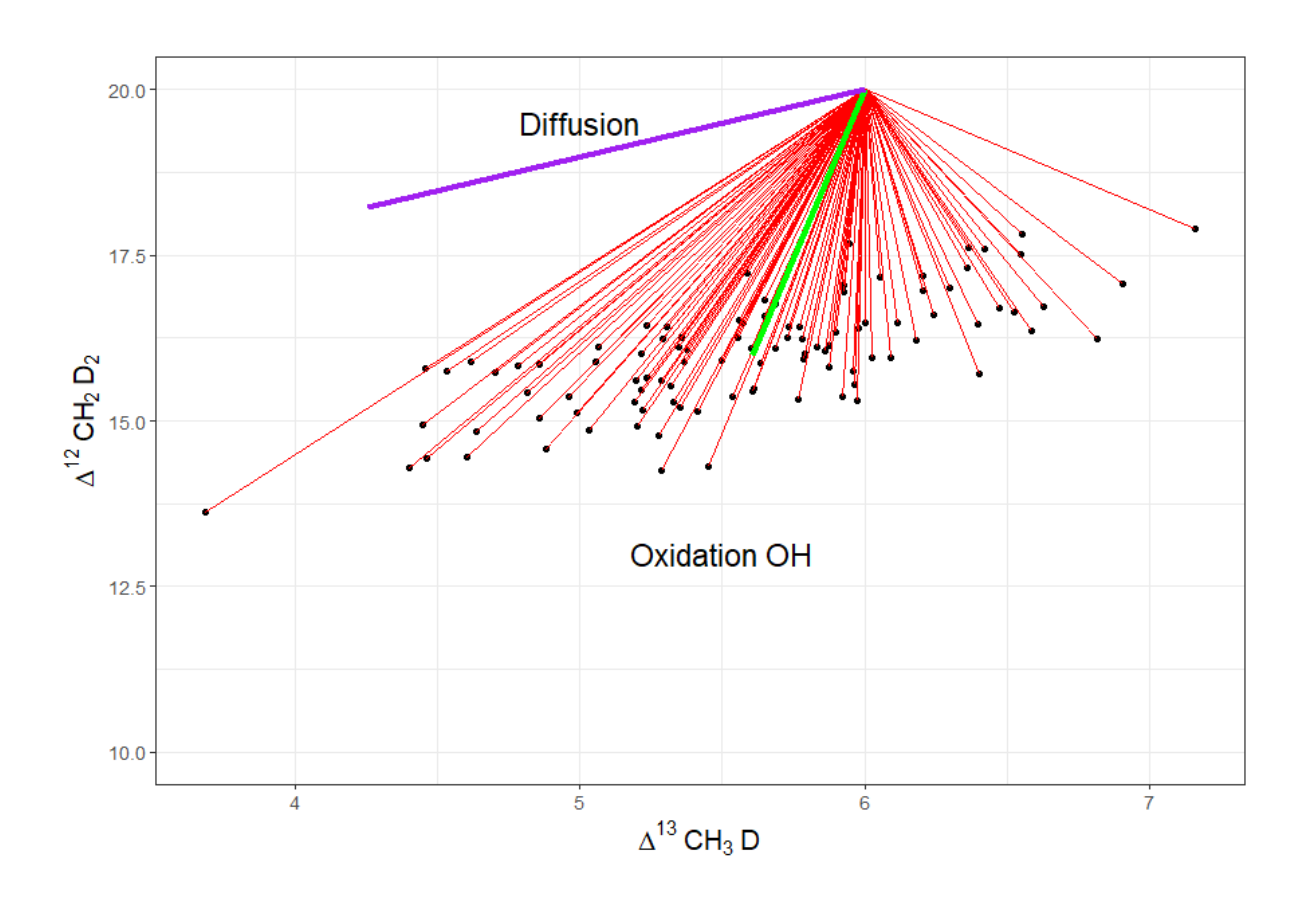


Figure 2: Monte Carlo simulation assuming a random error on the KIEs for OH oxidation at 1/10<sup>th</sup> of the initial error. Diffusion trend indicated with purple line, OH oxidation pathway indicated with green line for the KIEs reported in Haghnegahdar et al. (2017). Black dot indicated 50% gas loss.

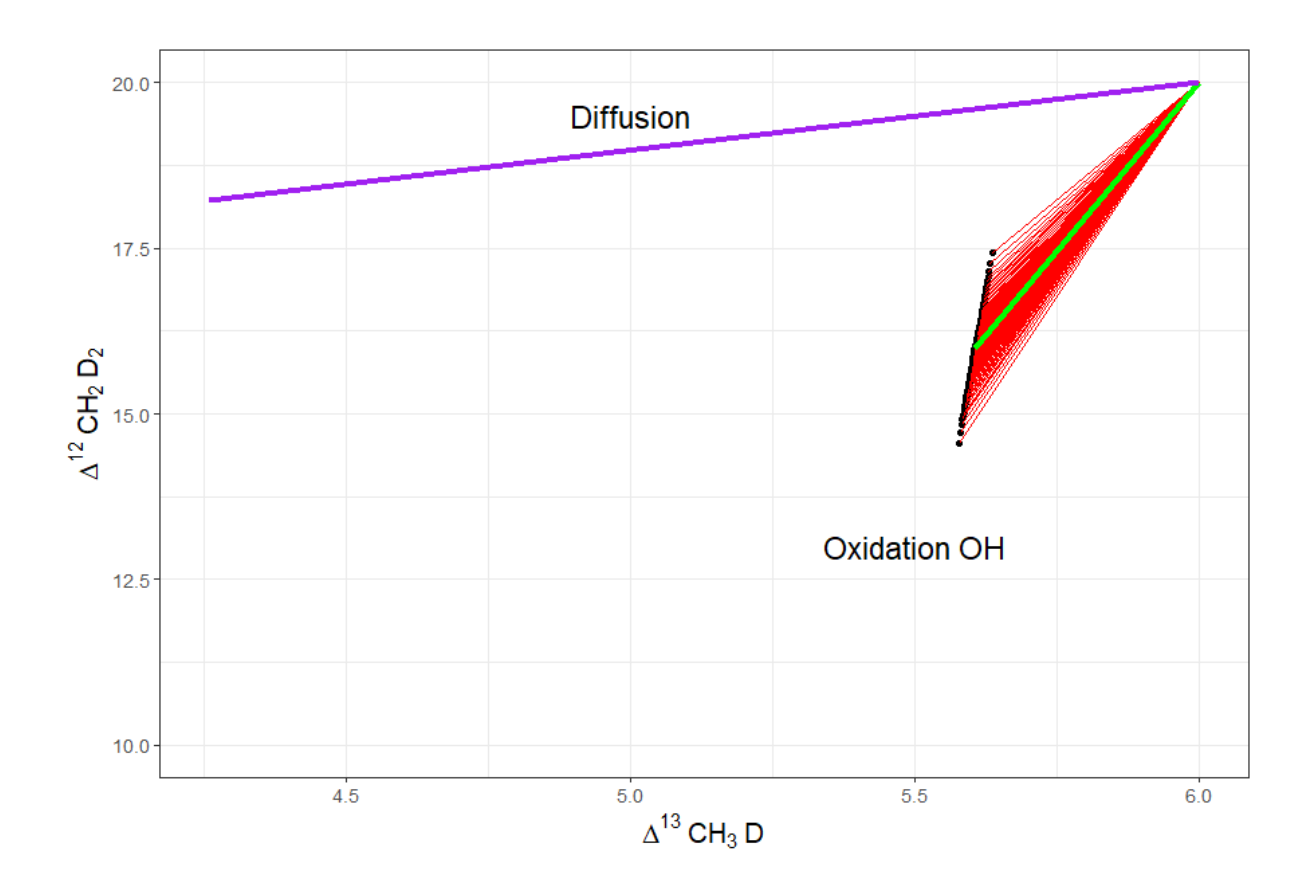


Figure 3: Monte Carlo simulation assuming a random error on the KIEs for OH oxidation at  $1/10^{th}$  of the initial error and assuming all the variables are correlated (r=1). Diffusion trend indicated with purple line, OH oxidation pathway indicated with green line for the KIEs reported in Haghnegahdar et al. (2017). Black dot indicated 50% gas loss.

# **Appendix III: Gas Chromatography and Mass Spectrometry Methodology**

### Gas Chromatography in SUERC

An injection gas chromatograph (GC) system was used for major gas composition measurements. The GC (Hewlett Packard 5890) uses a Hayesep-N stainless steel 1 mm internal diameter and 2.1 meters length packed column and a single filament thermal conductivity detector (TCD). This was used to identify and quantify the amount of air ( $N_2$  +  $O_2$  as a single peak), carbon dioxide, water vapour and hydrocarbon content ( $C_1$  to  $C_4$ ) in gas samples in 8 minutes. The gas components are passed through the column by a helium carrier gas, where the detector emits signal depending on the difference in thermal conductivity between the gases present in the sample compared to the carrier gas and the total amount of gas. Gas species arrive at different times at the TCD as they interact in a different way with the adsorbent material in the column. These different elution times from injection to the detector are known as retention times and can be found in Table S1.

Table 1: Retention times for each gas component identified by the current setup at SUERC.

Gas component	Retention Times (mins)
Nitrogen + Oxygen	0.63
Methane	0.89
Carbon dioxide	1.8
Ethane	2.43
Propane	4.14
Water	4.34
Butane	7.34

### **Preparation**

The GC system is connected to a helium cylinder to ensure a helium flow through the column and towards the detector. The helium pressure should be kept constant throughout the measurement at 35psi at the cylinder and 20 psi at the column head pressure. Once the helium flow is established, the oven and the detector can be activated. The oven temperature is

initially at 50°C and should be set at 150°C until the moment of injection, as it secures that the column is clean. If the system is not used for time periods above, a baking process at 150 °C between 30 mins and 60 mins is recommended. A blank measurement is suggested before the injection of standards or samples to confirm that the GC column is clean and water-free. Before the injection, the oven should be set at 50 °C and this normally requires 2-3mins for the system to cool down from 150 °C to 50 °C. As a last step, the button "Zero" on the GC controller allows to flatten out the baseline level usually between 10 to 14 mV. A negative value might be an indication of issues related to the helium stream and/or the detector.

#### Injection

The samples are introduced into the GC system through a rubber septum using a Trajan 100  $\mu$ L gas-tight syringe with a push-pull valve. Prior to the extraction, the syringe is connected to a vacuum line through a septum until the system reaches its baseline pressure in order to reduce the amount of air. Normally, 80 to 100  $\mu$ L of gas are sufficient for a gas composition measurement although that depends on the sample size. After the extraction of the gas, the syringe is locked using the push-pull valve and the sample is secured from atmospheric contamination. The syringe can be compressed between 20 to 50  $\mu$ L (depending on the initial sample pressure) before insertion to the GC system to reduce the amount of blank air in the injected sample. The syringe is transferred to the inlet of the GC and the sample is injected through the septum prior to unlocking the valve to allow the gas to expand into the GC column. Immediately after the injection, the start button on the GC controller should be pressed to begin the measurement.

Once the start button is pressed, the identified gas components will be observed on Data Acquisition option on Clarity software. The order of the peaks-components will follow the sequence presented in Table 1. The analysis takes about 8 mins to complete and 18-20 mins to present the results and bring the oven back to 50 °C. If another sample is going to be injected, the oven temperature should be set to 150 °C soon after the end of the previous analysis.

#### Working gas measurement

In this section, I describe the methods used to measure the C,H isotopes of the working gas (high purity CH<sub>4</sub>) in SUERC using conventional methods; firstly, the combustion of methane into water and carbon monoxide, and then introduction into two individual mass spectrometers. As described in Chapter 3, the precise determination of the bulk isotopic compositions  $\delta^{13}$ C and  $\delta$ D, is crucial to calculate the clumped isotopic compositions of CH<sub>4</sub>.

Initially, the tank of working gas is connected with the vacuum line, where the gas is expanded towards a U-trap immersed into an isopentane slush trap (-160°C) to capture any higher hydrocarbons (C<sub>2+</sub>), CO<sub>2</sub>, and water. At this temperature, methane is in gas phase and possible to isolate and handle across the line. The methane amount is semi-quantitatively determined using a pressure gauge, while a high purity oxygen (>99.9%) was added into the vacuum line, through a needle until pressure equilibration between the vacuum line and the atmosphere (Chen, 2021). The oxygen and methane mixture flows towards a platinumgranule furnace held at 960°C due to pressure gradient across the vacuum apparatus. The products of the CH<sub>4</sub> and O<sub>2</sub> reaction; CO<sub>2</sub> and H<sub>2</sub>O are both captured in a cold finger held at liquid nitrogen temperature (-196°C). Subsequently, any non-condensable gases are pumped out and the gases are separated by exchanging the liquid nitrogen trap to a dry ice – acetone slush trap (-80°C) which traps the water and releases the CO<sub>2</sub>. The CO<sub>2</sub> is expanded and trapped in an adjacent cold finger of calibrated volume, where the amount of gas can be determined. Both the CO<sub>2</sub> and H<sub>2</sub>O are isolated from the line using two removable containers equipped with valves for storage. The two analytes CO<sub>2</sub> and H<sub>2</sub>O are measured using two individual isotope ratio mass spectrometers to calculate the  $\delta^{13}$ C and  $\delta$ D, respectively.

The measurement of  $\delta^{13}$ C in CO<sub>2</sub> was conducted using a VG-SIRA II hosted in SUERC, which is a dual inlet isotope ratio mass spectrometer. The  $^{13}$ C/ $^{12}$ C ratio of the working gas was compared to the ratio of the reference standards NBS 19 and IAEA-CO-1. These reference materials have been widely used in the stable isotope community as standard reference materials (Ishimura et al., 2008). The  $\delta^{13}$ C of those standards is well-defined against the VPDB international standard, which allows the results to be easily reported into VPDB scale.

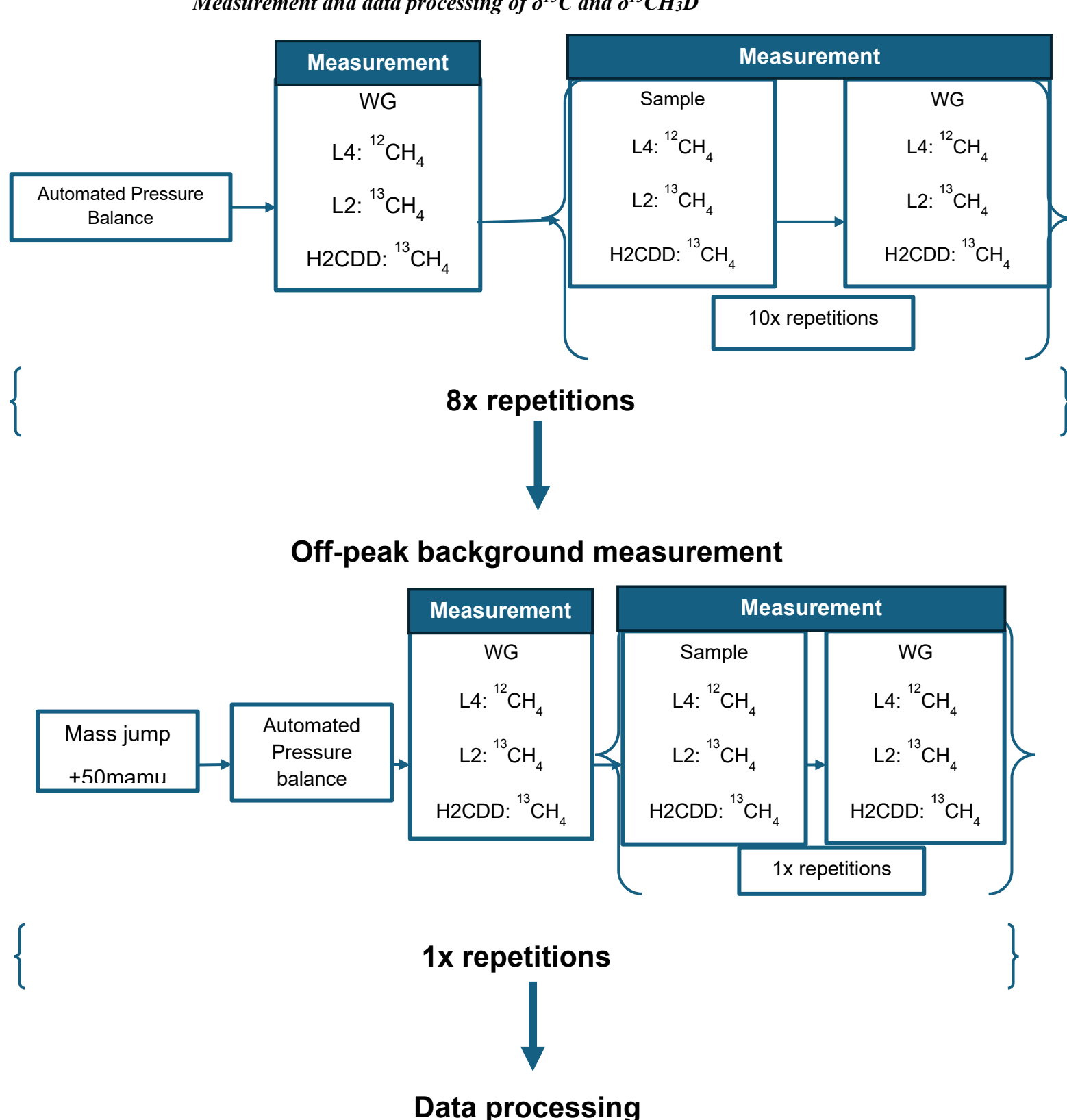
The tube containing the water produced from the CH<sub>4</sub>- O<sub>2</sub> reaction was connected to a preparation line attached to a VG Optima IRMS (Donnelly et al., 2001; Chen, 2021). This preparation line is equipped with a furnace held at 800 °C, which includes a chromium catalyst in order to reduce the H<sub>2</sub>O into H<sub>2</sub>. Initially, the tube is heated three times (or more time if water droplets can be traced into the system) using a heat gun to evaporate water and transfer it across the line. The water is captured into a cold finger held at liquid nitrogen temperatures (see above). The cold finger is heated three times thoroughly, to avoid any isotopic fractionation arising due to the evaporation and the movement of the water across the preparation line. The water is moved towards the furnace described above. The produced H<sub>2</sub> is expanded into the bellows of the mass spectrometer, where the δD of the working gas

can be determined. The VG Optima is calibrated in a daily basis using in-house standards of known isotopic composition against VSMOW scale (Donnelly et al., 2001; Chen, 2021).

The measurement of the working gas yielded external reproducibility ( $1\sigma$ ) of 0.05% for  $\delta^{13}C$  and 3% for  $\delta D$  over three measurements within a four-month period. More information about the purification and handling processes, and stable isotope measurements of carbon and hydrogen in SUERC can be found in Chen (2021).

## **Data processing**

Measurement and data processing of  $\delta^{13}C$  and  $\delta^{13}CH_3D$ 

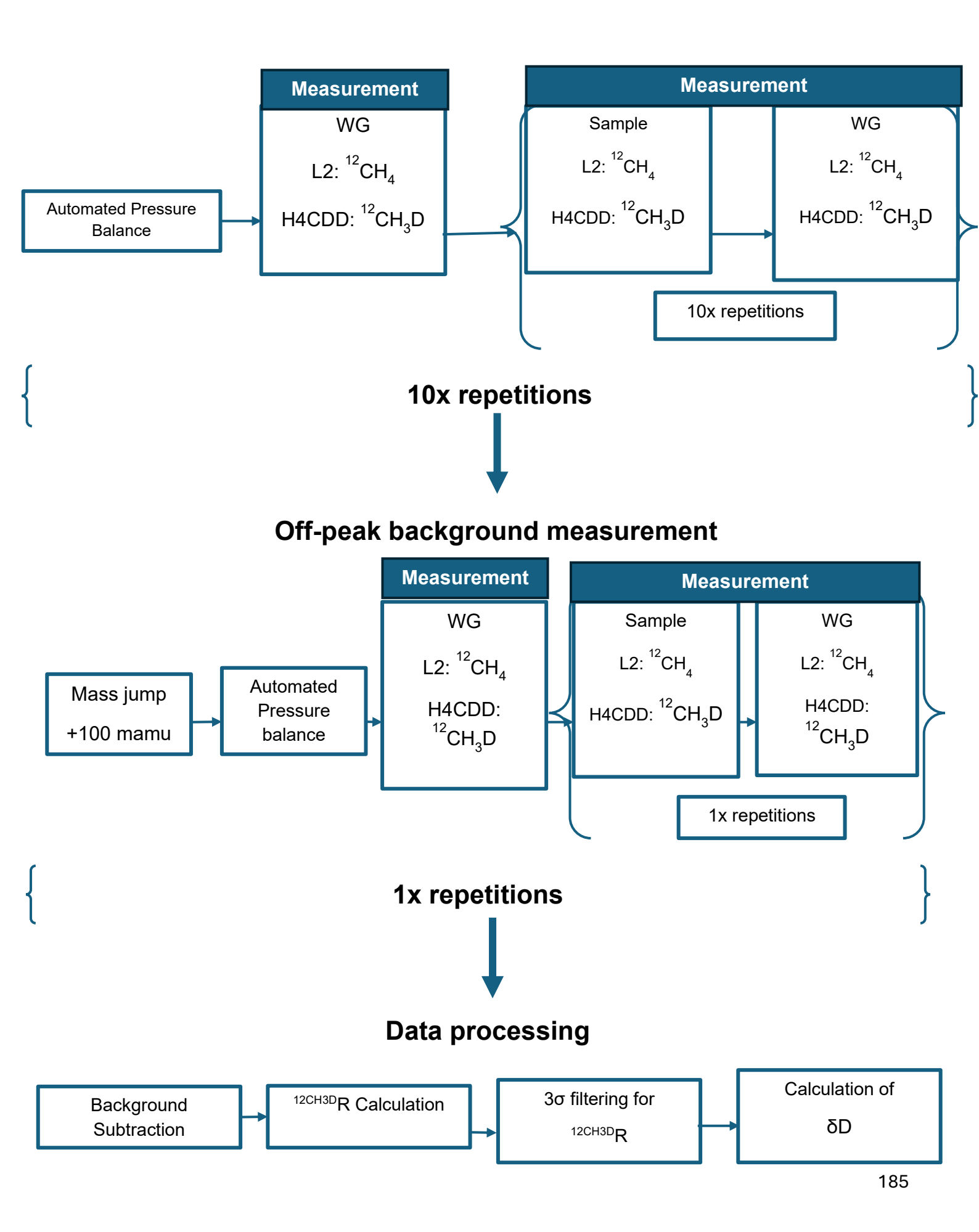


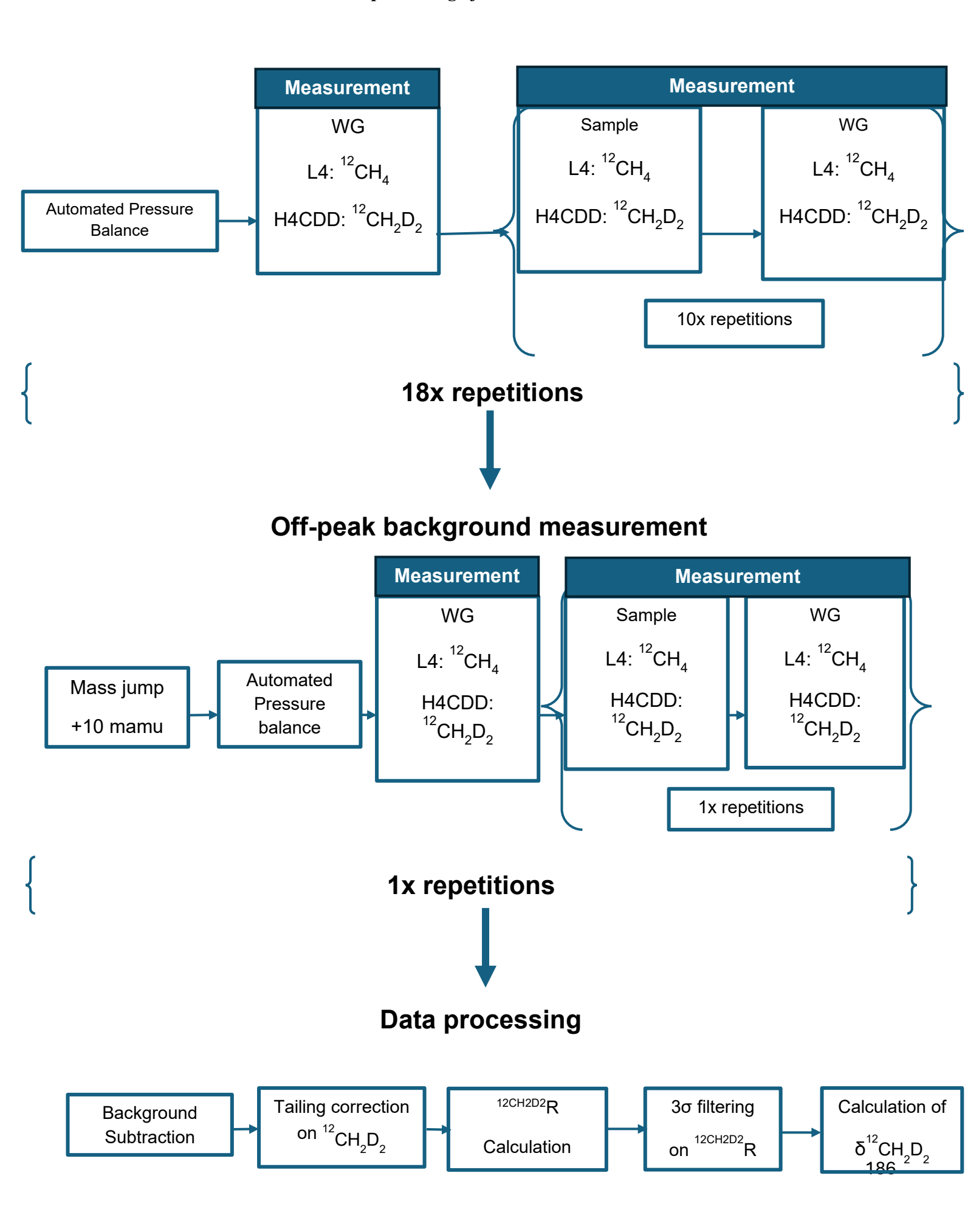
Background
Subtraction

13R & <sup>13CH3D</sup>R
Calculation

3σ filtering for

δ<sup>13</sup>C & δ<sup>13</sup>C H D
1884





# Appendix IV: Sampling map

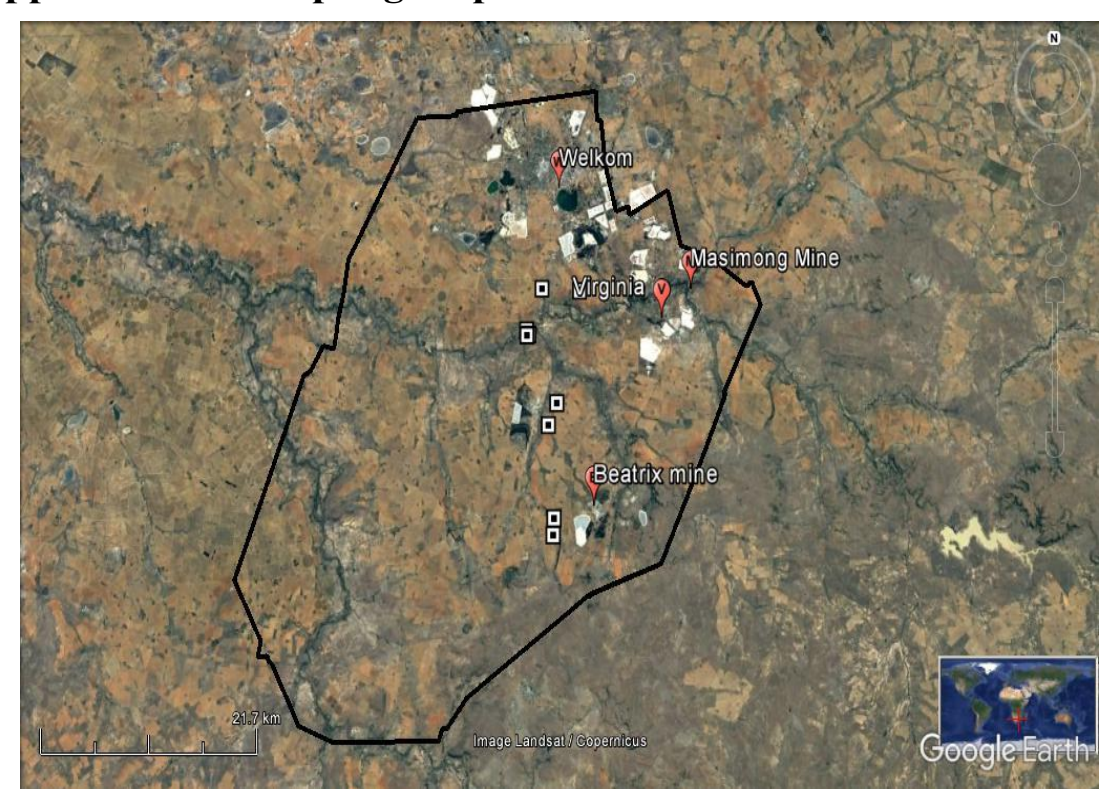


Figure 1: Map of sampled wells within Virginia gas field (black border) and adjacent gold mine and towns at Witwatersrand basin, South Africa.

# **Appendix V: Molecular and Isotopic Composition of Virginia** samples

Table 1: Summary of results for isotopic measurements of Virginia gas samples.

Sample	δ <sup>13</sup> C (‰)	δD (‰)	$\Delta^{13}$ CH <sub>3</sub> D	$\Delta^{12}\text{CH}_2\text{D}_2$
	(VPDB)	(VSMOW)	(‰)	(‰)
P15	-44.1	-218.7	13.6	6.81
MDR01	-55.7	-224	-	-
СЗРО	-48.1	-220.7	6.44	9.06
R2D2	-48.5	-219.8	6.34	11.83
NEA02	-58.8	-221.1	9.69	10.92
SPG3	-52.7	-215.2	7.47	12.93
EX01	-48.2	-220.8	6.69	10.7
PO7	-41.6	-220.6	8.3	8.94
ST23	-51	-226.5	-	-
HDR01	-49.2	-220.1	6.96	20.8
2190A	-50	-225	7.26	9.53

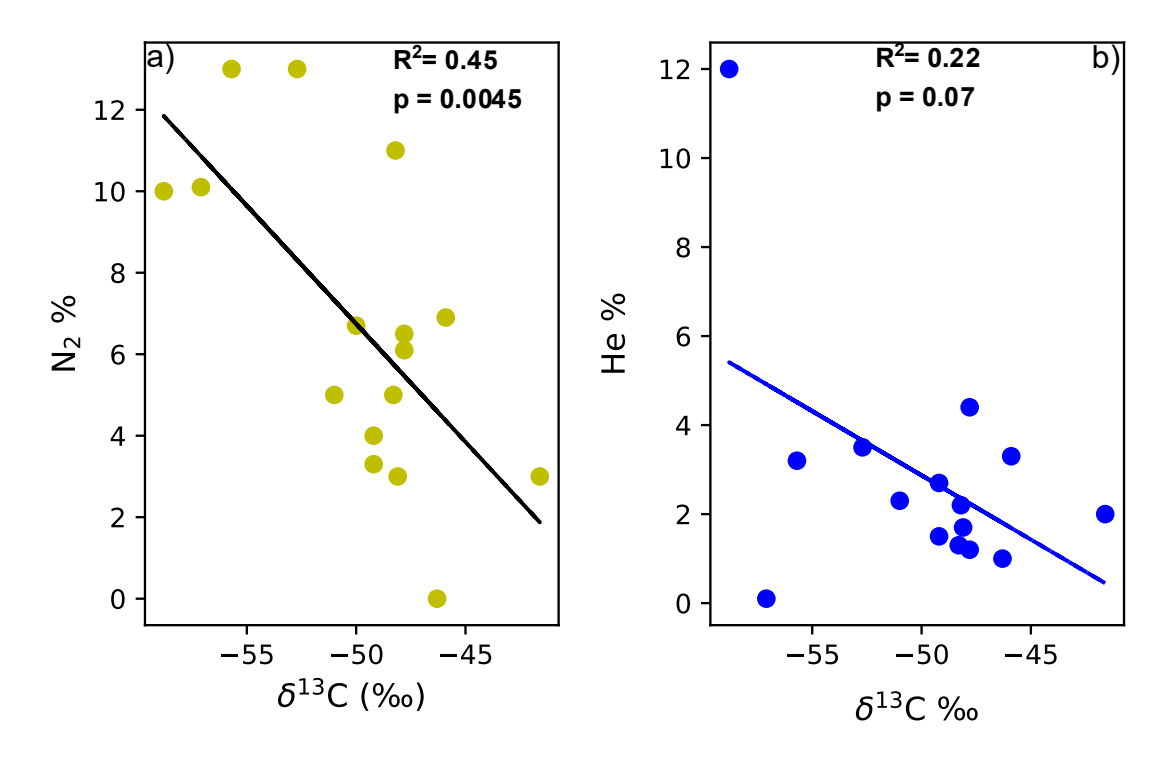


Figure 2: Regression plots and statistics of  $\delta^{13}C$  against  $N_2$  and helium, demonstrating the relationships between  $\delta^{13}C$  and gas concentrations.

# Appendix VI: AOM model outputs

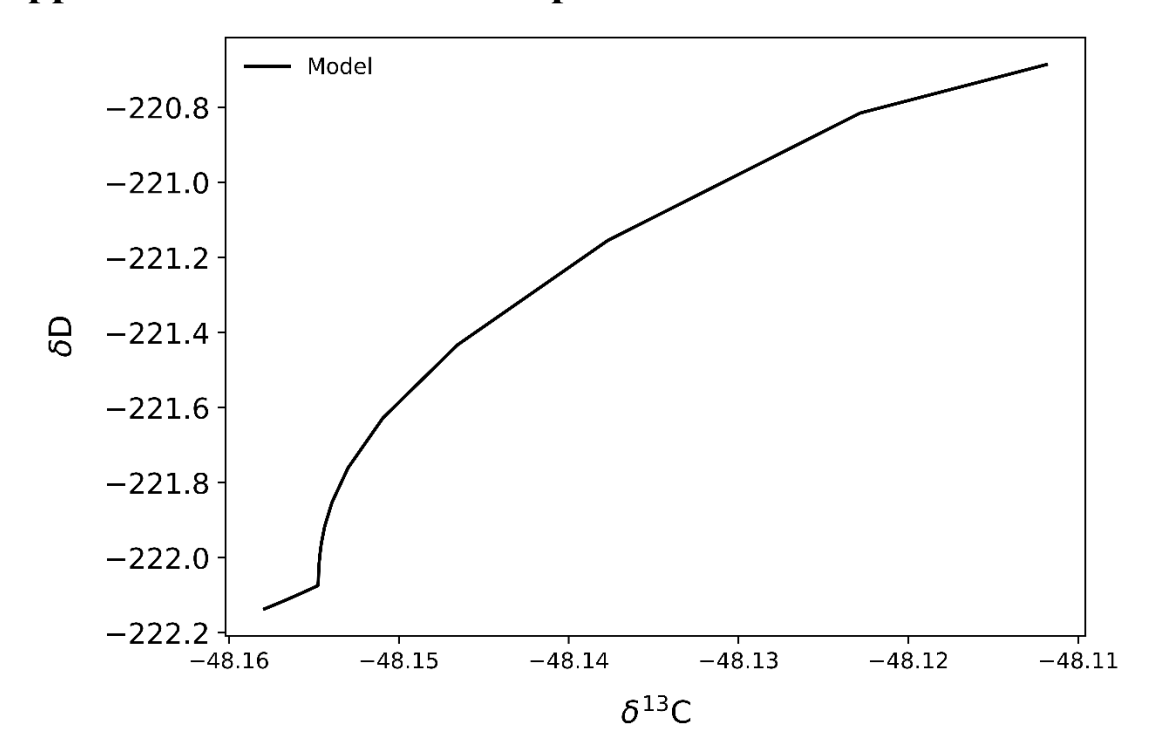


Figure 3: AOM model outputs for stable isotopic compositions  $\delta^{13}C$  and  $\delta D$  ( $\phi$  = 2 x  $10^{-6}$ ).

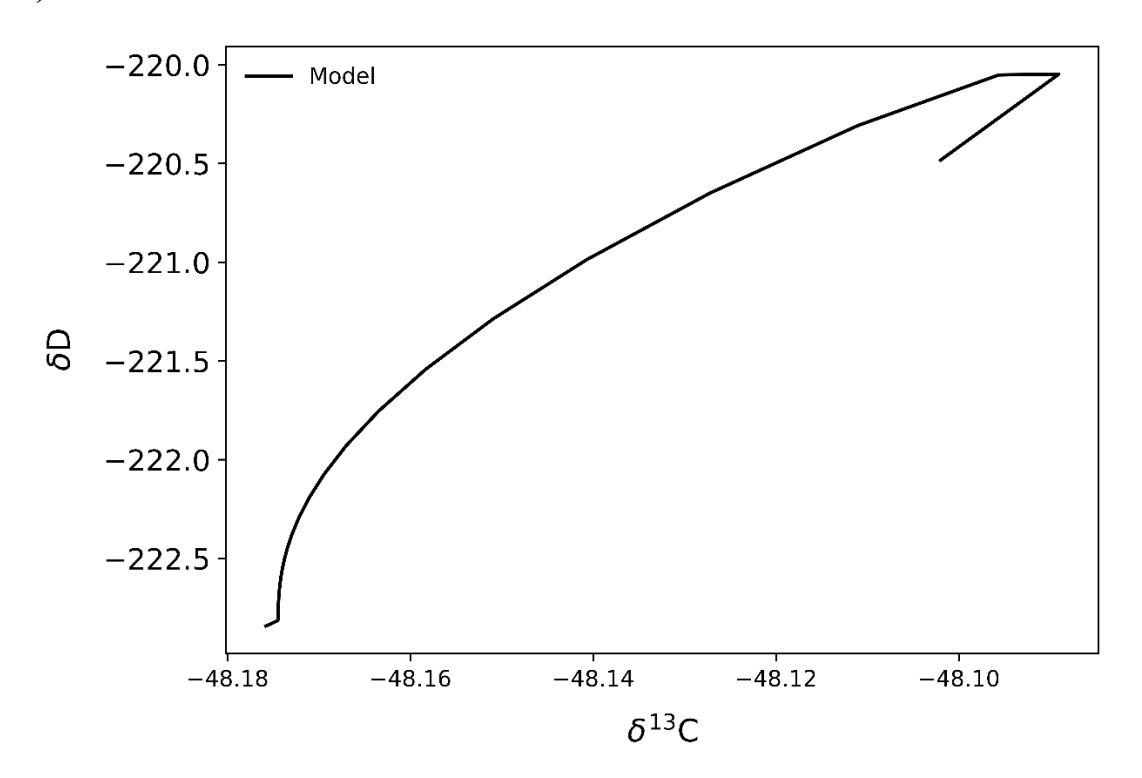


Figure 4: AOM model outputs for stable isotopic compositions  $\delta^{13}C$  and  $\delta D$  ( $\phi=5$  x  $10^{-7}$ ).

## **Appendix VII: Calcites Results and Data Processing**

#### **Correction Scheme**

I applied corrections for the data acquired in the interval between the 2023/11/28 and the 2023/12/19, as I identified an upward trend in the  $\Delta_{47}$  of the standards used, which was creating measurable offsets from the actual values for the standards ETH1, ETH2, ETH3, ETH4. Consequently, I assume that the identified measurement drift should have a similar impact on the measurements of our samples for this interval. For this reason, I correct the measuring value  $\Delta_{47}$  of the samples by fitting the offsets from the standards using a linear function. Subsequently, we apply for both measurement intervals before and after the 2023/12/19 the Peirce's criterion in order to filter out any outliers.

Table 2: Summary of results for calcite measurements.

Sample	δ <sup>13</sup> C	δ <sup>18</sup> O(‰)	δ <sup>18</sup> O (‰)	T47	Terror	Depth	δ <sup>18</sup> O fluid
	(‰)	(VPDB)	(VSMOW)	(°C)	(°C)	(m)	(‰)
							(VSMOW)
Sample1	-3.34	-19.36	10.96	158.17	9.63	476.15	1.24
Sample2	-2.78	-21.23	9.04	180.49	12.73	506.04	1.38
Sample3	-2.93	-20.44	9.85	115.57	7.05	541.92	-4.43
Sample4	-4.75	-21.28	8.98	174.28	10.75	586.12	0.77
Sample5	-9.06	-21.19	9.07	142.56	14.97	623.1	-2.25
Sample6	-6.13	-20.57	9.71	199.37	12.67	707.1	3.64
Sample7	-4.31	-17.16	13.23	64.35	4.61	716.1	-8.1
Sample8	-2.21	-18.22	12.13	149.59	7.85	753.19	1.75
Sample9	-8.79	-21.55	8.71	150.31	9.42	764.1	-1.77
Sample10	-6.82	-20.32	9.97	164.75	8.73	766.75	0.89
Sample11	-3.28	-21.72	8.52	130.07	7.87	779.05	-0.55
Sample12	-3.99	-19.42	10.9	207.73	13.36	836.07	5.49
Sample13	-1.57	-20.78	9.5	172.59	10.63	899.59	1.14
Sample14	-3.1	-21.02	9.25	130.09	7.87	935.59	-3.36

# Appendix VIII: Example of Monte Carlo simulation for error propagation.

An example of Python code is shared to run a Monte Carlo simulation for error propagation for the calculation of the isotopic signatures. In this case, I share the Python code for the calculation of  $\delta D$ , however in a similar way the code can be adjusted for calculating  $\delta^{13}C$ ,  $\Delta^{13}CH_3D$  and  $\Delta^{12}CH_2D_2$ . The code has been adapted from the supplementary material of Eldridge et al. (2019).

### **Python Code**

```
import pandas as pd
import statistics
import numpy as np
import random
#Read data from measurement
data = pd.read csv('//file.csv')
#Number of simulations
n = 100000
#Fragmentation Rate
f = 0.81
#True D/H ratio of working gas
R2 r = float(data["R2 r"])
#Measured values compared to working gas
dD= float(data["dD"])
dD sd = float(data["dD sd"])
#Randon number generation-Simulations
hy = np.random.normal(dDf,dD sd,n)
\#Calculate \ \delta D \ of \ sample
R2 wg = ((hy/1000) + 1)*R2 r*4/(1+3*f*R2 r)
R2 \text{ sa} = R2 \text{ s/}(4 - 3*R2 \text{ wg*f})
dD sa = (((R2 \text{ sa}/0.00015576)-1)*1000)
print(statistics.mean(dD sa),statistics.stdev(dD sa))
```

## References

- Abrajano, T.A., Sturchio, N.C., Kennedy, B.M., Lyon, G.L., Muehlenbachs, K., Bohlke, J.K., 1990. Geochemistry of reduced gas related to serpentinization of the Zambales ophiolite, Philippines. Applied Geochemistry, Water-Rock Interactions Special Memorial Issue Ivan Barnes (1931–1989) 5, 625–630. https://doi.org/10.1016/0883-2927(90)90060-I
- Affek, H.P., 2013. Clumped isotopic equilibrium and the rate of isotope exchange between CO2 and water. American Journal of Science 313, 309–325. https://doi.org/10.2475/04.2013.02
- Aizenshtat, Z., Amrani, A., 2004. Significance of δ34S and evaluation of its imprint on sedimentary sulfur rich organic matter II: Thermal changes of kerogens type II-S catagenetic stage controlled mechanisms. A study and conceptual overview, in: Hill, R.J., Leventhal, J., Aizenshtat, Z., Baedecker, M.J., Claypool, G., Eganhouse, R., Goldhaber, M., Peters, K. (Eds.), The Geochemical Society Special Publications, Geochemical Investigations in Earth and Space Science: A Tribute to Isaac R. Kaplan. Elsevier, pp. 35–50. https://doi.org/10.1016/S1873-9881(04)80005-1
- Akam, S.A., Coffin, R.B., Abdulla, H.A.N., Lyons, T.W., 2020. Dissolved Inorganic Carbon Pump in Methane-Charged Shallow Marine Sediments: State of the Art and New Model Perspectives. Front. Mar. Sci. 7, 206. https://doi.org/10.3389/fmars.2020.00206
- Akam, S.A., Swanner, E.D., Yao, H., Hong, W.-L., Peckmann, J., 2023. Methane-derived authigenic carbonates A case for a globally relevant marine carbonate factory. Earth-Science Reviews 243, 104487. https://doi.org/10.1016/j.earscirev.2023.104487
- Allan, W., Struthers, H., Lowe, D.C., 2007. Methane carbon isotope effects caused by atomic chlorine in the marine boundary layer: Global model results compared with Southern Hemisphere measurements. J. Geophys. Res. 112, 2006JD007369. https://doi.org/10.1029/2006JD007369
- Alvarez, R.A., Pacala, S.W., Winebrake, J.J., Chameides, W.L., Hamburg, S.P., 2012. Greater focus needed on methane leakage from natural gas infrastructure. Proceedings of the National Academy of Sciences 109, 6435–6440. https://doi.org/10.1073/pnas.1202407109
- Anderson, G.M., 1976. Error propagation by the Monte Carlo method in geochemical calculations. Geochimica et Cosmochimica Acta 40, 1533–1538. https://doi.org/10.1016/0016-7037(76)90092-2
- Andresen, B., Throndsen, T., Barth, T., Bolstad, J., 1994. Thermal generation of carbon dioxide and organic acids from different source rocks. Organic Geochemistry 21, 1229–1242. https://doi.org/10.1016/0146-6380(94)90166-X
- Angelidaki, I., Karakashev, D., Batstone, D.J., Plugge, C.M., Stams, A.J.M., 2011. Chapter sixteen Biomethanation and Its Potential, in: Rosenzweig, A.C., Ragsdale, S.W. (Eds.), Methods in Enzymology, Methods in Methane Metabolism, Part A. Academic Press, pp. 327–351. https://doi.org/10.1016/B978-0-12-385112-3.00016-0
- Apps J.A, V.D.K.P.C., 1993. Energy gases of abiogenic origin in the Earth's crust.
- Ash, J.L., Egger, M., Treude, T., Kohl, I., Cragg, B., Parkes, R.J., Slomp, C.P., Sherwood Lollar, B., Young, E.D., 2019. Exchange catalysis during anaerobic methanotrophy revealed by 12CH2D2 and 13CH3D in methane. Geochem. Persp. Let. 26–30. https://doi.org/10.7185/geochemlet.1910
- Bajnai, D., 2021. isogeochem: Tools for Stable Isotope Geochemistry. https://doi.org/10.32614/CRAN.package.isogeochem

- Bajnai, D., Guo, W., Spötl, C., Coplen, T.B., Methner, K., Löffler, N., Krsnik, E., Gischler,
  E., Hansen, M., Henkel, D., Price, G.D., Raddatz, J., Scholz, D., Fiebig, J., 2020.
  Dual clumped isotope thermometry resolves kinetic biases in carbonate formation temperatures. Nat Commun 11, 4005. https://doi.org/10.1038/s41467-020-17501-0
- Bau, M., Romer, R.L., Lüders, V., Beukes, N.J., 1999. Pb, O, and C isotopes in silicified Mooidraai dolomite (Transvaal Supergroup, South Africa): implications for the composition of Paleoproterozoic seawater and 'dating' the increase of oxygen in the Precambrian atmosphere. Earth and Planetary Science Letters 174, 43–57. https://doi.org/10.1016/S0012-821X(99)00261-7
- Baur, P.A., Henry Pinilla, D., Glatzel, S., 2024. Is ebullition or diffusion more important as methane emission pathway in a shallow subsaline lake? Science of The Total Environment 912, 169112. https://doi.org/10.1016/j.scitotenv.2023.169112
- Beal, E.J., House, C.H., Orphan, V.J., 2009. Manganese- and Iron-Dependent Marine Methane Oxidation. Science 325, 184–187. https://doi.org/10.1126/science.1169984
- Becker, J.F., Sauke, T.B., Loewenstein, M., 1992. Stable isotope analysis using tunable diode laser spectroscopy. Appl. Opt., AO 31, 1921–1927. https://doi.org/10.1364/AO.31.001921
- Bergamaschi, P., Karstens, U., Manning, A.J., Saunois, M., Tsuruta, A., Berchet, A., Vermeulen, A.T., Arnold, T., Janssens-Maenhout, G., Hammer, S., Levin, I., Schmidt, M., Ramonet, M., Lopez, M., Lavric, J., Aalto, T., Chen, H., Feist, D.G., Gerbig, C., Haszpra, L., Hermansen, O., Manca, G., Moncrieff, J., Meinhardt, F., Necki, J., Galkowski, M., O'Doherty, S., Paramonova, N., Scheeren, H.A., Steinbacher, M., Dlugokencky, E., 2018. Inverse modelling of European CH4 emissions during 2006–2012 using different inverse models and reassessed atmospheric observations. Atmospheric Chemistry and Physics 18, 901–920. https://doi.org/10.5194/acp-18-901-2018
- Bergamaschi, P., Schupp, M., Harris, G.W., 1994. High-precision direct measurements of <sup>13</sup>CH<sub>4</sub>/<sup>12</sup>CH<sub>4</sub> and <sup>12</sup>CH<sub>3</sub>D/<sup>12</sup>CH<sub>4</sub> ratios in atmospheric methane sources by means of a long-path tunable diode laser absorption spectrometer. Appl. Opt., AO 33, 7704–7716. https://doi.org/10.1364/AO.33.007704
- Bernard, B., Brooks, J.M., Sackett, W.M., 1977. A Geochemical Model For Characterization Of Hydrocarbon Gas Sources In Marine Sediments. Presented at the Offshore Technology Conference, OnePetro. https://doi.org/10.4043/2934-MS
- Bernard, B.B., Brooks, J.M., Sackett, W.M., 1978. Light hydrocarbons in recent Texas continental shelf and slope sediments. J. Geophys. Res. 83, 4053–4061. https://doi.org/10.1029/JC083iC08p04053
- Bernasconi, S.M., Daëron, M., Bergmann, K.D., Bonifacie, M., Meckler, A.N., Affek, H.P., Anderson, N., Bajnai, D., Barkan, E., Beverly, E., Blamart, D., Burgener, L., Calmels, D., Chaduteau, C., Clog, M., Davidheiser-Kroll, B., Davies, A., Dux, F., Eiler, J., Elliott, B., Fetrow, A.C., Fiebig, J., Goldberg, S., Hermoso, M., Huntington, K.W., Hyland, E., Ingalls, M., Jaggi, M., John, C.M., Jost, A.B., Katz, S., Kelson, J., Kluge, T., Kocken, I.J., Laskar, A., Leutert, T.J., Liang, D., Lucarelli, J., Mackey, T.J., Mangenot, X., Meinicke, N., Modestou, S.E., Müller, I.A., Murray, S., Neary, A., Packard, N., Passey, B.H., Pelletier, E., Petersen, S., Piasecki, A., Schauer, A., Snell, K.E., Swart, P.K., Tripati, A., Upadhyay, D., Vennemann, T., Winkelstern, I., Yarian, D., Yoshida, N., Zhang, N., Ziegler, M., 2021. InterCarb: A Community Effort to Improve Interlaboratory Standardization of the Carbonate Clumped Isotope Thermometer Using Carbonate Standards. Geochem Geophys Geosyst 22, e2020GC009588. https://doi.org/10.1029/2020GC009588
- Bernasconi, S.M., Hu, B., Wacker, U., Fiebig, J., Breitenbach, S.F.M., Rutz, T., 2013.

- Background effects on Faraday collectors in gas-source mass spectrometry and implications for clumped isotope measurements. Rapid Comm Mass Spectrometry 27, 603–612. https://doi.org/10.1002/rcm.6490
- Bernasconi, S.M., Müller, I.A., Bergmann, K.D., Breitenbach, S.F.M., Fernandez, A., Hodell, D.A., Jaggi, M., Meckler, A.N., Millan, I., Ziegler, M., 2018. Reducing Uncertainties in Carbonate Clumped Isotope Analysis Through Consistent Carbonate-Based Standardization. Geochem Geophys Geosyst 19, 2895–2914. https://doi.org/10.1029/2017GC007385
- Beukes, N.J., Klein, C., Kaufman, A.J., Hayes, J.M., 1990. Carbonate petrography, kerogen distribution, and carbon and oxygen isotope variations in an early Proterozoic transition from limestone to iron-formation deposition, Transvaal Supergroup, South Africa. Economic Geology 85, 663–690. https://doi.org/10.2113/gsecongeo.85.4.663
- Bevington, P.R., Robinson, D.K., 2003. Data reduction and error analysis for the physical sciences, 3rd ed. ed. McGraw-Hill, Boston.
- Bianchi, F., Careri, M., 2021. 4 Mass spectrometry in food authenticity and traceability, in: Galanakis, C.M. (Ed.), Food Authentication and Traceability. Academic Press, pp. 101–130. https://doi.org/10.1016/B978-0-12-821104-5.00008-8
- Blamey, N.J.F., Parnell, J., McMahon, S., Mark, D.F., Tomkinson, T., Lee, M., Shivak, J., Izawa, M.R.M., Banerjee, N.R., Flemming, R.L., 2015. Evidence for methane in Martian meteorites. Nat Commun 6, 7399. https://doi.org/10.1038/ncomms8399
- Boschetti, T., Etiope, G., Toscani, L., 2013. Abiotic Methane in the Hyperalkaline Springs of Genova, Italy. Procedia Earth and Planetary Science, Proceedings of the Fourteenth International Symposium on Water-Rock Interaction, WRI 14 7, 248–251. https://doi.org/10.1016/j.proeps.2013.02.004
- Bothun, G., 2021. Past and Future Global Energy Mix, in: Leal Filho, W., Marisa Azul, A., Brandli, L., Lange Salvia, A., Wall, T. (Eds.), Affordable and Clean Energy. Springer International Publishing, Cham, pp. 965–982. https://doi.org/10.1007/978-3-319-95864-4 60
- Bottinga, Y., 1969. Calculated fractionation factors for carbon and hydrogen isotope exchange in the system calcite-carbon dioxide-graphite-methane-hydrogen-water vapor. Geochimica et Cosmochimica Acta 33, 49–64. https://doi.org/10.1016/0016-7037(69)90092-1
- Bouquet, A., Mousis, O., Waite, J.H., Picaud, S., 2015. Possible evidence for a methane source in Enceladus' ocean. Geophysical Research Letters 42, 1334–1339. https://doi.org/10.1002/2014GL063013
- Bourg, I.C., Sposito, G., 2008. Isotopic fractionation of noble gases by diffusion in liquid water: Molecular dynamics simulations and hydrologic applications. Geochimica et Cosmochimica Acta 72, 2237–2247. https://doi.org/10.1016/j.gca.2008.02.012
- Brand, U., Blamey, N., Garbelli, C., Griesshaber, E., Posenato, R., Angiolini, L., Azmy, K., Farabegoli, E., Came, R., 2016. Methane Hydrate: Killer cause of Earth's greatest mass extinction. Palaeoworld, The Brachiopod World 25, 496–507. https://doi.org/10.1016/j.palwor.2016.06.002
- Brand, W.A., Coplen, T.B., Vogl, J., Rosner, M., Prohaska, T., 2014. Assessment of international reference materials for isotope-ratio analysis (IUPAC Technical Report). Pure and Applied Chemistry 86, 425–467. https://doi.org/10.1515/pac-2013-1023
- Brass, M., Röckmann, T., 2010. Continuous-flow isotope ratio mass spectrometry method for carbon and hydrogen isotope measurements on atmospheric methane.

  Atmospheric Measurement Techniques 3, 1707–1721. https://doi.org/10.5194/amt-3-1707-2010
- Budai, J.M., Martini, A.M., Walter, L.M., Ku, T.C.W., 2002. Fracture-fill calcite as a

- record of microbial methanogenesis and fluid migration: a case study from the Devonian Antrim Shale, Michigan Basin. Geofluids 2, 163–183. https://doi.org/10.1046/j.1468-8123.2002.00036.x
- Burnham, A.K., 2017. Global Chemical Kinetics of Fossil Fuels. Springer International Publishing, Cham. https://doi.org/10.1007/978-3-319-49634-4
- Candy, I., Stephens, M., Hancock, J., Waghorne, R., 2011. 3 Palaeoenvironments of Ancient Humans in Britain: The Application of Oxygen and Carbon Isotopes to the Reconstruction of Pleistocene Environments, in: Ashton, N., Lewis, S.G., Stringer, C. (Eds.), Developments in Quaternary Sciences, The Ancient Human Occupation of Britain. Elsevier, pp. 23–37. https://doi.org/10.1016/B978-0-444-53597-9.00003-0
- Cantrell, C.A., Shetter, R.E., McDaniel, A.H., Calvert, J.G., Davidson, J.A., Lowe, D.C., Tyler, S.C., Cicerone, R.J., Greenberg, J.P., 1990. Carbon kinetic isotope effect in the oxidation of methane by the hydroxyl radical. J. Geophys. Res. 95, 22455–22462. https://doi.org/10.1029/JD095iD13p22455
- Castanier, S., Le Métayer-Levrel, G., Perthuisot, J.-P., 1999. Ca-carbonates precipitation and limestone genesis the microbiogeologist point of view. Sedimentary Geology 126, 9–23. https://doi.org/10.1016/S0037-0738(99)00028-7
- Chapman, R.E., 1988. PETROLEUM GEOLOGYPetroleum geology, in: General Geology. Springer US, Boston, MA, pp. 631–638. https://doi.org/10.1007/0-387-30844-X 85
- Chen, B., Stuart, F.M., Xu, S., Györe, D., Liu, C., 2022. The effect of Cenozoic basin inversion on coal-bed methane in Liupanshui Coalfield, Southern China. International Journal of Coal Geology 250, 103910. https://doi.org/10.1016/j.coal.2021.103910
- Chen, B., Stuart, F.M., Xu, S., Györe, D., Liu, C., 2019. Evolution of coal-bed methane in Southeast Qinshui Basin, China: Insights from stable and noble gas isotopes. Chemical Geology 529, 119298. https://doi.org/10.1016/j.chemgeo.2019.119298
- Chen, H., Gan, Q., Fan, C., 2020. Methyl-Coenzyme M Reductase and Its Post-translational Modifications. Front. Microbiol. 11, 578356. https://doi.org/10.3389/fmicb.2020.578356
- Chong, Z.R., Yin, Z., Zhao, J., Linga, P., 2017. Recovering Natural Gas from Gas Hydrates using Horizontal Wellbore. Energy Procedia, Leveraging Energy Technologies and Policy Options for Low Carbon Cities 143, 780–785. https://doi.org/10.1016/j.egypro.2017.12.762
- Chung, E., Arnold, T., 2021. Potential of Clumped Isotopes in Constraining the Global Atmospheric Methane Budget. Global Biogeochemical Cycles 35, e2020GB006883. https://doi.org/10.1029/2020GB006883
- Chung, H.M., Gormly, J.R., Squires, R.M., 1988. Origin of gaseous hydrocarbons in subsurface environments: Theoretical considerations of carbon isotope distribution. Chemical Geology, Origins of Methane in the Earth 71, 97–104. https://doi.org/10.1016/0009-2541(88)90108-8
- Chung, H.M., Sackett, W.M., 1979. Use of stable carbon isotope compositions of pyrolytically derived methane as maturity indices for carbonaceous materials. Geochimica et Cosmochimica Acta 43, 1979–1988. https://doi.org/10.1016/0016-7037(79)90010-3
- Clayton, C., 1991. Carbon isotope fractionation during natural gas generation from kerogen. Marine and Petroleum Geology 8, 232–240. https://doi.org/10.1016/0264-8172(91)90010-X
- Clog, M., Lawson, M., Peterson, B., Ferreira, A.A., Santos Neto, E.V., Eiler, J.M., 2018. A reconnaissance study of 13C–13C clumping in ethane from natural gas. Geochimica et Cosmochimica Acta 223, 229–244.

- https://doi.org/10.1016/j.gca.2017.12.004
- Clog, M., Lindgren, P., Modestou, S., McDonald, A., Tait, A., Donnelly, T., Mark, D., Lee, M., 2024. Clumped isotope and Δ170 measurements of carbonates in CM carbonaceous chondrites: New insights into parent body thermal and fluid evolution. Geochimica et Cosmochimica Acta 369, 1–16. https://doi.org/10.1016/j.gca.2024.01.023
- Conrad, R., 2020. Importance of hydrogenotrophic, aceticlastic and methylotrophic methanogenesis for methane production in terrestrial, aquatic and other anoxic environments: A mini review. Pedosphere 30, 25–39. https://doi.org/10.1016/S1002-0160(18)60052-9
- Conrad, R., 2009. The global methane cycle: recent advances in understanding the microbial processes involved. Environ Microbiol Rep 1, 285–292. https://doi.org/10.1111/j.1758-2229.2009.00038.x
- Conrad, R., 2005. Quantification of methanogenic pathways using stable carbon isotopic signatures: a review and a proposal. Organic Geochemistry, Stable isotope applications in methane cycle studies 36, 739–752. https://doi.org/10.1016/j.orggeochem.2004.09.006
- Cook, A., n.d. Safety in Mines Research Advisory Committee.
- Cooper, J., Stamford, L., Azapagic, A., 2016. Shale Gas: A Review of the Economic, Environmental, and Social Sustainability. Energy Technology 4, 772–792. https://doi.org/10.1002/ente.201500464
- Coward, M.P., Spencer, R.M., Spencer, C.E., 1995. Development of the Witwatersrand Basin, South Africa. Geological Society, London, Special Publications 95, 243–269. https://doi.org/10.1144/GSL.SP.1995.095.01.15
- Craig, H., 1953. The geochemistry of the stable carbon isotopes. Geochimica et Cosmochimica Acta 3, 53–92. https://doi.org/10.1016/0016-7037(53)90001-5
- Crippa, M., Guizzardi, D., Pisoni, E., Solazzo, E., Guion, A., Muntean, M., Florczyk, A., Schiavina, M., Melchiorri, M., Hutfilter, A.F., 2021. Global anthropogenic emissions in urban areas: patterns, trends, and challenges. Environ. Res. Lett. 16, 074033. https://doi.org/10.1088/1748-9326/ac00e2
- Criss, R.E., 1999. Principles of Stable Isotope Distribution. Oxford University Press. https://doi.org/10.1093/oso/9780195117752.001.0001
- Cui, L., Wang, X., 2014. Determination of clumped isotopes in carbonate using isotope ratio mass spectrometer: Effects of extraction potential and long-term stability. International Journal of Mass Spectrometry 372, 46–50. https://doi.org/10.1016/j.ijms.2014.08.006
- Cui, M., Ma, A., Qi, H., Zhuang, X., Zhuang, G., 2015. Anaerobic oxidation of methane: an "active" microbial process. MicrobiologyOpen 4, 1–11. https://doi.org/10.1002/mbo3.232
- Daëron, M., Blamart, D., Peral, M., Affek, H.P., 2016a. Absolute isotopic abundance ratios and the accuracy of Δ47 measurements. Chemical Geology 442, 83–96. https://doi.org/10.1016/j.chemgeo.2016.08.014
- Daëron, M., Blamart, D., Peral, M., Affek, H.P., 2016b. Absolute isotopic abundance ratios and the accuracy of Δ47 measurements. Chemical Geology 442, 83–96. https://doi.org/10.1016/j.chemgeo.2016.08.014
- Dai, J., Ni, Y., Huang, S., Peng, W., Han, W., Gong, D., Wei, W., 2017. Genetic types of gas hydrates in China. Petroleum Exploration and Development 44, 887–898. https://doi.org/10.1016/S1876-3804(17)30101-5
- Danabalan, D., Gluyas, J.G., Macpherson, C.G., Abraham-James, T.H., Bluett, J.J., Barry, P.H., Ballentine, C.J., 2022. The principles of helium exploration. PG 28, petgeo2021-029. https://doi.org/10.1144/petgeo2021-029
- DasSarma, S., Coker, J.A., DasSarma, P., 2009. Archaea (overview), in: Encyclopedia of

- Microbiology. Elsevier, pp. 1–23. https://doi.org/10.1016/B978-012373944-5.00108-5
- Defratyka, S.M., Paris, J.-D., Yver-Kwok, C., Loeb, D., France, J., Helmore, J., Yarrow, N., Gros, V., Bousquet, P., 2021. Ethane measurement by Picarro CRDS G2201-i in laboratory and field conditions: potential and limitations. Atmospheric Measurement Techniques 14, 5049–5069. https://doi.org/10.5194/amt-14-5049-2021
- Del Prado, A., Vibart, R.E., Bilotto, F.M., Faverin, C., Garcia, F., Henrique, F.L., Leite, F.F.G.D., Mazzetto, A.M., Ridoutt, B.G., Yáñez-Ruiz, D.R., Bannink, A., 2025. Feed additives for methane mitigation: Assessment of feed additives as a strategy to mitigate enteric methane from ruminants—Accounting; How to quantify the mitigating potential of using antimethanogenic feed additives. Journal of Dairy Science 108, 411–429. https://doi.org/10.3168/jds.2024-25044
- Delaygue, G., 2009. Oxygen Isotopes, in: Gornitz, V. (Ed.), Encyclopedia of Paleoclimatology and Ancient Environments. Springer Netherlands, Dordrecht, pp. 666–673. https://doi.org/10.1007/978-1-4020-4411-3 163
- Dempster, A. J., n.d. A new method of positive ray analysis. Phys. Rev. 11 (4), 316–325. https://doi.org/DOI: 10.1103/PhysRev.11.316
- Diaconescu, C.C., Kieckhefer, R.M., Knapp, J.H., 2001. Geophysical evidence for gas hydrates in the deep water of the South Caspian Basin, Azerbaijan. Marine and Petroleum Geology 18, 209–221. https://doi.org/10.1016/S0264-8172(00)00061-1
- Dietzel, M., 2011. Carbonates, in: Reitner, J., Thiel, V. (Eds.), Encyclopedia of Geobiology. Springer Netherlands, Dordrecht, pp. 261–266. https://doi.org/10.1007/978-1-4020-9212-1 50
- Dones, R., Heck, T., Faist Emmenegger, M., Jungbluth, N., 2005. Life Cycle Inventories for the Nuclear and Natural Gas Energy Systems, and Examples of Uncertainty Analysis (14 pp). Int J Life Cycle Assessment 10, 10–23. https://doi.org/10.1065/lca2004.12.181.2
- Dong, G., Xie, H., Formolo, M., Lawson, M., Sessions, A., Eiler, J., 2021a. Clumped isotope effects of thermogenic methane formation: Insights from pyrolysis of hydrocarbons. Geochimica et Cosmochimica Acta 303, 159–183. https://doi.org/10.1016/j.gca.2021.03.009
- Dong, G., Xie, H., Formolo, M., Lawson, M., Sessions, A., Eiler, J., 2021b. Clumped isotope effects of thermogenic methane formation: Insights from pyrolysis of hydrocarbons. Geochimica et Cosmochimica Acta 303, 159–183. https://doi.org/10.1016/j.gca.2021.03.009
- Donnelly, T., Waldron, S., Tait, A., Dougans, J., Bearhop, S., 2001. Hydrogen isotope analysis of natural abundance and deuterium-enriched waters by reduction over chromium on-line to a dynamic dual inlet isotope-ratio mass spectrometer. Rapid Comm Mass Spectrometry 15, 1297–1303. https://doi.org/10.1002/rcm.361
- Douglas, P.M.J., Stolper, D.A., Eiler, J.M., Sessions, A.L., Lawson, M., Shuai, Y., Bishop, A., Podlaha, O.G., Ferreira, A.A., Santos Neto, E.V., Niemann, M., Steen, A.S., Huang, L., Chimiak, L., Valentine, D.L., Fiebig, J., Luhmann, A.J., Seyfried, W.E., Etiope, G., Schoell, M., Inskeep, W.P., Moran, J.J., Kitchen, N., 2017. Methane clumped isotopes: Progress and potential for a new isotopic tracer. Organic Geochemistry 113, 262–282. https://doi.org/10.1016/j.orggeochem.2017.07.016
- Dowd, W.S., Schuler, C.J., Santelli, C.M., Toner, B.M., Sheik, C.S., Pehr, K., McDermott, J.M., 2022. Potential energy sources for the deep continental biosphere in isolated anoxic brines. Earth and Planetary Science Letters 595, 117720. https://doi.org/10.1016/j.epsl.2022.117720
- Drake, H., Åström, M.E., Heim, C., Broman, C., Åström, J., Whitehouse, M., Ivarsson, M., Siljeström, S., Sjövall, P., 2015. Extreme 13C depletion of carbonates formed

- during oxidation of biogenic methane in fractured granite. Nat Commun 6, 7020. https://doi.org/10.1038/ncomms8020
- Drennan, G.R., Robb, L.J., 2006. The nature of hydrocarbons and related fluids in the Witwatersrand Basin, South Africa: Their role in metal redistribution, in: Processes on the Early Earth. Geological Society of America. https://doi.org/10.1130/2006.2405(18)
- Dubey, L., Speirs, J., Balcombe, P., Tariq, N., Brandon, N., Hawkes, A., 2023. Future use of natural gas under tightening climate targets. Futures 150, 103158. https://doi.org/10.1016/j.futures.2023.103158
- Ehhalt, D.H., 1974. The atmospheric cycle of methane. Tellus 26, 58–70. https://doi.org/10.1111/j.2153-3490.1974.tb01952.x
- Eiler, J.M., 2007. "Clumped-isotope" geochemistry—The study of naturally-occurring, multiply-substituted isotopologues. Earth and Planetary Science Letters 262, 309—327. https://doi.org/10.1016/j.epsl.2007.08.020
- Eiler, J.M., Clog, M., Magyar, P., Piasecki, A., Sessions, A., Stolper, D., Deerberg, M., Schlueter, H.-J., Schwieters, J., 2013. A high-resolution gas-source isotope ratio mass spectrometer. International Journal of Mass Spectrometry 335, 45–56. https://doi.org/10.1016/j.ijms.2012.10.014
- Eldridge, D.L., Korol, R., Lloyd, M.K., Turner, A.C., Webb, M.A., Miller, T.F., Stolper, D.A., 2019. Comparison of Experimental vs Theoretical Abundances of CH<sub>3</sub> D and CH<sub>2</sub> D<sub>2</sub> for Isotopically Equilibrated Systems from 1 to 500 °C. ACS Earth Space Chem. 3, 2747–2764. https://doi.org/10.1021/acsearthspacechem.9b00244
- Emrich, K., Ehhalt, D.H., Vogel, J.C., 1970. Carbon isotope fractionation during the precipitation of calcium carbonate. Earth and Planetary Science Letters 8, 363–371. https://doi.org/10.1016/0012-821X(70)90109-3
- England, G.L., Rasmussen, B., Krapez, B., Groves, D.I., 2002. Archaean oil migration in the Witwatersrand Basin of South Africa. JGS 159, 189–201. https://doi.org/10.1144/0016-764900-197
- England, W.A., 1994. Secondary Migration and Accumulation of Hydrocarbons, in: Magoon, L.B., Dow, W.G. (Eds.), The Petroleum System—From Source to Trap. American Association of Petroleum Geologists, p. 0. https://doi.org/10.1306/M60585C12
- Epstein, S., Buchsbaum, R., Lowenstam, H., Urey, H.C., 1951. CARBONATE-WATER ISOTOPIC TEMPERATURE SCALE. Geol Soc America Bull 62, 417. https://doi.org/10.1130/0016-7606(1951)62[417:CITS]2.0.CO;2
- Etheridge, D.M., Steele, L.P., Francey, R.J., Langenfelds, R.L., 1998. Atmospheric methane between 1000 A.D. and present: Evidence of anthropogenic emissions and climatic variability. Journal of Geophysical Research: Atmospheres 103, 15979–15993. https://doi.org/10.1029/98JD00923
- Etiope, G., 2023. Massive release of natural hydrogen from a geological seep (Chimaera, Turkey): Gas advection as a proxy of subsurface gas migration and pressurised accumulations. International Journal of Hydrogen Energy 48, 9172–9184. https://doi.org/10.1016/j.ijhydene.2022.12.025
- Etiope, G., 2018. Natural Gas, in: White, W.M. (Ed.), Encyclopedia of Geochemistry: A Comprehensive Reference Source on the Chemistry of the Earth. Springer International Publishing, Cham, pp. 961–965. https://doi.org/10.1007/978-3-319-39312-4 152
- Etiope, G., 2015. Natural Gas Seepage: The Earth's Hydrocarbon Degassing. Springer International Publishing, Cham. https://doi.org/10.1007/978-3-319-14601-0
- Etiope, G., Ionescu, A., 2015. Low-temperature catalytic CO2 hydrogenation with geological quantities of ruthenium: a possible abiotic CH4 source in chromitite-rich serpentinized rocks. Geofluids 15, 438–452. https://doi.org/10.1111/gfl.12106

- Etiope, G., Schoell, M., 2014. Abiotic Gas: Atypical, But Not Rare. Elements 10, 291–296. https://doi.org/10.2113/gselements.10.4.291
- Etiope, G., Schoell, M., Hosgörmez, H., 2011. Abiotic methane flux from the Chimaera seep and Tekirova ophiolites (Turkey): Understanding gas exhalation from low temperature serpentinization and implications for Mars. Earth and Planetary Science Letters 310, 96–104. https://doi.org/10.1016/j.epsl.2011.08.001
- Etiope, G., Sherwood Lollar, B., 2013. ABIOTIC METHANE ON EARTH. Reviews of Geophysics 51, 276–299. https://doi.org/10.1002/rog.20011
- Fa, G., Wang, Zuo-qian, Gao, F., Wang, Zhong-sheng, Li, Z., 2022. Global Natural Gas Production and Development Status, Supply and Demand Situation Analysis and Prospects, in: Lin, J. (Ed.), Proceedings of the International Field Exploration and Development Conference 2021. Springer Nature, Singapore, pp. 574–585. https://doi.org/10.1007/978-981-19-2149-0 53
- Farooqi, A.S., Allam, A.N., Shahid, M.Z., Aqil, A., Fajri, K., Park, S., Abdelaziz, O.Y., Abdelnaby, M.M., Hossain, M.M., Habib, M.A., Hasnain, S.M.W. ul, Nabavi, A., Zhu, M., Manovic, V., Nemitallah, M.A., 2025. Advancements in sorption-enhanced steam reforming for clean hydrogen production: A comprehensive review. Carbon Capture Science & Technology 14, 100336. https://doi.org/10.1016/j.ccst.2024.100336
- Feilberg, K.L., Griffith, D.W.T., Johnson, M.S., Nielsen, C.J., 2005. The 13C and D kinetic isotope effects in the reaction of CH4 with Cl. International Journal of Chemical Kinetics 37, 110–118. https://doi.org/10.1002/kin.20058
- Fenchel, T., Blackburn, T.H., King, G.M., 2012. Bacterial biogeochemistry: the ecophysiology of mineral cycling, 3d edition. ed. Elsevier/AP, London.
- Fiebig, J., Bajnai, D., Löffler, N., Methner, K., Krsnik, E., Mulch, A., Hofmann, S., 2019. Combined high-precision Δ48 and Δ47 analysis of carbonates. Chemical Geology 522, 186–191. https://doi.org/10.1016/j.chemgeo.2019.05.019
- Figeac, N., Trably, E., Bernet, N., Delgenès, J.-P., Escudié, R., 2020. Temperature and Inoculum Origin Influence the Performance of Ex-Situ Biological Hydrogen Methanation. Molecules 25, 5665. https://doi.org/10.3390/molecules25235665
- Fisher, R., Lowry, D., Wilkin, O., Sriskantharajah, S., Nisbet, E.G., 2006. High-precision, automated stable isotope analysis of atmospheric methane and carbon dioxide using continuous-flow isotope-ratio mass spectrometry. Rapid Communications in Mass Spectrometry 20, 200–208. https://doi.org/10.1002/rcm.2300
- Fletcher, L.N., Orton, G.S., Teanby, N.A., Irwin, P.G.J., Bjoraker, G.L., 2009. Methane and its isotopologues on Saturn from Cassini/CIRS observations. Icarus 199, 351–367. https://doi.org/10.1016/j.icarus.2008.09.019
- Foustoukos, D.I., Seyfried, W.E., 2004. Hydrocarbons in Hydrothermal Vent Fluids: The Role of Chromium-Bearing Catalysts. Science 304, 1002–1005. https://doi.org/10.1126/science.1096033
- Frauenstein, F., Veizer, J., Beukes, N., Van Niekerk, H.S., Coetzee, L.L., 2009. Transvaal Supergroup carbonates: Implications for Paleoproterozoic δ18O and δ13C records. Precambrian Research 175, 149–160. https://doi.org/10.1016/j.precamres.2009.09.005
- Frimmel, H., 1997. Detrital origin of hydrothermal Witwatersrand gold—a review. Terra Nova 9, 192–197. https://doi.org/10.1046/j.1365-3121.1997.d01-23.x
- Frimmel, H.E., 2019. The Witwatersrand Basin and Its Gold Deposits, in: Kröner, A., Hofmann, A. (Eds.), The Archaean Geology of the Kaapvaal Craton, Southern Africa. Springer International Publishing, Cham, pp. 255–275. https://doi.org/10.1007/978-3-319-78652-0 10
- Frimmel, H.E., Hallbauer, D.K., 1999. Gold mobilizing fluids in the Witwatersrand Basin: composition and possible sources. Mineralogy and Petrology 66, 55–81.

- https://doi.org/10.1007/BF01161722
- Frimmel, H.E., Minter, W.E.L., 2002. Recent Developments Concerning the Geological History and Genesis of the Witwatersrand Gold Deposits, South Africa, in: Integrated Methods for Discovery<subtitle>Global Exploration in the Twenty-First Century</Subtitle>. Society of Economic Geologists. https://doi.org/10.5382/SP.09.02
- Frost, D.J., McCammon, C.A., 2008. The Redox State of Earth's Mantle. Annu. Rev. Earth Planet. Sci. 36, 389–420. https://doi.org/10.1146/annurev.earth.36.031207.124322
- Fu, Q., Sherwood Lollar, B., Horita, J., Lacrampe-Couloume, G., Seyfried, W.E., 2007. Abiotic formation of hydrocarbons under hydrothermal conditions: Constraints from chemical and isotope data. Geochimica et Cosmochimica Acta 71, 1982–1998. https://doi.org/10.1016/j.gca.2007.01.022
- Fuchs, S., Schumann, D., Martin, R.F., Couillard, M., 2021. The extensive hydrocarbon-mediated fixation of hydrothermal gold in the Witwatersrand Basin, South Africa. Ore Geology Reviews 138, 104313. https://doi.org/10.1016/j.oregeorev.2021.104313
- Gathorne-Hardy, A., 2013. A Life Cycle Assessment (LCA) of Greenhouse Gas Emissions from SRI and Flooded Rice Production in SE India. Taiwan Water Conservancy Journal. https://doi.org/10.35648/20.500.12413/11781/ii250
- Ghosh, P., Adkins, J., Affek, H., Balta, B., Guo, W., Schauble, E.A., Schrag, D., Eiler, J.M., 2006. 13C–18O bonds in carbonate minerals: A new kind of paleothermometer. Geochimica et Cosmochimica Acta 70, 1439–1456. https://doi.org/10.1016/j.gca.2005.11.014
- Ghosh, P., Eiler, J., Campana, S.E., Feeney, R.F., 2007a. Calibration of the carbonate 'clumped isotope' paleothermometer for otoliths. Geochimica et Cosmochimica Acta 71, 2736–2744. https://doi.org/10.1016/j.gca.2007.03.015
- Ghosh, P., Eiler, J., Campana, S.E., Feeney, R.F., 2007b. Calibration of the carbonate 'clumped isotope' paleothermometer for otoliths. Geochimica et Cosmochimica Acta 71, 2736–2744. https://doi.org/10.1016/j.gca.2007.03.015
- Giardini, A.A., Subbarayudu, G.V., Melton, C.E., 1976. The emission of occluded gas from rocks as a function of stress: Its possible use as a tool for predicting earthquakes. Geophysical Research Letters 3, 355–358. https://doi.org/10.1029/GL003i006p00355
- Gibson, R.L., Uwe Reimold, W., Stevens, G., 1998. Thermal-metamorphic signature of an impact event in the Vredefort dome, South Africa. Geol 26, 787. https://doi.org/10.1130/0091-7613(1998)026<0787:TMSOAI>2.3.CO;2
- Giggenbach, W.F., 1997. Relative importance of thermodynamic and kinetic processes in governing the chemical and isotopic composition of carbon gases in high-heatflow sedimentary basins. Geochimica et Cosmochimica Acta 61, 3763–3785. https://doi.org/10.1016/S0016-7037(97)00171-3
- Giunta, T., Labidi, J., Kohl, I.E., Ruffine, L., Donval, J.P., Géli, L., Çağatay, M.N., Lu, H., Young, E.D., 2021. Evidence for methane isotopic bond re-ordering in gas reservoirs sourcing cold seeps from the Sea of Marmara. Earth and Planetary Science Letters 553, 116619. https://doi.org/10.1016/j.epsl.2020.116619
- Giunta, T., Young, E.D., Labidi, J., Sansjofre, P., Jézéquel, D., Donval, J.-P., Brandily, C., Ruffine, L., 2022. Extreme methane clumped isotopologue bio-signatures of aerobic and anaerobic methanotrophy: Insights from the Lake Pavin and the Black Sea sediments. Geochimica et Cosmochimica Acta 338, 34–53. https://doi.org/10.1016/j.gca.2022.09.034
- Global Energy Review 2021 (2021). IEA. Available at: https://www.iea.org/reports/world-energy-outlook-2021 (Accessed: 31 March 2025).
- Gonzalez, Y., Nelson, D.D., Shorter, J.H., McManus, J.B., Dyroff, C., Formolo, M., Wang,

- D.T., Western, C.M., Ono, S., 2019. Precise Measurements of <sup>12</sup> CH<sub>2</sub> D<sub>2</sub> by Tunable Infrared Laser Direct Absorption Spectroscopy. Anal. Chem. 91, 14967–14974. https://doi.org/10.1021/acs.analchem.9b03412
- Goral, J., Panja, P., Deo, M., Andrew, M., Linden, S., Schwarz, J.-O., Wiegmann, A., 2020. Confinement Effect on Porosity and Permeability of Shales. Sci Rep 10, 49. https://doi.org/10.1038/s41598-019-56885-y
- Graniero, L.E., Gillikin, D.P., Surge, D., 2021. Evaluating Freshwater Mussel Shell  $\delta^{13}$  C Values as a Proxy for Dissolved Inorganic Carbon  $\delta^{13}$  C Values in a Temperate River. JGR Biogeosciences 126, e2020JG006003. https://doi.org/10.1029/2020JG006003
- Graven, H., Fischer, M.L., Lueker, T., Jeong, S., Guilderson, T.P., Keeling, R.F., Bambha, R., Brophy, K., Callahan, W., Cui, X., Frankenberg, C., Gurney, K.R., LaFranchi, B.W., Lehman, S.J., Michelsen, H., Miller, J.B., Newman, S., Paplawsky, W., Parazoo, N.C., Sloop, C., Walker, S.J., 2018. Assessing fossil fuel CO2 emissions in California using atmospheric observations and models. Environ. Res. Lett. 13, 065007. https://doi.org/10.1088/1748-9326/aabd43
- Graven, H., Hocking, T., Zazzeri, G., 2019. Detection of Fossil and Biogenic Methane at Regional Scales Using Atmospheric Radiocarbon. Earth's Future 7, 283–299. https://doi.org/10.1029/2018EF001064
- Gray, G.J., Lawrence, S.R., Kenyon, K., Cornford, C., 1998. Nature and origin of 'carbon' in the Archaean Witwatersrand Basin, South Africa. JGS 155, 39–59. https://doi.org/10.1144/gsjgs.155.1.0039
- Gregory, R.T., 1991. Oxygen isotope history of seawater revisited: timescales for boundary event changes in the oxygen isotope composition of seawater. Geochem. Soc. Special Publ. 3, 65–76.
- Gromov, S., Brenninkmeijer, C.A.M., Jöckel, P., 2018. A very limited role of tropospheric chlorine as a sink of the greenhouse gas methane. Atmospheric Chemistry and Physics 18, 9831–9843. https://doi.org/10.5194/acp-18-9831-2018
- Grossman, E.L., 1998. oxygen isotopesOxygen isotopes, in: Geochemistry. Springer Netherlands, Dordrecht, pp. 469–474. https://doi.org/10.1007/1-4020-4496-8\_234
- Grove, D., Harris, C., 2010. O- AND H-ISOTOPE STUDY OF THE CARBON LEADER REEF AT THE TAU TONA AND SAVUKA MINES (WESTERN DEEP LEVELS), SOUTH AFRICA: IMPLICATIONS FOR THE ORIGIN AND EVOLUTION OF WITWATERSRAND BASIN FLUIDS. South African Journal of Geology 113, 73–86. https://doi.org/10.2113/gssajg.113.1-73
- Guo, W., Eiler, J.M., 2007. Temperatures of aqueous alteration and evidence for methane generation on the parent bodies of the CM chondrites. Geochimica et Cosmochimica Acta 71, 5565–5575. https://doi.org/10.1016/j.gca.2007.07.029
- Gürsan, C., de Gooyert, V., 2021. The systemic impact of a transition fuel: Does natural gas help or hinder the energy transition? Renewable and Sustainable Energy Reviews 138, 110552. https://doi.org/10.1016/j.rser.2020.110552
- Györe, D., Stuart, F.M., Gilfillan, S.M.V., Waldron, S., 2015. Tracing injected CO2 in the Cranfield enhanced oil recovery field (MS, USA) using He, Ne and Ar isotopes. International Journal of Greenhouse Gas Control 42, 554–561. https://doi.org/10.1016/j.ijggc.2015.09.009
- H. Craig, LI Gordon, n.d. Deuterium and oxygen 18 variations in the ocean and marine atmosphere. Spoleto Meeting on Nuclear Geology, Stable Isotopes in Oceanography Studies and Paleo Temperature.
- Haghnegahdar, M.A., Hultquist, N., Hamovit, N.D., Yarwood, S.A., Bouyon, A., Kaufman, A.J., Sun, J., Magen, C., Farquhar, J., 2024. A Better Understanding of Atmospheric Methane Sources Using<sup>13</sup> CH<sub>3</sub> D and<sup>12</sup> CH<sub>2</sub> D<sub>2</sub> Clumped Isotopes. JGR Biogeosciences 129, e2024JG008172. https://doi.org/10.1029/2024JG008172

- Haghnegahdar, M.A., Schauble, E.A., Young, E.D., 2017. A model for 12CH2D2 and 13CH3D as complementary tracers for the budget of atmospheric CH4. Global Biogeochemical Cycles 31, 1387–1407. https://doi.org/10.1002/2017GB005655
- Hakami, A., Ellis, L., Al-Ramadan, K., Abdelbagi, S., 2016. Mud gas isotope logging application for sweet spot identification in an unconventional shale gas play: A case study from Jurassic carbonate source rocks in Jafurah Basin, Saudi Arabia. Marine and Petroleum Geology 76, 133–147. https://doi.org/10.1016/j.marpetgeo.2016.05.003
- Hannun, R.M., Abdul Razzaq, A.H., 2022. Air Pollution Resulted from Coal, Oil and Gas Firing in Thermal Power Plants and Treatment: A Review. IOP Conf. Ser.: Earth Environ. Sci. 1002, 012008. https://doi.org/10.1088/1755-1315/1002/1/012008
- Hanson, R.S., Hanson, T.E., 1996. Methanotrophic bacteria. Microbiol Rev 60, 439–471. https://doi.org/10.1128/mr.60.2.439-471.1996
- Haroon, M.F., Hu, S., Shi, Y., Imelfort, M., Keller, J., Hugenholtz, P., Yuan, Z., Tyson, G.W., 2013. Anaerobic oxidation of methane coupled to nitrate reduction in a novel archaeal lineage. Nature 500, 567–570. https://doi.org/10.1038/nature12375
- Hayes, J.M., Waldbauer, J.R., 2006. The carbon cycle and associated redox processes through time. Phil. Trans. R. Soc. B 361, 931–950. https://doi.org/10.1098/rstb.2006.1840
- He, B., Olack, G.A., Colman, A.S., 2012. Pressure baseline correction and high-precision CO<sub>2</sub> clumped-isotope (Δ<sub>47</sub>) measurements in bellows and micro-volume modes. Rapid Comm Mass Spectrometry 26, 2837–2853. https://doi.org/10.1002/rcm.6436
- He, Z., Cai, C., Wang, J., Xu, X., Zheng, P., Jetten, M.S.M., Hu, B., 2016. A novel denitrifying methanotroph of the NC10 phylum and its microcolony. Sci Rep 6, 32241. https://doi.org/10.1038/srep32241
- Heard, A.W., Warr, O., Borgonie, G., Linage, B., Kuloyo, O., Fellowes, J.W., Magnabosco, C., Lau, M.C.Y., Erasmus, M., Cason, E.D., van Heerden, E., Kieft, T.L., Mabry, J.C., Onstott, T.C., Sherwood Lollar, B., Ballentine, C.J., 2018. South African crustal fracture fluids preserve paleometeoric water signatures for up to tens of millions of years. Chemical Geology 493, 379–395. https://doi.org/10.1016/j.chemgeo.2018.06.011
- Henkes, G.A., Passey, B.H., Grossman, E.L., Shenton, B.J., Yancey, T.E., Pérez-Huerta, A., 2018. Temperature evolution and the oxygen isotope composition of Phanerozoic oceans from carbonate clumped isotope thermometry. Earth and Planetary Science Letters 490, 40–50. https://doi.org/10.1016/j.epsl.2018.02.001
- Hoefs, J., 2015. Stable isotope geochemistry, Seventh edition. ed. Springer, Cham, Switzerland.
- Hoefs, J., Schidlowski, M., 1967. Carbon Isotope Composition of Carbonaceous Matter from the Precambrian of the Witwatersrand System. Science 155, 1096–1097. https://doi.org/10.1126/science.155.3766.1096
- Holler, T., Wegener, G., Knittel, K., Boetius, A., Brunner, B., Kuypers, M.M.M., Widdel, F., 2009. Substantial<sup>13</sup> C/<sup>12</sup> C and D/H fractionation during anaerobic oxidation of methane by marine consortia enriched *in vitro*. Environ Microbiol Rep 1, 370–376. https://doi.org/10.1111/j.1758-2229.2009.00074.x
- Holloway, J.R., 1984. Graphite-CH4-H2O-CO2 equilibria at low-grade metamorphic conditions. Geol 12, 455. https://doi.org/10.1130/0091-7613(1984)12<455:GEALMC>2.0.CO;2
- Horibe, Y., Craig, H., 1995. DH<math><mtext>D</mtext><mtext>H</mtext></math> fractionation in the system methane-hydrogen-water. Geochimica et Cosmochimica Acta 59, 5209–5217. https://doi.org/10.1016/0016-7037(95)00391-6
- Horita, J., 2001. Carbon isotope exchange in the system CO2-CH4 at elevated temperatures. Geochimica et Cosmochimica Acta 65, 1907–1919.

- https://doi.org/10.1016/S0016-7037(01)00570-1
- Houston, A., Gazetas, O., Defratyka, S., Arnold, T., Clog, M., 2025. Further Cryogenic Separation and Mass Spectrometry Developments: Towards Ambient Air Methane Clumped Isotopes Measurements https://doi.org/10.5194/egusphere-egu24-11447
- Hugo, P.J., 1963. Helium in the Orange Free State Goldfield. Bulletin of the Geological Survey of South Africa 39, 28.
- Hunt, J.M., 1996. Petroleum geochemistry and geology, 2nd ed. ed. Freeman, New York.
- Huntington, K.W., Eiler, J.M., Affek, H.P., Guo, W., Bonifacie, M., Yeung, L.Y.,
  Thiagarajan, N., Passey, B., Tripati, A., Daëron, M., Came, R., 2009. Methods and limitations of 'clumped' CO<sub>2</sub> isotope (Δ<sub>47</sub>) analysis by gas-source isotope ratio mass spectrometry. J. Mass Spectrom. 44, 1318–1329. https://doi.org/10.1002/jms.1614
- Huntington, K.W., Lechler, A.R., 2015. Carbonate clumped isotope thermometry in continental tectonics. Tectonophysics 647–648, 1–20. https://doi.org/10.1016/j.tecto.2015.02.019
- Huntington, K.W., Petersen, S.V., 2023. Frontiers of Carbonate Clumped Isotope Thermometry. Annual Review of Earth and Planetary Sciences 51, 611–641. https://doi.org/10.1146/annurev-earth-031621-085949
- I Friedman, J.R O'neil, 1977. Compilation of stable isotope fractionation factors of geochemical interest. USGS Prof. Paper 440KK.
- Intergovernmental Panel On Climate Change, 2007. Climate Change 2007: Mitigation of Climate Change. Cambridge University Press, Cambridge. https://doi.org/10.1017/CBO9780511546013
- Isaksen, I.S.A., Berntsen, T.K., Dalsøren, S.B., Eleftheratos, K., Orsolini, Y., Rognerud, B., Stordal, F., Søvde, O.A., Zerefos, C., Holmes, C.D., 2014. Atmospheric Ozone and Methane in a Changing Climate. Atmosphere 5, 518–535. https://doi.org/10.3390/atmos5030518
- Ishidoya, S., Sugawara, S., Okazaki, A., 2025. Diurnal, seasonal, and interannual variations in  $\delta(^{18}\mathrm{O})$  of atmospheric  $\mathrm{O}_2$  and its application to evaluate natural and anthropogenic changes in oxygen, carbon, and water cycles. Atmospheric Chemistry and Physics 25, 1965–1987. https://doi.org/10.5194/acp-25-1965-2025
- Iversen, N., Jorgensen, B.B., 1985. Anaerobic methane oxidation rates at the sulfate-methane transition in marine sediments from Kattegat and Skagerrak (Denmark)1. Limnology & Oceanography 30, 944–955. https://doi.org/10.4319/lo.1985.30.5.0944
- Jackson, R.B., Saunois, M., Bousquet, P., Canadell, J.G., Poulter, B., Stavert, A.R., Bergamaschi, P., Niwa, Y., Segers, A., Tsuruta, A., 2020. Increasing anthropogenic methane emissions arise equally from agricultural and fossil fuel sources. Environ. Res. Lett. 15, 071002. https://doi.org/10.1088/1748-9326/ab9ed2
- Jaffrés, J.B.D., Shields, G.A., Wallmann, K., 2007. The oxygen isotope evolution of seawater: A critical review of a long-standing controversy and an improved geological water cycle model for the past 3.4 billion years. Earth-Science Reviews 83, 83–122. https://doi.org/10.1016/j.earscirev.2007.04.002
- Jaguin, J., Boulvais, P., Poujol, M., Boiron, M.C., Cathelineau, M., 2010. STABLE ISOTOPE COMPOSITION OF QUARTZ-CALCITE VEINS IN THE WITWATERSRAND BASIN, SOUTH AFRICA: IMPLICATION FOR BASIN-SCALE FLUID CIRCULATION. South African Journal of Geology 113, 169–182. https://doi.org/10.2113/gssajg.113.2.169
- Jautzy, J.J., Douglas, P.M.J., Xie, H., Eiler, J.M., Clark, I.D., 2021. CH4 isotopic ordering records ultra-slow hydrocarbon biodegradation in the deep subsurface. Earth and Planetary Science Letters 562, 116841. https://doi.org/10.1016/j.epsl.2021.116841

- Joelsson, L.M.T., Forecast, R., Schmidt, J.A., Meusinger, C., Nilsson, E.J.K., Ono, S., Johnson, M.S., 2014. Relative rate study of the kinetic isotope effect in the 13CH3D + Cl reaction. Chemical Physics Letters 605–606, 152–157. https://doi.org/10.1016/j.cplett.2014.05.022
- Joelsson, L.M.T., Schmidt, J.A., Nilsson, E.J.K., Blunier, T., Griffith, D.W.T., Ono, S., Johnson, M.S., 2016. Kinetic isotope effects of <sup>12</sup>CH<sub>3</sub>D + OH and <sup>13</sup>CH<sub>3</sub>D + OH from 278 to 313 K. Atmospheric Chemistry and Physics 16, 4439–4449. https://doi.org/10.5194/acp-16-4439-2016
- Johnson, D., Heltzel, R., Oliver, D., 2019. Temporal Variations in Methane Emissions from an Unconventional Well Site. ACS Omega 4, 3708–3715. https://doi.org/10.1021/acsomega.8b03246
- Johnson, H., Doré, A.G., 2010. Unconventional oil and gas resources and the geological storage of carbon dioxide: overview. PGC 7, 1061–1063. https://doi.org/10.1144/0071061
- Jones, M.Q.W., 1988. Heat flow in the Witwatersrand Basin and environs and its significance for the South African Shield Geotherm and lithosphere thickness. J. Geophys. Res. 93, 3243–3260. https://doi.org/10.1029/JB093iB04p03243
- Kandiyoti, R., Herod, A.A., Bartle, K.D., 2006. Solid fuels and heavy hydrocarbon liquids: thermal characterization and analysis. Elsevier, Amsterdam.
- Kantnerová, K., Yu, L., Zindel, D., Zahniser, M.S., Nelson, D.D., Tuzson, B., Nakagawa, M., Toyoda, S., Yoshida, N., Emmenegger, L., Bernasconi, S.M., Mohn, J., 2020. First investigation and absolute calibration of clumped isotopes in N<sub>2</sub> O by mid-infrared laser spectroscopy. Rapid Comm Mass Spectrometry 34, e8836. https://doi.org/10.1002/rcm.8836
- Karolytė, R., Warr, O., van Heerden, E., Flude, S., de Lange, F., Webb, S., Ballentine, C.J., Sherwood Lollar, B., 2022. The role of porosity in H2/He production ratios in fracture fluids from the Witwatersrand Basin, South Africa. Chemical Geology 595, 120788. https://doi.org/10.1016/j.chemgeo.2022.120788
- Kerrich, R., Ludden, J., 2000. The role of fluids during formation and evolution of the southern Superior Province lithosphere: an overview. Can. J. Earth Sci. 37, 135–164. https://doi.org/10.1139/e99-098
- Keunecke, A., Dossow, M., Dieterich, V., Spliethoff, H., Fendt, S., 2024. Insights into Fischer–Tropsch catalysis: current perspectives, mechanisms, and emerging trends in energy research. Front. Energy Res. 12. https://doi.org/10.3389/fenrg.2024.1344179
- Kim, S.-T., Coplen, T.B., Horita, J., 2015. Normalization of stable isotope data for carbonate minerals: Implementation of IUPAC guidelines. Geochimica et Cosmochimica Acta 158, 276–289. https://doi.org/10.1016/j.gca.2015.02.011
- Kim, S.-T., Mucci, A., Taylor, B.E., 2007. Phosphoric acid fractionation factors for calcite and aragonite between 25 and 75 °C: Revisited. Chemical Geology 246, 135–146. https://doi.org/10.1016/j.chemgeo.2007.08.005
- Kim, S.-T., O'Neil, J.R., 1997. Equilibrium and nonequilibrium oxygen isotope effects in synthetic carbonates. Geochimica et Cosmochimica Acta 61, 3461–3475. https://doi.org/10.1016/S0016-7037(97)00169-5
- Kirschke, S., Bousquet, P., Ciais, P., Saunois, M., Canadell, J.G., Dlugokencky, E.J., Bergamaschi, P., Bergmann, D., Blake, D.R., Bruhwiler, L., Cameron-Smith, P., Castaldi, S., Chevallier, F., Feng, L., Fraser, A., Heimann, M., Hodson, E.L., Houweling, S., Josse, B., Fraser, P.J., Krummel, P.B., Lamarque, J.-F., Langenfelds, R.L., Le Quéré, C., Naik, V., O'Doherty, S., Palmer, P.I., Pison, I., Plummer, D., Poulter, B., Prinn, R.G., Rigby, M., Ringeval, B., Santini, M., Schmidt, M., Shindell, D.T., Simpson, I.J., Spahni, R., Steele, L.P., Strode, S.A., Sudo, K., Szopa, S., Van Der Werf, G.R., Voulgarakis, A., Van Weele, M., Weiss,

- R.F., Williams, J.E., Zeng, G., 2013. Three decades of global methane sources and sinks. Nature Geosci 6, 813–823. https://doi.org/10.1038/ngeo1955
- Knutsen, E.W., Villanueva, G.L., Liuzzi, G., Crismani, M.M.J., Mumma, M.J., Smith, M.D., Vandaele, A.C., Aoki, S., Thomas, I.R., Daerden, F., Viscardy, S., Erwin, J.T., Trompet, L., Neary, L., Ristic, B., Lopez-Valverde, M.A., Lopez-Moreno, J.J., Patel, M.R., Karatekin, O., Bellucci, G., 2021. Comprehensive investigation of Mars methane and organics with ExoMars/NOMAD. Icarus 357, 114266. https://doi.org/10.1016/j.icarus.2020.114266
- Kocken, I.J., Müller, I.A., Ziegler, M., 2019. Optimizing the Use of Carbonate Standards to Minimize Uncertainties in Clumped Isotope Data. Geochem Geophys Geosyst 20, 5565–5577. https://doi.org/10.1029/2019GC008545
- Kokkinos, N.C., Nkagbu, D.C., Marmanis, D.I., Dermentzis, K.I., Maliaris, G., 2022. Evolution of Unconventional Hydrocarbons: Past, Present, Future and Environmental FootPrint. JESTR 15, 15–24. https://doi.org/10.25103/jestr.154.03
- Kotelnikova, S., 2002. Microbial production and oxidation of methane in deep subsurface. Earth-Science Reviews 58, 367–395. https://doi.org/10.1016/S0012-8252(01)00082-4
- Krause, S.J.E., Liu, J., Young, E.D., Treude, T., 2022. Δ 13 CH 3 D and Δ 12 CH 2 D 2 signatures of methane aerobically oxidized by Methylosinus trichosporium with implications for deciphering the provenance of methane gases. Earth and Planetary Science Letters 593, 117681. https://doi.org/10.1016/j.epsl.2022.117681
- Kuang, Y., Lin, B., 2023. Unwatched pollution reduction: The effect of natural gas utilization on air quality. Energy 273, 127247. https://doi.org/10.1016/j.energy.2023.127247
- Kump, L.R., Arthur, M.A., 1999. Interpreting carbon-isotope excursions: carbonates and organic matter. Chemical Geology 161, 181–198. https://doi.org/10.1016/S0009-2541(99)00086-8
- Kurth, J.M., Op Den Camp, H.J.M., Welte, C.U., 2020. Several ways one goal—methanogenesis from unconventional substrates. Appl Microbiol Biotechnol 104, 6839–6854. https://doi.org/10.1007/s00253-020-10724-7
- Kvenvolden, K.A., 1995. A review of the geochemistry of methane in natural gas hydrate. Organic Geochemistry 23, 997–1008. https://doi.org/10.1016/0146-6380(96)00002-2
- Kvenvolden, K.A., 1993. Gas hydrates—geological perspective and global change. Reviews of Geophysics 31, 173–187. https://doi.org/10.1029/93RG00268
- Labidi, J., McCollom, T.M., Giunta, T., Sherwood Lollar, B., Leavitt, W.D., Young, E.D., 2024. Clumped Isotope Signatures of Abiotic Methane: The Role of the Combinatorial Isotope Effect. JGR Solid Earth 129, e2023JB028194. https://doi.org/10.1029/2023JB028194
- Labidi, J., Young, E.D., 2022. The origin and dynamics of nitrogen in the Earth's mantle constrained by 15N15N in hydrothermal gases. Chemical Geology 591, 120709. https://doi.org/10.1016/j.chemgeo.2022.120709
- Labidi, J., Young, E.D., Giunta, T., Kohl, I.E., Seewald, J., Tang, H., Lilley, M.D., Früh-Green, G.L., 2020. Methane thermometry in deep-sea hydrothermal systems: Evidence for re-ordering of doubly-substituted isotopologues during fluid cooling. Geochimica et Cosmochimica Acta 288, 248–261. https://doi.org/10.1016/j.gca.2020.08.013
- Lalk, E., Pape, T., Gruen, D.S., Kaul, N., Karolewski, J.S., Bohrmann, G., Ono, S., 2022. Clumped methane isotopologue-based temperature estimates for sources of methane in marine gas hydrates and associated vent gases. Geochimica et Cosmochimica Acta 327, 276–297. https://doi.org/10.1016/j.gca.2022.04.013
- Lan, X., Dlugokencky, E.J., 2024. Atmospheric constraints on changing Arctic CH4

- emissions. Front. Environ. Sci. 12. https://doi.org/10.3389/fenvs.2024.1382621
- Lau, M.C.Y., Kieft, T.L., Kuloyo, O., Linage-Alvarez, B., van Heerden, E., Lindsay, M.R., Magnabosco, C., Wang, W., Wiggins, J.B., Guo, L., Perlman, D.H., Kyin, S., Shwe, H.H., Harris, R.L., Oh, Y., Yi, M.J., Purtschert, R., Slater, G.F., Ono, S., Wei, S., Li, L., Sherwood Lollar, B., Onstott, T.C., 2016. An oligotrophic deepsubsurface community dependent on syntrophy is dominated by sulfur-driven autotrophic denitrifiers. Proceedings of the National Academy of Sciences 113, E7927–E7936. https://doi.org/10.1073/pnas.1612244113
- Lauerwald, R., Allen, G.H., Deemer, B.R., Liu, S., Maavara, T., Raymond, P., Alcott, L., Bastviken, D., Hastie, A., Holgerson, M.A., Johnson, M.S., Lehner, B., Lin, P., Marzadri, A., Ran, L., Tian, H., Yang, X., Yao, Y., Regnier, P., 2023a. Inland Water Greenhouse Gas Budgets for RECCAP2: 1. State-Of-The-Art of Global Scale Assessments. Global Biogeochemical Cycles 37, e2022GB007657. https://doi.org/10.1029/2022GB007657
- Lauerwald, R., Allen, G.H., Deemer, B.R., Liu, S., Maavara, T., Raymond, P., Alcott, L., Bastviken, D., Hastie, A., Holgerson, M.A., Johnson, M.S., Lehner, B., Lin, P., Marzadri, A., Ran, L., Tian, H., Yang, X., Yao, Y., Regnier, P., 2023b. Inland Water Greenhouse Gas Budgets for RECCAP2: 2. Regionalization and Homogenization of Estimates. Global Biogeochemical Cycles 37, e2022GB007658. https://doi.org/10.1029/2022GB007658
- Law, S.J., Allison, S.D., Davies, A.B., Flores-Moreno, H., Wijas, B.J., Yatsko, A.R., Zhou, Y., Zanne, A.E., Eggleton, P., 2024. The challenge of estimating global termite methane emissions. Global Change Biology 30, e17390. https://doi.org/10.1111/gcb.17390
- Lee, J.-H., Lee, J.-Y., Kang, Y.-G., Kim, J.-H., Oh, T.-K., 2023a. Evaluating methane emissions from rice paddies: A study on the cultivar and transplanting date. Science of The Total Environment 902, 166174. https://doi.org/10.1016/j.scitotenv.2023.166174
- Lee, J.-H., Lee, J.-Y., Kang, Y.-G., Kim, J.-H., Oh, T.-K., 2023b. Evaluating methane emissions from rice paddies: A study on the cultivar and transplanting date. Science of The Total Environment 902, 166174. https://doi.org/10.1016/j.scitotenv.2023.166174
- Lee, P.S., Majkowski, R.F., 1986. High resolution infrared diode laser spectroscopy for isotope analysis—Measurement of isotopic carbon monoxide. Applied Physics Letters 48, 619–621. https://doi.org/10.1063/1.96722
- Lewan, M.D., 1983. Effects of thermal maturation on stable organic carbon isotopes as determined by hydrous pyrolysis of Woodford Shale. Geochimica et Cosmochimica Acta 47, 1471–1479. https://doi.org/10.1016/0016-7037(83)90306-X
- Lewan, M.D., Ulmishek, G.F., Harrison, W., Schreiner, F., 1991. Gamma 60Co-irradiation of organic matter in the Phosphoria Retort Shale. Geochimica et Cosmochimica Acta 55, 1051–1063. https://doi.org/10.1016/0016-7037(91)90163-Y
- Lin, L.-H., Slater, G.F., Sherwood Lollar, B., Lacrampe-Couloume, G., Onstott, T.C., 2005. The yield and isotopic composition of radiolytic H2, a potential energy source for the deep subsurface biosphere. Geochimica et Cosmochimica Acta 69, 893–903. https://doi.org/10.1016/j.gca.2004.07.032
- Lin, L.-H., Wang, P.-L., Rumble, D., Lippmann-Pipke, J., Boice, E., Pratt, L.M., Sherwood Lollar, B., Brodie, E.L., Hazen, T.C., Andersen, G.L., DeSantis, T.Z., Moser, D.P., Kershaw, D., Onstott, T.C., 2006. Long-term sustainability of a high-energy, low-diversity crustal biome. Science 314, 479–482. https://doi.org/10.1126/science.1127376
- Lippmann, J., Stute, M., Torgersen, T., Moser, D.P., Hall, J.A., Lin, L., Borcsik, M., Bellamy, R.E.S., Onstott, T.C., 2003. Dating ultra-deep mine waters with noble

- gases and 36Cl, Witwatersrand Basin, South Africa. Geochimica et Cosmochimica Acta 67, 4597–4619. https://doi.org/10.1016/S0016-7037(03)00414-9
- Lippmann-Pipke, J., Sherwood Lollar, B., Niedermann, S., Stroncik, N.A., Naumann, R., van Heerden, E., Onstott, T.C., 2011. Neon identifies two billion year old fluid component in Kaapvaal Craton. Chemical Geology 283, 287–296. https://doi.org/10.1016/j.chemgeo.2011.01.028
- Liu, J., Harris, R.L., Ash, J.L., Ferry, J.G., Krause, S.J.E., Labidi, J., Prakash, D., Sherwood Lollar, B., Treude, T., Warr, O., Young, E.D., 2023. Reversibility controls on extreme methane clumped isotope signatures from anaerobic oxidation of methane. Geochimica et Cosmochimica Acta 348, 165–186. https://doi.org/10.1016/j.gca.2023.02.022
- Liu, L., Zhuang, Q., Oh, Y., Shurpali, N.J., Kim, S., Poulter, B., 2020. Uncertainty Quantification of Global Net Methane Emissions From Terrestrial Ecosystems Using a Mechanistically Based Biogeochemistry Model. JGR Biogeosciences 125, e2019JG005428. https://doi.org/10.1029/2019JG005428
- Liu, M., Song, Y., Matsui, H., Shang, F., Kang, L., Cai, X., Zhang, H., Zhu, T., 2024. Enhanced atmospheric oxidation toward carbon neutrality reduces methane's climate forcing. Nat Commun 15, 3148. https://doi.org/10.1038/s41467-024-47436-9
- Liu, S., Yu, S., Lu, X., Yang, H., Li, Y., Xu, X., Lu, H., Fang, Y., 2022. Microbial communities associated with thermogenic gas hydrate-bearing marine sediments in Qiongdongnan Basin, South China Sea. Front. Microbiol. 13. https://doi.org/10.3389/fmicb.2022.1032851
- Lloyd, M.K., Eldridge, D.L., Stolper, D.A., 2021. Clumped 13CH2D and 12CHD2 compositions of methyl groups from wood and synthetic monomers: Methods, experimental and theoretical calibrations, and initial results. Geochimica et Cosmochimica Acta 297, 233–275. https://doi.org/10.1016/j.gca.2020.10.008
- Lloyd, M.K., Ryb, U., Eiler, J.M., 2018. Experimental calibration of clumped isotope reordering in dolomite. Geochimica et Cosmochimica Acta 242, 1–20. https://doi.org/10.1016/j.gca.2018.08.036
- Lollar, B.S., Lacrampe-Couloume, G., Voglesonger, K., Onstott, T.C., Pratt, L.M., Slater, G.F., 2008a. Isotopic signatures of CH4 and higher hydrocarbon gases from Precambrian Shield sites: A model for abiogenic polymerization of hydrocarbons. Geochimica et Cosmochimica Acta 72, 4778–4795. https://doi.org/10.1016/j.gca.2008.07.004
- Lollar, B.S., Lacrampe-Couloume, G., Voglesonger, K., Onstott, T.C., Pratt, L.M., Slater, G.F., 2008b. Isotopic signatures of CH4 and higher hydrocarbon gases from Precambrian Shield sites: A model for abiogenic polymerization of hydrocarbons. Geochimica et Cosmochimica Acta 72, 4778–4795. https://doi.org/10.1016/j.gca.2008.07.004
- Lollar, G.S., Warr ,Oliver, Telling ,Jon, Osburn ,Magdalena R., and Lollar, B.S., 2019. 'Follow the Water': Hydrogeochemical Constraints on Microbial Investigations 2.4 km Below Surface at the Kidd Creek Deep Fluid and Deep Life Observatory. Geomicrobiology Journal 36, 859–872. https://doi.org/10.1080/01490451.2019.1641770
- Lowry, D., Fisher, R.E., France, J.L., Coleman, M., Lanoisellé, M., Zazzeri, G., Nisbet, E.G., Shaw, J.T., Allen, G., Pitt, J., Ward, R.S., 2020. Environmental baseline monitoring for shale gas development in the UK: Identification and geochemical characterisation of local source emissions of methane to atmosphere. Science of The Total Environment 708, 134600. https://doi.org/10.1016/j.scitotenv.2019.134600
- Loyd, S.J., Sample, J., Tripati, R.E., Defliese, W.F., Brooks, K., Hovland, M., Torres, M.,

- Marlow, J., Hancock, L.G., Martin, R., Lyons, T., Tripati, A.E., 2016. Methane seep carbonates yield clumped isotope signatures out of equilibrium with formation temperatures. Nat Commun 7, 12274. https://doi.org/10.1038/ncomms12274
- Lu, F.H., 2023. A review of carbon isotopes and maturity determinations of paleozoic unconventional shale gases. Marine and Petroleum Geology 149, 106080. https://doi.org/10.1016/j.marpetgeo.2022.106080
- Luz, B., Barkan, E., 2011. The isotopic composition of atmospheric oxygen: ISOTOPIC COMPOSITION OF AIR OXYGEN. Global Biogeochem. Cycles 25, n/a-n/a. https://doi.org/10.1029/2010GB003883
- Lyu, Z., Shao, N., Akinyemi, T., Whitman, W.B., 2018. Methanogenesis. Current Biology 28, R727–R732. https://doi.org/10.1016/j.cub.2018.05.021
- Ma, K., Liu, X., Dong, X., 2006. Methanosaeta harundinacea sp. nov., a novel acetate-scavenging methanogen isolated from a UASB reactor. International Journal of Systematic and Evolutionary Microbiology 56, 127–131. https://doi.org/10.1099/ijs.0.63887-0
- Mac Kinnon, M.A., Brouwer, J., Samuelsen, S., 2018. The role of natural gas and its infrastructure in mitigating greenhouse gas emissions, improving regional air quality, and renewable resource integration. Progress in Energy and Combustion Science 64, 62–92. https://doi.org/10.1016/j.pecs.2017.10.002
- MacDonald, J.M., Faithfull, J.W., Roberts, N.M.W., Davies, A.J., Holdsworth, C.M., Newton, M., Williamson, S., Boyce, A., John, C.M., 2019. Clumped-isotope palaeothermometry and LA-ICP-MS U–Pb dating of lava-pile hydrothermal calcite veins. Contrib Mineral Petrol 174, 63. https://doi.org/10.1007/s00410-019-1599-x
- Madhusudhan, N., Sarkar, S., Constantinou, S., Holmberg, M., Piette, A.A.A., Moses, J.I., 2023. Carbon-bearing Molecules in a Possible Hycean Atmosphere. ApJL 956, L13. https://doi.org/10.3847/2041-8213/acf577
- Magnabosco, C., Ryan, K., Lau, M.C.Y., Kuloyo, O., Sherwood Lollar, B., Kieft, T.L., van Heerden, E., Onstott, T.C., 2016. A metagenomic window into carbon metabolism at 3 km depth in Precambrian continental crust. The ISME Journal 10, 730–741. https://doi.org/10.1038/ismej.2015.150
- Magyar, P.M., Orphan, V.J., Eiler, J.M., 2016a. Measurement of rare isotopologues of nitrous oxide by high-resolution multi-collector mass spectrometry. Rapid Communications in Mass Spectrometry 30, 1923–1940. https://doi.org/10.1002/rcm.7671
- Magyar, P.M., Orphan, V.J., Eiler, J.M., 2016b. Measurement of rare isotopologues of nitrous oxide by high-resolution multi-collector mass spectrometry. Rapid Comm Mass Spectrometry 30, 1923–1940. https://doi.org/10.1002/rcm.7671
- Mangenot, X., Tarantola, A., Mullis, J., Girard, J.-P., Le, V.-H., Eiler, J.M., 2021. Geochemistry of clumped isotopologues of CH4 within fluid inclusions in Alpine tectonic quartz fissures. Earth and Planetary Science Letters 561, 116792. https://doi.org/10.1016/j.epsl.2021.116792
- Manzi, M.S.D., Durrheim, R.J., Hein, K.A.A., King, N., 2012. 3D edge detection seismic attributes used to map potential conduits for water and methane in deep gold mines in the Witwatersrand basin, South Africa. GEOPHYSICS 77, WC133–WC147. https://doi.org/10.1190/geo2012-0135.1
- McCollom, T.M., Seewald, J.S., 2007. Abiotic Synthesis of Organic Compounds in Deep-Sea Hydrothermal Environments. Chem. Rev. 107, 382–401. https://doi.org/10.1021/cr0503660
- McCollom, T.M., Seewald, J.S., 2003. Experimental constraints on the hydrothermal reactivity of organic acids and acid anions: I. Formic acid and formate. Geochimica et Cosmochimica Acta 67, 3625–3644. https://doi.org/10.1016/S0016-7037(03)00136-4

- McCormick, C.A., Corlett, H., Clog, M., Boyce, A.J., Tartèse, R., Steele-MacInnis, M., Hollis, C., 2023. Basin scale evolution of zebra textures in fault-controlled, hydrothermal dolomite bodies: Insights from the Western Canadian Sedimentary Basin. Basin Research 35, 2010–2039. https://doi.org/10.1111/bre.12789
- McManus, J.B., Kebabian, P.L., Zahniser, M.S., 1995. Astigmatic mirror multipass absorption cells for long-path-length spectroscopy. Appl. Opt. 34, 3336. https://doi.org/10.1364/AO.34.003336
- Meijide, A., Manca, G., Goded, I., Magliulo, V., di Tommasi, P., Seufert, G., Cescatti, A., 2011. Seasonal trends and environmental controls of methane emissions in a rice paddy field in Northern Italy. Biogeosciences 8, 3809–3821. https://doi.org/10.5194/bg-8-3809-2011
- Milkov, A.V., Etiope, G., 2018. Revised genetic diagrams for natural gases based on a global dataset of >20,000 samples. Organic Geochemistry 125, 109–120. https://doi.org/10.1016/j.orggeochem.2018.09.002
- Mizuno, T., Suzuki, Y., Milodowski, A.E., Iwatsuki, T., 2023. Isotopic signals in fracture-filling calcite showing anaerobic oxidation of methane in a granitic basement. Applied Geochemistry 150, 105571. https://doi.org/10.1016/j.apgeochem.2023.105571
- Mkhabela, M., Manzi, M., 2017. Detection of potential methane gas pathways in deep South African gold mines. Journal of Geophysics and Engineering 14, 960–974. https://doi.org/10.1088/1742-2140/aa6fc8
- Moore, M.T., Vinson, D.S., Whyte, C.J., Eymold, W.K., Walsh, T.B., Darrah, T.H., 2018. Differentiating between biogenic and thermogenic sources of natural gas in coalbed methane reservoirs from the Illinois Basin using noble gas and hydrocarbon geochemistry. SP 468, 151–188. https://doi.org/10.1144/SP468.8
- Moran, J.J., Beal, E.J., Vrentas, J.M., Orphan, V.J., Freeman, K.H., House, C.H., 2008a. Methyl sulfides as intermediates in the anaerobic oxidation of methane. Environ Microbiol 10, 162–173. https://doi.org/10.1111/j.1462-2920.2007.01441.x
- Moran, J.J., Beal, E.J., Vrentas, J.M., Orphan, V.J., Freeman, K.H., House, C.H., 2008b. Methyl sulfides as intermediates in the anaerobic oxidation of methane. Environmental Microbiology 10, 162–173. https://doi.org/10.1111/j.1462-2920.2007.01441.x
- Moses Chung, H., Sackett, W.M., 1980. Carbon isotope effects during the pyrolytic formation of early methane from carbonaceous materials. Physics and Chemistry of the Earth 12, 705–710. https://doi.org/10.1016/0079-1946(79)90151-4
- Murguia-Flores, F., Jaramillo, V.J., Gallego-Sala, A., 2023. Assessing Methane Emissions From Tropical Wetlands: Uncertainties From Natural Variability and Drivers at the Global Scale. Global Biogeochemical Cycles 37, e2022GB007601. https://doi.org/10.1029/2022GB007601
- Murray, K.K., 2022. Resolution and Resolving Power in Mass Spectrometry. J. Am. Soc. Mass Spectrom. 33, 2342–2347. https://doi.org/10.1021/jasms.2c00216
- Murray, L.T., Fiore, A.M., Shindell, D.T., Naik, V., Horowitz, L.W., 2021. Large uncertainties in global hydroxyl projections tied to fate of reactive nitrogen and carbon. Proceedings of the National Academy of Sciences 118, e2115204118. https://doi.org/10.1073/pnas.2115204118
- Murrell, J.C., 2010. The Aerobic Methane Oxidizing Bacteria (Methanotrophs), in: Timmis, K.N. (Ed.), Handbook of Hydrocarbon and Lipid Microbiology. Springer, Berlin, Heidelberg, pp. 1953–1966. https://doi.org/10.1007/978-3-540-77587-4 143
- Naik, V., Voulgarakis, A., Fiore, A.M., Horowitz, L.W., Lamarque, J.-F., Lin, M., Prather, M.J., Young, P.J., Bergmann, D., Cameron-Smith, P.J., Cionni, I., Collins, W.J., Dalsøren, S.B., Doherty, R., Eyring, V., Faluvegi, G., Folberth, G.A., Josse, B.,

- Lee, Y.H., MacKenzie, I.A., Nagashima, T., van Noije, T.P.C., Plummer, D.A., Righi, M., Rumbold, S.T., Skeie, R., Shindell, D.T., Stevenson, D.S., Strode, S., Sudo, K., Szopa, S., Zeng, G., 2013. Preindustrial to present-day changes in tropospheric hydroxyl radical and methane lifetime from the Atmospheric Chemistry and Climate Model Intercomparison Project (ACCMIP). Atmospheric Chemistry and Physics 13, 5277–5298. https://doi.org/10.5194/acp-13-5277-2013
- Naumenko-Dèzes, M., Kloppmann, W., Blessing, M., Bondu, R., Gaucher, E.C., Mayer, B., 2022. Natural gas of radiolytic origin: An overlooked component of shale gas. Proc. Natl. Acad. Sci. U.S.A. 119, e2114720119. https://doi.org/10.1073/pnas.2114720119
- Nier, A.O., 1947. A Mass Spectrometer for Isotope and Gas Analysis. Review of Scientific Instruments 18, 398–411. https://doi.org/10.1063/1.1740961
- Nisbet, E.G., Manning, M.R., Dlugokencky, E.J., Fisher, R.E., Lowry, D., Michel, S.E., Myhre, C.L., Platt, S.M., Allen, G., Bousquet, P., Brownlow, R., Cain, M., France, J.L., Hermansen, O., Hossaini, R., Jones, A.E., Levin, I., Manning, A.C., Myhre, G., Pyle, J.A., Vaughn, B.H., Warwick, N.J., White, J.W.C., 2019. Very Strong Atmospheric Methane Growth in the 4 Years 2014–2017: Implications for the Paris Agreement. Global Biogeochemical Cycles 33, 318–342. https://doi.org/10.1029/2018GB006009
- Nisbet, E.G., Manning, M.R., Dlugokencky, E.J., Michel, S.E., Lan, X., Röckmann, T., Denier van der Gon, H.A.C., Schmitt, J., Palmer, P.I., Dyonisius, M.N., Oh, Y., Fisher, R.E., Lowry, D., France, J.L., White, J.W.C., Brailsford, G., Bromley, T., 2023. Atmospheric Methane: Comparison Between Methane's Record in 2006–2022 and During Glacial Terminations. Global Biogeochemical Cycles 37, e2023GB007875. https://doi.org/10.1029/2023GB007875
- Nishimura, H., Kouduka, M., Fukuda, A., Ishimura, T., Amano, Y., Beppu, H., Miyakawa, K., Suzuki, Y., 2023. Anaerobic methane-oxidizing activity in a deep underground borehole dominantly colonized by *CA*. Methanoperedenaceae. Environ Microbiol Rep 15, 197–205. https://doi.org/10.1111/1758-2229.13146
- Nisson, D.M., Kieft, T.L., Drake, H., Warr, O., Sherwood Lollar, B., Ogasawara, H., Perl, S.M., Friefeld, B.M., Castillo, J., Whitehouse, M.J., Kooijman, E., Onstott, T.C., 2023. Hydrogeochemical and isotopic signatures elucidate deep subsurface hypersaline brine formation through radiolysis driven water-rock interaction. Geochimica et Cosmochimica Acta 340, 65–84. https://doi.org/10.1016/j.gca.2022.11.015
- Nisson, Devan M., Walters, C.C., Chacón-Patiño, M.L., Weisbrod, C.R., Kieft, T.L., Sherwood Lollar, B., Warr, O., Castillo, J., Perl, S.M., Cason, E.D., Freifeld, B.M., Onstott, T.C., 2023. Radiolytically reworked Archean organic matter in a habitable deep ancient high-temperature brine. Nat Commun 14, 6163. https://doi.org/10.1038/s41467-023-41900-8
- Nnabuife, S.G., Oko, E., Kuang, B., Bello, A., Onwualu, A.P., Oyagha, S., Whidborne, J., 2023. The prospects of hydrogen in achieving net zero emissions by 2050: A critical review. Sustainable Chemistry for Climate Action 2, 100024. https://doi.org/10.1016/j.scca.2023.100024
- Nooitgedacht, C.W., van der Lubbe, H.J.L., de Graaf, S., Ziegler, M., Staudigel, P.T., Reijmer, J.J.G., 2021. Restricted internal oxygen isotope exchange in calcite veins: Constraints from fluid inclusion and clumped isotope-derived temperatures. Geochimica et Cosmochimica Acta 297, 24–39. https://doi.org/10.1016/j.gca.2020.12.008
- Nothaft, D.B., Templeton, A.S., Rhim, J.H., Wang, D.T., Labidi, J., Miller, H.M., Boyd, E.S., Matter, J.M., Ono, S., Young, E.D., Kopf, S.H., Kelemen, P.B., Conrad, M.E., Team, T.O.D.P.S., 2021. Geochemical, Biological, and Clumped Isotopologue

- Evidence for Substantial Microbial Methane Production Under Carbon Limitation in Serpentinites of the Samail Ophiolite, Oman. Journal of Geophysical Research: Biogeosciences 126, e2020JG006025. https://doi.org/10.1029/2020JG006025
- Nozhevnikova, A.N., Simankova, M.V., Parshina, S.N., Kotsyurbenko, O.R., 2001. Temperature characteristics of methanogenic archaea and acetogenic bacteria isolated from cold environments. Water Science and Technology 44, 41–48. https://doi.org/10.2166/wst.2001.0460
- Okumura, T., Kawagucci, S., Saito, Y., Matsui, Y., Takai, K., Imachi, H., 2016. Hydrogen and carbon isotope systematics in hydrogenotrophic methanogenesis under H2-limited and H2-enriched conditions: implications for the origin of methane and its isotopic diagnosis. Prog. in Earth and Planet. Sci. 3, 14. https://doi.org/10.1186/s40645-016-0088-3
- Omar, G.I., Onstott, T.C., Hoek, J., n.d. The origin of deep subsurface microbial communities in the Witwatersrand Basin, South Africa as deduced from apatite fission track analyses.
- O'Neil, J.R., Clayton, R.N., Mayeda, T.K., 1969. Oxygen Isotope Fractionation in Divalent Metal Carbonates. The Journal of Chemical Physics 51, 5547–5558. https://doi.org/10.1063/1.1671982
- Ono, S., Rhim, J.H., Gruen, D.S., Taubner, H., Kölling, M., Wegener, G., 2021. Clumped isotopologue fractionation by microbial cultures performing the anaerobic oxidation of methane. Geochimica et Cosmochimica Acta 293, 70–85. https://doi.org/10.1016/j.gca.2020.10.015
- Ono, S., Rhim, J.H., Ryberg, E.C., 2022. Rate limits and isotopologue fractionations for microbial methanogenesis examined with combined pathway protein cost and isotopologue flow network models. Geochimica et Cosmochimica Acta 325, 296–315. https://doi.org/10.1016/j.gca.2022.03.017
- Ono, S., Wang, D.T., Gruen, D.S., Sherwood Lollar, B., Zahniser, M.S., McManus, B.J., Nelson, D.D., 2014. Measurement of a Doubly Substituted Methane Isotopologue, <sup>13</sup> CH<sub>3</sub> D, by Tunable Infrared Laser Direct Absorption Spectroscopy. Anal. Chem. 86, 6487–6494. https://doi.org/10.1021/ac5010579
- Onstott, T.C., Lin ,L.-H., Davidson ,M., Mislowack ,B., Borcsik ,M., Hall ,J., Slater ,G., Ward ,J., Lollar ,B. Sherwood, Lippmann-Pipke ,J., Boice ,E., Pratt ,L. M., Pfiffner ,S., Moser ,D., Gihring ,T., Kieft ,Thomas L., Phelps ,Tommy J., Vanheerden ,E., Litthaur ,D., Deflaun ,M., Rothmel ,R., Wanger ,G., and Southam, G., 2006. The Origin and Age of Biogeochemical Trends in Deep Fracture Water of the Witwatersrand Basin, South Africa. Geomicrobiology Journal 23, 369–414. https://doi.org/10.1080/01490450600875688
- Onstott, T.C., Moser, D.P., Pfiffner, S.M., Fredrickson, J.K., Brockman, F.J., Phelps, T.J., White, D.C., Peacock, A., Balkwill, D., Hoover, R., Krumholz, L.R., Borscik, M., Kieft, T.L., Wilson, R., 2003. Indigenous and contaminant microbes in ultradeep mines. Environmental Microbiology 5, 1168–1191. https://doi.org/10.1046/j.1462-2920.2003.00512.x
- Östlund, H.G., Possnert, G., Swift, J.H., 1987. Ventilation rate of the deep Arctic Ocean from carbon 14 data. J. Geophys. Res. 92, 3769–3777. https://doi.org/10.1029/JC092iC04p03769
- Othman, A., Glatz, G., Aljawad, M.S., Alafnan, S., Alarifi, S.A., Al Ramadan, M., 2022. Review of Kerogen's Geomechanical Properties: Experiments and Molecular Simulation. ACS Omega 7, 32829–32839. https://doi.org/10.1021/acsomega.2c03136
- Pagel, M., Bonifacie, M., Schneider, D.A., Gautheron, C., Brigaud, B., Calmels, D., Cros, A., Saint-Bezar, B., Landrein, P., Sutcliffe, C., Davis, D., Chaduteau, C., 2018. Improving paleohydrological and diagenetic reconstructions in calcite veins and

- breccia of a sedimentary basin by combining  $\Delta 47$  temperature,  $\delta 180$ water and U-Pb age. Chemical Geology 481, 1–17. https://doi.org/10.1016/j.chemgeo.2017.12.026
- Palmer, I., 2010. Coalbed methane completions: A world view. International Journal of Coal Geology, Asia Pacific Coalbed Methane Symposium: Selected papers from the 2008 Brisbane symposium on coalbed methane and CO-enhanced coalbed methane 82, 184–195. https://doi.org/10.1016/j.coal.2009.12.010
- Pang, B., Chen, J.-Q., Pang, X.-Q., Hu, T., Sheng, Y., 2023. Driving forces and their relative contributions to hydrocarbon expulsion from deep source rocks: A case of the Cambrian source rocks in the Tarim Basin. Petroleum Science 20, 20–33. https://doi.org/10.1016/j.petsci.2022.08.011
- Pansu, M., Gautheyrou, J., 2006. Handbook of Soil Analysis. Springer Berlin Heidelberg, Berlin, Heidelberg. https://doi.org/10.1007/978-3-540-31211-6
- Passey, B.H., Henkes, G.A., 2012. Carbonate clumped isotope bond reordering and geospeedometry. Earth and Planetary Science Letters 351–352, 223–236. https://doi.org/10.1016/j.epsl.2012.07.021
- Pataki, D.E., Bowling, D.R., Ehleringer, J.R., 2003. Seasonal cycle of carbon dioxide and its isotopic composition in an urban atmosphere: Anthropogenic and biogenic effects. J. Geophys. Res. 108, 2003JD003865. https://doi.org/10.1029/2003JD003865
- Pathways to Discovery in Astronomy and Astrophysics for the 2020s, 2023. National Academies Press, Washington, D.C. https://doi.org/10.17226/26141
- Patra, A., Park, T., Kim, M., Yu, Z., 2017. Rumen methanogens and mitigation of methane emission by anti-methanogenic compounds and substances. J Anim Sci Biotechnol 8, 13. https://doi.org/10.1186/s40104-017-0145-9
- Patra, S., Anders, C., Schummel, P.H., Winter, R., 2018. Antagonistic effects of natural osmolyte mixtures and hydrostatic pressure on the conformational dynamics of a DNA hairpin probed at the single-molecule level. Phys. Chem. Chem. Phys. 20, 13159–13170. https://doi.org/10.1039/C8CP00907D
- Petersen, S.V., Defliese, W.F., Saenger, C., Daëron, M., Huntington, K.W., John, C.M., Kelson, J.R., Bernasconi, S.M., Colman, A.S., Kluge, T., Olack, G.A., Schauer, A.J., Bajnai, D., Bonifacie, M., Breitenbach, S.F.M., Fiebig, J., Fernandez, A.B., Henkes, G.A., Hodell, D., Katz, A., Kele, S., Lohmann, K.C., Passey, B.H., Peral, M.Y., Petrizzo, D.A., Rosenheim, B.E., Tripati, A., Venturelli, R., Young, E.D., Winkelstern, I.Z., 2019. Effects of Improved<sup>17</sup> O Correction on Interlaboratory Agreement in Clumped Isotope Calibrations, Estimates of Mineral-Specific Offsets, and Temperature Dependence of Acid Digestion Fractionation. Geochem Geophys Geosyst 20, 3495–3519. https://doi.org/10.1029/2018GC008127
- Peterson, J.T., Komhyr, W.D., Harris, T.B., Chin, J.F.S., 1977. NOAA carbon dioxide measurements at Mauna Loa Observatory, 1974–1976. Geophysical Research Letters 4, 354–356. https://doi.org/10.1029/GL004i009p00354
- Popa, M.E., Paul, D., Janssen, C., Röckmann, T., 2019. H<sub>2</sub> clumped isotope measurements at natural isotopic abundances. Rapid Comm Mass Spectrometry 33, 239–251. https://doi.org/10.1002/rcm.8323
- Potter, J., Konnerup-Madsen, J., 2003. A review of the occurrence and origin of abiogenic hydrocarbons in igneous rocks. SP 214, 151–173. https://doi.org/10.1144/GSL.SP.2003.214.01.10
- Poursanidis, K., Sharanik, J., Hadjistassou, C., 2024. World's largest natural gas leak from nord stream pipeline estimated at 478,000 tonnes. iScience 27, 108772. https://doi.org/10.1016/j.isci.2023.108772
- Quay, P., Stutsman, J., Wilbur, D., Snover, A., Dlugokencky, E., Brown, T., 1999. The isotopic composition of atmospheric methane. Global Biogeochemical Cycles 13,

- 445–461. https://doi.org/10.1029/1998GB900006
- Raghoebarsing, A.A., Pol, A., Van De Pas-Schoonen, K.T., Smolders, A.J.P., Ettwig, K.F., Rijpstra, W.I.C., Schouten, S., Damsté, J.S.S., Op Den Camp, H.J.M., Jetten, M.S.M., Strous, M., 2006. A microbial consortium couples anaerobic methane oxidation to denitrification. Nature 440, 918–921. https://doi.org/10.1038/nature04617
- Rasigraf, O., Vogt, C., Richnow, H.-H., Jetten, M.S.M., Ettwig, K.F., 2012. Carbon and hydrogen isotope fractionation during nitrite-dependent anaerobic methane oxidation by *Methylomirabilis oxyfera*. Geochimica et Cosmochimica Acta 89, 256–264. https://doi.org/10.1016/j.gca.2012.04.054
- Reller, A., Padeste, C., Hug, P., 1987. Formation of organic carbon compounds from metal carbonates. Nature 329, 527–529. https://doi.org/10.1038/329527a0
- Rhim, J.H., Ono, S., 2022. Combined carbon, hydrogen, and clumped isotope fractionations reveal differential reversibility of hydrogenotrophic methanogenesis in laboratory cultures. Geochimica et Cosmochimica Acta 335, 383–399. https://doi.org/10.1016/j.gca.2022.07.027
- Rice, D.D., 1993. Biogenic gas: Controls, habitats, and resource potential. United States Geological Survey, Professional Paper; (United States) 1570.
- Richter, F.M., Mendybaev, R.A., Christensen, J.N., Hutcheon, I.D., Williams, R.W., Sturchio, N.C., Beloso, A.D., 2006. Kinetic isotopic fractionation during diffusion of ionic species in water. Geochimica et Cosmochimica Acta 70, 277–289. https://doi.org/10.1016/j.gca.2005.09.016
- Rinsland, C.P., Goldman, A., Murcray, F.J., Murcray, F.H., Blatherwick, R.D., Murcray, D.G., 1988. Infrared measurements of atmospheric gases above Mauna Loa, Hawaii, in February 1987. Journal of Geophysical Research: Atmospheres 93, 12607–12626. https://doi.org/10.1029/JD093iD10p12607
- Röckmann, T., Popa, M.E., Krol, M.C., Hofmann, M.E.G., 2016. Statistical clumped isotope signatures. Sci Rep 6, 31947. https://doi.org/10.1038/srep31947
- Romanek, C.S., Grossman, E.L., Morse, J.W., 1992. Carbon isotopic fractionation in synthetic aragonite and calcite: Effects of temperature and precipitation rate. Geochimica et Cosmochimica Acta 56, 419–430. https://doi.org/10.1016/0016-7037(92)90142-6
- Rosentreter, J.A., Alcott, L., Maavara, T., Sun, X., Zhou, Y., Planavsky, N.J., Raymond, P.A., 2024. Revisiting the Global Methane Cycle Through Expert Opinion. Earth's Future 12, e2023EF004234. https://doi.org/10.1029/2023EF004234
- Ruppel, C.D., Waite, W.F., 2020. Timescales and Processes of Methane Hydrate Formation and Breakdown, With Application to Geologic Systems. Journal of Geophysical Research: Solid Earth 125, e2018JB016459. https://doi.org/10.1029/2018JB016459
- Sackett, W.M., 1984. Determination of kerogen maturity by the pyrolysis-carbon isotope method. Organic Geochemistry 6, 359–363. https://doi.org/10.1016/0146-6380(84)90058-5
- Sackett, W.M., 1978. Carbon and hydrogen isotope effects during the thermocatalytic production of hydrocarbons in laboratory simulation experiments. Geochimica et Cosmochimica Acta 42, 571–580. https://doi.org/10.1016/0016-7037(78)90002-9
- Sackett, W.M., Nakaparksin, S., Dalrymple, D., 1970. CARBON ISOTOPE EFFECTS IN METHANE PRODUCTION BY THERMAL CRACKING, in: Advances in Organic Geochemistry. Elsevier, pp. 37–53. https://doi.org/10.1016/B978-0-08-012758-3.50006-2
- Sánchez-López, A., López-Puertas, M., García-Comas, M., Funke, B., Fouchet, T., Snellen, I.A.G., 2022. The CH<sub>4</sub> abundance in Jupiter's upper atmosphere. A&A 662, A91. https://doi.org/10.1051/0004-6361/202141933

- Sassen, R., MacDonald, I.R., 1994. Evidence of structure H hydrate, Gulf of Mexico continental slope. Organic Geochemistry 22, 1029–1032. https://doi.org/10.1016/0146-6380(94)90036-1
- Saueressig, G., Bergamaschi, P., Crowley, J.N., Fischer, H., Harris, G.W., 1995. Carbon kinetic isotope effect in the reaction of CH<sub>4</sub> with Cl atoms. Geophysical Research Letters 22, 1225–1228. https://doi.org/10.1029/95GL00881
- Saueressig, G., Crowley, J.N., Bergamaschi, P., Brühl, C., Brenninkmeijer, C.A.M., Fischer, H., 2001. Carbon 13 and D kinetic isotope effects in the reactions of CH<sub>4</sub> with O(<sup>1</sup> D) and OH: New laboratory measurements and their implications for the isotopic composition of stratospheric methane. J. Geophys. Res. 106, 23127–23138. https://doi.org/10.1029/2000JD000120
- Saunois, M., Bousquet, P., Poulter, B., Peregon, A., Ciais, P., Canadell, J.G., Dlugokencky, E.J., Etiope, G., Bastviken, D., Houweling, S., Janssens-Maenhout, G., Tubiello, F.N., Castaldi, S., Jackson, R.B., Alexe, M., Arora, V.K., Beerling, D.J., Bergamaschi, P., Blake, D.R., Brailsford, G., Brovkin, V., Bruhwiler, L., Crevoisier, C., Crill, P., Covey, K., Curry, C., Frankenberg, C., Gedney, N., Höglund-Isaksson, L., Ishizawa, M., Ito, A., Joos, F., Kim, H.-S., Kleinen, T., Krummel, P., Lamarque, J.-F., Langenfelds, R., Locatelli, R., Machida, T., Maksyutov, S., McDonald, K.C., Marshall, J., Melton, J.R., Morino, I., Naik, V., O'Doherty, S., Parmentier, F.-J.W., Patra, P.K., Peng, C., Peng, S., Peters, G.P., Pison, I., Prigent, C., Prinn, R., Ramonet, M., Riley, W.J., Saito, M., Santini, M., Schroeder, R., Simpson, I.J., Spahni, R., Steele, P., Takizawa, A., Thornton, B.F., Tian, H., Tohjima, Y., Viovy, N., Voulgarakis, A., van Weele, M., van der Werf, G.R., Weiss, R., Wiedinmyer, C., Wilton, D.J., Wiltshire, A., Worthy, D., Wunch, D., Xu, X., Yoshida, Y., Zhang, B., Zhang, Z., Zhu, Q., 2016. The global methane budget 2000–2012. Earth System Science Data 8, 697–751. https://doi.org/10.5194/essd-8-697-2016
- Saunois, M., Martinez, A., Poulter, B., Zhang, Z., Raymond, P., Regnier, P., Canadell, J.G., Jackson, R.B., Patra, P.K., Bousquet, P., Ciais, P., Dlugokencky, E.J., Lan, X., Allen, G.H., Bastviken, D., Beerling, D.J., Belikov, D.A., Blake, D.R., Castaldi, S., Crippa, M., Deemer, B.R., Dennison, F., Etiope, G., Gedney, N., Höglund-Isaksson, L., Holgerson, M.A., Hopcroft, P.O., Hugelius, G., Ito, A., Jain, A.K., Janardanan, R., Johnson, M.S., Kleinen, T., Krummel, P., Lauerwald, R., Li, T., Liu, X., McDonald, K.C., Melton, J.R., Mühle, J., Müller, J., Murguia-Flores, F., Niwa, Y., Noce, S., Pan, S., Parker, R.J., Peng, C., Ramonet, M., Riley, W.J., Rocher-Ros, G., Rosentreter, J.A., Sasakawa, M., Segers, A., Smith, S.J., Stanley, E.H., Thanwerdas, J., Tian, H., Tsuruta, A., Tubiello, F.N., Weber, T.S., Van Der Werf, G., Worthy, D.E., Xi, Y., Yoshida, Y., Zhang, W., Zheng, B., Zhu, Qing, Zhu, Qiuan, Zhuang, Q., 2024. Global Methane Budget 2000–2020. https://doi.org/10.5194/essd-2024-115
- Saunois, M., Stavert, A.R., Poulter, B., Bousquet, P., Canadell, J.G., Jackson, R.B.,
  Raymond, P.A., Dlugokencky, E.J., Houweling, S., Patra, P.K., Ciais, P., Arora,
  V.K., Bastviken, D., Bergamaschi, P., Blake, D.R., Brailsford, G., Bruhwiler, L.,
  Carlson, K.M., Carrol, M., Castaldi, S., Chandra, N., Crevoisier, C., Crill, P.M.,
  Covey, K., Curry, C.L., Etiope, G., Frankenberg, C., Gedney, N., Hegglin, M.I.,
  Höglund-Isaksson, L., Hugelius, G., Ishizawa, M., Ito, A., Janssens-Maenhout, G.,
  Jensen, K.M., Joos, F., Kleinen, T., Krummel, P.B., Langenfelds, R.L., Laruelle,
  G.G., Liu, L., Machida, T., Maksyutov, S., McDonald, K.C., McNorton, J., Miller,
  P.A., Melton, J.R., Morino, I., Müller, J., Murguia-Flores, F., Naik, V., Niwa, Y.,
  Noce, S., O'Doherty, S., Parker, R.J., Peng, C., Peng, S., Peters, G.P., Prigent, C.,
  Prinn, R., Ramonet, M., Regnier, P., Riley, W.J., Rosentreter, J.A., Segers, A.,
  Simpson, I.J., Shi, H., Smith, S.J., Steele, L.P., Thornton, B.F., Tian, H., Tohjima,

- Y., Tubiello, F.N., Tsuruta, A., Viovy, N., Voulgarakis, A., Weber, T.S., van Weele, M., van der Werf, G.R., Weiss, R.F., Worthy, D., Wunch, D., Yin, Y., Yoshida, Y., Zhang, W., Zhang, Z., Zhao, Y., Zheng, B., Zhu, Qing, Zhu, Qiuan, Zhuang, Q., 2020. The Global Methane Budget 2000–2017. Earth System Science Data 12, 1561–1623. https://doi.org/10.5194/essd-12-1561-2020
- Schauble, E.A., Ghosh, P., Eiler, J.M., 2006. Preferential formation of 13C–18O bonds in carbonate minerals, estimated using first-principles lattice dynamics. Geochimica et Cosmochimica Acta 70, 2510–2529. https://doi.org/10.1016/j.gca.2006.02.011
- Schmider, D., Maier, L., Deutschmann, O., 2021. Reaction Kinetics of CO and CO2 Methanation over Nickel. Ind. Eng. Chem. Res. 60, 5792–5805. https://doi.org/10.1021/acs.iecr.1c00389
- Schoell, M., 1988. Multiple origins of methane in the Earth. Chemical Geology 71, 1–10. https://doi.org/10.1016/0009-2541(88)90101-5
- Schoell, M., 1980. The hydrogen and carbon isotopic composition of methane from natural gases of various origins. Geochimica et Cosmochimica Acta 44, 649–661. https://doi.org/10.1016/0016-7037(80)90155-6
- Schumacher, M., Werner, R.A., Meijer, H.A.J., Jansen, H.G., Brand, W.A., Geilmann, H., Neubert, R.E.M., 2011. Oxygen isotopic signature of CO<sub>2</sub> from combustion processes. Atmos. Chem. Phys. 11, 1473–1490. https://doi.org/10.5194/acp-11-1473-2011
- Schwietzke, S., Sherwood, O.A., Bruhwiler, L.M.P., Miller, J.B., Etiope, G., Dlugokencky, E.J., Michel, S.E., Arling, V.A., Vaughn, B.H., White, J.W.C., Tans, P.P., 2016a. Upward revision of global fossil fuel methane emissions based on isotope database. Nature 538, 88–91. https://doi.org/10.1038/nature19797
- Schwietzke, S., Sherwood, O.A., Bruhwiler, L.M.P., Miller, J.B., Etiope, G., Dlugokencky, E.J., Michel, S.E., Arling, V.A., Vaughn, B.H., White, J.W.C., Tans, P.P., 2016b. Upward revision of global fossil fuel methane emissions based on isotope database. Nature 538, 88–91. https://doi.org/10.1038/nature19797
- Schwietzke, S., Sherwood, O.A., Bruhwiler, L.M.P., Miller, J.B., Etiope, G., Dlugokencky, E.J., Michel, S.E., Arling, V.A., Vaughn, B.H., White, J.W.C., Tans, P.P., 2016c. Upward revision of global fossil fuel methane emissions based on isotope database. Nature 538, 88–91. https://doi.org/10.1038/nature19797
- Scott, H.P., Hemley, R.J., Mao, H., Herschbach, D.R., Fried, L.E., Howard, W.M., Bastea, S., 2004. Generation of methane in the Earth's mantle: In situ high pressure—temperature measurements of carbonate reduction. Proceedings of the National Academy of Sciences 101, 14023–14026. https://doi.org/10.1073/pnas.0405930101
- Seewald, J.S., Zolotov, M.Yu., McCollom, T., 2006. Experimental investigation of single carbon compounds under hydrothermal conditions. Geochimica et Cosmochimica Acta 70, 446–460. https://doi.org/10.1016/j.gca.2005.09.002
- Segarra, K.E.A., Schubotz, F., Samarkin, V., Yoshinaga, M.Y., Hinrichs, K.-U., Joye, S.B., 2015. High rates of anaerobic methane oxidation in freshwater wetlands reduce potential atmospheric methane emissions. Nat Commun 6, 7477. https://doi.org/10.1038/ncomms8477
- Selley, R.C., Sonnenberg, S.A., 2023. Elements of petroleum geology, Fourth edition. ed. Elsevier, an imprint of Academic Press, London.
- Serovaiskii, A., Kutcherov, V., 2020. Formation of complex hydrocarbon systems from methane at the upper mantle thermobaric conditions. Sci Rep 10, 4559. https://doi.org/10.1038/s41598-020-61644-5
- Sherwood Lollar, B., Frape, S.K., Weise, S.M., Fritz, P., Macko, S.A., Welhan, J.A., 1993. Abiogenic methanogenesis in crystalline rocks. Geochimica et Cosmochimica Acta 57, 5087–5097. https://doi.org/10.1016/0016-7037(93)90610-9
- Sherwood Lollar, B., Heuer, V.B., McDermott, J., Tille, S., Warr, O., Moran, J.J., Telling,

- J., Hinrichs, K.-U., 2021. A window into the abiotic carbon cycle Acetate and formate in fracture waters in 2.7 billion year-old host rocks of the Canadian Shield. Geochimica et Cosmochimica Acta 294, 295–314. https://doi.org/10.1016/j.gca.2020.11.026
- Sherwood Lollar, B., Lacrampe-Couloume, G., Slater, G.F., Ward, J., Moser, D.P., Gihring, T.M., Lin, L.-H., Onstott, T.C., 2006. Unravelling abiogenic and biogenic sources of methane in the Earth's deep subsurface. Chemical Geology 226, 328–339. https://doi.org/10.1016/j.chemgeo.2005.09.027
- Shuai, Y., Douglas, P.M.J., Zhang, S., Stolper, D.A., Ellis, G.S., Lawson, M., Lewan, M.D., Formolo, M., Mi, J., He, K., Hu, G., Eiler, J.M., 2018. Equilibrium and non-equilibrium controls on the abundances of clumped isotopologues of methane during thermogenic formation in laboratory experiments: Implications for the chemistry of pyrolysis and the origins of natural gases. Geochimica et Cosmochimica Acta 223, 159–174. https://doi.org/10.1016/j.gca.2017.11.024
- Siddhantakar, A., Santillán-Saldivar, J., Kippes, T., Sonnemann, G., Reller, A., Young, S.B., 2023. Helium resource global supply and demand: Geopolitical supply risk analysis. Resources, Conservation and Recycling 193, 106935. https://doi.org/10.1016/j.resconrec.2023.106935
- Silva, R.C., Snowdon, L.R., Huang, H., Nightingale, M., Becker, V., Taylor, S., Mayer, B., Pedersen, J.H., di Primio, R., Larter, S., 2019. Radiolysis as a source of 13C depleted natural gases in the geosphere. Organic Geochemistry 138, 103911. https://doi.org/10.1016/j.orggeochem.2019.103911
- Simkus, D.N., Slater, G.F., Lollar, B.S., Wilkie, K., Kieft, T.L., Magnabosco, C., Lau, M.C.Y., Pullin, M.J., Hendrickson, S.B., Wommack, K.E., Sakowski, E.G., Heerden, E.V., Kuloyo, O., Linage, B., Borgonie, G., Onstott, T.C., 2016. Variations in microbial carbon sources and cycling in the deep continental subsurface. Geochimica et Cosmochimica Acta 173, 264–283. https://doi.org/10.1016/j.gca.2015.10.003
- Sivan, M., Röckmann, T., Van Der Veen, C., Popa, M.E., 2024. Extraction, purification, and clumped isotope analysis of methane ( $\Delta^{13}$  CDH<sub>3</sub> and  $\Delta^{12}$  CD<sub>2</sub> H<sub>2</sub>) from sources and the atmosphere. Atmos. Meas. Tech. 17, 2687–2705. https://doi.org/10.5194/amt-17-2687-2024
- Skeie, R.B., Hodnebrog, Ø., Myhre, G., 2023. Trends in atmospheric methane concentrations since 1990 were driven and modified by anthropogenic emissions. Commun Earth Environ 4, 1–14. https://doi.org/10.1038/s43247-023-00969-1
- Skrzypek, G., Sadler, R., Paul, D., 2010. Error propagation in normalization of stable isotope data: a Monte Carlo analysis. Rapid Comm Mass Spectrometry 24, 2697–2705. https://doi.org/10.1002/rcm.4684
- Soeder, D.J., Borglum, S.J., 2019. The fossil fuel revolution: shale gas and tight oil. Elsevier, Amsterdam Cambridge, Mass.
- Spangenberg, J.E., Frimmel, H.E., 2001. Basin-internal derivation of hydrocarbons in the Witwatersrand Basin, South Africa: evidence from bulk and molecular  $\delta$ 13C data. Chemical Geology 173, 339–355. https://doi.org/10.1016/S0009-2541(00)00283-7
- Spencer, C., Kim, S.-T., 2015. Carbonate clumped isotope paleothermometry: a review of recent advances in CO2 gas evolution, purification, measurement and standardization techniques. Geosci J 19, 357–374. https://doi.org/10.1007/s12303-015-0018-1
- Srivastava, A., Michael Verkouteren, R., 2018. Metrology for stable isotope reference materials: 13C/12C and 18O/16O isotope ratio value assignment of pure carbon dioxide gas samples on the Vienna PeeDee Belemnite-CO2 scale using dual-inlet mass spectrometry. Anal Bioanal Chem 410, 4153–4163. https://doi.org/10.1007/s00216-018-1064-0

- Stahl, W., 1974. Carbon isotope fractionations in natural gases. Nature 251, 134–135. https://doi.org/10.1038/251134a0
- Stahl, W.J., 1977. Carbon and nitrogen isotopes in hydrocarbon research and exploration. Chemical Geology 20, 121–149. https://doi.org/10.1016/0009-2541(77)90041-9
- Stephan, T., Trappitsch, R., 2023. Reliable uncertainties: Error correlation, rotated error bars, and linear regressions in three-isotope plots and beyond. International Journal of Mass Spectrometry 491, 117053. https://doi.org/10.1016/j.ijms.2023.117053
- Stolper, D.A., Eiler, J.M., 2015. The kinetics of solid-state isotope-exchange reactions for clumped isotopes: A study of inorganic calcites and apatites from natural and experimental samples. American Journal of Science 315, 363–411. https://doi.org/10.2475/05.2015.01
- Stolper, D.A., Eiler, J.M., Higgins, J.A., 2018. Modeling the effects of diagenesis on carbonate clumped-isotope values in deep- and shallow-water settings. Geochimica et Cosmochimica Acta 227, 264–291. https://doi.org/10.1016/j.gca.2018.01.037
- Stolper, D. A., Lawson, M., Davis, C.L., Ferreira, A.A., Neto, E.V.S., Ellis, G.S., Lewan, M.D., Martini, A.M., Tang, Y., Schoell, M., Sessions, A.L., Eiler, J.M., 2014. Formation temperatures of thermogenic and biogenic methane. Science 344, 1500–1503. https://doi.org/10.1126/science.1254509
- Stolper, D.A., Martini, A.M., Clog, M., Douglas, P.M., Shusta, S.S., Valentine, D.L., Sessions, A.L., Eiler, J.M., 2015. Distinguishing and understanding thermogenic and biogenic sources of methane using multiply substituted isotopologues. Geochimica et Cosmochimica Acta 161, 219–247. https://doi.org/10.1016/j.gca.2015.04.015
- Stolper, D.A., Sessions, A.L., Ferreira, A.A., Santos Neto, E.V., Schimmelmann, A., Shusta, S.S., Valentine, D.L., Eiler, J.M., 2014. Combined 13C–D and D–D clumping in methane: Methods and preliminary results. Geochimica et Cosmochimica Acta 126, 169–191. https://doi.org/10.1016/j.gca.2013.10.045
- Sugisaki, R., 1984. Relation between hydrogen emission and seismic activities. PAGEOPH 122, 175–184. https://doi.org/10.1007/BF00874591
- Sun, J., Ma, L., Ni, W., Zheng, L., 2013. Reducing China's energy consumption and CO2 emissions by more efficient use of energy, in: 2013 International Conference on Materials for Renewable Energy and Environment. Presented at the 2013 International Conference on Materials for Renewable Energy and Environment, pp. 802–808. https://doi.org/10.1109/ICMREE.2013.6893795
- Swart, P.K., Lu, C., Moore, E.W., Smith, M.E., Murray, S.T., Staudigel, P.T., 2021. A calibration equation between  $\Delta_{48}$  values of carbonate and temperature. Rapid Comm Mass Spectrometry 35, e9147. https://doi.org/10.1002/rcm.9147
- Swart, P.K., Murray, S.T., Staudigel, P.T., Hodell, D.A., 2019. Oxygen Isotopic Exchange Between CO<sub>2</sub> and Phosphoric Acid: Implications for the Measurement of Clumped Isotopes in Carbonates. Geochem Geophys Geosyst 20, 3730–3750. https://doi.org/10.1029/2019GC008209
- Taenzer, L., Labidi, J., Masterson, A.L., Feng, X., Rumble, D., Young, E.D., Leavitt, W.D., 2020. Low Δ 12 CH 2 D 2 values in microbialgenic methane result from combinatorial isotope effects. Geochimica et Cosmochimica Acta 285, 225–236. https://doi.org/10.1016/j.gca.2020.06.026
- Taguchi, K., Yamamoto, T., Nakagawa, M., Gilbert, A., Ueno, Y., 2020. A fluorination method for measuring the <sup>13</sup> C-<sup>13</sup> C isotopologue of C<sub>2</sub> molecules. Rapid Comm Mass Spectrometry 34, e8761. https://doi.org/10.1002/rcm.8761
- Taipabu, M.I., Viswanathan, K., Wu, W., Hattu, N., Atabani, A.E., 2022. A critical review of the hydrogen production from biomass-based feedstocks: Challenge, solution, and future prospect. Process Safety and Environmental Protection 164, 384–407. https://doi.org/10.1016/j.psep.2022.06.006

- Takai, K., Moser, D.P., DeFlaun, M., Onstott, T.C., Fredrickson, J.K., 2001. Archaeal Diversity in Waters from Deep South African Gold Mines. Applied and Environmental Microbiology 67, 5750–5760. https://doi.org/10.1128/AEM.67.21.5750-5760.2001
- Takai, K., Nakamura, K., Toki, T., Tsunogai, U., Miyazaki, M., Miyazaki, J., Hirayama, H., Nakagawa, S., Nunoura, T., Horikoshi, K., 2008. Cell proliferation at 122°C and isotopically heavy CH4 production by a hyperthermophilic methanogen under high-pressure cultivation. Proceedings of the National Academy of Sciences 105, 10949–10954. https://doi.org/10.1073/pnas.0712334105
- Takriti, M., Wynn, P.M., Elias, D.M.O., Ward, S.E., Oakley, S., McNamara, N.P., 2021. Mobile methane measurements: Effects of instrument specifications on data interpretation, reproducibility, and isotopic precision. Atmospheric Environment 246, 118067. https://doi.org/10.1016/j.atmosenv.2020.118067
- Tan, J.N., Ratra, K., Singer, S.W., Simmons, B.A., Goswami, S., Awasthi, D., 2024. Methane to bioproducts: unraveling the potential of methanotrophs for biomanufacturing. Current Opinion in Biotechnology 90, 103210. https://doi.org/10.1016/j.copbio.2024.103210
- Taran, Y.A., Kliger, G.A., Sevastianov, V.S., 2007. Carbon isotope effects in the open-system Fischer–Tropsch synthesis. Geochimica et Cosmochimica Acta 71, 4474–4487. https://doi.org/10.1016/j.gca.2007.06.057
- Taubner, R.-S., Pappenreiter, P., Zwicker, J., Smrzka, D., Pruckner, C., Kolar, P., Bernacchi, S., Seifert, A.H., Krajete, A., Bach, W., Peckmann, J., Paulik, C., Firneis, M.G., Schleper, C., Rittmann, S.K.-M.R., 2018. Biological methane production under putative Enceladus-like conditions. Nat Commun 9, 748. https://doi.org/10.1038/s41467-018-02876-y
- Tavakoli, A., 2021. Geochemistry and petrology of selected sediments from Bukit Song, Miri, Sarawak, Malaysia, with emphasis on organic matter characterization. J Petrol Explor Prod Technol 11, 3663–3688. https://doi.org/10.1007/s13202-021-01275-2
- Thanwerdas, J., Saunois, M., Berchet, A., Pison, I., Bousquet, P., 2024. Investigation of the renewed methane growth post-2007 with high-resolution 3-D variational inverse modeling and isotopic constraints. Atmospheric Chemistry and Physics 24, 2129–2167. https://doi.org/10.5194/acp-24-2129-2024
- Thiagarajan, N., Adkins, J., Eiler, J., 2011. Carbonate clumped isotope thermometry of deep-sea corals and implications for vital effects. Geochimica et Cosmochimica Acta 75, 4416–4425. https://doi.org/10.1016/j.gca.2011.05.004
- Thiagarajan, N., Kitchen, N., Xie, H., Ponton, C., Lawson, M., Formolo, M., Eiler, J., 2020a. Identifying thermogenic and microbial methane in deep water Gulf of Mexico Reservoirs. Geochimica et Cosmochimica Acta 275, 188–208. https://doi.org/10.1016/j.gca.2020.02.016
- Thiagarajan, N., Xie, H., Ponton, C., Kitchen, N., Peterson, B., Lawson, M., Formolo, M., Xiao, Y., Eiler, J., 2020b. Isotopic evidence for quasi-equilibrium chemistry in thermally mature natural gases. Proceedings of the National Academy of Sciences 117, 3989–3995. https://doi.org/10.1073/pnas.1906507117
- Thompson, M.A., Krissansen-Totton, J., Wogan, N., Telus, M., Fortney, J.J., 2022. The case and context for atmospheric methane as an exoplanet biosignature. Proceedings of the National Academy of Sciences 119, e2117933119. https://doi.org/10.1073/pnas.2117933119
- Thoning, K., Dlugokencky, E., Lan, X., NOAA Global Monitoring Laboratory, 2022.

  Trends in globally-averaged CH4, N2O, and SF6. https://doi.org/10.15138/P8XG-AA10
- Tissot, B.P., Welte, D.H., 1984. Petroleum Formation and Occurrence. Springer Berlin Heidelberg, Berlin, Heidelberg. https://doi.org/10.1007/978-3-642-87813-8

- Tissot, B.P., Welte, D.H., 1978. Petroleum Formation and Occurrence. Springer Berlin Heidelberg, Berlin, Heidelberg. https://doi.org/10.1007/978-3-642-96446-6
- Tomory, L., 2010. William Brownrigg's Papers on Fire-Damps. Notes and Records of the Royal Society of London 64, 261–270.
- Toon, O.B., McKay, C.P., Courtin, R., Ackerman, T.P., 1988. Methane rain on Titan. Icarus 75, 255–284. https://doi.org/10.1016/0019-1035(88)90005-X
- Townsend-Small, A., Ferrara, T.W., Lyon, D.R., Fries, A.E., Lamb, B.K., 2016. Emissions of coalbed and natural gas methane from abandoned oil and gas wells in the United States. Geophysical Research Letters 43, 2283–2290. https://doi.org/10.1002/2015GL067623
- Tripati, A.K., Eagle, R.A., Thiagarajan, N., Gagnon, A.C., Bauch, H., Halloran, P.R., Eiler, J.M., 2010. 13C–18O isotope signatures and 'clumped isotope' thermometry in foraminifera and coccoliths. Geochimica et Cosmochimica Acta 74, 5697–5717. https://doi.org/10.1016/j.gca.2010.07.006
- Tucker, M.E., Wright, V.P., 1990. Carbonate Sedimentology, 1st ed. Wiley. https://doi.org/10.1002/9781444314175
- Tucker, R.F., Viljoen, R.P., Viljoen, M.J., 2016. A Review of the Witwatersrand Basin The World's Greatest Goldfield. Episodes 39, 104–133. https://doi.org/10.18814/epiiugs/2016/v39i2/95771
- Turner, A.C., Pester, N.J., Bill, M., Conrad, M.E., Knauss, K.G., Stolper, D.A., 2022. Experimental determination of hydrogen isotope exchange rates between methane and water under hydrothermal conditions. Geochimica et Cosmochimica Acta 329, 231–255. https://doi.org/10.1016/j.gca.2022.04.029
- Tyler, S.C., Ajie, H.O., Rice, A.L., Cicerone, R.J., Tuazon, E.C., 2000. Experimentally determined kinetic isotope effects in the reaction of CH<sub>4</sub> with Cl: Implications for atmospheric CH<sub>4</sub>. Geophysical Research Letters 27, 1715–1718. https://doi.org/10.1029/1999GL011168
- Urey, H.C., 1951. The origin and development of the earth and other terrestrial planets. Geochimica et Cosmochimica Acta 1, 209–277. https://doi.org/10.1016/0016-7037(51)90001-4
- Valentine, D.L., Chidthaisong, A., Rice, A., Reeburgh, W.S., Tyler, S.C., 2004. Carbon and hydrogen isotope fractionation by moderately thermophilic methanogens 1 1Associate editor: N. E. Ostrom. Geochimica et Cosmochimica Acta 68, 1571–1590. https://doi.org/10.1016/j.gca.2003.10.012
- Valentine, D.L., Reeburgh, W.S., 2000. New perspectives on anaerobic methane oxidation: Minireview. Environmental Microbiology 2, 477–484. https://doi.org/10.1046/j.1462-2920.2000.00135.x
- Van der Westhuizen, W.A., De Bruiyn, H., Meintjes, P.G., 1991. The Ventersdorp supergroup: an overview. Journal of African Earth Sciences (and the Middle East), Precambrian sedimentary basins of Southern Africa 13, 83–105. https://doi.org/10.1016/0899-5362(91)90045-Z
- Van Herpen, M.M.J.W., Li, Q., Saiz-Lopez, A., Liisberg, J.B., Röckmann, T., Cuevas, C.A., Fernandez, R.P., Mak, J.E., Mahowald, N.M., Hess, P., Meidan, D., Stuut, J.-B.W., Johnson, M.S., 2023. Photocatalytic chlorine atom production on mineral dust—sea spray aerosols over the North Atlantic. Proc. Natl. Acad. Sci. U.S.A. 120, e2303974120. https://doi.org/10.1073/pnas.2303974120
- Varma, A.K., Hazra, B., Samad, S.K., Panda, S., Mendhe, V.A., 2014. Methane sorption dynamics and hydrocarbon generation of shale samples from West Bokaro and Raniganj basins, India. Journal of Natural Gas Science and Engineering 21, 1138–1147. https://doi.org/10.1016/j.jngse.2014.11.011
- Vaughn, T.L., Bell, C.S., Pickering, C.K., Schwietzke, S., Heath, G.A., Pétron, G., Zimmerle, D.J., Schnell, R.C., Nummedal, D., 2018. Temporal variability largely

- explains top-down/bottom-up difference in methane emission estimates from a natural gas production region. Proceedings of the National Academy of Sciences 115, 11712–11717. https://doi.org/10.1073/pnas.1805687115
- Vervoort, P., Adloff, M., Greene, S.E., Kirtland Turner, S., 2019. Negative carbon isotope excursions: an interpretive framework. Environ. Res. Lett. 14, 085014. https://doi.org/10.1088/1748-9326/ab3318
- Vincent, S.G.T., Salahudeen, J.H., Godson, P.S., Abhijith, S.R., Nath, A.V., Krishnan, K.A., Magesh, N.S., Kumar, S.K., Moses, S.A., 2021. Environmental factors influencing methanogenic activity in two contrasting tropical lake sediments. https://doi.org/10.22438/jeb/42/2/mrn-1413
- Visser, J.N.J., Grobler, N.J., 1985. Syndepositional volcanism in the Rietgat and arenaceous Bothaville Formations, Ventersdorp Supergroup (late Archaean—early Proterozoic), in South Africa. Precambrian Research 30, 153–174. https://doi.org/10.1016/0301-9268(85)90049-X
- Vogt, R., Crutzen, P.J., Sander, R., 1996. A mechanism for halogen release from sea-salt aerosol in the remote marine boundary layer. Nature 383, 327–330. https://doi.org/10.1038/383327a0
- von Glasow, R., 2006. Importance of the surface reaction OH + Cl− on sea salt aerosol for the chemistry of the marine boundary layer a model study.

  Atmospheric Chemistry and Physics 6, 3571–3581. https://doi.org/10.5194/acp-6-3571-2006
- Von Schneidemesser, E., Driscoll, C., Rieder, H.E., Schiferl, L.D., 2020. How will air quality effects on human health, crops and ecosystems change in the future? Phil. Trans. R. Soc. A. 378, 20190330. https://doi.org/10.1098/rsta.2019.0330
- Wagner, Thomas, Magill, C.R., Herrle, J.O., 2018. Carbon Isotopes, in: White, W.M. (Ed.), Encyclopedia of Geochemistry: A Comprehensive Reference Source on the Chemistry of the Earth. Springer International Publishing, Cham, pp. 194–204. https://doi.org/10.1007/978-3-319-39312-4 176
- Wagner, Tristan, Watanabe, T., Shima, S., 2018. Hydrogenotrophic Methanogenesis, in: Stams, A.J.M., Sousa, D. (Eds.), Biogenesis of Hydrocarbons. Springer International Publishing, Cham, pp. 1–29. https://doi.org/10.1007/978-3-319-53114-4 3-1
- Wang, D.T., Gruen, D.S., Lollar, B.S., Hinrichs, K.-U., Stewart, L.C., Holden, J.F., Hristov, A.N., Pohlman, J.W., Morrill, P.L., Könneke, M., Delwiche, K.B., Reeves, E.P., Sutcliffe, C.N., Ritter, D.J., Seewald, J.S., McIntosh, J.C., Hemond, H.F., Kubo, M.D., Cardace, D., Hoehler, T.M., Ono, S., 2015. Nonequilibrium clumped isotope signals in microbial methane. Science 348, 428–431. https://doi.org/10.1126/science.aaa4326
- Wang, D.T., Sattler, A., Paccagnini, M., Chen, F.G., 2020. Method for calibrating methane clumped isotope measurements via catalytic equilibration of methane isotopologues on γ-alumina. Rapid Comm Mass Spectrometry 34, e8555. https://doi.org/10.1002/rcm.8555
- Wang, D.T., Welander, P.V., Ono, S., 2016. Fractionation of the methane isotopologues 13CH4, 12CH3D, and 13CH3D during aerobic oxidation of methane by Methylococcus capsulatus (Bath). Geochimica et Cosmochimica Acta 192, 186–202. https://doi.org/10.1016/j.gca.2016.07.031
- Wang, H., Ma, F., Tong, X., Liu, Z., Zhang, X., Wu, Z., Li, D., Wang, B., Xie, Y., Yang, L., 2016. Assessment of global unconventional oil and gas resources. Petroleum Exploration and Development 43, 925–940. https://doi.org/10.1016/S1876-3804(16)30111-2
- Wang, X., Jacob, D.J., Eastham, S.D., Sulprizio, M.P., Zhu, L., Chen, Q., Alexander, B., Sherwen, T., Evans, M.J., Lee, B.H., Haskins, J.D., Lopez-Hilfiker, F.D., Thornton,

- J.A., Huey, G.L., Liao, H., 2019. The role of chlorine in global tropospheric chemistry. Atmos. Chem. Phys. 19, 3981–4003. https://doi.org/10.5194/acp-19-3981-2019
- Wang, X., Liu, C.-Q., Zhang, N., Xu, S., Pang, Z., Li, S.-L., Ding, H., Chen, J., Xie, Z., Ellam, R.M., 2023. Clumped methane isotopologues (13CH3D and 12CH2D2) of natural samples measured using a high-resolution mass spectrometer with an improved pretreatment system. J. Anal. At. Spectrom. 38, 186–196. https://doi.org/10.1039/D2JA00315E
- Wang, Z., Nelson, D.D., Dettman, D.L., McManus, J.B., Quade, J., Huntington, K.W., Schauer, A.J., Sakai, S., 2020. Rapid and Precise Analysis of Carbon Dioxide Clumped Isotopic Composition by Tunable Infrared Laser Differential Spectroscopy. Anal. Chem. 92, 2034–2042. https://doi.org/10.1021/acs.analchem.9b04466
- Wankel, S.D., Adams, M.M., Johnston, D.T., Hansel, C.M., Joye, S.B., Girguis, P.R., 2012. Anaerobic methane oxidation in metalliferous hydrothermal sediments: influence on carbon flux and decoupling from sulfate reduction. Environmental Microbiology 14, 2726–2740. https://doi.org/10.1111/j.1462-2920.2012.02825.x
- Warr, O., Ballentine, C.J., Onstott, T.C., Nisson, D.M., Kieft, T.L., Hillegonds, D.J., Sherwood Lollar, B., 2022. 86Kr excess and other noble gases identify a billion-year-old radiogenically-enriched groundwater system. Nat Commun 13, 3768. https://doi.org/10.1038/s41467-022-31412-2
- Warr, O., Giunta, T., Onstott, T.C., Kieft, T.L., Harris, R.L., Nisson, D.M., Lollar, B.S., 2021a. The role of low-temperature 18O exchange in the isotopic evolution of deep subsurface fluids. Chemical Geology 561, 120027. https://doi.org/10.1016/j.chemgeo.2020.120027
- Warr, O., Young, E.D., Giunta, T., Kohl, I.E., Ash, J.L., Sherwood Lollar, B., 2021b. High-resolution, long-term isotopic and isotopologue variation identifies the sources and sinks of methane in a deep subsurface carbon cycle. Geochimica et Cosmochimica Acta 294, 315–334. https://doi.org/10.1016/j.gca.2020.12.002
- Warsame, A.A., Sheik-Ali, I.A., Abdi, A.H., Sarkodie, S.A., 2024. An Overview of Natural Gas Supply and Infrastructure, in: Ayodele, B.V., Mustapa, S.I., Sarkodie, S.A. (Eds.), Sustainable Utilization of Natural Gas for Low-Carbon Energy Production: Attaining Low-Carbon Energy Production Through Sustainable Natural Gas Utilization. Springer Nature, Singapore, pp. 3–21. https://doi.org/10.1007/978-981-97-6282-8 1
- Watkins, J.M., Hunt, J.D., Ryerson, F.J., DePaolo, D.J., 2014. The influence of temperature, pH, and growth rate on the *δ*18O composition of inorganically precipitated calcite. Earth and Planetary Science Letters 404, 332–343. https://doi.org/10.1016/j.epsl.2014.07.036
- Webster, C.R., Mahaffy, P.R., Pla-Garcia, J., Rafkin, S.C.R., Moores, J.E., Atreya, S.K., Flesch, G.J., Malespin, C.A., Teinturier, S.M., Kalucha, H., Smith, C.L., Viúdez-Moreiras, D., Vasavada, A.R., 2021. Day-night differences in Mars methane suggest nighttime containment at Gale crater. A&A 650, A166. https://doi.org/10.1051/0004-6361/202040030
- Webster, C.R., May, R.D., 1992. In situ stratospheric measurements of CH4, 13CH4, N2O, and OC18O using the Bliss tunable diode laser spectrometer. Geophysical Research Letters 19, 45–48. https://doi.org/10.1029/91GL02782
- Wegener, G., Gropp, J., Taubner, H., Halevy, I., Elvert, M., 2021. Sulfate-dependent reversibility of intracellular reactions explains the opposing isotope effects in the anaerobic oxidation of methane. Sci. Adv. 7, eabe4939. https://doi.org/10.1126/sciadv.abe4939
- Welhan, J.A., 1988. Origins of methane in hydrothermal systems. Chemical Geology,

- Origins of Methane in the Earth 71, 183–198. https://doi.org/10.1016/0009-2541(88)90114-3
- Welp, L.R., Keeling, R.F., Meijer, H.A.J., Bollenbacher, A.F., Piper, S.C., Yoshimura, K., Francey, R.J., Allison, C.E., Wahlen, M., 2011. Interannual variability in the oxygen isotopes of atmospheric CO2 driven by El Niño. Nature 477, 579–582. https://doi.org/10.1038/nature10421
- Whitehill, A.R., Joelsson, L.M.T., Schmidt, J.A., Wang, D.T., Johnson, M.S., Ono, S., 2017. Clumped isotope effects during OH and Cl oxidation of methane. Geochimica et Cosmochimica Acta 196, 307–325. https://doi.org/10.1016/j.gca.2016.09.012
- Whiticar, M.J., 1999. Carbon and hydrogen isotope systematics of bacterial formation and oxidation of methane. Chemical Geology 161, 291–314. https://doi.org/10.1016/S0009-2541(99)00092-3
- Whiticar, M.J., Faber, E., Schoell, M., 1986. Biogenic methane formation in marine and freshwater environments: CO2 reduction *vs.* acetate fermentation—Isotope evidence. Geochimica et Cosmochimica Acta 50, 693–709. https://doi.org/10.1016/0016-7037(86)90346-7
- Winter, H. de la R., 1995. Tectonic events affecting the Witwatersrand Basin with special reference to responses in the Bezuidenhout Valley. South African Journal of Geology 98, 356–370. <a href="https://doi.org/10.10520/EJC-943489e62">https://doi.org/10.10520/EJC-943489e62</a>
- World Energy Outlook 2009 Analysis (2009) IEA. Available at: https://www.iea.org/reports/world-energy-outlook-2009 (Accessed: 31 March 2025).
- World Energy Outlook 2016 Analysis (2016) IEA. Available at: https://www.iea.org/reports/world-energy-outlook-2016 (Accessed: 31 March 2025).
- Wostbrock, J.A.G., Witts, J.D., Gao, Y., Peshek, C., Myers, C.E., Henkes, G., Sharp, Z.D., 2025. Reconstructing paleoenvironments of the Late Cretaceous Western Interior Seaway, USA, using paired triple oxygen and carbonate clumped isotope measurements. Geological Society of America Bulletin 137, 297–314. https://doi.org/10.1130/B37543.1
- Xia, X., Gao, Y., 2021. Methane from microbial hydrogenolysis of sediment organic matter before the Great Oxidation Event. Nat Commun 12, 5032. https://doi.org/10.1038/s41467-021-25336-6
- Xie, H., Dong, G., Formolo, M., Lawson, M., Liu, J., Cong, F., Mangenot, X., Shuai, Y., Ponton, C., Eiler, J., 2021. The evolution of intra- and inter-molecular isotope equilibria in natural gases with thermal maturation. Geochimica et Cosmochimica Acta 307, 22–41. https://doi.org/10.1016/j.gca.2021.05.012
- Yeung, L.Y., 2016. Combinatorial effects on clumped isotopes and their significance in biogeochemistry. Geochimica et Cosmochimica Acta 172, 22–38. https://doi.org/10.1016/j.gca.2015.09.020
- Young, E.D., 2019. A Two-Dimensional Perspective on CH4 Isotope Clumping:
  Distinguishing Process from Source, in: Orcutt, B.N., Daniel, I., Dasgupta, R. (Eds.), Deep Carbon. Cambridge University Press, pp. 388–414.
  https://doi.org/10.1017/9781108677950.013
- Young, E.D., Kohl, I.E., Lollar, B.S., Etiope, G., Rumble, D., Li (李姝宁), S., Haghnegahdar, M.A., Schauble, E.A., McCain, K.A., Foustoukos, D.I., Sutclife, C., Warr, O., Ballentine, C.J., Onstott, T.C., Hosgormez, H., Neubeck, A., Marques, J.M., Pérez-Rodríguez, I., Rowe, A.R., LaRowe, D.E., Magnabosco, C., Yeung, L.Y., Ash, J.L., Bryndzia, L.T., 2017. The relative abundances of resolved 12CH2D2 and 13CH3D and mechanisms controlling isotopic bond ordering in abiotic and biotic methane gases. Geochimica et Cosmochimica Acta 203, 235—

- 264. https://doi.org/10.1016/j.gca.2016.12.041
- Young, E.D., Rumble, D., Freedman, P., Mills, M., 2016a. A large-radius high-mass-resolution multiple-collector isotope ratio mass spectrometer for analysis of rare isotopologues of O2, N2, CH4 and other gases. International Journal of Mass Spectrometry 401, 1–10. https://doi.org/10.1016/j.ijms.2016.01.006
- Young, E.D., Rumble, D., Freedman, P., Mills, M., 2016b. A large-radius high-mass-resolution multiple-collector isotope ratio mass spectrometer for analysis of rare isotopologues of O2, N2, CH4 and other gases. International Journal of Mass Spectrometry 401, 1–10. https://doi.org/10.1016/j.ijms.2016.01.006
- Yung, Y.L., Chen, P., Nealson, K., Atreya, S., Beckett, P., Blank, J.G., Ehlmann, B., Eiler, J., Etiope, G., Ferry, J.G., Forget, F., Gao, P., Hu, R., Kleinböhl, A., Klusman, R., Lefèvre, F., Miller, C., Mischna, M., Mumma, M., Newman, S., Oehler, D., Okumura, M., Oremland, R., Orphan, V., Popa, R., Russell, M., Shen, L., Sherwood Lollar, B., Staehle, R., Stamenković, V., Stolper, D., Templeton, A., Vandaele, A.C., Viscardy, S., Webster, C.R., Wennberg, P.O., Wong, M.L., Worden, J., 2018. Methane on Mars and Habitability: Challenges and Responses. Astrobiology 18, 1221–1242. https://doi.org/10.1089/ast.2018.1917
- Yurimoto, H., 2017. Oxygen Isotopes, in: White, W.M. (Ed.), Encyclopedia of Geochemistry: A Comprehensive Reference Source on the Chemistry of the Earth. Springer International Publishing, Cham, pp. 1–7. https://doi.org/10.1007/978-3-319-39193-9 346-1
- Zarrouk, S.J., McLean, K., 2019. Geothermal well test analysis: fundamentals, applications and advanced techniques. Academic Press, Elsevier, London San Diego, CA.
- Zazzeri, G., Graven, H., Xu, X., Saboya, E., Blyth, L., Manning, A.J., Chawner, H., Wu, D., Hammer, S., 2023. Radiocarbon Measurements Reveal Underestimated Fossil CH4 and CO2 Emissions in London. Geophysical Research Letters 50, e2023GL103834. https://doi.org/10.1029/2023GL103834
- Zazzeri, G., Lowry, D., Fisher, R.E., France, J.L., Lanoisellé, M., Grimmond, C.S.B., Nisbet, E.G., 2017. Evaluating methane inventories by isotopic analysis in the London region. Sci Rep 7, 4854. https://doi.org/10.1038/s41598-017-04802-6
- Zeebe, R.E., Wolf-Gladrow, D.A., 2001. CO<sub>2</sub> in seawater: equilibrium, kinetics, isotopes, Elsevier oceanography series. Elsevier, Amsterdam; New York.
- Zerr, A., Serghiou ,G., Boehler ,R., and Ross, M., 2006. Decomposition of alkanes at high pressures and temperatures. High Pressure Research 26, 23–32. https://doi.org/10.1080/08957950600608931
- Zgonnik, V., 2020. The occurrence and geoscience of natural hydrogen: A comprehensive review. Earth-Science Reviews 203, 103140. https://doi.org/10.1016/j.earscirev.2020.103140
- Zhang, N., Prokhorov, I., Kueter, N., Li, G., Tuzson, B., Magyar, P.M., Ebert, V., Sivan, M., Nakagawa, M., Gilbert, A., Ueno, Y., Yoshida, N., Röckmann, T., Bernasconi, S.M., Emmenegger, L., Mohn, J., 2025. Rapid High-Sensitivity Analysis of Methane Clumped Isotopes (Δ13CH3D and Δ12CH2D2) Using Mid-Infrared Laser Spectroscopy. Anal. Chem. 97, 1291–1299. https://doi.org/10.1021/acs.analchem.4c05406
- Zhang, N., Snyder, G.T., Lin, M., Nakagawa, M., Gilbert, A., Yoshida, N., Matsumoto, R., Sekine, Y., 2021. Doubly substituted isotopologues of methane hydrate (13CH3D and 12CH2D2): Implications for methane clumped isotope effects, source apportionments and global hydrate reservoirs. Geochimica et Cosmochimica Acta 315, 127–151. https://doi.org/10.1016/j.gca.2021.08.027
- Zhang, T., Krooss, B.M., 2001. Experimental investigation on the carbon isotope fractionation of methane during gas migration by diffusion through sedimentary rocks at elevated temperature and pressure. Geochimica et Cosmochimica Acta 65,

- 2723-2742. https://doi.org/10.1016/S0016-7037(01)00601-9
- Zhao, B., Robb, L.J., Harris, C., Jordaan, L.J., 2006. Origin of hydrothermal fluids and gold mineralization associated with the Ventersdorp Contact Reef, Witwatersrand Basin, South Africa: Constraints from S, O, and H isotopes, in: Processes on the Early Earth. Geological Society of America. https://doi.org/10.1130/2006.2405(17)
- Zhuo, Y., Hu, R., Xiao, J., Zhao, C., Huang, Y., Yan, J., Li, Jinwei, Gao, W., Li, Jinxiang, 2019. Trace elements and C-O isotopes of calcite from Carlin-type gold deposits in the Youjiang Basin, SW China: Constraints on ore-forming fluid compositions and sources. Ore Geology Reviews 113, 103067. https://doi.org/10.1016/j.oregeorev.2019.103067
- Zimmerman, P.R., Greenberg, J.P., Wandiga, S.O., Crutzen, P.J., 1982. Termites: A Potentially Large Source of Atmospheric Methane, Carbon Dioxide, and Molecular Hydrogen. Science 218, 563–565. https://doi.org/10.1126/science.218.4572.563
  Zou, C., 2017. Unconventional petroleum geology, 2nd ed. ed. Elsevier, Amsterdam.